Dynamics and breakdown in quantum Hall systems and quantum dots

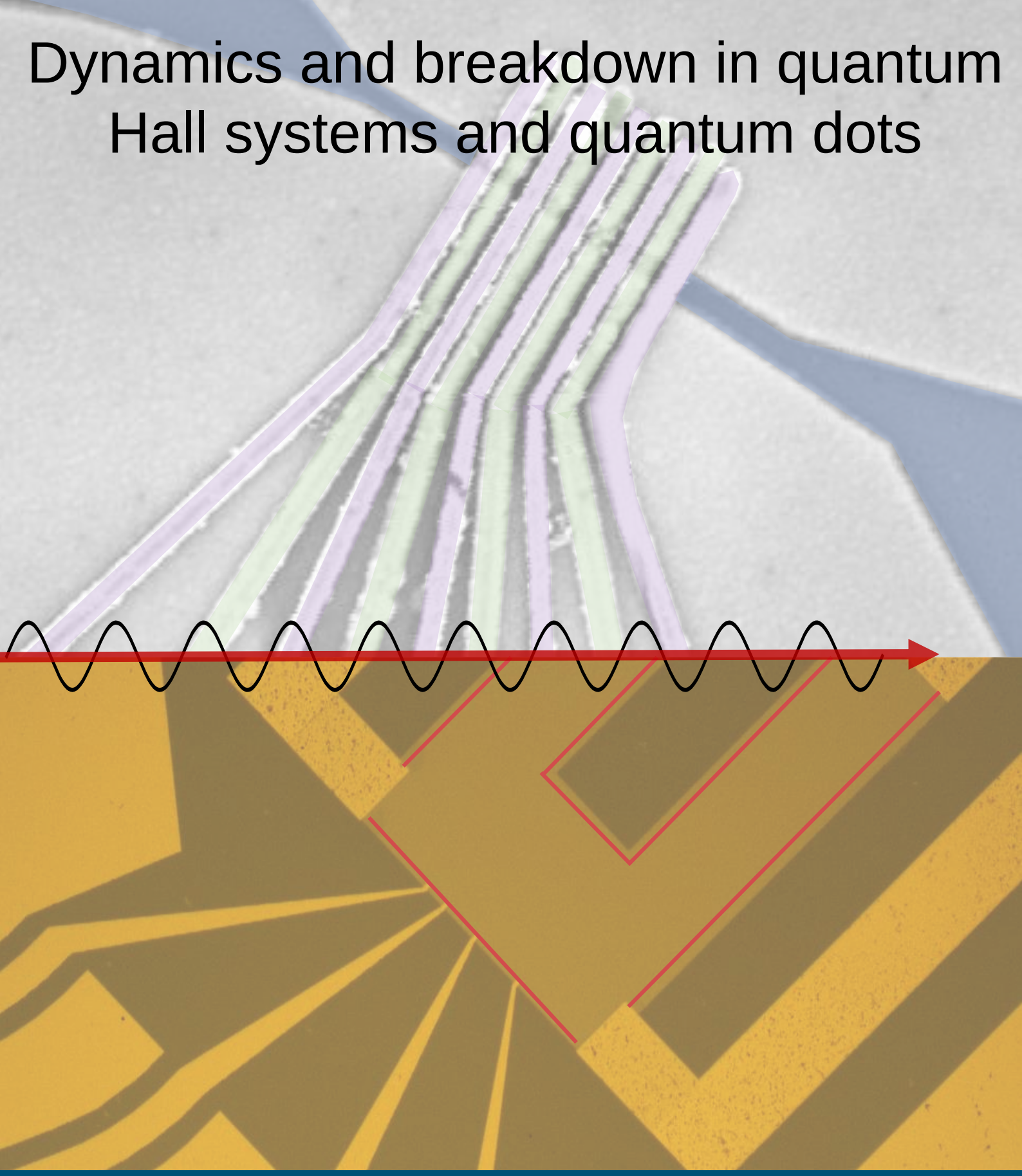

Torsten Röper

2026

UNIVERSITY OF COLOGNE

Dynamics and breakdown in quantum Hall systems and quantum dots

DOCTORAL THESIS

for
the award of the doctoral degree
of the Faculty of Mathematics and Natural Sciences
of the University of Cologne

submitted by

Torsten Röper

Köln, 2026

Abstract

High-frequency transport experiments provide access to relaxation, coherence, and interaction effects beyond the reach of dc measurements. The central objective of this thesis is to develop and apply radio-frequency techniques to probe the dynamical properties of charge transport in two complementary material platforms: quantum anomalous Hall (QAH) insulators and gate-defined quantum dots in bilayer graphene (BLG).

In the first part, edge plasmon propagation in QAH edge states formed in thin films of V-doped $(\mathrm{Bi},\mathrm{Sb})_2\mathrm{Te}_3$ is investigated using broadband, phase-resolved microwave measurements. The velocity and dissipation of edge plasmons are characterized as a function of frequency, excitation voltage, temperature, and magnetic field. Despite dissipationless transport in dc measurements, finite losses are observed at microwave frequencies, which are attributed to coupling between the chiral edge channel and localized bulk states.

The breakdown of quantized transport under strong electric fields is studied in both QAH and quantum Hall devices. Breakdown measurements reveal a crossover from a non-Ohmic to an Ohmic transport regime with increasing electric field. In QAH samples, Joule heating of localized bulk states is identified as the dominant dissipation mechanism.

In the second part, microwave transport in BLG quantum dots is explored as a route toward controlled single-electron emission at zero magnetic field. Low-frequency transport measurements establish the formation and tunability of gate-defined quantum dots, while radio-frequency excitation enables dynamical control of the dot potential. Although quantized single-electron emission is not yet achieved, we identify the key limitations of the current device architecture and outline a path toward a reliable single-electron source in BLG.

Together, these results establish microwave-based transport techniques as a powerful tool for studying both collective and single-particle charge dynamics in low-dimensional quantum conductors. Potential future applications of the high-frequency methods developed in this thesis include reduced-dissipation QAH plasmonics, interaction-induced charge fractionalization, and time-resolved investigations of hybrid BLG–superconductor systems.

Contents

Introduction

Understanding how electrons propagate, dissipate energy, and interact in low-dimensional systems is a central topic of modern condensed-matter physics. When charge transport is confined to one-dimensional channels, interactions and disorder govern the dynamics and fundamentally modify the nature of transport. High-frequency techniques provide essential tools for probing transport characteristics such as relaxation processes, coherence, and the breakdown of quantized transport in such systems, as they access dynamical properties that remain hidden in dc measurements.

This thesis develops experimental techniques for the high-frequency study of zero- and one-dimensional electronic systems. We apply radio-frequency (rf) methods to two complementary regimes. First, the chiral edge channels of a quantum anomalous Hall (QAH) system form a one-dimensional system in which we study the collective response (edge plasmons) of the edge excitations. Second, we explore a zero-dimensional system in the form of a quantum dot in bilayer graphene, creating a mesoscopic capacitor with the goal of realizing controlled electron emission. Together, these experiments examine how collective excitations and individual electrons move through zero- and one-dimensional systems, and how this motion is affected by imperfections in the material, applied electric fields, and externally controlled parameters.

The central goal of this thesis is to develop and apply high-frequency techniques for probing the dynamical transport properties of zero- and one-dimensional quantum conductors. In the following, we will introduce the main concepts of this work, starting with a short review of transport in quantum Hall (QH) systems.

Quantum Hall effects and chiral edge transport

The QH effect, discovered in 1980 by von Klitzing [2], manifests itself when a two-dimensional electron gas is subjected to strong perpendicular magnetic fields (a few T) at low temperatures (below a few K). Under these conditions, the Hall resistance R_{yx} becomes quantized for certain magnetic fields, as shown

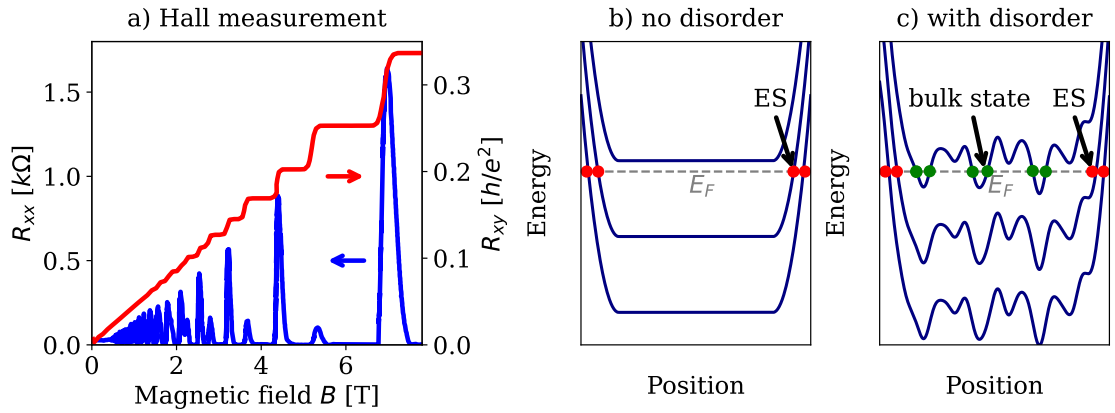

Figure 1: Quantum Hall effect. (a) Hall (R_{yx}) and longitudinal (R_{xx}) resistances of a GaAs/AlGaAs two-dimensional electron gas as a function of magnetic field. Reprinted from Ref. [1]. (b) Bending of Landau levels (blue lines) near the sample edge in the absence of disorder. Where Landau levels cross the Fermi level E_F, chiral edge states (ES) (red dots) emerge in an otherwise insulating bulk. (c) Same as (b) with local density fluctuations due to disorder, which creates localized bulk states (green dots).

in Fig. 1a, and develops plateaus at

$$R_{\mathrm{yx}} = \frac{h}{ne^2}, \tag{1}$$

where h is Planck's constant, e the elementary charge, and n the integer filling factor (corresponding to the number of filled Landau levels as shown for $n = 2$ on Fig. 1b). On these plateaus, the longitudinal resistance R_{xx} vanishes [2].
This quantization originates from the formation of discrete Landau levels in the bulk, together with the emergence of one-dimensional chiral edge channels at the sample boundaries, schematically shown in Fig. 1b and Fig. 2a. Each edge channel constitutes a single one-dimensional transport mode with a quantized two-terminal conductance of e^2/h. On the other hand, the bulk is insulating, meaning that backscattering between counter-propagating edge states on opposite sides of the sample is suppressed, resulting in dissipationless transport along the edge states.
Disorder plays a crucial role in this regime. It manifests in local density fluctuations as shown in Fig. 1c. In the absence of disorder, the plateau would correspond to a single point in the magnetic field. Local density fluctuations lead to localized bulk states that extend the quantized Hall plateau over a range of magnetic fields, thereby stabilizing the QH plateau. At the same time, these localized states can mediate hopping conduction when thermally or electrically activated [3, 4]. Strong electric fields or high current densities can therefore

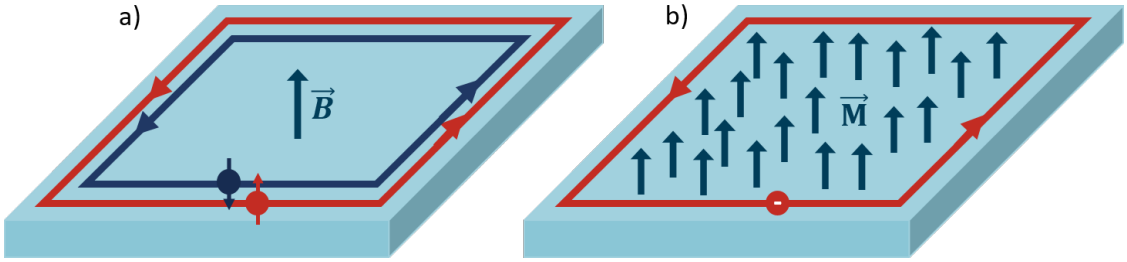

Figure 2: Quantum Hall vs. quantum anomalous Hall. (a) Quantum Hall effect: an external magnetic field B forms Landau levels in the electron gas (bright blue slab), giving rise to chiral edge states (blue/red). (b) Quantum anomalous Hall effect: a thin magnetic insulator exhibits a spontaneous magnetization M, resulting in a single chiral edge state (red) in the absence of an external field.

drive the system into a breakdown regime where dissipation emerges. Since breakdown mechanisms form a central theme of this thesis, we will later revisit how bulk activation, field-assisted hopping, and electron heating destroy quantization under strong driving. Before, we will introduce the QAH effect in the following section.

Quantum anomalous Hall insulators

The QAH effect shares the defining features of an insulating bulk and chiral edge states with the QH effect, as illustrated in Fig. 2, but arises in the absence of an external magnetic field. In QAH insulators, time-reversal symmetry is broken by intrinsic magnetism instead of external magnetic fields, allowing the state to persist at zero magnetic field. The ferromagnetic order is typically introduced via magnetic dopants such as Cr or V incorporated into a topological insulator host material [5]. In this work, we study thin films of the magnetic topological insulator V-doped $(Bi_xSb_{1-x})_2Te_3$, whose band structure exhibits a nonzero Chern number and supports a single chiral edge state at zero magnetic field.
The QAH effect was first realized experimentally by Chang et al. [5] in 2013 in Cr-doped $(Bi_xSb_{1-x})_2Te_3$. Since then, QAH states have been observed in several other material platforms, including intrinsic magnetic topological insulators such as $MnBi_2Te_4$ [6], as well as moiré heterostructures such as twisted bilayer graphene [7], rhombohedral graphene [8], and $MoTe_2/WSe_2$ [9]. More recently, fractional QAH states have been reported in twisted rhombohedral bilayers of $MoTe_2$ [10, 11] and in pentalayer graphene/hBN moiré systems [12], extending fractional QH physics to the zero-field limit [13, 14]. These developments underscore the continued interest in QAH physics and its potential for realizing topological transport phenomena without external magnetic fields.

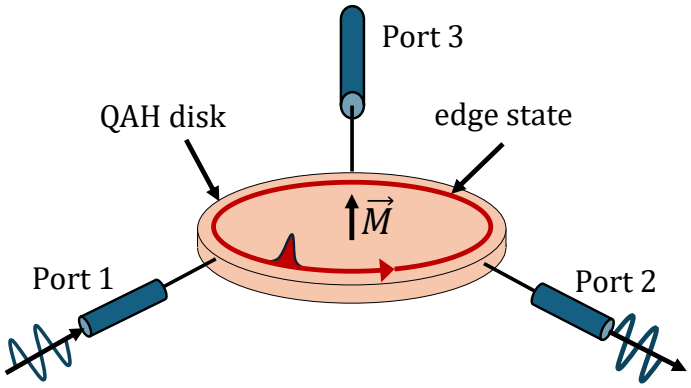

Figure 3: Quantum anomalous Hall circulator. Schematic of a microwave circulator based on a QAH disk. A signal injected at port 1 propagates chirally along the edge and is transmitted to port 2, while being isolated from port 3. The circulation direction is set by the magnetization M.

Plasmonics and microwave transport in chiral edge states

Chiral edge channels support not only dc transport but also propagating charge-density excitations, commonly referred to as edge plasmons. Owing to their velocities of $v_\mathrm{p} \sim 3\text{–}5 \times 10^5\,\mathrm{m/s}$, these modes are promising building blocks for compact on-chip interferometers and nonreciprocal microwave devices. The chiral edge channel acts as an effective microwave gyrator, i.e., a nonreciprocal two-port element that introduces different phase shifts for opposite propagation directions. Combined with capacitive coupling between multiple ports, this gyrator-like response enables the realization of a three-port microwave circulator [15, 16].

A QAH-based circulator is schematically illustrated in Fig. 3. A microwave signal injected at port 1 propagates chirally along the edge of the QAH disk and is transmitted to port 2, while being strongly suppressed at port 3. This nonreciprocal signal routing arises from interference between direct capacitive coupling and the chiral propagation of edge magnetoplasmons around the disk.

Mahoney et al. [16] demonstrated a proof-of-principle nonreciprocal microwave circulator based on a QAH disk, achieving a circulation amplitude of approximately 20 dB. However, more recent experiments in QAH materials have revealed unexpectedly strong damping of edge plasmons [17]. This dissipation is commonly attributed to capacitive and resistive coupling between the chiral edge channel and disorder-induced charge puddles in the bulk [18, 19], which limits the performance of QAH-based plasmonic devices at microwave frequencies. So far, dissipation has been discussed in the regime of low electric fields.

At higher electric fields, however, additional dissipation channels emerge, ultimately leading to the breakdown of quantized transport, as discussed in the following section.

Breakdown of quantized transport

When the applied electric field becomes sufficiently strong, the dissipationless transport in QH systems breaks down. In this regime, localized bulk states may become electrically or thermally activated, enabling charge transport through the bulk and leading to the breakdown of quantized Hall plateaus. Breakdown is typically accompanied by electronic heating, an increase in longitudinal resistance, and a loss of precise Hall quantization.
A wide range of low-frequency and dc transport experiments have investigated breakdown phenomena in QH and QAH systems [4, 20–26]. These studies have associated breakdown with mechanisms such as electric-field–assisted hopping between localized states, avalanche-type processes, and Joule heating of the electronic system. While these approaches have established a general phenomenology of breakdown, the relative importance of field-driven and heating-driven mechanisms remains an active topic of discussion and depends sensitively on material properties, disorder, and geometry.
In contrast, breakdown under high-frequency or time-dependent driving has received little attention, although it is relevant for rf applications. In this regime, the drive frequency and electronic relaxation times introduce additional energy scales, which can affect the onset and characteristics of breakdown. Understanding these effects is important for determining the operational limits of QH–based devices.

Single-electron sources in bilayer graphene

Complementary to the collective plasmonic regime, single-electron sources (SES) provide controlled access to the transport of individual charge carriers. SES devices enable the on-demand emission of single electrons and allow interference-based experiments analogous to those in quantum optics [27–29]. In QH systems, such experiments typically rely on magnetic fields to confine electrons in mesoscopic capacitors.
The same operating principle can, however, be transferred to other material platforms. In particular, quantum dots offer a versatile approach for the controlled

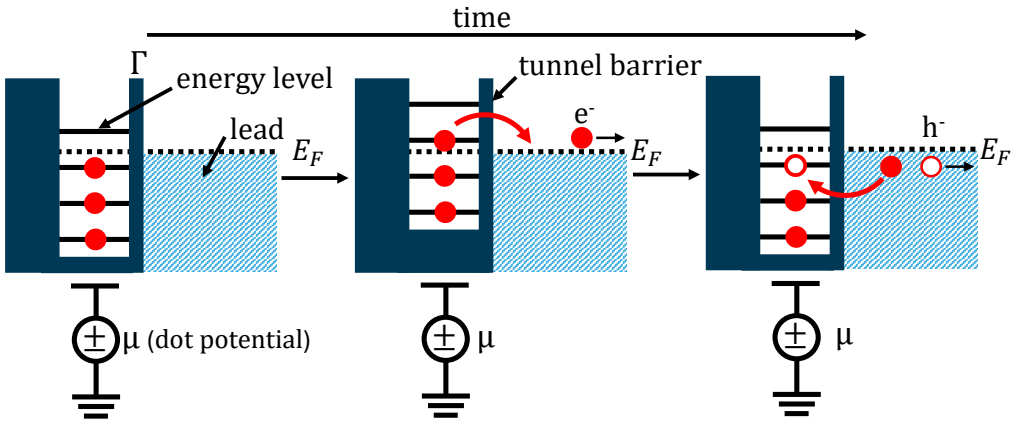

Figure 4: Single-electron source based on a mesoscopic capacitor. Schematic of a quantum dot tunnel-coupled to a lead with transparency Γ. The dot electrochemical potential μ is modulated by an rf gate. Raising μ above the Fermi level emits a single electron into the lead, while returning μ to its initial value emits a hole, completing one cycle.

trapping and emission of single electrons. Bilayer graphene (BLG) is a promising candidate due to its high carrier mobility, long phase-coherence lengths, and strong electrostatic tunability [30–32]. Several dc and low-frequency studies have demonstrated the formation of electrostatically defined quantum dots in BLG [32–34]. The quantum dot hosts discrete energy levels as illustrated in Fig. 4 and is connected to a lead via a controllable tunnel barrier with rate Γ.
On-demand single-electron emission can be achieved by periodically modulating the electrochemical potential of the dot using rf excitation. During one half-cycle, a dot level is driven above the Fermi energy E_F of the lead, allowing a single electron to tunnel into the lead. During the opposite half-cycle, the level is driven below E_F, and an electron tunnels back into the dot, corresponding to the emission of a hole. In contrast to QH–based implementations, this approach relies solely on electrostatic confinement and time-dependent gating. As a result, a zero-field SES based on BLG is compatible with superconducting hybrid structures and provides a flexible platform for studying single-particle dynamics in tunable mesoscopic systems.

Thesis overview

The thesis is organized as follows:

- **Chapter 1** introduces radio-frequency transport, transmission lines, and edge plasmons, and develops the theoretical tools used throughout the thesis.

- **Chapter 2** presents the condensed-matter background relevant for transport experiments in magnetic topological insulators, including the quantum anomalous Hall effect, electron–hole puddles, and variable-range hopping.
- **Chapter 3** reports broadband microwave measurements of plasmon propagation in QAH edge channels and analyzes their velocity, damping, and gate coupling, with implications for QAH-based microwave circuits.
- **Chapter 4** investigates the electric field-driven breakdown of quantized Hall transport in QAH and graphene devices, focusing on the role of bulk transport and electronic heating under strong driving.
- **Chapter 5** explores radio-frequency transport in BLG quantum dots at zero magnetic field and examines their operation as on-demand single-electron sources.
- **Chapter 6** summarizes the main results and discusses perspectives for microwave transport and single-electron control in low-dimensional systems.

Chapter 1

Radio-frequency transport in mesoscopic systems

All experiments in this thesis share the common feature that they employ electrical transport measurements in the radio-frequency (rf) range. The rf regime spans frequencies from approximately 30 MHz to 300 GHz, corresponding to electromagnetic wavelengths $\lambda = c/f$ between 10 m and 1 mm in vacuum ($c \simeq 3 \times 10^8\,\mathrm{m/s}$). A wide range of modern technologies use rf signals, including radio broadcasting, radar systems, cellular communication, wireless local area networks (WLAN), global positioning systems (GPS), and Bluetooth. In most of these applications, electromagnetic waves are emitted and detected using antennas that radiate energy into free space.

From a physics perspective, rf measurements provide access to the dynamical response of mesoscopic systems. Unlike dc and low-frequency transport experiments, which probe only static conductance, rf signals can resolve propagation velocities and relaxation mechanisms. For this reason, rf and microwave techniques are now routinely used in superconducting circuits, for example, in the readout and control of superconducting qubits [35, 36], or in the study of 1D systems such as carbon nanotubes [37] and edge states in the QH and QAH regimes [38, 39]. In these systems, the charge carriers form collective modes whose dynamics occur at microwave frequencies, making rf transport a sensitive probe of interactions, disorder, and energy relaxation.

In our experiments, rf signals need to be guided rather than radiated. Transmission lines such as coaxial cables or coplanar waveguides confine the electromagnetic fields between conductors and allow controlled, low-loss routing of signals to a cryogenic device. The same transmission line concepts that describe these engineered structures also provide a framework for understanding mesoscopic conductors themselves. In particular, the propagating charge excitations (plasmons) of a 1D electronic channel can be mapped to an effective transmission line.

This can be applied to QH and QAH edge states, where chirality suppresses backscattering and leads to well-defined, unidirectional plasmon modes whose velocity and dissipation can be measured with rf techniques.
In this thesis, we make use of this unified description: transmission lines guide the rf signals from the source to the sample, define how the device is coupled to the measurement environment, and are ultimately used to describe the charge propagation in the edge state. The rf engineering concepts introduced here reappear throughout this thesis: in Chapter 3 when modeling edge plasmon propagation and impedance mismatch, in Chapter 4 when quantifying field-driven breakdown via microwave transport, and in Chapter 5 when driving and detecting a single-electron source with rf signals. To establish the necessary background, this chapter is structured as follows.
We begin with a detailed discussion of transmission line theory in Sec. 1.1, since most of the experimentally relevant features can be expressed in this language. We introduce the basic theory of transmission lines and microwave networks, including distributed circuit models, scattering parameters, and impedance matching. These concepts form the foundation for analyzing rf transport in mesoscopic devices.
In Sec. 1.2, we apply this formalism to plasmon transport in 1D edge states. We show explicitly how edge channels can be modeled as transmission lines, discuss their dispersion and dissipation mechanisms, and describe their capacitive coupling to external gates and coplanar waveguides.
Finally, in Sec. 1.3, we present the rf measurement setup, including the cryogenic wiring, vector network analyzers, amplifiers, attenuators, and filters used throughout this thesis. We also discuss calibration techniques required to correct distortions introduced by the setup itself at high frequencies.

1.1 Transmission line theory

Two transmission line geometries are used throughout this thesis. The first is the coaxial geometry, which is the standard for commercial rf cables. Its cross-section is shown in Fig. 1.1a. Here, the electromagnetic field is confined in the dielectric region between the inner conductor and the cylindrical outer conductor, which acts as the ground. This geometry is mechanically robust and can be bent without degrading its electrical properties.
On-chip routing, however, is restricted to planar structures. Therefore, we use

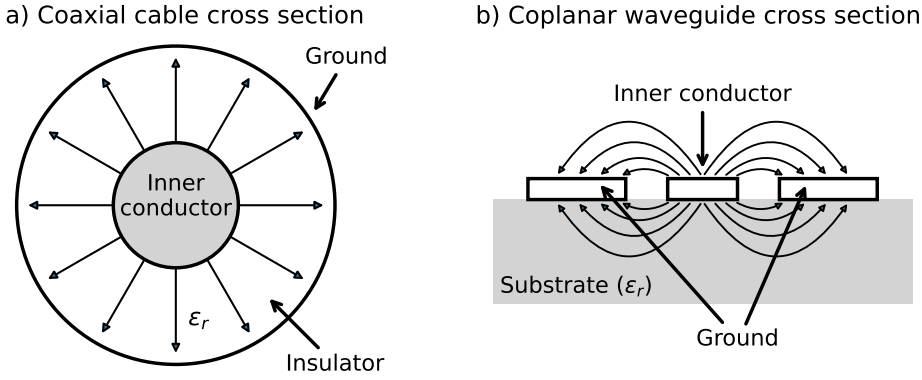

Figure 1.1: Transmission lines. a) Sketch of the cross-section of a coaxial cable. The electric field is confined in the dielectric insulator between the inner conductor and the ground, as highlighted by the arrows. b) Cross-section of a coplanar waveguide on top of a substrate with permittivity ϵ_r. The electric field is again confined between the inner conductor and the ground in an elliptic shape, as schematically illustrated by the arrows.

coplanar waveguides (CPWs), shown in Fig. 1.1b. CPWs consist of a central conductor flanked by two ground planes, all defined in a single metallic layer on top of a dielectric substrate. Their planar geometry allows for arbitrary routing in two dimensions and direct integration with lithographically patterned devices. In this work, CPWs are used both on the printed circuit board (PCB) sample holder and directly on the InP substrate.

In this subsection, we briefly summarize the standard transmission line formalism needed later to model both coaxial cables and chiral edge channels. Readers familiar with microwave engineering may skim this section and refer back as needed. These concepts will later allow us to interpret measured scattering parameters in terms of plasmon propagation along the edge channel and to identify distortions arising from impedance mismatch and standing waves, which play a central role in Chapter 3.

At rf frequencies, the physical size of a circuit becomes comparable to the wavelength. In this regime, standard lumped-element circuit theory is insufficient, and wave propagation must be taken into account. Transmission lines are therefore described using distributed circuit models, where voltage and current depend on both position and time. This is justified in the quasi–transverse electromagnetic (quasi-TEM) regime, where the electromagnetic fields are predominantly transverse to the propagation direction. We can do this approximation as long as the wavelength is much larger than the transverse dimensions of the line [40, 41].

An infinitesimal segment of a general transmission line is shown in Fig. 1.2. Each

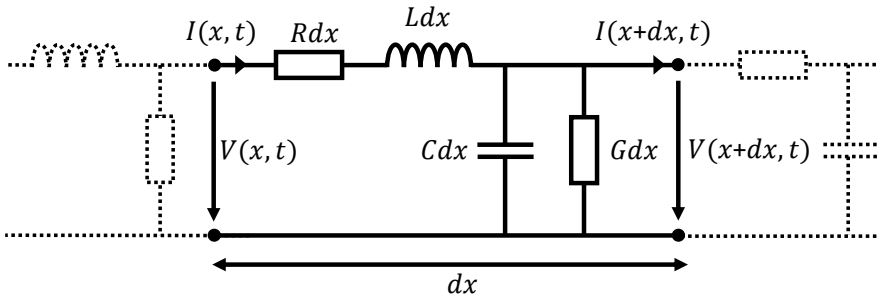

Figure 1.2: Distributed circuit model of a transmission line. Infinitesimal segment of a transmission line of length dx. On this scale, the line can be described using lumped elements: series inductance L and series resistance R, and shunt capacitance C and shunt conductance G, all defined per unit length.

segment is characterized by four quantities, which are all given per unit length:

- **Shunt capacitance** C: the geometric capacitance between the inner and outer conductors,
- **Series inductance** L: the self-inductance of the conductors,
- **Series resistance** R: representing Ohmic losses in the metal,
- **Shunt conductance** G: modeling dielectric losses in the dielectric material.

Applying Kirchhoff's current and voltage laws to this distributed network yields the time-domain telegrapher's equations [40]:

$$\frac{dV(x,t)}{dx} = -R\,I(x,t) - L\frac{dI(x,t)}{dt}, \tag{1.1a}$$

$$\frac{dI(x,t)}{dx} = -G\,V(x,t) - C\frac{dV(x,t)}{dt}. \tag{1.1b}$$

For a sinusoidal signal at angular frequency ω, we write $V(x,t) = V(x)e^{i\omega t}$ and $I(x,t) = I(x)e^{i\omega t}$. Inserting this into Eq. (1.1) gives:

$$\frac{dV(x)}{dx} = -(R + i\omega L)\cdot I(x), \tag{1.2a}$$

$$\frac{dI(x)}{dx} = -(G + j\omega C)\cdot V(x). \tag{1.2b}$$

Differentiating the first equation and substituting the second yields a wave equation for the voltage:

$$\frac{d^2V(x)}{dx^2} = \gamma^2 V(x), \tag{1.3}$$

with the propagation constant

$$\gamma = \sqrt{(R + i\omega L)(G + i\omega C)} = \alpha + i\beta, \tag{1.4}$$

where α describes attenuation and β describes phase evolution. The general solutions are:

$$V(x) = V_0^+ e^{-\gamma x} + V_0^- e^{+\gamma x}, \tag{1.5a}$$

$$I(x) = I_0^+ e^{-\gamma x} + I_0^- e^{+\gamma x}, \tag{1.5b}$$

corresponding to forward- and backward-propagating waves. Using the first telegrapher equation, we obtain the characteristic impedance Z:

$$Z = \frac{V_0^+}{I_0^+} = -\frac{V_0^-}{I_0^-} = \sqrt{\frac{R + i\omega L}{G + i\omega C}}. \tag{1.6}$$

The impedance relates the magnitudes of the electric and magnetic fields. In a vacuum, electromagnetic waves propagate with a characteristic impedance of $Z_0 = \sqrt{\mu_0/\epsilon_0} \approx 376\,\Omega$. The characteristic impedance also controls how signals reflect at interfaces. For an incident wave at the interface from an impedance Z_1 to Z_2, the reflection and transmission coefficients are:

$$r = \frac{Z_2 - Z_1}{Z_2 + Z_1}, \qquad t = \frac{2Z_2}{Z_2 + Z_1}, \tag{1.7}$$

which can be derived by solving the equations of current and power conservation. In Chapter 3, we will see that the strong impedance mismatch between the edge channel and the $50\,\Omega$ environment produces pronounced reflection patterns in the measured transmission spectra, which can only be understood using these relations. The other quantity of interest describing the propagation of a wave in a transmission line is its phase velocity v_p. We can find it by describing the voltage in the time domain as:

$$V(x,t) = |V_0^+| \cdot \cos(\omega t - \beta x + \phi^+) \cdot e^{-\alpha x} + |V_0^-| \cdot \cos(\omega t + \beta x + \phi^-) \cdot e^{\alpha x} \tag{1.8}$$

where $\phi^\pm$ is the phase of the complex voltages $V_0^\pm$. The phase velocity is given by $v_p = \omega/\beta$. Losses are described by the constant α, which describes the decay of the amplitude by unit length. Losses stem from the imaginary part of Eq. 1.6, e.g., a finite resistance R. For a lossless transmission line where the series resistance R and the shunt conductance G are zero, we find the following expression for

the impedance and velocity:

$$Z = \sqrt{\frac{L}{C}}, \qquad v_p = \frac{1}{\sqrt{LC}}. \tag{1.9}$$

Beyond the circuit description, it is useful to view a transmission line as a continuum of harmonic oscillators. The Hamiltonian H of a transmission line is given by:

$$H = \frac{1}{2}\int dx \left[\frac{q(x,t)^2}{C} + L\, I(x,t)^2\right], \tag{1.10}$$

where $q = CV$ is the charge per unit length. This will allow us in the next section to map the bosonized edge-state Hamiltonian to an effective transmission line [37].

1.2 Plasmon transport in 1D edge states

We now turn to charge propagation in 1D chiral edge states. The discussion applies equally to edge modes of the QH and QAH effects, as long as the charge is confined to a 1D channel. At low excitation amplitudes, transport is governed by collective density oscillations, which are referred to as edge plasmons. We derive the plasmon Hamiltonian and show explicitly that the edge channel is equivalent to a transmission line.

Single-particle description

In the absence of interactions, we can write the Hamiltonian of the 1D system with a fixed number of electrons as:

$$H = \sum_k \epsilon(k)\, c^\dagger(k) c(k), \tag{1.11}$$

where $c^\dagger(k)$ and $c(k)$ are the fermionic creation and annihilation operators for an electron with quasi-momentum k. For a chiral edge state, the dispersion relation is linear[1] [43, 44]:

$$\epsilon(k) = \hbar v_F k, \tag{1.12}$$

where v_F is the Fermi velocity. Since only one propagation direction exists, exciting an electron from momentum k to $k' = k + q$ necessarily creates a hole at k, as

[1] This is correct for a QAH edge state. Other 1D electronic systems feature a parabolic dispersion relation. However, also for a parabolic dispersion, the low-energy excitations are quasi-linear and can be described by the same bosonization scheme [42].

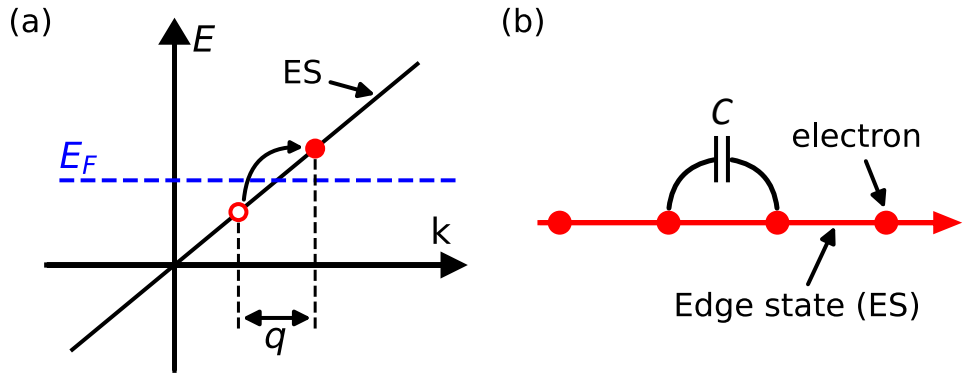

Figure 1.3: Edge transport schematics. (a) Linear dispersion of a chiral edge state (ES). Exciting an electron above the Fermi level leaves a hole behind, forming an electron–hole pair of momentum q. (b) Real-space picture of a chiral edge channel. Coulomb repulsion (schematically represented by a capacitance C) leads to collective, plasmonic transport.

schematically shown in Fig. 1.3a. The excitation, therefore, carries a well-defined momentum q and an energy

$$\varepsilon(q) = \varepsilon(k+q) - \varepsilon(k) = \hbar v_F q. \tag{1.13}$$

Thus, all particle–hole excitations disperse linearly, which is characteristic of chiral 1D systems. And it allows us to describe the system as a collective bosonic system, as we will outline in the following section.

Bosonization

Before introducing the bosonization scheme, it is helpful to recall why a bosonic description naturally appears in a 1D chiral system. Since all electrons propagate in the same direction, the relevant low-energy excitations can be seen as small deformations of the filled Fermi sea rather than individual particles. These particle–hole excitations add coherently and can be treated as a single collective charge mode. Bosonization provides a compact way to describe this collective degree of freedom. To formalize this idea, we reorganize the particle–hole excitations into bosonic operators [45]. For $q > 0$, we define

$$b^\dagger(q) = \sqrt{\frac{2\pi}{Lq}} \sum_k c^\dagger(k+q)c(k), \qquad b(q) = \sqrt{\frac{2\pi}{Lq}} \sum_k c^\dagger(k-q)c(k), \tag{1.14}$$

where the prefactor ensures proper normalization. These operators satisfy the canonical commutation relation

$$[b(q), b^\dagger(q')] = \delta_{q,q'}, \tag{1.15}$$

demonstrating that the elementary excitations of the chiral edge are bosonic plasmons rather than fermionic quasiparticles [37, 42]. The next step is to express these excitations in real space. Introducing the bosonic field operator $\phi(x)$,

$$\phi(x) = -i \sum_{q>0} \sqrt{\frac{2\pi}{Lq}}\, b(q)\, q\, e^{iqx} + i \sum_{q<0} \sqrt{\frac{2\pi}{Lq}}\, b^\dagger(q)\, q\, e^{-iqx}. \tag{1.16}$$

We obtain a continuum description in which $\phi(x)$ plays the role of a displacement field for the chiral plasmon. Its spatial derivative encodes the local variation of the charge density,

$$\rho(x) = \frac{1}{2\pi} \frac{d\phi(x)}{dx}. \tag{1.17}$$

Inserting this form into the fermionic Hamiltonian yields the quadratic bosonic Hamiltonian,

$$H = \frac{hv_F}{2} \int \rho(x)^2\, dx = \frac{\hbar v_F}{4\pi} \int \left(\frac{d\phi(x)}{dx}\right)^2 dx. \tag{1.18}$$

This compact expression is the central result of chiral bosonization: the complex many-fermion problem reduces to a single elastic mode whose dynamics are governed by spatial gradients of the bosonic field. In later sections, we will show how this Hamiltonian maps directly onto that of a lossless transmission line, allowing us to describe the edge channel using familiar rf concepts such as inductance, capacitance, and impedance. A detailed pedagogical derivation can be found in the lecture notes of C. L. Kane [42].

Including Coulomb interactions

So far, we have described the edge state as a 1D system of non-interacting electrons. In reality, electrons in an edge state are subject to Coulomb interactions. Because the system is chiral and backscattering is forbidden, these interactions do not lead to counter-propagating modes, but instead modify the propagation of the charge density itself. One may picture this as electrons "pushing" each other forward, as sketched in Fig. 1.3b, which results in a collective plasmon mode with an interaction-renormalized velocity. To leading order, Coulomb

interactions contribute an additional quadratic term in the density fluctuations,

$$H_{\text{int}} \propto \int \rho^2(x)\, dx, \tag{1.19}$$

since regions of enhanced charge density increase the electrostatic energy. Substituting the bosonized expression for $\rho(x)$ yields

$$H_{\text{int}} = \frac{g}{(2\pi)^2} \int \frac{1}{2} \left(\frac{d\phi(x)}{dx} \right)^2 dx, \tag{1.20}$$

where g parametrizes the interaction strength. The Coulomb interaction renormalizes the plasmon velocity. Adding both contributions yields the total Hamiltonian:

$$H = \frac{\hbar v}{4\pi} \int \left(\frac{d\phi(x)}{dx} \right)^2 dx, \tag{1.21}$$

with

$$v = v_F \left(1 + \frac{g}{h v_F} \right). \tag{1.22}$$

Thus, strong Coulomb interactions increase the velocity of plasmon propagation, a key effect that has been observed in experiments [18, 46].

1.2.1 Transmission line model of edge state transport

The bosonized Hamiltonian in Eq. (1.21) is mathematically identical to that of a lossless transmission line. To make this correspondence explicit, we express the bosonic fields in terms of physical charge and current densities:

$$q_e(x) = -e\, \rho(x) = \frac{-e}{2\pi} \frac{d\phi}{dx}, \tag{1.23a}$$

$$I_e(x) = -e\, \rho(x)\, v = \frac{-ev}{2\pi} \frac{d\phi}{dx}. \tag{1.23b}$$

Substituting these relations into Eq. (1.21) gives:

$$H = \frac{1}{2} \int dx \left[\frac{hv}{e^2}\, q_e(x)^2 + \frac{h}{ve^2}\, I_e(x)^2 \right]. \tag{1.24}$$

Comparing with the Hamiltonian of a classical transmission line,

$$H_{\text{TL}} = \frac{1}{2} \int dx \left(\frac{1}{c_e} q^2 + l_e I^2 \right). \tag{1.25}$$

We identify the effective line parameters:

$$c_e = \frac{1}{vR_K}, \qquad l_e = \frac{R_K}{v}, \tag{1.26}$$

where $R_K = h/e^2$ is the von Klitzing constant. Accordingly, the characteristic impedance is

$$Z_e = \sqrt{\frac{l_e}{c_e}} = R_K. \tag{1.27}$$

Thus, a chiral edge channel behaves exactly like a 1D transmission line with quantized impedance. The coincidence of the characteristic impedance with the von Klitzing constant R_K is not accidental: it encodes the fact that the edge channel supports a single conductance quantum e^2/h of current per applied voltage. In practice, this means that the microwave response of the edge channel can be treated exactly as the response of a transmission line with these parameters. This viewpoint forms the basis of the fitting model used in Chapter 3 to extract velocities and dissipation rates from the measured scattering parameters.
Before discussing the coupling from the gate contacts to the edge state, we briefly summarize the physical origin of its inductance and capacitance:

- **Inductance l_e:** The total inductance is the sum of magnetic and kinetic contributions. While the magnetic inductance is small ($\sim 1\,\mathrm{pH/\mu m}$ [37]), the kinetic inductance of a 1D channel is extremely large, $l_K = \frac{R_K}{v_F} \simeq 64\,\mathrm{nH/\mu m}$, and therefore dominates the dynamics.

- **Capacitance c_e:** The total capacitance has a geometric component ($\sim 50\,\mathrm{pF/m}$ for an ungated edge [37]) and a quantum contribution, $c_q = \frac{1}{R_K v_F} \simeq 100\,\mathrm{pF/m}$, arising from the finite density of states of the 1D system. The geometric component was neglected in the derivation, but since they are of similar size, both must be accounted for to describe the plasmon velocity accurately in an experiment.

1.2.2 Coupling of the edge channel to a gate

After establishing transmission lines as a framework to model our setup and the plasmon transport in the edge state, the only missing component is the capacitive coupling of an edge state to the setup. We describe the capacitive coupling via the effective capacitance C_g, which corresponds to the series of a geometric

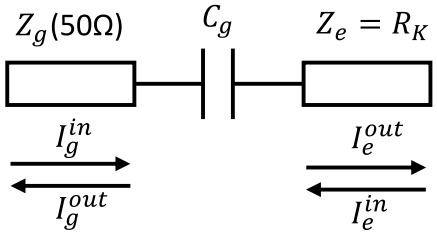

Figure 1.4: Capacitive coupling of the edge channel to a gate. Equivalent transmission line circuit of the gate with impedance Z_g and the edge channel with impedance Z_e via a capacitor C_g. The incoming currents $I_{g,e}^{\mathrm{IN}}$ and outgoing currents $I_{g,e}^{\mathrm{OUT}}$ are illustrated as arrows.

capacitance C_{geo} and a quantum capacitance C_e:

$$C_g = \frac{C_{geo} \cdot C_e}{C_{geo} + C_e} \tag{1.28}$$

The equivalent transmission line model is shown in Fig. 1.4: the rf gate has an impedance of 50 Ω and is coupled via C_g to the edge state with impedance R_K. This description is only valid for short gates or sufficiently low frequencies, such that the phase accumulated by the plasmon underneath the gate remains small, $\phi = \omega L/v$. Otherwise, the finite spatial extent of the gate must be taken into account. In our experiments, we use narrow contacts of approximately 3 µm and frequencies below 4 GHz. Under these conditions, the accumulated phase remains small, justifying the use of a lumped capacitance C_g to describe the capacitive coupling. For wider contacts or higher frequencies, the coupling depends on the accumulated charge density below the gate $\rho \propto \int \sin(\phi)$.
We are interested in the scattering parameter that describes the transmission and reflection of the currents at this interface. The scattering matrix S is given by:

$$\begin{pmatrix} I_e^{\mathrm{out}} \\ I_g^{\mathrm{out}} \end{pmatrix} = \begin{pmatrix} S_{ee} & S_{eg} \\ S_{ge} & S_{gg} \end{pmatrix} \begin{pmatrix} I_e^{\mathrm{in}} \\ I_g^{\mathrm{in}} \end{pmatrix} \tag{1.29}$$

Here, S_{eg} describes the current emitted into the edge when driving the gate, and S_{ge} describes how much current is transmitted from the edge state to the gate. The coefficients S_{gg} and S_{ee} represent the corresponding reflection amplitudes.

We can find the scattering parameter by considering Kirchhoff's law at the interface:

$$I_g^{\text{in}} - I_g^{\text{out}} + I_e^{\text{in}} - I_e^{\text{out}} = 0 \tag{1.30a}$$

$$Z_g(I_g^{\text{in}} - I_g^{\text{out}}) - Z_e(I_e^{\text{in}} - I_e^{\text{out}}) = \frac{I_g^{\text{in}} - I_g^{\text{out}}}{i\omega C_g} \tag{1.30b}$$

The scattering matrix is hence given by:

$$S = \begin{pmatrix} \frac{1+i\omega C_g(Z_g-Z_e)}{1+i\omega C_g(Z_g+Z_e)} & \frac{2i\omega Z_e C_g}{1+i\omega C_g(Z_g+Z_e)} \\ \frac{2i\omega Z_g C_g}{1+i\omega C_g(Z_g+Z_e)} & \frac{1+i\omega C_g(Z_e-Z_g)}{1+i\omega C_g(Z_g+Z_e)} \end{pmatrix} \tag{1.31}$$

with $Z_g = 50\,\Omega$. In order to develop intuition for the behavior of the coupling, it is useful to consider the low- and high-frequency limits of the scattering matrix. For $\omega C_g(Z_e + Z_g) \ll 1$, the coupling capacitor presents a large impedance and effectively blocks current between gate and edge. In this regime, $S_{ee} \approx 1$ and $S_{gg} \approx 1$, while the cross terms scale linearly with frequency, $S_{eg}, S_{ge} \propto i\omega C_g$. Physically, at low frequencies, the capacitor blocks charge transfer, so the gate is effectively decoupled from the edge. In the opposite limit, $\omega C_g(Z_e + Z_g) \gg 1$, the capacitive impedance becomes small, and the interface behaves like a direct connection between two transmission lines of very different impedance. The scattering matrix elements approaches

$$S \to \begin{pmatrix} \frac{Z_g-Z_e}{Z_g+Z_e} & \frac{2Z_e}{Z_g+Z_e} \\ \frac{2Z_g}{Z_g+Z_e} & \frac{Z_e-Z_g}{Z_g+Z_e} \end{pmatrix} \tag{1.32}$$

Because the edge impedance greatly exceeds the gate impedance, $Z_e \gg Z_g$, these limits simplify to

$$S_{ge} \longrightarrow \frac{2Z_g}{Z_e} \ll 1, \qquad S_{eg} \longrightarrow 2. \tag{1.33}$$

$S_{ge} \ll 1$ means that only a tiny fraction of the current injected from the gate enters the edge channel. This is expected: most of the power is reflected due to the strong impedance mismatch. At the same time, $S_{eg} \to 2$ might be confusing. It arises because, for a severely mismatched interface, the current wave arriving from the high-impedance edge must split into reflected and transmitted components such that current is conserved. Since the incident current in a high-impedance line is extremely small, the normalization of the scattering formalism

results in a coefficient of order 2 even though the transferred power is negligible [2].
These scattering parameters are the building blocks of the fit model we use in Chapter 3 to fit the transmission data of plasmon transport in the QAH edge states. In the following section, we will present our rf setup and sketch some basic calibration techniques.

1.3 Radio-frequency setup and calibration techniques

All experiments presented in this thesis rely on the rf setup installed in our dilution refrigerator, schematically shown in Fig. 1.5. The cryostat is equipped with six coaxial rf lines: four input lines (IN1–IN4) for excitation and two output lines (OUT1–OUT2) for detection. These lines differ mainly in their attenuation and intended use.
The input lines IN1–IN3 are broadband (40 GHz) and contain attenuators at each temperature stage. These attenuators serve two purposes: (i) they reduce thermal noise originating from higher temperature stages, and (ii) they ensure proper thermalization of the inner conductor to prevent sample heating. The total attenuation amounts to 41 dB for IN1/IN2 and 18 dB for IN3. Line IN4 has only 3 dB attenuation and is used when large excitation amplitudes are required or as a detection line without an amplifier for experiments with ultra-wide bandwidth.
The output lines contain a cryogenic high-electron-mobility transistor (HEMT) amplifier at the 4 K stage with a bandwidth of 0.3–14 GHz and a gain of 37 dB. The amplifier operates at a noise temperature of approximately 3.6 K. We placed an additional 10 dB attenuator between the sample and the amplifier. Although this reduces the total gain by 10 dB, it suppresses standing waves (arising from the strong impedance mismatch between the sample and the 50 Ω microwave environment) by 20 dB. The origin and consequences of these standing waves will be discussed in detail in Chapter 3.
In addition, we mounted four Bias-Tees on the mixing chamber stage on lines OUT1, OUT2, IN1, and IN3. A Bias-Tee separates low-frequency and rf-frequency components: the dc port is connected via an inductor, blocking

[2] This is an artifact of our framework, where we define the scattering parameter for the currents. In rf engineering, the scattering parameters are usually defined for the square root of the power $(V + Z \cdot I)/\sqrt{Z}$ [40]

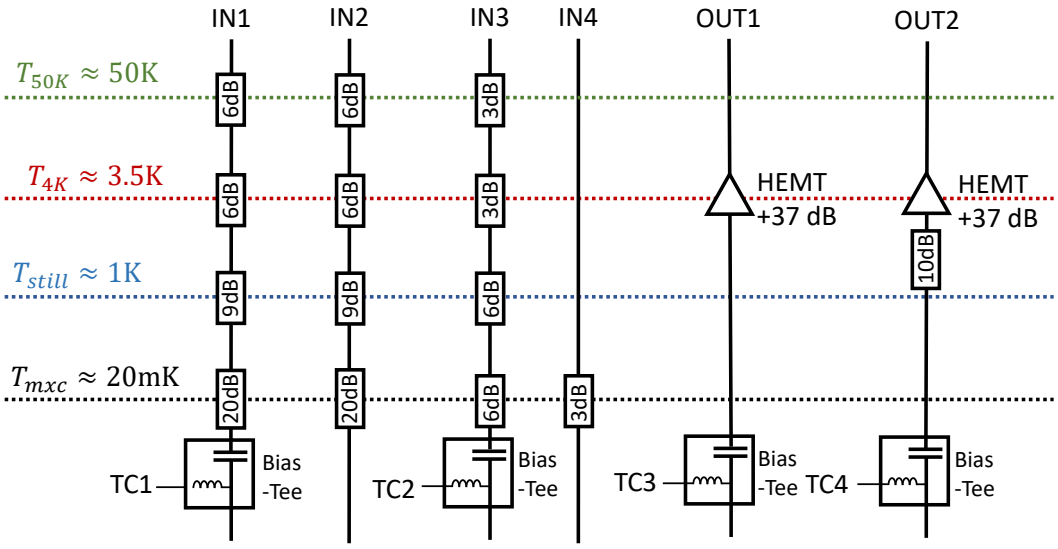

Figure 1.5: Schematic of the rf setup in the dilution refrigerator. The horizontal colored bars indicate the cryostat temperature stages, decreasing from room temperature (top) to the mixing chamber (bottom). Each input line contains attenuators at each stage for thermalization. Each output line contains a cryogenic HEMT amplifier (Low Noise Factory LNC 0.3–14 GHz, 37 dB). Line OUT2 additionally includes a −10 dB attenuator to suppress standing waves. Several lines feature Bias-Tees (Anritsu K250) at the mixing chamber (MXC), enabling simultaneous rf and dc operation.

high-frequency signals, while the rf port is connected via a capacitor, blocking dc signals. This allows us to apply (or measure) dc biases simultaneously with microwave signals. The Bias-Tees have a low insertion loss (about 1 dB) and provide a bandwidth of 40 GHz.

The entire microwave setup is designed for broadband operation. Apart from the amplifier-limited bandwidth of 0.3–14 GHz, the remaining components support DC–40 GHz operation. This broadband design is advantageous for our rf measurements, but it comes with drawbacks: (i) we cannot install isolators or circulators (which are narrow-band devices) to suppress reflections, which inevitably results in standing waves, (ii) the broadband lines transmit more noise than narrow-band configurations would. These trade-offs are an intrinsic challenge of wideband microwave experiments.

1.3.1 Vector network analyzer

Having described the cryogenic part of the microwave setup, we now turn to its central instrument: the vector network analyzer (VNA). The VNA generates and detects microwave signals and measures the complex scattering parameters of a device under test (DUT). Because rf engineering heavily relies on concepts such

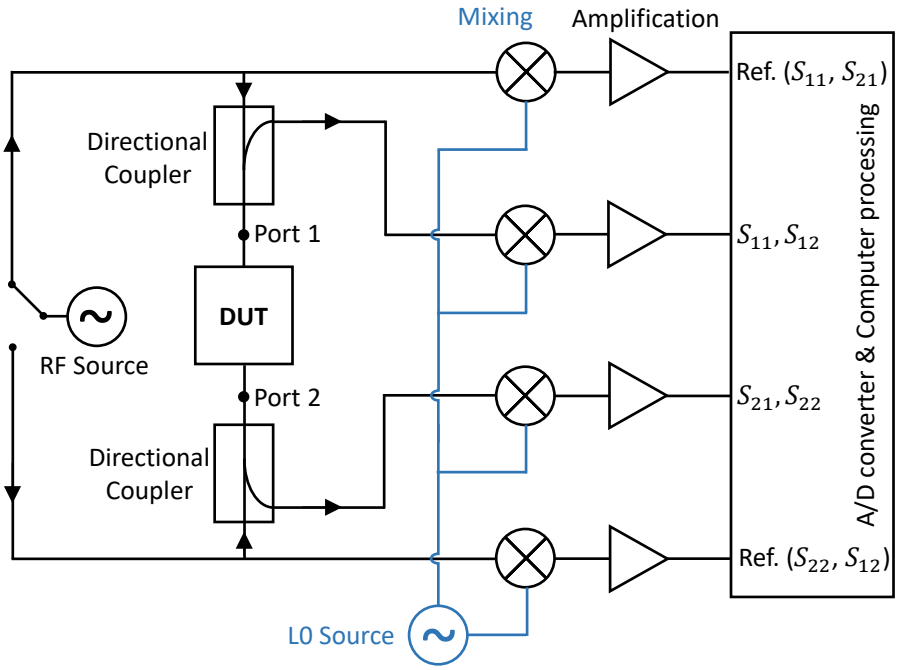

Figure 1.6: Schematic of a 2-port vector network analyzer. The rf source generates a monochromatic signal that is routed to the DUT and simultaneously used as a reference. Directional couplers separate incident and reflected waves. Mixing with a local oscillator (LO) down-converts the rf signal to an intermediate frequency (IF), from which the amplitude and phase of each scattering parameter are extracted. Adapted from Ref. [40]

as heterodyne detection, mixing, and reference synchronization, we provide a concise overview of the VNA functionality in Fig. 1.6 as it serves as a pedagogical example of rf engineering.

The VNA measures the relationship between incoming and outgoing wave amplitudes,

$$V_i^{\text{out}} = S_{ij}\, V_j^{\text{in}}, \tag{1.34}$$

where S_{ij} is the complex scattering parameter for excitation at port j and detection at port i. The rf source emits a signal with tunable frequency and amplitude (here from 10 MHz to 26.5 GHz). A part of this signal is routed to the DUT, and another part serves as an internal reference. Directional couplers separate incident and reflected waves such that both S_{11} and S_{21} (for excitation at port 1) can be measured.

To digitize the signal, the VNA employs a heterodyne detection scheme, in which the high-frequency rf tone is down-converted to an intermediate-frequency (IF) signal. For completeness, we briefly recall how mixing with a local oscillator (LO) generates the IF signal from which the amplitude and phase are extracted.

The outgoing rf wave,

$$V_i^{\text{out}}(t) = |V_i^{\text{out}}| \cos(\omega_{\text{RF}} t + \phi_i), \tag{1.35}$$

is mixed with a local oscillator at frequency $\omega_{\text{LO}} = \omega_{\text{RF}} + \omega_{\text{IF}}$. Multiplying the two signals gives:

$$V_i^{\text{out}} \cdot V_{\text{LO}} = \frac{1}{2} |V_i^{\text{out}}| \, |V_{\text{LO}}| \big[\underbrace{\cos(\omega_{\text{IF}} t + \phi_i)}_{\text{IF signal}} + \underbrace{\cos\left((2\omega_{\text{RF}} + \omega_{\text{IF}})t + \phi_i\right)}_{\text{up-converted term}} \big]. \tag{1.36}$$

The first term is the down-converted IF signal, which carries the amplitude and phase information of the original rf tone. The second term oscillates at a much higher frequency and is removed by filtering. In practice, the IF is chosen between a few tens of kilohertz and a few megahertz, where digitizers can record the signal with high dynamic range.
Modern VNAs use multi-stage (superheterodyne) down-conversion to achieve high dynamic range and excellent noise performance [40]. Since the LO, rf source, and digitizer share the same clock reference, long-term phase coherence is maintained, which is essential for reproducible phase measurements. When a VNA is combined with external instruments (e.g., AWGs or signal generators), additional synchronization precautions are necessary. We compare different synchronization schemes in Appendix A.

1.3.2 Principles of calibration

Although the VNA provides an internal reference for amplitude and phase, the measured waves are distorted by electronic components in the signal path: directional couplers have insertion loss, cables introduce phase delay, connectors are imperfect, and amplifiers add gain and ripple. These distortions must be removed through microwave calibration. Without correcting for these effects, the intrinsic sample response cannot be extracted. A widely used calibration method is the SOLT (Short–Open–Load–Through) technique. Each calibration standard provides a known impedance environment [40, 41]:

- **Short,** $Z = 0$, perfect reflection with phase 180°,
- **Open,** $Z \to \infty$, perfect reflection with phase 0°,
- **Load,** $Z = 50\,\Omega$, matched termination with no reflection,
- **Through,** direct connection between VNA ports, ideally $S_{21} = 1$.

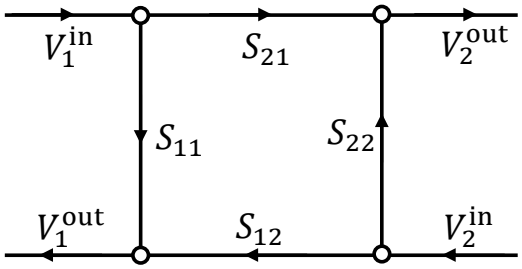

Figure 1.7: Signal flow graph. A graphical representation of a general 2-port microwave network. Each branch is weighted by a scattering parameter S_{ij}, and voltages at nodes follow from summing all entering signals.

By comparing the measured S-parameters with their ideal values, one extracts the error coefficients of the measurement system, enabling reconstruction of the true device response. In our experiments, SOLT calibration is performed up to the cryostat feedthrough. Ideally, calibration would extend all the way to the sample holder, but this is impractical: the cryostat wiring is inaccessible during operation. One could utilize cryogenic microwave switches to perform SOLT operations at the sample level, which would improve the accuracy of our measurements [47, 48]. However, they still have the drawback that the cryogenic amplifier is non-reciprocal and does not allow for reflection measurements of S_{22}. Therefore, we approximate the distortions inside the cryostat using a simplified model.

One such approximation is to describe the entire microwave chain using a signal flow graph. This provides an intuitive framework for representing and simplifying multi-component microwave networks. A signal flow graph consists of nodes connected by branches carrying scattering parameters as illustrated in Fig. 1.7. For a two-port network,

$$V_2^{\text{out}} = S_{21}V_1^{\text{in}} + S_{22}V_2^{\text{in}}, \tag{1.37}$$

and similar relations hold for V_1^{out}. Such diagrams allow us to collapse complex networks, neglect reflections where justified, incorporate feedback loops, or isolate particular distortions. This makes them extremely valuable when a full SOLT calibration is not possible. We will apply this calibration strategy directly when analyzing the plasmon transmission data in Chapter 3, where multiple reflections inside the cryostat play a major role in shaping the measured spectra. The concepts introduced in this section form the basis for all rf measurements discussed later in this thesis. The treatment of transmission lines, the use of scattering parameters, and the calibration strategies described above are essential

for extracting reliable amplitudes and phases from our devices. In the following chapters, we will apply these tools directly to the microwave response of 1D edge states and use them to analyze their velocity, dissipation, and coupling to the environment. In the next chapter, we will introduce the theoretical foundation of the transport experiments by introducing the quantum anomalous Hall effect and other phenomena that we observe in our experiments, such as variable range hopping or Joule heating.

Chapter 2

Theory of the transport in a magnetic topological insulator

In this chapter, we introduce the necessary theoretical foundation for the transport experiments on the quantum anomalous Hall (QAH) insulator that we present in the following chapter. The chapter is structured as follows. We begin with the theoretical description of the quantum anomalous Hall effect in Sec. 2.1. The role of electron–hole puddles arising from charge disorder, which is important for interpreting the experimental results, is discussed in Sec. 2.2. Finally, we will introduce the framework of variable range hopping (VRH) in Sec. 2.3, which is the dominant transport mechanism for bulk transport in quantum Hall (QH) and QAH insulators. The concept of VRH will also be important in Chapter 3 and Chapter 4, where we will discuss the plasmon propagation and the electric field-driven breakdown of edge transport.

2.1 The quantum anomalous Hall effect

The QAH effect describes the quantized Hall conductance $\sigma_{\mathrm{yx}} = e^2/h$ that occurs in the absence of an external magnetic field. It can be regarded as the zero-field counterpart of the QH effect, where a topologically nontrivial band structure replaces the role of Landau quantization. The necessary breaking of time-reversal symmetry is provided by an intrinsic magnetization, which opens an exchange gap in the band structure and gives rise to a single chiral edge state along the sample boundaries. The orientation of the magnetization determines the direction of the chiral edge state. A slab of a uniformly magnetized QAH insulator is shown in Fig. 2.1a. When the Fermi level is tuned into the band gap of the 3D bulk states and the exchange gap of the 2D surface states (see Fig. 2.1b), the transport is restricted to the 1D edge state. To understand the emergence of this band structure, we will first introduce the concept of a topological insulator and

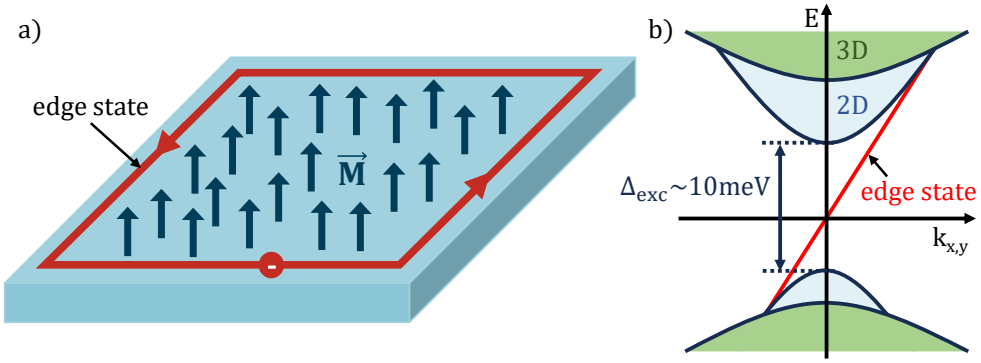

Figure 2.1: Band structure of a quantum anomalous Hall (QAH) insulator. a) Illustration of a thin magnetic insulator (bright blue), that shows a spontaneous magnetization M as shown by dark blue arrows. The chiral edge state is shown in red. b) Energy spectrum of a QAH insulator. The surface states (blue) are gapped by the exchange gap $\Delta_{\mathrm{exc}} \sim 10\,\mathrm{meV}$ [49, 50], which closes at the edges, giving rise to the chiral edge state. The bulk valence and conduction bands (shown in green) are well separated from the surface bands.

then present a minimal two-band model that captures the essential physics of topological band inversion and exchange splitting [51, 52].

2.1.1 Topological insulator

A three-dimensional topological insulator is characterized by an insulating bulk and metallic surface states that arise from a nontrivial band topology [53]. When the Fermi level lies inside the bulk gap, transport occurs exclusively through these 2D surface channels, whose dispersion relation forms a single Dirac cone, as shown in Fig. 2.2a. The surface states exhibit spin–momentum locking: electrons moving in opposite directions carry opposite spins (Fig. 2.2b). The effective Dirac Hamiltonian captures the low-energy physics

$$H = \hbar v_{\mathrm{F}}(k_y\sigma_x - k_x\sigma_y), \tag{2.1}$$

which encodes the helical spin texture of the surface states. Time-reversal symmetry protects these states by forbidding elastic backscattering between Kramers partners at k and $-k$, ensuring robust metallic conduction in the presence of nonmagnetic disorder [53].
Breaking time-reversal symmetry lifts this protection. Magnetic doping or proximity to a ferromagnet introduces an exchange field M that adds a mass term to the Dirac Hamiltonian and opens a gap in the surface-state spectrum [51, 54]. This exchange-induced gap is the essential ingredient that enables the QAH effect. In the next section, we outline a minimal two-band model that captures

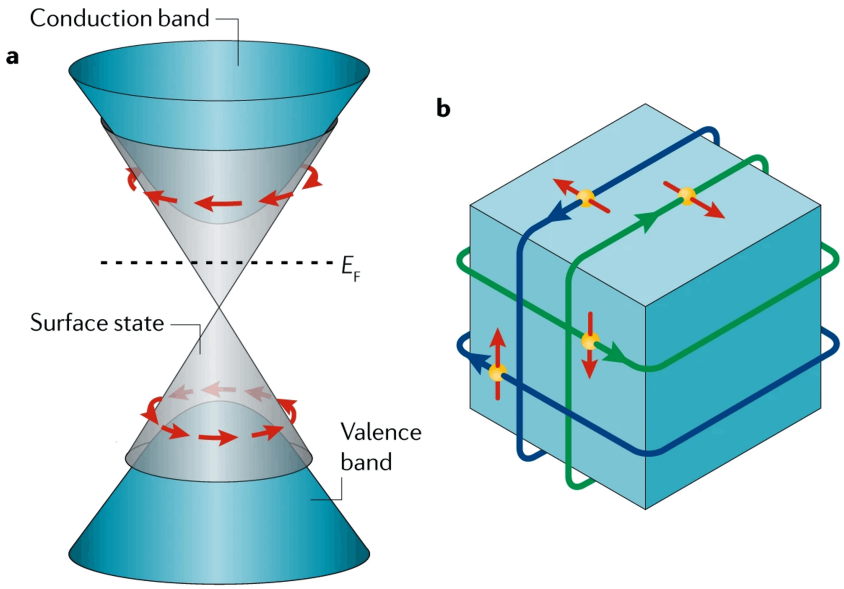

Figure 2.2: Topological insulator. (a) Band structure of a 3D topological insulator showing the bulk valence and conduction bands (blue) and the massless Dirac-like dispersion of the surface states (grey). (b) Real-space illustration of spin–momentum locking: charge carriers with opposite spin orientations move in opposite directions on the surface of the topological insulator. Reproduced from Ref. [54] with permission from Springer Nature.

how the exchange interaction drives the system into a Chern-insulating phase with a single chiral edge state.

2.1.2 Two-band model and topological band inversion

In a thin film of a three-dimensional topological insulator, the top and bottom surface states interact through hybridization and magnetic exchange. The QAH effect can be understood starting from these two coupled Dirac surface states under an exchange field M. The effective Hamiltonian for the top (t) and bottom (b) surfaces can be written as [51, 52]:

$$H_{t,b} = \pm\hbar v_{\mathrm{F}} \left(k_y\sigma_x - k_x\sigma_y\right) + gM\sigma_z, \tag{2.2}$$

where $\sigma_{x,y,z}$ are the Pauli matrices acting on the spin degree of freedom, v_{F} is the Fermi velocity, and g is the effective g-factor describing the strength of the exchange coupling. The first term represents the massless Dirac surface states with opposite chirality on the top and bottom surfaces, while the second term

introduces an exchange-induced Zeeman splitting that breaks time-reversal symmetry. When the two surfaces are in proximity, as in a thin film, their wavefunctions overlap, allowing tunneling between the top and bottom surfaces. This hybridization opens a small energy gap, which can be expressed as a momentum-dependent mass term m_k. This term can be approximated as a parabolic function:

$$m_k = m_0 + B(k_x^2 + k_y^2), \tag{2.3}$$

where m_0 is the hybridization energy at $k = 0$ and B determines the curvature of the bands. Combining hybridization and magnetic exchange and projecting onto a given block of the thin-film Hamiltonian yields an effective 2×2 Dirac Hamiltonian

$$h_\pm(k) = \big[m_0 + B(k_x^2 + k_y^2) \pm gM\big]\sigma_z + v_\mathrm{F}(k_y\sigma_x - k_x\sigma_y), \tag{2.4}$$

where the $\pm$ sign corresponds to the symmetric and antisymmetric combinations of the top and bottom surface states, respectively. The exchange field M therefore shifts the Dirac mass in opposite directions in the two blocks. The sign of the ratio m_0/B determines whether the system is topologically trivial or inverted when $M = 0$. A negative m_0/B corresponds to an inverted band structure and a quantum spin Hall phase [55], while a negative ratio yields a trivial insulator. These two cases are illustrated schematically in Fig. 2.3a and Fig. 2.3b. Introducing the exchange field M shifts the band inversion condition. For an initially trivial configuration ($m_0/B > 0$), a sufficiently strong $|M|$ reverses the band ordering and drives the system into a Chern-insulating state. For an initially inverted configuration ($m_0/B < 0$), the exchange field reinforces the inversion of one spin sector while removing it for the other. In both cases, spin–orbit coupling gaps the resulting band crossings, and the system acquires a Chern number $C = \pm 1$ [51]. The fact that both trivial and inverted starting points flow into the same QAH phase when $|M|$ is large enough is important for real devices. Thin-film TIs often exhibit thickness variations that locally modify the hybridization gap and therefore the band topology [44]. Because both regimes ultimately yield a QAH state with a single chiral edge channel, the quantized Hall plateau remains robust against such inhomogeneities. Thinner films are still preferred experimentally, as they suppress residual bulk conduction and improve the quality of the quantized Hall response [52].

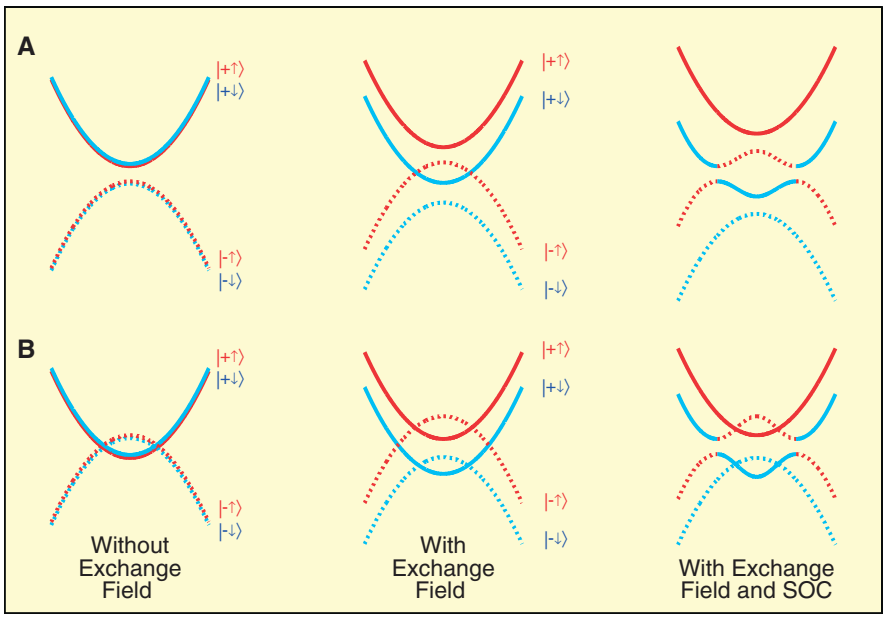

Figure 2.3: Evolution of the QAH band structure. Evolution of the four bands with exchange field and spin orbit coupling (SOC) for initially trivial (A) and inverted phase (B). The color coding shows the spin of the sub-band, while dashed/solid lines correspond to odd/even parity, respectively. For the initially trivial phase (A), the exchange field causes a band inversion of two sub-bands. For the initially inverted phase (B), the lift the band inversion of the $|+\uparrow\rangle$ and $|-\downarrow\rangle$ and increases the band version of the other $|-\uparrow\rangle$ and $|+\downarrow\rangle$. The SOC lifts the degeneracy at the band crossings, realizing an insulating state. However, the band structure is non-trivial for both initial scenarios and leads to a gap closing at the interface to a trivial insulator, giving rise to edge transport. Reproduced from Yu et al. [51] with permission from AAAS.

2.1.3 Motivation and applications of QAH materials

The primary advantage of the QAH effect is the realization of quantized Hall transport without an external magnetic field. This zero-field quantization not only simplifies experimental conditions but also enables integration with superconducting circuits, Josephson junctions, and microwave platforms that are incompatible with strong magnetic fields. Several potential applications have been proposed:

1. **Metrology:** The QAH effect enables a quantized resistance standard at zero field [22, 56–59]. The absence of a magnetic field allows direct integration with Josephson voltage standards, which is not possible for conventional QH devices. The best QAH-based standards currently achieve a precision at the level of a few parts per billion [59], approaching that of established QH systems.

2. **Topological superconductivity:** When a QAH insulator is coupled to a superconductor, it can give rise to topological superconductivity and host Majorana excitations [60, 61]. Depending on the geometry, these may appear either as propagating chiral Majorana edge modes along the boundary of a topological superconductor or as localized Majorana bound states at vortices. In contrast to Majorana bound states, which are spatially localized zero-energy excitations, chiral Majorana modes are extended one-dimensional edge channels that transport energy along the sample boundary. Both types of excitations are predicted to obey non-Abelian braiding statistics and have been proposed as building blocks for fault-tolerant quantum computation. Superconducting proximity effects in QAH systems have been demonstrated experimentally [62], but topological Josephson junctions remain to be realized.

3. **Magnetic memory and logic:** The magnetization of QAH insulators can be switched electrically [63, 64], allowing for potential applications in low-power magnetic memory. Recently, Liu et al. [65] demonstrated that a QAH insulator can act as a memristive element suitable for cryogenic in-memory computing.

4. **Microwave and plasmonic applications:** The relatively low plasmon phase velocity ($v_\mathrm{p} \simeq 3\text{–}5 \times 10^5\,\mathrm{m/s}$) enables the realization of compact on-chip microwave circuits based on interferometric principles [15, 16]. Mahoney et al. [16] demonstrated a proof-of-principle nonreciprocal microwave circulator using a QAH disk, achieving a circulation amplitude of approximately $20\,\mathrm{dB}$. Such a device is shown in Fig. 2.4. A key limitation is the large impedance mismatch between the metallic gate and the high-impedance edge channel. However, it can be mitigated by employing impedance-matching techniques [66–68].

These proposed applications underscore the technological potential of QAH materials and motivate efforts to understand the microscopic mechanisms that limit their performance. In particular, the role of disorder, localized bulk states, and edge–bulk coupling becomes central for interpreting both dc transport and the microwave experiments presented in the following sections.

2.1.4 Experimental signatures

The QAH effect can be experimentally verified by a Hall experiment, where a QAH insulator is etched into a Hall bar geometry, and Ohmic contacts are

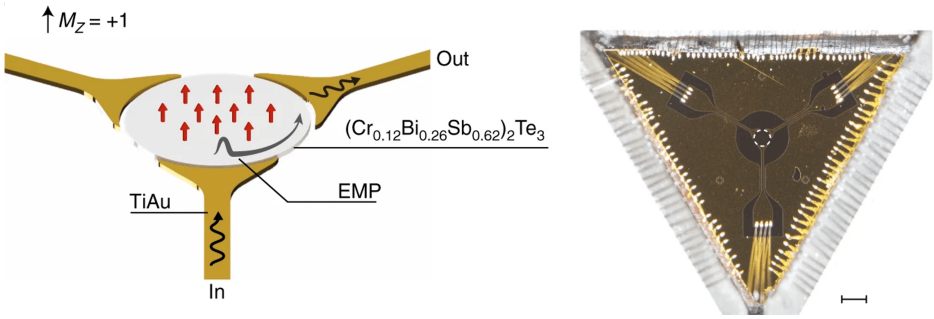

Figure 2.4: Quantum anomalous Hall circulator. Left: Schematic view of the 3-port circulator based on a quantum anomalous Hall disk (center). A signal injected in the port IN is transmitted to the port OUT and isolated from the third port. Right: Microscope image of a circulator device fabricated from Cr-doped $(Bi_xSb_{1-x})_2Te_3$. Reprinted from Ref. [16].

defined as sketched in Fig. 2.5a. By applying a current I_{xx} and measuring the longitudinal voltage U_{xx} and the Hall voltage U_{yx}, we can infer the longitudinal resistance R_{xx} and the Hall resistance R_{yx}. An example measurement is shown in Fig. 2.5b. It features a hysteretic Hall resistance $R_{yx}(\mu_0 H)$ with quantized plateaus at $\pm h/e^2$ in the magnetized states and a vanishing longitudinal resistance R_{xx}. Upon magnetization reversal, R_{xx} shows peaks, indicating the temporary coexistence of oppositely magnetized domains. These domain boundaries host counter-propagating edge states, which cause additional dissipation until full magnetization is restored [56, 69].

In practice, finite bulk conduction prevents perfectly dissipationless transport, even in the magnetized state. The residual R_{xx} becomes finite at low temperatures (hundreds of millikelvin) or under small biases (tens of nanoamperes), marking the onset of dissipative bulk transport [20, 21, 58]. This breakdown is attributed to various mechanisms: variable-range hopping [70], bootstrap electron heating [22], and percolation through charge puddles (locally conducting regions which form in the bulk due to Coulomb disorder [5, 71–73]) driven by electric fields [20]. Such mechanisms are further discussed in the following section, where we address the role of electron–hole puddles and disorder in limiting the transport properties of QAH insulators.

2.2 Charge puddles in disordered material

In a QAH insulator, it is crucial to tune the Fermi level into both the topological band gap of the 3D bulk and the exchange gap of the 2D surface state, as illustrated in Fig. 2.1b. While the bulk band gap is typically of the order of a

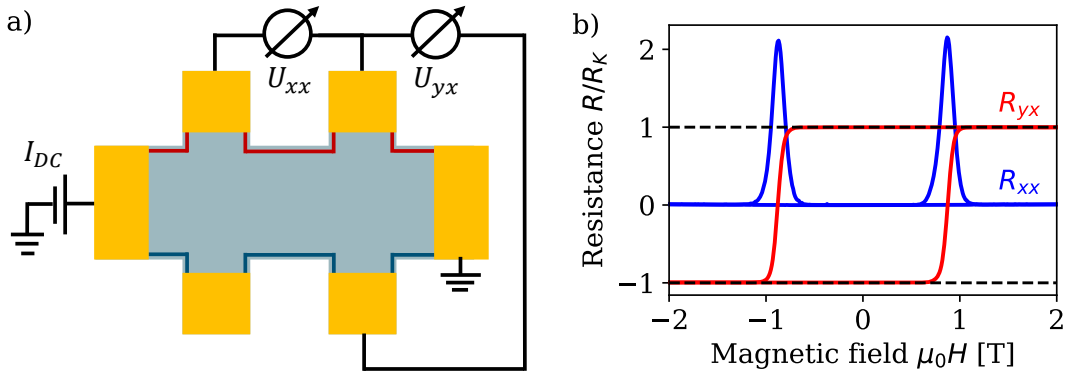

Figure 2.5: Hall Measurement of a QAH insulator. a) Sketch of a Hall bar made of a quantum anomalous Hall insulator (blue) with six Ohmic contacts (gold). A current bias is applied from the left to the right lead, while measuring the longitudinal voltage U_{xx} and the transversal voltage U_{yx}. The high potential edge state, which carries the current, is shown in red, while the grounded edge state is shown in blue. b) R_{xx} and R_{yx} vs. $\mu_0 H$. R_{yx} shows a hysteresis loop and is quantised to $\pm R_{\mathrm{K}}$ in the magnetized state. R_{xx} is vanishing in the magnetized state and shows peaks upon magnetization reversal. The measurement is taken on sample $\mathrm{MBE\_VBST\_20221204a}$ at a temperature of $T \simeq 20\,\mathrm{mK}$.

few hundred meV [74], the magnetic exchange gap of the surface states is much smaller, typically only a few tens of meV [49, 50]. Experimentally, the Fermi level can be tuned either by electrostatic gating or by chemical doping. In our case, we use the ternary compound $(\mathrm{Bi_xSb_{1-x}})_2\mathrm{Te_3}$, which allows tuning of the Fermi level by adjusting the Bi/Sb ratio x. $\mathrm{Bi_2Te_3}$ is naturally n-type, with the Fermi level in the conduction band, whereas $\mathrm{Sb_2Te_3}$ is p-type, with the Fermi level in the valence band. By carefully choosing the Bi–Sb ratio, the Fermi level can be placed within the bulk band gap, achieving near-perfect charge compensation [75, 76].

Even in the case of ideal charge compensation, local variations in the chemical potential persist due to the random spatial distribution of donors and acceptors. Empty donor sites act as positively charged centers, while occupied acceptors are negatively charged. Because of the low carrier density in these materials, electrostatic screening is weak, and the resulting Coulomb potential fluctuates strongly over a length scale of tens of nanometers [73, 77, 78]. These potential fluctuations distort the conduction and valence band edges, causing the Fermi level to locally cross into either the conduction or the valence band. The resulting metallic regions form electron and hole puddles, as schematically shown in Fig. 2.6a. This formation of charge puddles is a well-known feature of compensated semiconductors and topological insulators [5, 71–73].

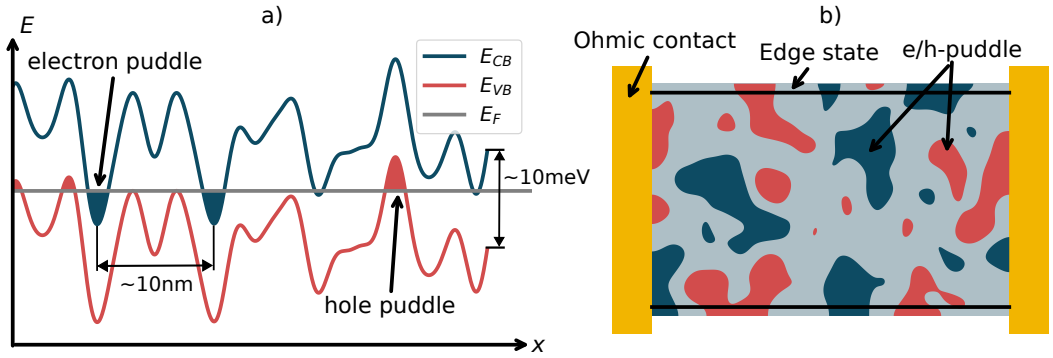

Figure 2.6: Electron– and hole–puddles in a QAH insulator. (a) Real-space schematic of the band structure in a compensated semiconductor. The Fermi level E_{F} lies near the center of the unperturbed conduction (E_{CB}) and valence bands (E_{VB}). Poorly screened Coulomb potentials from charged impurities locally bend the bands, producing regions where E_{F} crosses into the conduction (electron puddles) or valence band (hole puddles). (b) 2D schematic of a QAH bar showing electron and hole puddles (blue/red regions). The effective bulk conductance connecting the edge states on opposite sides of the bar depends on the activated or hopping transport between these localized regions.

A schematic view of a charge puddle network in a thin QAH film is shown in Fig. 2.6b. The puddles represent small, localized metallic regions in an otherwise insulating bulk. Although individual puddles are spatially isolated, they can still couple via thermal activation or tunneling processes [20, 22, 70, 79]. When this occurs, charge carriers can traverse the bulk by hopping between puddles, providing a finite bulk conduction path that connects the counter-propagating edge states on opposite sides of the sample. This mechanism leads to back-scattering between edge channels and thereby breaks the zero-resistance state of chiral edge transport. When the overlap between the electronic wave functions of neighboring puddles is small, the conduction mechanism follows the VRH model [80–83]. In this regime, the transport between puddles is dominated by phonon-assisted hopping between localized states. We will discuss this mechanism in more detail in the following section. Also, as we will see in Chapters 3 and 4, these puddles not only give rise to a finite longitudinal resistance in dc transport but also provide a dominant dissipation channel for edge plasmons through capacitive and resistive coupling to the bulk.

2.3 Variable range hopping

At sufficiently high temperatures, charge carriers can be thermally excited above the mobility edge, resulting in activated transport. This originates from the thermal broadening of the Fermi–Dirac distribution, leading to a Boltzmann

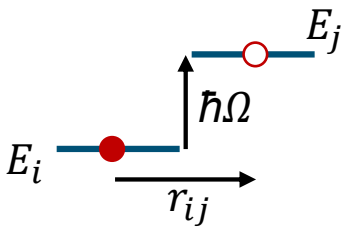

Figure 2.7: Schematic of a hopping event. A charge carrier on site i hops to an empty site j at a distance r_{ij}. The energy difference $\Delta E_{ij} = E_j - E_i$ is absorbed or emitted by a phonon of energy $\hbar\Omega$, depending on the sign of ΔE_{ij}.

factor $\exp[-(E_C - E_F)/k_\mathrm{B}T]$. In a low-temperature regime where $k_\mathrm{B}T \ll E_C - E_F$, activated transport is suppressed, and bulk conduction is dominated by hopping between localized states.

A schematic hopping event is shown in Fig. 2.7. A charge carrier hops from an occupied site i to an empty site j separated by a distance $r_{ij} = |\vec{r}_i - \vec{r}_j|$. The two sites are generally at different energies, E_i and E_j. To ensure energy conservation, the energy difference $\Delta E_{ij} = E_j - E_i$ is exchanged with the phonon bath. In thermally activated hopping, this energy is provided or absorbed by a phonon of energy $\hbar\Omega$. If $\Delta E_{ij} > 0$, a phonon of energy $\hbar\Omega$ is absorbed, and if $\Delta E_{ij} < 0$, a phonon is emitted. The total conductivity in this regime is proportional to the hopping probability P_{ij}, which for phonon absorption can be expressed as [81, 82, 84]:

$$P_{ij} = \gamma_{ij}\, e^{-2r_{ij}/\xi}\, f_i(1 - f_j)\, N(\hbar\Omega). \tag{2.5}$$

Here, γ_{ij} is a statistical prefactor that depends on the electron–phonon coupling strength (assumed constant for simplicity [81]), and $e^{-2r_{ij}/\xi}$ accounts for the overlap of the two exponentially localized wavefunctions with the localization length ξ. The Fermi factors f_i and $(1 - f_j)$ represent the probabilities that site i is occupied and site j is empty, respectively. The last term, $N(\hbar\Omega)$, describes the probability of absorbing a phonon of energy $\hbar\Omega$ according to the Bose–Einstein distribution. For phonon emission, the term $N(\hbar\Omega)$ is replaced by $(1 + N(\hbar\Omega))$ to account for stimulated and spontaneous emission.

To obtain an expression for the conductivity, we relate the hopping distance r_{ij} to the energy difference ΔE_{ij}. In general, sites that are close in energy are far apart in space, reflecting the trade-off between spatial overlap and energetic alignment that characterizes VRH transport. Assuming a constant density of states g_0 near the Fermi level (valid for the 2D case), the average distance r_c between two sites

with energy separation ΔE_{ij} is given by [85, 86]:

$$r_c^2 g_0 \Delta E_{ij} = 1 \quad \Rightarrow \quad \Delta E_{ij} = \frac{1}{g_0 r_c^2}. \tag{2.6}$$

The factor $r_c^2 g_0 \Delta E_{ij}$ represents the number of available states within a disk of radius r_c and energy window ΔE_{ij}, which must be of order unity for a hopping event to occur. For simplicity, we consider symmetric site energies $E_{i,j} = \pm \Delta E_{ij}/2$. At low temperatures, the Fermi and Bose–Einstein distributions can be approximated as

$$f_i(-\Delta E_{ij}/2)(1 - f_j(\Delta E_{ij}/2))N(\Delta E_{ij}) \approx \exp(-\Delta E_{ij}/k_\mathrm{B}T). \tag{2.7}$$

Using these approximations, the hopping probability can be written as

$$P_{ij} = \gamma_{ij} \cdot \exp\left(-\frac{2r_c}{\xi}\right) \exp\left(-\frac{1}{g_0 r_c^2 k_\mathrm{B} T}\right). \tag{2.8}$$

Because the hopping probability depends exponentially on both the spatial separation and the energy mismatch between localized states, the conductivity is dominated by hops with the smallest total exponent. The critical-path method approximates transport by the percolating network of least-resistive hops, and the characteristic hopping distance r_c is obtained by maximizing the hopping probability (equivalently minimizing the hopping exponent). We estimate r_c by setting the derivative dP_{ij}/dr_{ij} to zero, yielding

$$r_c = \left(\frac{\xi}{g_0 k_\mathrm{B} T}\right)^{1/3}. \tag{2.9}$$

This result shows that r_c decreases as temperature increases. At higher T, hops to energetically nearby states dominate, corresponding to nearest-neighbor hopping. At lower T, energy conservation becomes restrictive, leading to longer, variable-range hops [84]. The resulting temperature dependence of the conductivity follows

$$\sigma(T) \propto \exp\left[-\left(\frac{T_0}{T}\right)^{1/3}\right], \tag{2.10}$$

where $T_0 = (g_0 k_\mathrm{B} \xi^2)^{-1}$ is the characteristic temperature scale. This expression corresponds to the well-known 2D Mott law for variable-range hopping [81, 82]. However, this is based on the assumption of a constant density of states $g(E) = g(\mu)$. Efros and Shklovskii showed that there is a Coulomb gap due to the

Coulomb interaction between charge carriers [81, 83]. The Coulomb gap modulates the density of states and scales as $g(E) \propto |E - \mu|$ for a 2D semiconductor. This also affects the temperature dependence of the conductivity:

$$\sigma(T) = \frac{\sigma_0}{T} \exp\left[-\left(\frac{T_{ES}}{T} \right)^{1/2} \right], \tag{2.11}$$

which is valid for 2D and 3D systems. The characteristic temperature T_{ES} depends on the localization length ξ and is given by:

$$k_B T_{ES} = \frac{Ce^2}{\epsilon \xi}, \tag{2.12}$$

where ϵ effective dielectric constant and C is a numerical constant ($C = 2.8$ in 3D and $C = 6.2$ in 2D [83, 87]). Shortly after the discovery of the QH effect, it was found that the law by Efros and Shklovskii applies to QH systems [88, 89]. We will later demonstrate that it is also suitable to describe the bulk transport in a QAH insulator.

Field- and photon-assisted hopping

So far, we have considered phonon-assisted hopping transport at finite temperature. However, hopping can also be assisted by strong electric fields [24, 90] or by photons [85, 86]. Under an applied electric field, two complementary mechanisms can govern the transport depending on the rate of energy dissipation and carrier thermalization.

In the non-Ohmic regime, the applied electric field E directly modifies the tunneling probability, while Joule heating is negligible because of the exponentially small conductance. Polyakov and Shklovskii [90] showed that E acts analogously to temperature, introducing an effective tunneling energy $k_{\mathrm{B}} T_{\mathrm{eff}} = e\xi E/2 \propto U$. This linear scaling of T_{eff} with bias has been observed experimentally [24, 25]. T_{eff} represents the effective temperature governing the Boltzmann distribution, driven by field-induced tunneling rather than phonon excitation [91].

At higher bias, when the conductance is no longer exponentially small, Joule heating becomes significant as we will show in Sec. 4.2.1. In this Ohmic regime, electrons are no longer in thermal equilibrium with the lattice because power dissipation exceeds the cooling rate through phonons. We will discuss the crossover between these two regimes in more detail in Sec. 4.3.

Finally, photon-assisted hopping has been theoretically analyzed by Zvyagin [85] and Keiper [86]. In this case, photons of energy $\hbar\omega$ can provide the necessary energy for hopping between localized sites. However, in a monochromatic electric field, only transitions satisfying $\Delta E_{ij} = \hbar\omega$ are allowed, leading to a very small conductance. The dominant process is therefore a second-order transition involving both a phonon and a photon, where the phonon relaxes the strict energy-matching condition. To the best of our knowledge, there are so far no experimental reports of photon-assisted hopping transport in monochromatic electric fields.

Finally, we would like to discuss the applicability of the VRH framework to puddle networks. There is, of course, one striking difference: a puddle has a finite spatial extent, whereas the VRH framework assumes atom-like defect states. It is therefore important to distinguish between the inter- and intra-puddle conductance. The intra-puddle conductance is dominated by the metallic surface and bulk states of the QAH insulator. The inter-puddle conductance, on the other hand, is weak and governed by hopping processes, which replace the role of atomic-site hopping in the classical VRH model. As long as the transport is dominated by inter-puddle conductance, the VRH framework can be applied, as demonstrated experimentally [56, 70]. However, we will later see that at higher frequencies, the intra-puddle conductance also contributes to the dissipation of edge transport.

In Chapter 4, we will show that the longitudinal resistance of our QAH devices in the bulk-dominated regime follows an Efros–Shklovskii law, allowing us to extract an effective localization length and to identify the dominant transport mechanism. We will also use the field-dependent hopping framework and the Joule-heating model discussed above to interpret the electric-field-driven breakdown of the QAH state and to distinguish between direct field-assisted tunneling and bootstrap electron heating.

Chapter 3

Plasmon transport in quantum anomalous Hall edge states

In this chapter, we investigate the propagation, dissipation, and breakdown of edge plasmon transport in quantum anomalous Hall (QAH) edge states. Understanding the high-frequency response of QAH insulators is exciting for both fundamental studies and technological applications. From a fundamental perspective, edge plasmons offer a sensitive probe of disorder, interactions, and bulk–edge coupling [39, 92, 93]. From an applied perspective, many prospective applications, such as compact non-reciprocal microwave components [15, 16] and platforms for flying Majorana qubits [60, 61], rely on low-loss high-frequency signal propagation. A quantitative characterization of plasmon velocity, dispersion, and dissipation is therefore vital to assess the practical viability of QAH-based technologies.

Previous experimental efforts have mainly focused on narrow-band measurements centered around 1 GHz using resonator geometries [16, 17, 67]. These studies, conducted on Cr-doped $(\mathrm{Bi_xSb_{1-x}})_2\mathrm{Te_3}$, reported plasmon velocities of $3-5\times10^5\,\mathrm{m/s}$ and provided first insights into dissipation mechanisms. However, Cr-doped films exhibit relatively small coercive fields ($H_c \simeq 0.2\,\mathrm{T}$), leading to reduced magnetic stability.

In this work, we perform broadband measurements of the plasmon dispersion $k(\omega)$ in V-doped $(\mathrm{Bi_xSb_{1-x}})_2\mathrm{Te_3}$, a material system that exhibits a significantly larger coercive field ($H_c \simeq 0.9\,\mathrm{T}$) and a more robust zero-field QAH state [5, 22, 56]. This enhanced stability allows us to systematically explore how the plasmon velocity and dissipation evolve with frequency, excitation voltage, magnetic field, and temperature. Our measurements reveal clear signatures of how bulk charge puddles influence edge dynamics, thereby providing a unified picture of high-frequency QAH transport.

The chapter is organized as follows. In Sec. 3.1, we introduce the sample fabrication and experimental setup, including molecular-beam epitaxy, cleanroom processing, and the mounting of the devices in the cryogenic measurement setup. We describe both the low-frequency and microwave measurement setups. In Sec. 3.2, we present the first high-frequency data and detail the calibration procedure required to isolate the transmission coefficient S_{21} associated with edge-state propagation, removing contributions from cables, connectors, and parasitic elements. Based on this calibration, Sec. 3.3 extracts the phase of S_{21} as a function of frequency and propagation length, allowing us to determine the (phase) velocity of the edge plasmons. Sec. 3.4 introduces a distributed circuit model for the QAH edge channel that captures both capacitive coupling to the environment and dissipative channels associated with bulk conduction. Finally, in Sec. 3.5, we apply this model to the full dataset and systematically analyze the dependence of plasmon transport on temperature, magnetic field, and excitation voltage. Across all three control parameters, we identify a crossover from frequency-dependent dissipation in the well-quantized QAH regime to frequency-independent losses at higher temperatures, fields, or voltages. We attribute this crossover to the activation of bulk conduction channels via the percolation of charge puddles, which ultimately governs the breakdown of the QAH effect. The results in this chapter are partially published in Ref. [94]

3.1 Sample fabrication and experimental setup

To measure the microwave propagation along the edge states of a QAH insulator, we need to locally excite plasmons in the edge channel and detect their amplitude and phase after a propagation over a distance L along the sample's edge. To achieve this, the QAH film is patterned into an rf Hall bar: a modified Hall bar that, in addition to standard Ohmic contacts, includes narrow rf gates for the excitation and detection of plasmons. We will first show the layout of the rf Hall bar before showing the fabrication of the devices.

Sample layout

A microscope image of a sample is shown in Fig. 3.1a. The sample contains three standard Hall bars used for dc transport measurements to assess the film quality and verify that the QAH effect is observed. The rf Hall bar, used for the microwave experiments, is located in the upper right corner of the sample. A

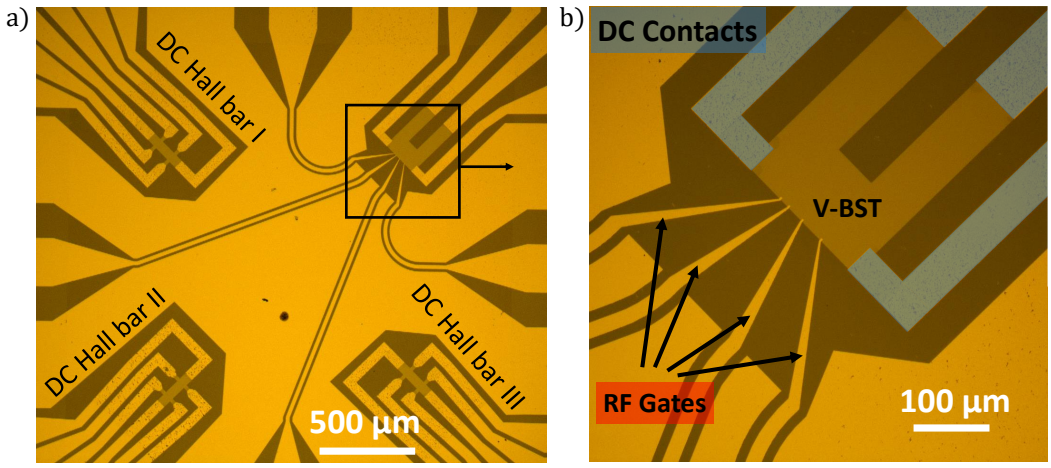

Figure 3.1: Microscope image of QAH sample. a) Overview image of Sample containing one rf Hall bar and three dc Hall bars. The rf signals are guided via coplanar waveguides (CPW). A large ground plane acts as the ground of the CPW. The 8 nm-thick V-BST film appears slightly brighter compared to the InP substrate. b) Magnified image of rf Hall bar. The π-shaped mesa (bright brown) is contacted via Ohmic contacts highlighted in blue for dc measurements of R_{xx} and R_{yx}. A set of four narrow rf gates allows for driving and reading out microwave signals in varying gate combinations, yielding the transmission coefficients S_{21} for different edge path lengths l ranging from 30 to 70 µm in this device. Both images are from sample MBE_VBST_20250206a.

magnified image of this rf Hall bar is shown in Fig. 3.1b. It has four Ohmic contacts for dc characterisation. The rf measurements are performed using narrow finger gates (bottom left of Fig. 3.1b), which are connected to the measurement setup via coplanar waveguides (CPWs) and are capacitively coupled to the edge of the V-BST layer through a 10 nm-thick Al_2O_3 dielectric layer. We choose capacitive contacts over Ohmic contacts, as they are almost transparent at GHz frequencies and have a less complex behavior than Ohmic contacts, which show a mixture of resistive and capacitive coupling due to finite contact resistances. The device in Fig. 3.1b has four rf gates for measuring the propagation for three different distances ranging from 20 µm to 70 µm. Each gate covers an area of approximately 3 µm $\times$ 3 µm, which results in a coupling capacitance of approximately 5 to 50 fF.

At microwave frequencies, the experiment measures the transmission coefficient S_{21} between two rf gates using a vector network analyzer (VNA). The rf gates act as capacitive excitation and detection ports for edge plasmons. From the complex S_{21} signal, the phase gives access to the plasmon velocity, while the amplitude provides a measure of the plasmon attenuation along the edge.

The rf Hall bar has a π-shaped geometry, which serves a specific technical purpose. The direction of edge-state propagation is set by the magnetization M and

reverses when M is reversed. In this layout, two neighboring rf gates are separated by a short propagation path of at most 100 µm, while the alternative path around the opposite side of the mesa exceeds 2 mm (in case of magnetization reversal). This long path is sufficiently long for complete plasmon dissipation. The measurement along this path is used as a reference for the short-path measurements. This will be explained in more detail in Sec. 3.2. In the following section, we will describe the fabrication of the samples in detail.

MBE growth

The entire fabrication procedure is sketched in Fig. 3.2. The first step is the molecular beam epitaxy (MBE) growth of the V-doped $(Bi_xSb_{1-x})_2Te_3$ films on InP(111)A substrates. Molecular beam epitaxy is a thin-film deposition technique in which high-purity elemental sources are thermally evaporated in an ultra-high-vacuum environment. The resulting molecular beams impinge on a heated substrate, where the atoms condense and form a crystalline thin film. The low background pressure and precise control of the individual fluxes allow accurate tuning of thickness, stoichiometry, and doping levels, which is essential for growing high-quality topological insulators [52, 95].
In our case, V-doped $(Bi_xSb_{1-x})_2Te_3$ was grown by co-evaporating Bi, Sb, Te, and V onto InP(111)A substrates at 190 °C, with Te supplied in excess and the Bi:Sb ratio adjusted to achieve charge compensation. The films have a thickness of approximately 8 nm and are capped with a Al_2O_3 layer to prevent degradation. Atomic layer deposition (ALD) is used to grow the 4 nm-thick layer of Al_2O_3. The samples are stored in a vacuum after the growth to avoid surface oxidation. The MBE process requires maintaining precisely controlled growth conditions throughout deposition and is highly sensitive to small variations in the process parameters. Achieving quantized QAH transport in particular demands near-perfect charge compensation, which is technically very challenging. This step is the most critical and demanding part of the entire fabrication. All samples used in this work were kindly grown by Dr. Alexey Taskin from the group of Prof. Yoichi Ando. For further details on the MBE growth of V-BST films, we refer the reader to the PhD thesis of Gertjan Lippertz [52] and Andrea Bliesener [96], who developed and optimized the growth procedures in the group of Prof. Yoichi Ando.

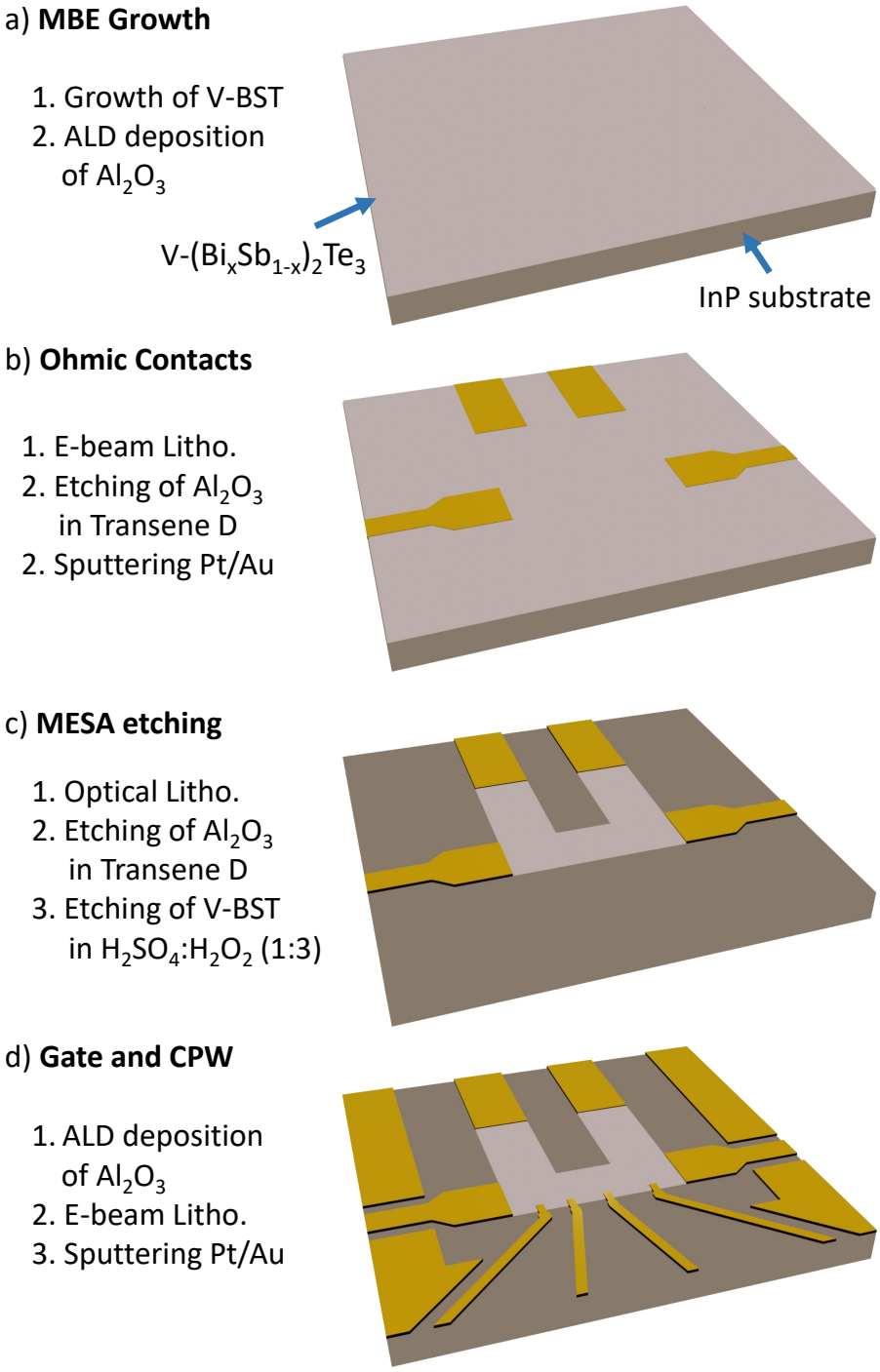

Figure 3.2: Schematic of the fabrication of QAH sample. (a) An 8 nm-thick V-doped $(Bi_xSb_{1-x})_2Te_3$ (V-BST) film is grown on an InP substrate by molecular beam epitaxy (MBE) and capped with an Al_2O_3 layer to prevent oxidation. (b) Ohmic contacts are defined by electron-beam lithography (EBL): the capping layer is etched in Transene D, followed by deposition of Pt/Au. (c) The mesa is patterned by optical lithography and sequentially etched—first the Al_2O_3 capping layer with Transene D, then the V-BST with $H_2SO_4 : H_2O_2$ (1:3). (d) A thin Al_2O_3 dielectric is deposited by atomic layer deposition (ALD), after which rf gates and coplanar waveguides (CPWs) are defined by EBL and metallized with Pt/Au.

3.1.1 Cleanroom fabrication

The cleanroom fabrication begins with defining the Ohmic contacts to the V-BST film, before patterning the mesa. While many microfabrication schemes follow the opposite order, we identified during process optimization that the timing of the Ohmic contact fabrication plays a crucial role in their quality. Contacts fabricated immediately after growth consistently show lower contact resistance than contacts made several days later. In addition, defining the Ohmic contacts first allows us to write alignment markers in the same lithography step, reducing the overall number of processing steps and limiting the exposure of the film to chemicals and elevated temperatures.
The V-BST layer degrades rapidly when heated, especially above 120 °C. All fabrication steps were therefore carried out below this temperature. In the following, we describe the fabrication steps. A full process recipe with exact parameters is provided in Appendix B.

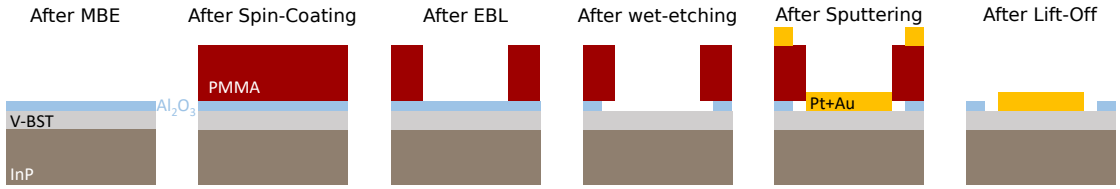

Figure 3.3: Ohmic contacts. Schematic drawing of all fabrication steps from left to right: Spin-Coating of PMMA resist, Electron-Beam lithography (EBL), wet-etching of Al_2O_3 in Transene D, sputtering of 5 nm of Pt and 30 nm of Au, Lift-Off in NMP.

1. Ohmic contacts The Ohmic contact areas are defined using electron-beam lithography (EBL) as schematically shown in Fig. 3.3. First, a 200 nm-thick polymethylmethacrylat (PMMA) resist layer is spin-coated onto the sample and baked for 10 min at 120 °C. The resist is patterned with a 10 kV electron beam. In this step, we also write alignment markers that are used to align all subsequent lithography steps to the first one. The exposed resist is developed for 30 s in MIBK, removing the PMMA in the patterned regions.
To expose the V-BST surface, the 4 nm Al_2O_3 capping layer is etched by immersing the sample for approximately 8 s in Transene D at 50 °C. Transene D is a mixture of phosphoric acid, sodium-*m*-nitrobenzenesulfonate, and acetic acid, and selectively etches Al_2O_3 without significantly attacking the V-BST layer. The sample is then rinsed in deionized water and dried with nitrogen.
Immediately after etching, the sample is loaded into the sputtering system to minimize surface oxidation, which would degrade the contact quality. A 5 nm

adhesion layer of Pt and 30 nm of Au are deposited, followed by lift-off in N-methyl-2-pyrrolidone (NMP) for one hour. NMP dissolves the resist beneath the metal, allowing the unwanted metal to be gently removed with a pipette so that Pt/Au remains only in the desired regions. If lift-off is incomplete, heating the NMP to reduce viscosity can help. Ultrasonic agitation may also assist, but must be applied with great care, as it can lift metal inside the contact areas. After lift-off, the sample is cleaned in acetone and isopropanol (IPA). It is advisable to inspect the lift-off while the sample is still submerged in IPA. Once it dried, the residual metal adheres strongly and becomes difficult to remove.

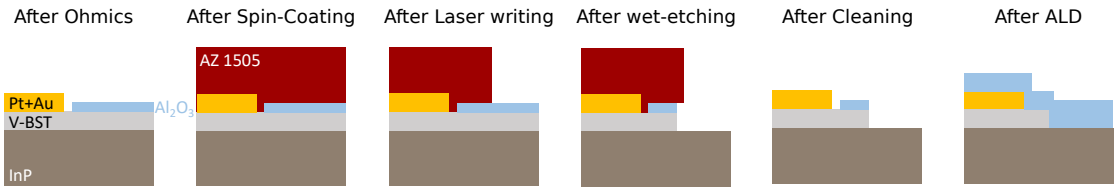

Figure 3.4: Mesa definition. Schematic drawing of all fabrication steps from left to right: Spin-Coating of AZ 1505 resist, optical lithography using a laser writer, wet-etching of Al_2O_3 in Transene D, wet-etching of the V-BST in $H_2SO_4 : H_2O_2$ (1:3) solution, Sample cleaning in Acetone and IPA.

2. Mesa etching The mesa etching process in schematically illustrated in Fig. 3.4. The mesa is defined using optical lithography. A 500 nm-thick layer of AZ 1505 is spin-coated and baked at 100 °C for 1 min. The resist is patterned using a 400 nm laser writer and developed for 30 s in the TMAH-based developer AZ MIR 701. TMAH not only develops the resist but also etches the Al_2O_3 capping layer and the V-BST beneath it. This is acceptable for mesa definition, but makes optical lithography unsuitable for Ohmic contacts or gate contacts.
After patterning, the Al_2O_3 capping layer is removed again using the same Transene D process. The V-BST is then etched in a $H_2SO_4 : H_2O_2$ (1:3) solution for approximately 15 s. The etch rate is laterally bigger than vertically, producing an undercut of roughly 500 nm relative to the resist mask. This undercut must be taken into account when designing the mesa dimensions. After etching, the sample is rinsed in deionized water to remove residues, then cleaned in acetone and IPA.
Immediately after the mesa etch, the sample is loaded into the ALD chamber to avoid surface oxidation. A further 10 nm of Al_2O_3 is deposited at 80 °C. This dielectric layer protects the underlying device and acts as the gate insulator for the rf gates.

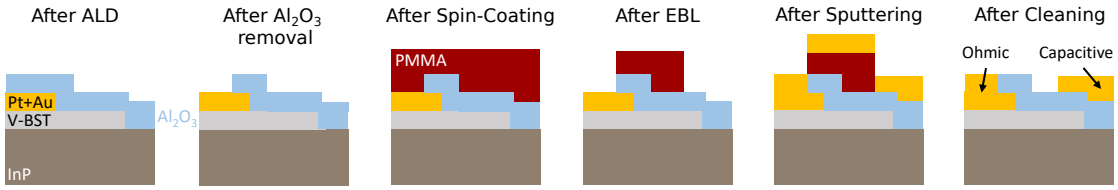

Figure 3.5: Gate and CPW definition. Schematic drawing of all fabrication steps from left to right: wet-etching of Al_2O_3 in Transene D on top of the Ohmic contacts using an optically defined resist mask, Spin-Coating of PMMA resist, Electron-Beam lithography (EBL), sputtering of 5 nm of Pt and 70 nm of Au, Lift-Off in NMP. The left contact is Ohmic while the right contact is capacitive, like the rf gates for microwave experiments.

3. rf gates and coplanar waveguides The deposition of the rf gates, bond pads, and CPW structures is done using another EBL process as sketched in Fig. 3.5. In a first step, the Al_2O_3 on top of the Ohmic contacts must be removed to ensure a good electrical connection to the bond pads. For this, we perform an optical lithography step and etch the dielectric for 30 s in Transene D at 50 °C, followed by rinsing in water and cleaning in acetone and IPA.
For the final metallisation, we use EBL with a double-layer resist stack consisting of 300 nm MMA and 300 nm PMMA. Each layer is baked for 10 min at 120 °C. The MMA layer develops faster than PMMA, creating an undercut that greatly facilitates lift-off of the relatively thick metal required for low-loss CPW transmission. The resist is patterned with a 10 kV electron beam and developed in MIBK. A final sputtering step deposits 5 nm Pt and 70 nm Au. Lift-off is again carried out in NMP for one hour, followed by gentle removal of excess metal. If needed, heating or light ultrasonic agitation may be used with caution. The sample is finally cleaned in acetone and IPA.

Mounting and bonding of the sample

To integrate the device into the measurement setup, the sample is mounted onto a printed circuit board (PCB) equipped with CPWs for rf readout (see Fig. 3.6c). The PCB contains a 3x3mm^2 cavity into which the sample is glued. The MBE growth is performed on InP substrates that typically have a triangular or parallelogram shape with edge lengths of approximately 1 cm. We therefore cut the sample into a 3x3mm^2 square after the cleanroom fabrication. Before cutting, a thin protective layer of AZ 1505 resist is spin-coated onto the sample to avoid mechanical damage. The sample is then cut with a high-precision DISCO dicing saw, cleaned in acetone and IPA, and inspected under an optical microscope.
The diced sample is glued onto the PCB using PMMA resist, which is baked at 120 °C for approximately 10 min. Electrical connections between the sample and

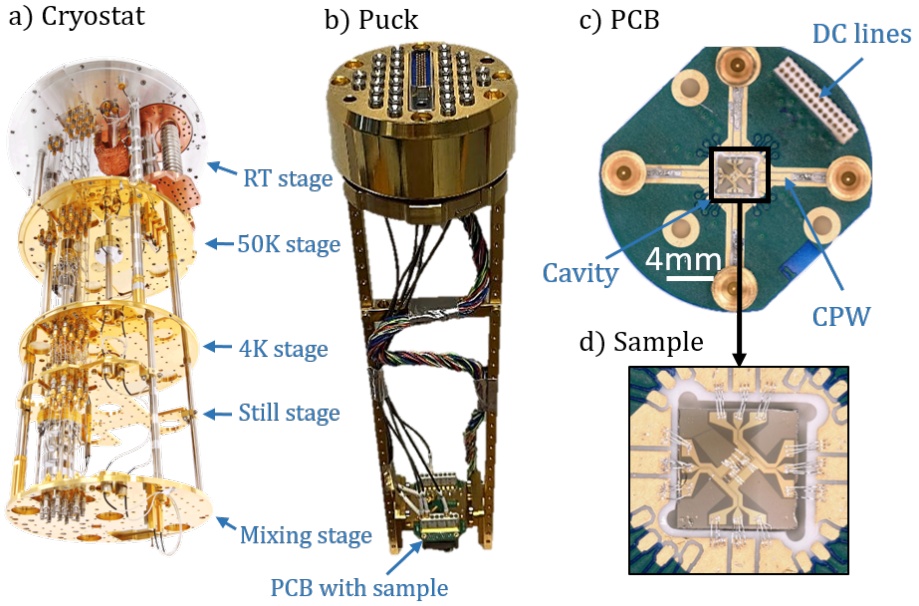

Figure 3.6: Mounting of samples into cryostat (a) Photograph of a BlueFors dilution refrigerator showing the temperature stages from room temperature (top) down to the mixing chamber (MC) at approximately 10 mK, where the sample is mounted. Image from BlueFors © 2025. b) Puck that is loaded into the cryostat in (a). Coaxial lines connect the rf lines from the docking interface to the cryostat to the sample, which is mounted at the bottom using a PCB shown in (c). (c) Image from a PCB, with a sample glued in the central cavity. It has four CPW for guiding rf signals towards the sample. (d) Magnified image of PCB with a mounted sample. Bond wires connect the PCB to the sample contacts. The sample itself is not the same as the one we used in this work, but it serves as an example.

PCB are wire bonded (see Fig. 3.6d). All Ohmic contacts are bonded with a single wire, whereas the CPW signal and ground lines are bonded more extensively: typically three wires on the signal line and three wires on each ground. This ensures efficient rf transmission and a well-defined ground reference, reducing cross-talk between neighboring CPWs. After wire bonding, the sample assembly is ready to be loaded into the cryostat.

For the experiments, we use a BlueFors dilution refrigerator, shown in Fig. 3.6a. It is a closed-cycle system that reaches temperatures below 10 mK at the mixing chamber, the coldest stage of the cryostat. The system features a 9 T solenoid magnet to apply out-of-plane magnetic fields. It is furthermore equipped with dedicated wiring, filters, and cryogenic amplifiers, which will be described in the next section. To avoid warming up and opening the entire cryostat for each sample change, we use the BlueFors fast-sample-exchanger (FSE) system, which allows a sample "puck" to be docked and undocked from the mixing chamber without breaking the vacuum. The mounted device is fixed to the puck using a

gold-plated bracket (see Fig. 3.6b). The dc lines of the sample connect to a multi-pin connector on the top of the puck, while the rf lines connect via an MSMP connector on the PCB to a corresponding SMP connector on the top of the puck. During loading, these connectors automatically connect with their counterparts on the mixing chamber, establishing contact with the cryostat wiring that will be discussed in the next section.

3.1.2 Experimental setup and dc characterisation

For the dc characterisation, we apply a bias current of $I_{xx} = 1\,\mathrm{nA}$ to the Hall bar by sourcing a 7 Hz, 10 mV ac signal through a 10 MΩ series resistor as shown in Fig. 3.7a. The current is monitored by measuring the voltage drop over a 10 kΩ series resistor using lock-in detection. Using the same principle, we detect the longitudinal voltage drop V_{xx} (or the Hall voltage V_{yx} for different wiring) to calculate the resistance $R_{xx} = V_{xx}/I_{xx}$. We measure R_{xx} and R_{yx} as a function of the out-of-plane magnetic field $\mu_0 H$ at a base temperature of $T \simeq 15\,\mathrm{mK}$ before rf measurements to check the film quality. An example measurement is shown in Fig. 2.5.
All samples used in this work exhibit a quantized Hall resistance $R_{yx} = R_K = h/e^2$, with deviations of less than two percent. However, the samples differ more strongly in their residual longitudinal resistance r_{xx}, ranging from 0.2 to 5.8 Ω/µm in zero field (calculated from the longitudinal R_{xx} measured along a distance of 80 µm between the Ohmic contacts). We will focus in this chapter on results taken from the sample with the lowest residual resistance of approximately 0.2 Ω/µm (Sample ID: $\mathrm{MBE\_VBST\_20231204a}$). In the following, we will describe the rf setup to measure the transmission coefficient S_{21} between neighboring finger gates.

The rf setup is shown in Fig. 3.7b. We use a vector network analyzer (VNA) to excite and detect plasmons in the sample. A VNA generates sinusoidal signals and measures their complex transmission and reflection coefficients. In our experiments, the VNA applies a small rf excitation to one rf gate and records the transmitted signal at a second gate, yielding the complex transmission coefficient $S_{21}(f)$. From the amplitude and phase of S_{21}, we extract the plasmon attenuation and the phase velocity along the QAH edge channel. The VNA is therefore the central instrument that allows us to probe the frequency-resolved plasmon dynamics in the device.
The VNA ports are connected via coaxial cables to feedthrough connectors at the top of the cryostat. The excitation line of the refrigerator is equipped with

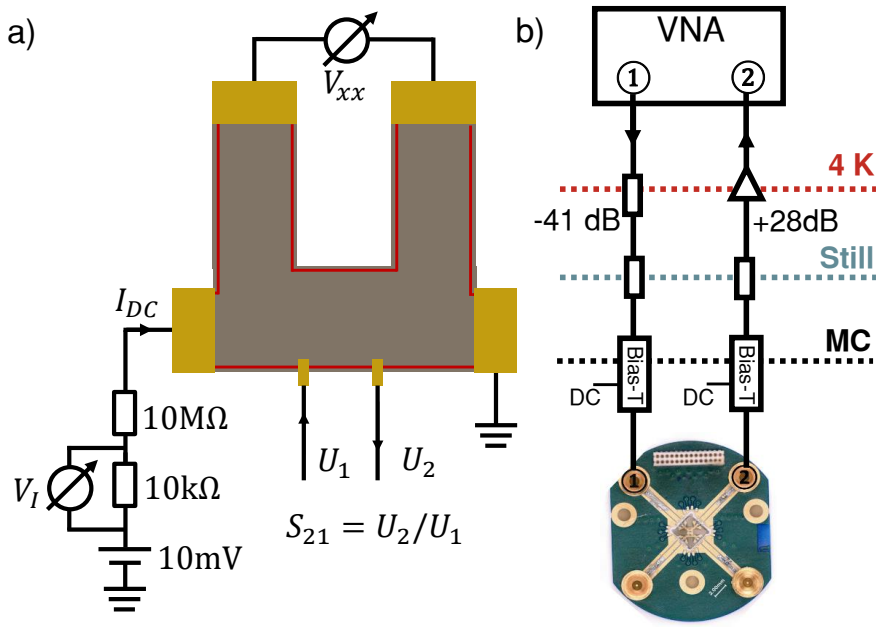

Figure 3.7: Experimental Setup. (a) dc setup for measuring R_{xx}. A small ac bias (10 mV, 7 Hz) is applied through a 10 MΩ series resistor, and the resulting current is monitored via the voltage V_I across a 10 kΩ resistor. The longitudinal voltage drop V_{xx} is measured between the top Ohmic contacts using lock-in detection. (b) The PCB with the sample is connected to the room-temperature electronics via broadband coaxial cables. The input line includes attenuators at each temperature stage (total 41 dB), and the output line contains an attenuator (10 dB) and a cryogenic low-noise amplifier (LNF-LNC0.3_14A, +38 dB). Bias-tees allow for the separation of dc and rf signals, but are not used in this work. A vector network analyzer (VNA) measures the transmission coefficient S_{21}.

attenuators at each temperature stage to ensure proper thermalization of the microwave cables and to avoid heating the electronic system inside the sample. The transmitted signal is amplified by a cryogenic low-noise amplifier with a gain of +38 dB and a bandwidth from 300 MHz to 14 GHz. At frequencies below approximately 3 GHz, the amplifier exhibits a strong input reflection, with $S_{11} > -5\,\mathrm{dB}$, which leads to standing waves between the amplifier and the sample if the sample is not impedance matched to the 50 Ω fridge lines. In our case, the QAH edge has an impedance of $Z_e = R_K \simeq 25.8\,\mathrm{k\Omega}$, resulting in an almost perfect reflection of $S_{11} \approx 0.99$, as discussed in Ref. [97].

A common way to suppress standing waves is to use a microwave isolator or circulator, which are non-reciprocal devices that transmit power only in one direction. However, they typically operate only in narrow frequency bands (e.g. $4\,\mathrm{GHz} - 8\,\mathrm{GHz}$), which is incompatible with the broadband measurements we perform ($300\,\mathrm{MHz} - 4\,\mathrm{GHz}$). Instead, we suppress the standing waves by inserting a 10 dB attenuator in front of the amplifier, as shown in Fig. 3.7b. This

reduces the effective gain to +28 dB and damps the standing waves by approximately 20 dB. While this approach reduces the overall sensitivity of the setup by 10 dB, most measurements presented in this thesis are not sensitivity-limited. The improved stability and reproducibility of the microwave response, therefore, outweigh the loss in signal amplitude.

3.2 RF measurements and calibration

For the rf experiment, we measure the transmission coefficient S_{21} between two neighboring rf gates, as sketched in Fig. 3.8a. The raw transmission $S_{21}(f)$ is shown in Fig. 3.8b for the positively magnetized state ($\mu_0 H = 2\,\mathrm{T}$) and the negatively magnetized state ($\mu_0 H = -2\,\mathrm{T}$). In both cases, the transmission exhibits pronounced oscillations with a frequency spacing of approximately 143 MHz. These oscillations arise from standing waves between the sample and the cryogenic amplifier, as discussed in the previous Section. The resonance condition follows that of a Fabry-Pérot cavity, where standing waves form when the round-trip phase accumulation equals an integer multiple of 2π. Using the resonance spacing $\Delta f = 143\,\mathrm{MHz}$ and a propagation velocity of $v = 2 \times 10^8\,\mathrm{m/s}$ in the coaxial line, we estimate an effective cavity length of $L = v/(2\Delta f) \approx 70\,\mathrm{cm}$. This is shorter than the nominal cable length of approximately 1 m, suggesting that either the propagation velocity is underestimated or the effective electrical length is shorter than the physical length. The origin of the standing waves is nevertheless confirmed by the observed shift of the resonance frequency upon changing the cable length.

In addition to these oscillations, the two magnetization configurations show a clear difference in the transmission. At low frequencies ($f \lesssim 2\,\mathrm{GHz}$), the transmission in the positive magnetization state is approximately 20 dB higher than for negative magnetization. This behavior results directly from the chirality of the QAH edge state. As illustrated in Fig. 3.8a, for negative magnetization, the excited plasmons propagate along the long path of the mesa ($L > 2\,\mathrm{mm}$), where they experience strong dissipation before reaching the detector. This dissipation stems from the long propagation path and the presence of four Ohmic contacts that drain the edge current. In this case, only a small background or stray transmission S_{stray} is recorded. For positive magnetization, however, the edge state connects the two rf gates along the short path of approximately 20 µm, allowing us to detect the sum of the edge-state signal and the stray background, $S_{\mathrm{edge}} + S_{\mathrm{stray}}$.

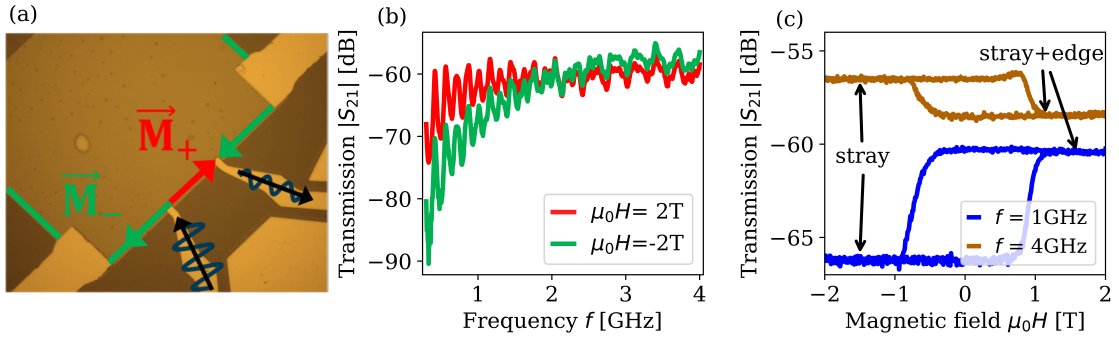

Figure 3.8: Raw transmission measurements on rf Hall bar. (a) Microscope image of the sample. The transmission S_{21} is measured from the left to the right rf gate. Plasmons propagate along the green path for negative magnification $\vec{M}_-$ and along the red path for positive magnetization $\vec{M}_+$. (b) The raw transmission coefficient S_{21} vs. the frequency f for $\mu_0 H = \pm 2\,\mathrm{T}$. (c) S_{21} vs. $\mu_0 H$ for a frequency of $f = 1\,\mathrm{GHz}$ and $f = 4\,\mathrm{GHz}$ showing magnetic field dependent hysteresis.

Importantly, the stray signal does not depend on the magnetization because it originates from parasitic coupling paths. It originates primarily from direct capacitive cross-talk between metallic rf structures on the PCB or on the chip, which is insensitive to the chirality of the edge state. This field independence is essential for our calibration procedure, because it allows us to use the negative-magnetization configuration—where the long propagation path suppresses S_{edge} entirely—as a direct measurement of the stray background. In other words, the negative magnetization state provides a reliable reference from which the true edge-state transmission can be extracted by subtraction.

This magnetization dependence is also visible in the field sweep shown in Fig. 3.8c, where the transmission exhibits the same hysteretic behavior as the dc Hall resistance in Fig. 2.5. Interestingly, above about 2 GHz the sign of the hysteresis reverses and the transmission becomes larger for negative magnetization. At first glance, this appears to contradict the picture described above. However, it must be emphasized that S_{edge} and S_{stray} are complex quantities whose amplitudes and phases are both frequency dependent. At high frequencies, the two contributions have comparable magnitude but acquire a relative phase shift. In the positive magnetization state, the complex sum $S_{\mathrm{edge}} + S_{\mathrm{stray}}$ can lead to partial cancellation, causing the transmission to become smaller than in the negative state and thereby reversing the hysteresis in Fig. 3.8c.

For a quantitative analysis of the edge-state propagation, we must therefore calibrate the data to remove the stray background and isolate the true edge-state transmission coefficient S_{edge}. The calibration procedure is described in the following section.

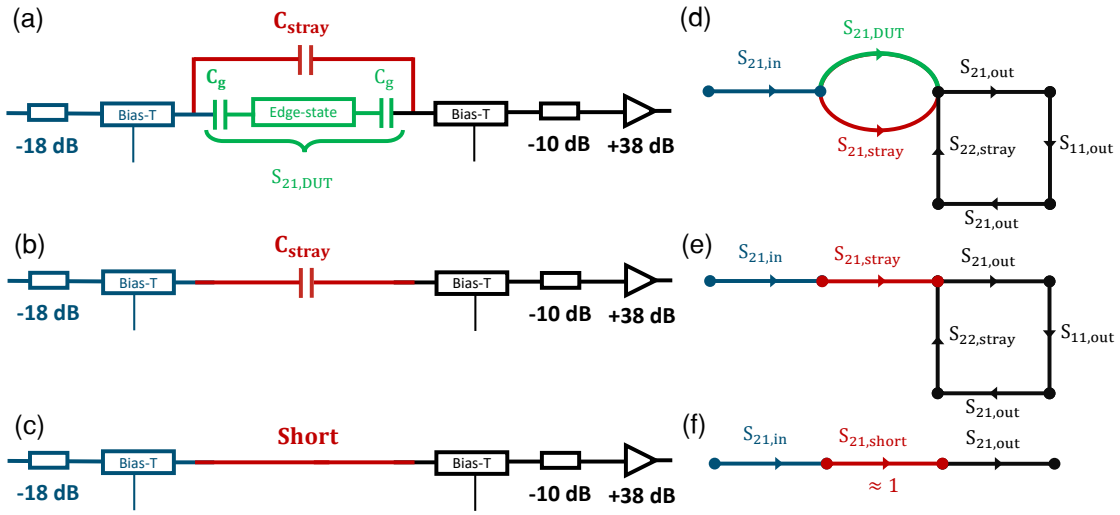

Figure 3.9: Signal graphs of microwave network. (a)-(c) Schematic drawing of microwave setup for transmission experiment with (a) QAH sample installed, (b) stray-reference installed, and (c) through-reference installed, corresponding to the samples (a)-(c) shown in Fig. 3.10. (d)-(f) Simplified signal graph describing the transmission in the microwave setups shown in (a)-(c).

3.2.1 Calibration procedure

Three main mechanisms alter the microwave signal in our measurement setup. First, all microwave components in the cryostat (coaxial cables, attenuators, bias-tees, amplifiers) contribute a frequency-dependent attenuation and phase shift. Second, as discussed previously, strong standing waves appear between the sample and the cryogenic amplifier, producing the oscillations visible in the VNA spectra in Fig. 3.8. Third, the chip itself introduces perturbations: the coplanar waveguides act as small antennas at gigahertz frequencies, leading to a parasitic, frequency-dependent stray coupling between rf ports. To account for these distortions, calibration measurements are done using two reference devices. Figure 3.9a-c illustrates the microwave network for the real sample and for the two reference devices. We can correct the majority of distortions by introducing a simplified signal-flow model and using two reference measurements. We describe the microwave setup in terms of the signal graph in Fig. 3.9d-f:

- **Input line:** $S_{21,\mathrm{in}}$ models all losses and phase shifts from the VNA to the excitation gate. It includes cables, attenuators, and a bias tee as shown in Fig 3.9a-c. Reflections are neglected, assuming they are sufficiently attenuated along the input chain.

- **Device under test (DUT):** The transmission mediated by the QAH edge

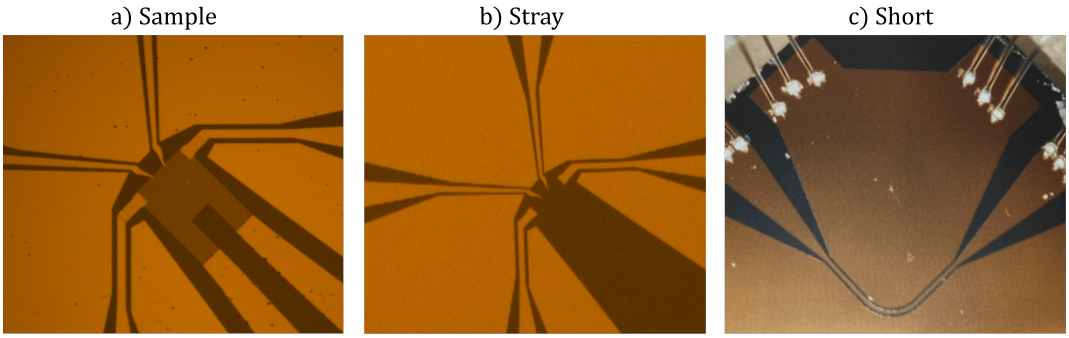

Figure 3.10: Reference samples. (a) Real sample with a QAH insulator mesa, (b) Stray-reference sample without QAH insulator for measurement of stray coupling on chip, (c) Through-reference sample where rf ports are directly connected via a CPW Through on InP substrate to calibrate distortions in the microwave setup installed in the cryostat.

channel is described by $S_{21,\mathrm{DUT}} = S_{eg} \cdot S_{\mathrm{edge}} \cdot S_{\mathrm{ge}}$, including 2 capacitive couplings (gate–edge S_{eg} and edge–gate coupling (S_{ge}) and propagation along the edge (S_{edge}). The corresponding circuit model is shown in green in Fig 3.9a. A stray background path $S_{21,\mathrm{stray}}$ runs in parallel (red in Fig 3.9a-b), acting as a single capacitor.

- **Output line with standing-wave loop:** The output chain (shown black red in Fig 3.9a-c) is modeled as a loop containing the transmission $S_{21,\mathrm{out}}$ between sample and amplifier (assumed equal in both directions), and the reflection coefficients at the sample plane and amplifier, $S_{11,\mathrm{out}}$ and $S_{22,\mathrm{stray}}$. This loop captures the standing waves giving rise to the oscillations in the raw spectra.

The whole transmission of this signal graph in Fig. 3.9d is given by:

$$S_{21,\mathrm{total}} = \frac{S_{21,\mathrm{in}} \cdot (S_{21,\mathrm{DUT}} + S_{21,\mathrm{stray}}) \cdot S_{21,\mathrm{out}}}{1 - S_{21,\mathrm{out}}^2 \cdot S_{11,\mathrm{out}} \cdot S_{22,\mathrm{stray}}} \tag{3.1}$$

Reference measurements

To separate the different contributions in $S_{21,\mathrm{total}}$, we use two reference samples. The first reference sample is a through-dummy. Here, the injection and detection ports are directly connected via an impedance-matched coplanar waveguide without reflections, as for the impedance-mismatched sample. Thus, this yields the response of the whole setup without sample or stray coupling. The reference sample is shown in Fig. 3.10c and the corresponding signal graph in Fig. 3.9f.

The total transmission with the through-dummy installed is:

$$S_{21,\mathrm{through}} = S_{21,\mathrm{in}} \cdot S_{21,\mathrm{out}} \tag{3.2}$$

The second reference is a stray dummy, a sample identical to those measured, but for which the V-BST layer is missing, as shown in Fig. 3.10b. This reference shows the stray coupling and the standing waves, as it has essentially the same impedance mismatch as the real sample (open vs. R_K differ only by $S_{11} \approx 1$ vs. 0.99). The signal graph of this device is sketched in Fig. 3.9f. Its transmission corresponds to:

$$S_{21,\mathrm{dummy}} = \frac{\mathrm{S}_{21,\mathrm{in}} \cdot \mathrm{S}_{21,\mathrm{stray}} \cdot \mathrm{S}_{21,\mathrm{out}}}{1 - S_{21,\mathrm{out}}^2 \cdot S_{11,\mathrm{out}} \cdot S_{22,\mathrm{stray}}} \tag{3.3}$$

Extracting the stray coupling and standing-wave contribution

Figure 3.11 shows the raw S_{21} spectra of the real sample, the stray-reference, and the through-reference. The stray-reference is nearly identical to the negatively magnetized QAH sample, confirming that the long edge path fully suppresses $S_{21,\mathrm{DUT}}$ and can itself serve as a stray-signal measurement. To isolate the true edge signal, we first separate stray coupling from the standing-wave pattern. We do this by fitting the ratio $|S_{21,\mathrm{dummy}}/S_{21,\mathrm{through}}|$, which includes both contributions, to the response of a simple capacitive coupling C in a $Z_0 = 50\,\Omega$ environment:

$$S_{21,\mathrm{capa}}(f) = \frac{A}{1 + \frac{j}{2\omega Z_0 C}}, \tag{3.4}$$

with the overall constant A[1]. This captures the monotonic increase of stray coupling with frequency. An example fit is shown in Fig. 3.12a. The remaining part is attributed to the standing-wave oscillations:

$$S_{21,\mathrm{osci}} = \frac{S_{21,\mathrm{dummy}}}{S_{21,\mathrm{through}} \cdot S_{21,\mathrm{capa}}}. \tag{3.5}$$

After isolating the stray coupling and the standing-wave oscillations, we can find the transmission coefficient $S_{21,\mathrm{DUT}}$ of the edge state transmission, which is obtained as:

$$S_{21,\mathrm{DUT}} = \frac{(S_{21,\mathrm{total}} - S_{21,\mathrm{dummy}}) \cdot S_{21,\mathrm{capa}}}{S_{21,\mathrm{dummy}}}. \tag{3.6}$$

[1]The constant A would ideally be one, but in our model, we leave it as a free fit parameter to account for additional frequency-independent losses.

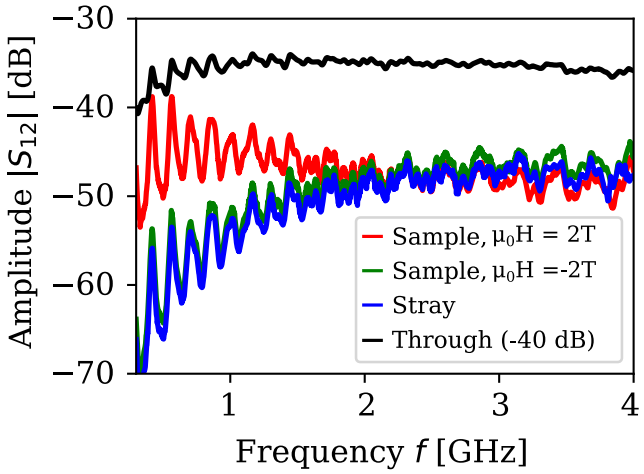

Figure 3.11: Calibration measurements. The raw data of the transmission coefficients S_{21} vs. the frequency f. The green and red curve corresponds to the transmission between two neighboring gates on a QAH sample at $\mu_0 H = \pm 2\,\mathrm{T}$. The black and blue curves show reference measurements for the Stray and the Through-reference, respectively. The trace of the Through-reference is offset by −40 dB for clarity.

With the corrected transmission coefficient $S_{21,\mathrm{DUT}}$ in hand, we can now extract the physical properties of the propagating edge plasmons. In the following section, we always refer to the corrected transmission and name it $S_{21} = S_{21,\mathrm{DUT}}$. After a short error analysis, we will analyze the frequency-dependent phase of S_{21} to obtain the plasmon phase velocity, and the frequency-dependent amplitude to determine the attenuation along the QAH edge. These two quantities, velocity and dissipation, form the basis for our study of edge-state propagation in the remainder of this chapter.

3.2.2 Error analysis

The main limitation of our calibration scheme lies in the capacitive-coupling fit, which carries significant uncertainty due to the strong standing-wave oscillations. Figure 3.12a shows the corrected stray signal and the corresponding capacitive fit. We estimate the error by fitting upper and lower envelopes of the oscillatory signal. The resulting standard deviation in amplitude and phase is shown in Fig. 3.12b. Both errors decrease with frequency but remain sizable: typically $> 10\%$ in amplitude and $> 0.1\,\mathrm{rad}$ in phase.
Additionally, the calibration changes slightly between cooldowns, introducing a small offset in amplitude and phase. However, this offset does not affect the main conclusions of this work. Finally, we note that our procedure does not correct

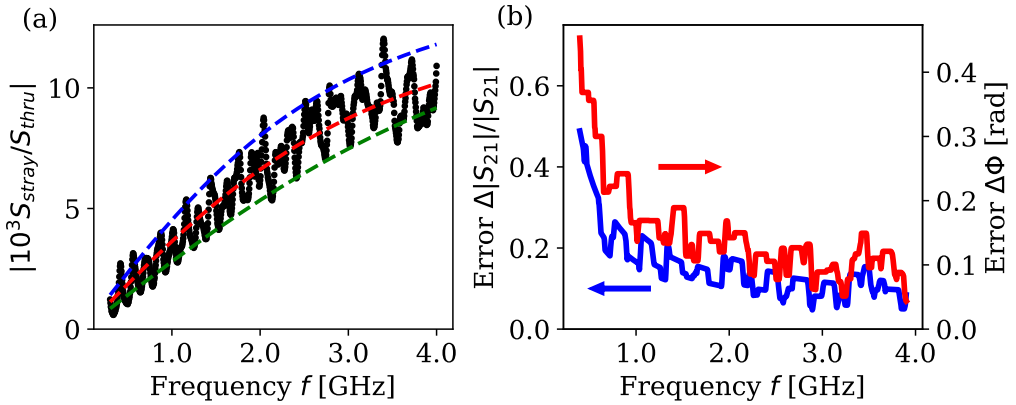

Figure 3.12: Fit quality and error estimation. (a) Corrected stray signal $S_{\text{stray}}/S_{\text{through}}$ (black dots) and capacitive fit (red). Upper and lower envelope fits (blue/green) are used to estimate systematic uncertainty. (b) Standard deviation of amplitude and phase extracted from these bounds.

for the capacitive gate–edge coupling of the finger gate itself. This contribution is considered part of the effective device response.

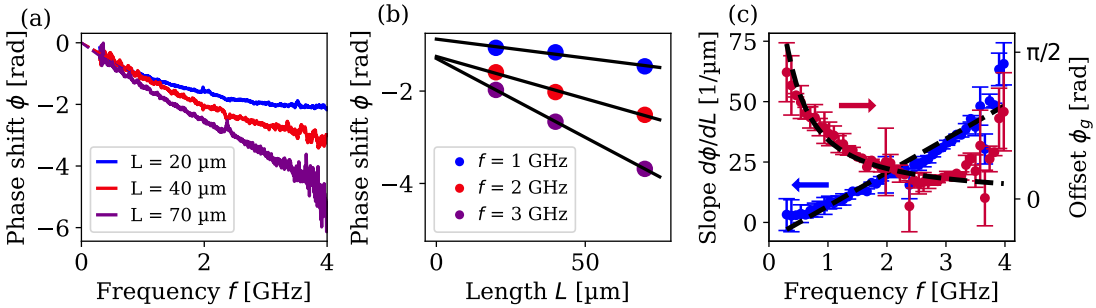

Figure 3.13: Extraction of plasmon velocity from phase measurements. (a) Corrected phase shift $\phi(f)$ for propagation lengths $L = 20$, 40, and 70 µm. Dashed lines show linear fits at low frequency, used to remove a constant phase offset introduced by the calibration. (b) Phase shift as a function of propagation length for three representative frequencies. Linear fits yield the slope $d\phi/dL = 2\pi f/v$ and the intercept $\phi_g(f)$. (c) Extracted slope (top) and intercept (bottom) as a function of frequency. The slope is well described by a linear fit, giving a plasmon velocity of $v = (4.5 \pm 0.5) \times 10^5\,\mathrm{m/s}$. The intercept agrees with the expected gate–edge coupling phase and yields a capacitance of $C_g = (19 \pm 2)\,\mathrm{fF}$. Error bars show fit uncertainties.

3.3 Velocity of plasmon transport

In this section, we extract the plasmon phase velocity from the frequency-dependent phase of the transmitted microwave signal. By comparing different propagation lengths, we isolate edge-state transport from parasitic gate-edge coupling and establish the characteristic velocity scale of QAH edge plasmons. After calibration, the phase shift is given by

$$\phi(f, L) = \arg(S_{21}) = \frac{2\pi f L}{v} + \phi_g(f), \tag{3.7}$$

where v is the plasmon velocity, L is the propagation length, and $\phi_g(f)$ denotes an additional phase originating from the capacitive coupling between the rf finger gate and the QAH edge channel (see Sec. 1.2). Importantly, ϕ_g depends on frequency but not on the propagation length.

Figure 3.13a shows the corrected phase shift $\phi(f)$ for three different gate spacings ($L = 20$, 40, and 70 µm) for an excitation amplitude of $U_{\mathrm{rf}} \simeq 225\,\mu\mathrm{V}$. Since the calibration procedure effectively uses the capacitive stray path as a phase reference, it introduces an unknown constant offset. To remove this offset, we subtract the phase at the lowest accessible frequency. Physically, a plasmon acquires no phase in the limit of $f \to 0$, so this subtraction should restore the correct reference point.

The phase decreases monotonically with frequency and with propagation length.

To separate the propagation contribution from the gate-coupling contribution, it is more convenient to analyze the phase as a function of L at fixed frequency, since the gate-coupling is independent of the propagation length L. Figure 3.13b shows representative curves of ϕ vs. L at 1, 2, and 3 GHz, together with linear fits of Eq. 3.7. The slope directly yields $d\phi/dL = 2\pi f/v$ and the intercept gives $\phi_g(f)$.

The extracted slope and intercept as a function of frequency are plotted in Fig. 3.13c. The slope grows linearly with frequency, as expected for plasmons with a linear dispersion relation. A linear fit of $d\phi/dL$ vs. f yields a plasmon velocity of $v = (4.5 \pm 0.2) \times 10^5\,\mathrm{m/s}$. The intercept $\phi_g(f)$ is well described by our simple capacitive coupling model (see Eq. 3.4), from which we extract a gate capacitance of $C_g = (19 \pm 2)\,\mathrm{fF}$. The agreement between model and experiment—in both the L-dependence and the frequency dependence—provides a strong consistency check of the calibration procedure.

Despite the uncertainties introduced by the standing-wave correction and the cooldown-to-cooldown variability, the extracted velocity is robust across samples and measurement configurations. The value $v \approx 4.5 \times 10^5\,\mathrm{m/s}$ is comparable to the velocities reported for Cr-doped BST devices [16, 17] and is close to the Fermi velocity of surface states measured by ARPES in related topological insulator compounds [98, 99]. It is, however, significantly lower than typical edge velocities in the QH regime of ungated GaAs-based devices [18], where electron–electron interactions enhance the plasmon velocity [100, 101]. The reduced velocity observed here suggests stronger screening, consistent with the presence of charge puddles caused by potential fluctuations around the Fermi level. Similar interaction screening effects have been identified in high-frequency edge-state transport in both the QH and quantum spin Hall regimes [17, 102, 103].

In the next sections, we build on these observations and introduce a circuit model incorporating the coupling to charge puddles to explain the measured dissipation and the deviation from ideal chiral plasmon propagation.

3.4 Fitting with circuit model

To describe propagation, dispersion, and dissipation on an equal footing, we model the QAH edge channel using a distributed circuit model. This model captures how the chiral edge plasmon interacts with localized charge puddles

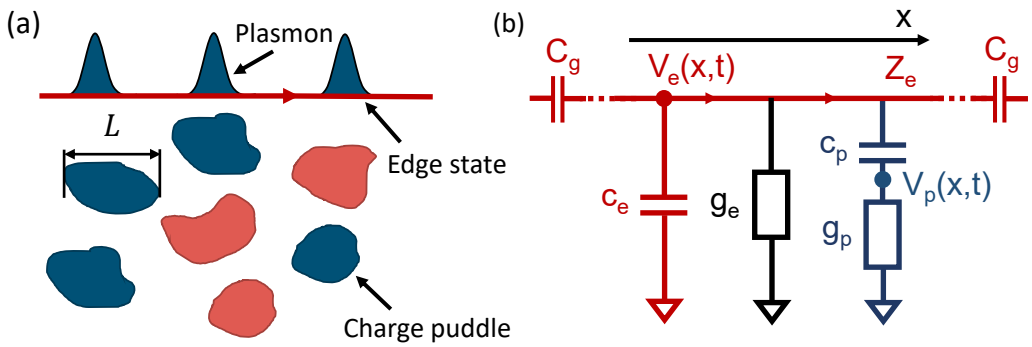

Figure 3.14: Circuit model for edge–puddle coupling. (a) Schematic QAH bar containing localized electron and hole puddles (blue/red regions). Plasmons propagating along the chiral edge channel couple capacitively to these puddles, which provide dissipation and additional screening. (b) Distributed circuit representation. The edge channel is modelled as a transmission line of characteristic impedance $Z_e = R_K$ and line capacitance c_e (quantum capacitance of the edge). The edge is capacitively coupled to the rf gates via C_g. Charge puddles are represented by a capacitance c_p and a conductance g_p, forming an RC element with characteristic frequency $f_p = g_p/(2\pi c_p)$. A frequency-independent dissipative channel g_e accounts for the residual longitudinal conductance observed in dc transport. The time-dependent potentials of the edge and puddles are denoted $V_e(x,t)$ and $V_p(x,t)$.

in the bulk, which act as dissipative and screening elements. The physical picture is sketched in Fig. 3.14a: the edge channel supports a chiral charge mode, while potential fluctuations create electron- and hole-like puddles that couple capacitively to the edge and provide additional channels for energy loss. We follow the approach introduced by Kumada et al. [38], adapting it to the present QAH system. The corresponding transmission-line representation is shown in Fig. 3.14b.

The edge itself is described as a chiral transmission line (red line in Fig. 3.14b) with impedance $R_K = h/e^2$ and quantum capacitance per unit length c_e. The term g_e (black line in Fig. 3.14b) represents a frequency-independent dissipation of the edge state, which we will later show to correlate with the finite longitudinal resistance extracted from dc measurements. The puddle network is represented by a distributed RC element with capacitance c_p (including geometric and quantum contributions) and conductance g_p (blue line in Fig. 3.14b). At low frequencies, the charge puddles follow the edge potential, yielding finite dissipation that scales with f^2. The frequency at which this becomes prominent is given by the cutoff frequency:

$$f_p = \frac{g_p}{2\pi c_p}. \tag{3.8}$$

Bagchi et al. [72] measured the bulk conductivity in the compensated $\mathrm{BiSbTeSe}$,

which is a related topological insulator compound that also hosts charge puddles. They showed an increase of conductivity that scales with f^2 with an effective cut-off frequency of $\lesssim 3\,\mathrm{GHz}$. They attribute this cut-off to the Thouless timescale $\tau_{\mathrm{Th}} = DL_p^2$, which is set by the size of L_p of the puddles and the local diffusion constant D [72, 104], puddle-size distribution of 0.1–3 µm for bulk $\mathrm{BiSbTeSe}$. As we are investigating a thin film, we expect a different puddle-size distribution, but it gives a baseline for the range of cutoff frequencies we expect. In the following, we will derive the dispersion relation of the circuit model and finally fit it to our transmission data.

Derivation of the dispersion relation

To obtain the dispersion relation of the coupled edge–puddle system, we apply Kirchhoff's current-conservation law to the distributed circuit (Fig. 3.14b), which gives:

$$c_e\,\partial_t V_e + \frac{1}{R_K}\,\partial_x V_e + g_e V_e + c_p(\partial_t V_e - \partial_t V_p) = 0, \tag{3.9a}$$

$$g_p V_p + c_p(\partial_t V_p - \partial_t V_e) = 0. \tag{3.9b}$$

The chirality of the edge channel is imposed in the first equation. Searching for plane wave solutions $V_{e/p} = V_{e/p,0}\cdot e^{i(2\pi f t - kx)}$, we rewrite the chiral wave equation, where $k(f)$ is the wave vector:

$$i2\pi f c_e V_e - \frac{ik}{R_K} V_e + g_e V_e + i2\pi f c_p(V_e - V_p) = 0, \tag{3.10a}$$

$$g_p V_p + i2\pi f c_p(V_p - V_e) = 0. \tag{3.10b}$$

Solving for $k(f)$ yields the complex dispersion relation:

$$k(f) = R_K c_e 2\pi f - iR_K g_e + \frac{R_K c_p 2\pi f}{1 + \frac{i2\pi f c_p}{g_p}}. \tag{3.11}$$

This expression contains three contributions:

1. The first term describes the bare edge dispersion $R_K c_e 2\pi f$, which describes a clean, interaction-renormalized chiral mode.

2. The second term $-iR_K g_e$ represents frequency-independent dissipation (e.g., due to weak bulk conduction).

3. The third term describes the puddle-induced dispersion and dissipation. The puddle network contributes an additional capacitance and a frequency-dependent loss channel.

For $f \ll f_p$, puddles follow the edge potential and add a large capacitive load. This increases total capacitance per unit length and reduces the plasmon velocity to $v \approx 1/[R_K(c_e + c_p)]$. In this frequency range, the dissipation grows as $\mathrm{Im}\,(k) \propto f^2$, consistent with observations by Martinez et al. [17]. For $f \gg f_p$, puddles cannot respond fast enough, and they only introduce a small imaginary contribution, which decreases with frequency.
We expect the edge capacitance c_e to be much smaller than the puddle capacitance c_p, as observed in similar cases [19, 103, 105], and will therefore neglect c_e in the following to reduce the number of fit parameters. This assumption is valid as long as we stay in the low frequency regime $f \ll f_p$. Based on the bulk studies by Bagchi et al. [72] and recent experiments on plasmon dissipation in Cr-doped BST by Martinez et al. [17], we expect this to be valid for frequencies up to 4 GHz.

Including the gate–edge coupling

The calibration procedure removes distortions of the microwave setup but does not correct for the intrinsic capacitive coupling between the rf gate and the edge state. We therefore explicitly include the gate–edge coupling using the scattering formalism derived in Sec. 1.2.2. The coupling is described by an effective series capacitance C_g that combines the geometric capacitance C_{geo} and the quantum capacitance C_e of the edge state (see Sec. 1.2.2 for details). The forward and backward coupling coefficients at the gate–edge interface are given by [106]

$$S_{eg} = \frac{2i\omega Z_e C_g}{1 + i\omega C_g (Z_g + Z_e)}, \qquad S_{ge} = \frac{Z_g}{R_K} S_{eg}, \tag{3.12}$$

with $Z_g = 50\,\Omega$. In the high-frequency limit ($\omega \gg 1/(Z_g C_g)$), the coupling saturates at $S_{eg} \simeq 2$ and $S_{ge} \simeq 2Z_g/R_K$, reflecting the strong impedance mismatch between the metallic gate and the high-impedance edge channel. In the opposite limit ($\omega \ll 1/(Z_g C_g)$), the capacitive coupling vanishes ($S_{eg}, S_{ge} \to 0$). The propagation along the edge over a distance L introduces the phase shift and attenuation, which is given by:

$$S_{\mathrm{edge}} = e^{-ikL}. \tag{3.13}$$

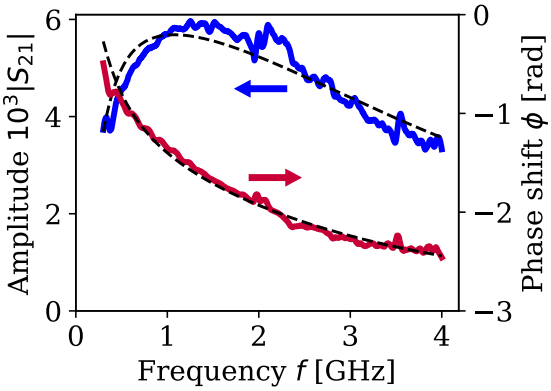

Figure 3.15: Fit of the circuit model to the complex transmission. Measured (solid lines) and fitted (dashed lines) amplitude $|S_{21}|$ (blue, left axis) and phase ϕ (orange, right axis) for device MBE_VBST_20221204a at $L = 20\,\mu\mathrm{m}$, $T = 20\,\mathrm{mK}$, $\mu_0 H = 2\,\mathrm{T}$, and excitation amplitude $U_{\mathrm{rf}} = 225\,\mu\mathrm{V}$. The circuit model reproduces both amplitude and phase over the full frequency range, allowing the extraction of the fit parameter: $c_p = (102 \pm 1)\,\mathrm{pF/m}$, $C_g = (24.4 \pm 0.2)\,\mathrm{fF}$, $f_p = (7.0 \pm 0.1)\,\mathrm{GHz}$, $g_e = (0.38 \pm 0.01)\,\mathrm{S/m}$.

Because the stray-reference calibration assigns the phase of the capacitive background as the zero-frequency reference, the measured phase contains an additional offset of $\pi/2$. We therefore write the full modeled transmission as:

$$S_{21} = S_{eg} \cdot S_{\mathrm{edge}} \cdot S_{ge} \cdot e^{-i\pi/2}. \tag{3.14}$$

We fit the complex model $S_{21}(f)$ to the calibrated data $S'_{21,\mathrm{DUT}}$ using the *curve_fit* routine from the *scipy* Python package, treating $c_p, g_p, g_e,$ and C_g as free parameters.

Fit of complex transmission data

Figure 3.15 shows the calibrated amplitude and phase of $S_{21}(f)$ for a propagation length of $L = 20\,\mu\mathrm{m}$, together with fits based on the circuit model introduced in Sec. 3.4. We first discuss the fit at base temperature ($T = 20\,\mathrm{mK}$), in the magnetized QAH state ($\mu_0 H = 2\,\mathrm{T}$), and at an excitation amplitude of $U_{\mathrm{rf}} \simeq 225\,\mu\mathrm{V}$. We then comment on how the extracted fit parameters evolve with temperature, magnetic field, and excitation amplitude in later sections. The model reproduces both amplitude and phase with high accuracy over the full frequency range ($R^2 = 0.98$), demonstrating that the distributed circuit representation provides a consistent microscopic description of edge plasmon transport in our device.
The fit yields a puddle capacitance per unit length of $c_p = (102 \pm 1)\,\mathrm{pF/m}$. Using $v = 1/[R_K(c_e + c_p)]$ (with $c_e \ll c_p$), this gives a plasmon velocity $v =$

$(3.8 \pm 0.1) \times 10^5\,\mathrm{m/s}$. This velocity agrees well with our earlier independent estimate (Fig. 3.13) and with values reported for Cr-doped BST [16, 17].
The extracted coupling capacitance is $C_g = (24.4 \pm 0.2)\,\mathrm{fF}$, which again agrees with our earlier independent estimate (Fig. 3.13). Using the total dielectric thickness of 14 nm and $\epsilon_r = 10$, the geometric capacitance density is $C/A \simeq 5.7\,\mathrm{fF/\mu m^2}$. Thus the fitted C_g corresponds to an effective gated area of $A \approx 4.3\,\mathrm{\mu m^2}$, which, given the gate width of 3 µm, implies an effective edge-channel width of $w \approx 1.4\,\mathrm{\mu m}$. Such widths are consistent with microwave studies in HgTe QSH edges [103] and InAs/GaSb quantum wells [102], which attribute this large width to disorder broadening by charge puddles. Recent observations of several micron-wide edge states via microwave impedance microscopy in V-doped BST align well with this interpretation [107].
From $f_p = g_p/(2\pi c_p)$, the fit yields $f_p = (7.0 \pm 0.1)\,\mathrm{GHz}$. This is reasonably close to cutoff frequencies ($\lesssim 3\,\mathrm{GHz}$) reported by Bagchi et al. [72] in the compensated topological insulator $\mathrm{BiSbTeSe_2}$, with the difference attributed to variations in puddle density or screening. For the frequency-independent loss-term g_e, the fit yields $g_e = (0.38 \pm 0.01)\,\mathrm{S/m}$. To compare this with dc transport, we estimate the bulk conductance from the measured longitudinal resistance ($R_{xx} \simeq 16\,\Omega$ for $L = 80\,\mathrm{\mu m}$):

$$g_{xx} = \frac{1}{L}\frac{R_{xx}}{R_{xx}^2 + R_{yx}^2} \simeq \frac{R_{xx}}{R_{yx}^2 L} \simeq 3 \times 10^{-4}\,\mathrm{S/m}. \tag{3.15}$$

This is several orders of magnitude smaller than g_e. This discrepancy is expected because the absolute gain calibration introduces systematic amplitude uncertainty ($\approx 2.5\,\mathrm{dB}$), and g_e collects all frequency-independent losses. The discrepancy in g_e corresponds to an error of 2.5 dB in amplitude, which is within the accuracy of our correction. Therefore, we are not able to evaluate the absolute value of g_e. Despite this, we show later that relative changes in g_e track changes in R_{xx}, meaning that g_e still captures meaningful trends in edge–bulk coupling even if its absolute magnitude is uncertain.

3.5 Dissipation of edge plasmons

In the previous section, we showed that the plasmon dispersion of a QAH edge state is well captured by the circuit model in Fig. 3.14. A key outcome of this model is that the dissipation grows quadratically with frequency, $\mathrm{Im}\,k \propto f^2$, up to a characteristic cut-off frequency between 4 GHz and 8 GHz, depending on the sample. This behavior has significant implications for the feasibility of

utilizing QAH edge states in low-loss rf quantum devices, as even moderate frequency increases result in rapidly increasing attenuation.
In this section, we examine how plasmon propagation in QAH edge states responds to increasing temperature, magnetic field, and excitation voltage. These control parameters provide complementary routes to activate bulk conduction, allowing us to identify the mechanisms responsible for microwave dissipation and to find the operational boundaries of low-loss QAH plasmonics. We again use the circuit model to separate and quantify the various contributions to loss, distinguishing between frequency-independent dissipation (g_e) and puddle-induced high-frequency attenuation (f_p, C_p). For completeness, we also comment on changes in the plasmon velocity, although these turn out to be relatively small compared to the changes in dissipation.

3.5.1 Breakdown at elevated temperatures

Before analyzing the breakdown of plasmon transport at elevated temperatures, we briefly summarize the dc characterization of the device. Figure 3.16a shows the Hall resistance R_{yx} as a function of out-of-plane magnetic field for temperatures between 10 mK and 30 K. At base temperature, R_{yx} is quantized to $\pm R_K$, and the coercive field H_c is approximately 0.9 T. With increasing temperature, both the amplitude of the Hall plateau and the coercive field decrease, and above the Curie temperature ($T \simeq 25\,\mathrm{K}$) the hysteresis disappears entirely, signaling loss of magnetization.
Figure 3.16b shows the amplitude of the microwave transmission $|S_{21}|$ as a function of the out-of-plane magnetic field for the same temperature range. The hysteretic behavior follows the dc data: at low temperatures, a strong signal is observed for positive magnetization (short edge path) and a strongly suppressed signal for negative magnetization (long edge path). This confirms again that, after calibration, the microwave transmission correctly isolates the edge-state contribution. The temperature dependence of the amplitude at fixed fields $\mu_0 H = \pm 2\,\mathrm{T}$ is summarized in Fig. 3.16c. Upon warming, the amplitude remains nearly constant up to $T \approx 200\,\mathrm{mK}$. Beyond this point, two changes occur: At $\mu_0 H = +2\,\mathrm{T}$, the edge-state signal decreases rapidly, marking the onset of thermally activated bulk carriers that introduce dissipation into the edge channel. At $\mu_0 H = -2\,\mathrm{T}$, where the long edge path dominates, a finite and increasing amplitude appears. This is consistent with a growing bulk contribution bridging the long-path geometry. Both effects directly mirror the temperature evolution of the dc transport, in which bulk conduction becomes finite above

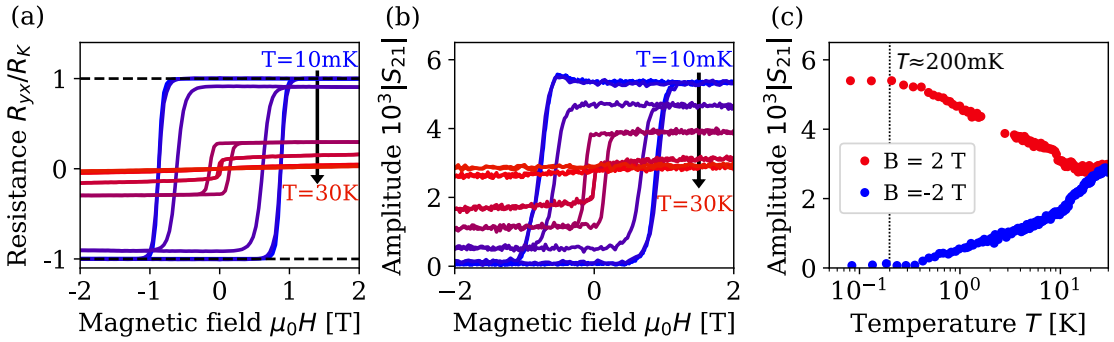

Figure 3.16: Temperature dependence of plasmon amplitude. (a) dc Hall resistance R_{yx}/R_K as a function of the out-of-plane magnetic field $\mu_0 H$ for temperatures between 10 mK and 30 K, showing the progressive suppression of quantization and the decrease of the coercive field. (b) Microwave transmission amplitude $|S_{21}|$ vs magnetic field for $L = 20\,\mu\text{m}$ at $f = 1\,\text{GHz}$ and the same set of temperatures as in (a). (c) Temperature dependence of the plasmon amplitude at $\mu_0 H = \pm 2\,\text{T}$ ($L = 20\,\mu\text{m}$, $U_{\text{rf}} \approx 125\,\mu\text{V}$, $f \approx 750\,\text{MHz}$). Measurements on device MBE_VBST_20221204a.

200 mK as observed in other studies [20, 56]. The correspondence between dc and microwave data confirms that the calibrated transmission coefficient indeed tracks edge transport and its breakdown. In this context, breakdown of plasmon transport refers to the loss of dissipationless, chiral edge transport in the QAH regime.

In Fig. 3.17, we show the temperature dependence of the fit parameters C_g, c_p, and g_e up to $T \simeq 1.6\,\text{K}$. The characteristic frequency f_p was found to be essentially temperature independent and is therefore not shown.

The coupling capacitance C_g increases moderately with temperature, rising from $\sim 29\,\text{fF}$ to $\sim 35\,\text{fF}$. A slightly enhanced coupling at higher temperatures is reasonable: as bulk carriers become thermally activated, the sample becomes more metallic, reducing the impedance mismatch between the edge channel and the rf gate. Alternatively, one can also picture the onset of C_g as the widening of the edge state due to screening [103], resulting in a bigger geometric capacitance C_{geo}. A similar trend is observed for the puddle capacitance c_p, which decreases with temperature. Because the plasmon velocity scales approximately as $v \propto 1/(Z_e c_p)$, a reduction in c_p corresponds to a higher velocity, again consistent with a more metallic response of the film at elevated temperatures.

The frequency–independent dissipation term is governed by the fit parameter g_e, which, as discussed in Sec. 3.4, represents the dc bulk conductivity seen by the edge channel. This allows a direct comparison to the longitudinal conductance g_{xx} extracted from the dc measurements via Eq. 3.15. To avoid the absolute calibration uncertainty in the rf amplitude, we focus on the relative

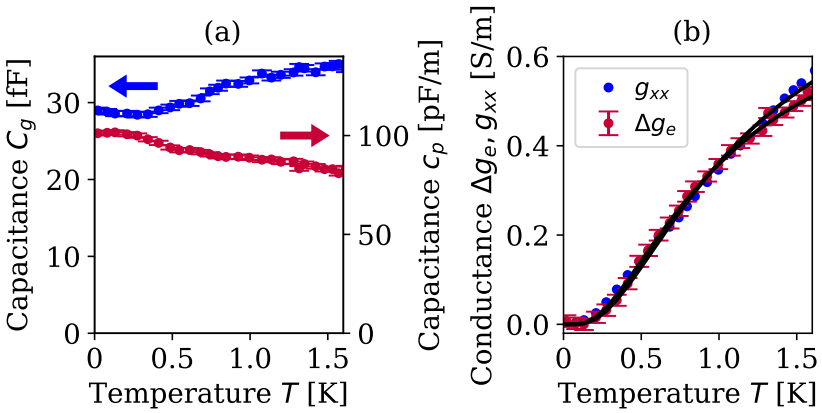

Figure 3.17: Temperature-dependence of Fit parameter. (a) Capacitance C_g and c_p vs. the temperature T. (b) Temperature dependence of the fitted conductivity g_e (red) and of the longitudinal conductance g_{xx} (blue), together with fits based on the variable range hopping model, yielding $T_0 = (17.4 \pm 0.6)\,\mathrm{K}$ and $T_0 = (15.4 \pm 0.2)\,\mathrm{K}$ respectively. ($L = 20\,\mu\mathrm{m}$, $U_{\mathrm{rf}} \simeq 125\,\mu\mathrm{V}$, Device MBE_VBST_20221204a).

change $\Delta g_e(T) = g_e(T) - g_e(T = 0)$. Fig. 3.17b shows that both g_e and g_{xx} exhibit the same temperature dependence: very small values below $0.05\,\mathrm{S/m}$ at base temperature, followed by a rapid increase once $T \gtrsim 200\,\mathrm{mK}$. Both quantities are well described by the Efros–Shklovskii variable–range hopping law $g(T) = g_0 \exp(-(T_0/T)^{1/2})/T$ (see Eq. 2.11). It yields $T_0 \simeq 16\,\mathrm{K}$ for both rf and dc data. This agreement strongly suggests that bulk hopping conduction dominates the frequency–independent plasmon dissipation.

The extracted activation temperature T_0 is similar to values reported in Cr-doped BST [17], but an order of magnitude smaller than those typically found in graphene [38]. This indicates significantly stronger disorder in magnetic topological insulators. As discussed in Sec. 2.3, we can estimate the localization length ξ from the temperature T_0. Using Eq. 2.12, and taking $\epsilon_r \simeq 12$ for InP[2], we estimate a localization length of $\xi = Ce^2/(\epsilon k_B T_0) \approx 5\,\mu\mathrm{m}$. Such a large ξ implies that bulk (or surface) states are only weakly localized—a conclusion consistent with the observed breakdown of the zero–resistance state already around $T \simeq 200\,\mathrm{mK}$. At low temperatures, plasmon losses are dominated by the frequency–dependent term $\mathrm{Im}(k) \propto f^2$ arising from the capacitive coupling to charge puddles. At higher temperatures, however, the dominant loss mechanism becomes the frequency–independent bulk dissipation associated with g_e and g_{xx}. The crossover between these two regimes marks the transition from edge-dominated to bulk-dominated (or surface-dominated) transport. In the

[2]In this context, C is a numerical constant and not a capacitance. Our films have a thickness of 8 nm, hence we use $C = 6.2$ for 2D hopping [83, 87].

next section, we investigate how strong out-of-plane magnetic fields influence both the plasmon velocity and the dissipation.

3.5.2 Magnetic field dependence of plasmon transport

So far, we have used the external out-of-plane magnetic field primarily to control the ferromagnetic order in the magnetic topological insulator. However, the magnetic field also affects the plasmon transport itself. Experimentally, the amplitude of S_{21} decreases with increasing magnetic field $\mu_0 H$, as shown in Fig. 3.18a. This reduction is observed across the full frequency range between 300 MHz and 4 GHz.

We again fit the circuit model at each magnetic field. The plasmon frequency f_p remains nearly field independent, changing only within the error margins as shown in Fig. 3.18b. This indicates that the intrinsic charging dynamics of the puddles do not change significantly. In contrast, the coupling capacitance C_g shows a pronounced increase, rising from approximately 8 fF at 0 T to 17 fF at 8 T (see Fig. 3.18b). The puddle capacitance c_p decreases slightly with the magnetic field as shown in Fig. 3.18c. Both effects suggest, as in the elevated-temperature case, that the bulk becomes more metallic at higher fields, reducing impedance mismatch and increasing the edge-plasmon velocity from about 2.3×10^5 m/s to 2.8×10^5 m/s.

This interpretation is supported by the behavior of the fitted bulk conductance g_e, shown in Fig. 3.19a. To account for amplitude-calibration uncertainties, we

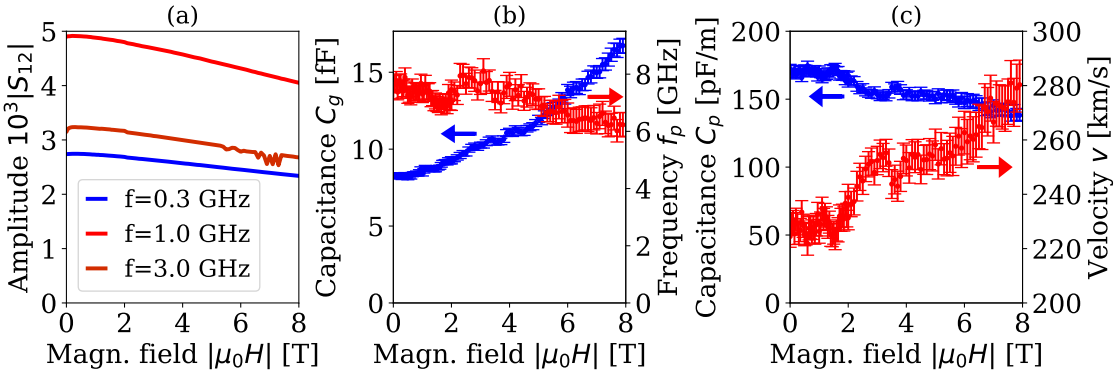

Figure 3.18: Plasmon transport in high magnetic fields. (a) Amplitude of transmission S_{21} as a function of the magnetic field for $f = 0.3, 1, 3$ GHz. (b) Fit parameter as a function of magnetic field. Coupling capacitance C_g (blue) and frequency f_p (red) are shown on the left and right axes, respectively. (c) Fitted capacitance C_p and velocity v, given by $1/(c_p R_K)$, vs. magnetic field $\mu_0 H$. All error bars correspond to the MSE of the fit. All measurements are taken at $T \simeq 20$ mK, using $U_{\mathrm{rf}} = 225\,\mu$V on Sample MBE_VBST_20230206a.

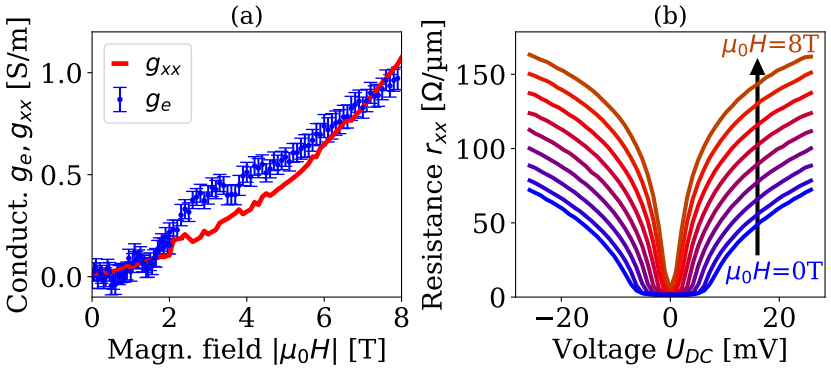

Figure 3.19: Bulk conduction in high magnetic fields. (a) The fit parameter conductivity g_e and the measured conductance g_{xx} as a function of the magnetic field $\mu_0 H$. (b) Electric field-driven breakdown of zero-resistance state in high magnetic fields. The onset of the longitudinal resistance r_{xx} shifts to lower bias voltages U_{DC} with increasing field. Measurements are taken at $T \simeq 20\,\mathrm{mK}$, using a 1 nA, 7 Hz modulation of the dc bias in addition to the dc offset U_{DC} or the $U_{\mathrm{rf}} = 225\,\mu\mathrm{V}$ on Sample MBE_VBST_20230206a.

again analyze the relative change $\Delta g_e = g_e(H) - g_e(0)$ and compare it to the longitudinal conductance g_{xx} from dc transport. Both quantities increase by roughly 1 S/m between 0 T and 9 T, indicating that bulk hopping conduction becomes more prominent at high magnetic fields. This produces an essentially frequency-independent plasmon dissipation dominated by the leakage into the bulk.

To further investigate this effect, we performed bias-driven breakdown measurements of the longitudinal resistance r_{xx} using a 1 nA, 7 Hz ac modulation. The resulting curves of r_{xx} as a function of U_{DC} for magnetic fields between 0 T and 8 T are shown in Fig. 3.19b. At zero field, we observe the characteristic plateau of vanishing resistance and a breakdown at $U_{BD} \simeq 5\,\mathrm{mV}$, consistent with earlier reports [20, 21, 58]. The notable feature in Fig. 3.19b is that U_{BD} decreases systematically with increasing magnetic field, in agreement with the measurements by Lippertz et al. [52].

Theory shows that increasing magnetic fields do more than simply align the magnetization [108, 109]. In particular, an orbital magnetic field induces Landau quantization in the bulk of the QAH insulator. The chiral edge mode can persist deep into this Landau-quantized regime, where it may coexist and hybridize with conventional quantum Hall edge states originating from the Landau levels. The QAH effect is ultimately suppressed only once the orbital field removes the underlying band inversion [108]. There are experimental studies which reported an increased fragility of the QAH effect at high magnetic fields, manifested by the growth of the longitudinal resistance R_{xx} [56] or a reduction of the breakdown current [52], as observed in our experiment.

Beyond these orbital effects, the magnetic field can also modify the electronic landscape of the bulk through its influence on charge inhomogeneities. Breunig *et al.* [110] showed that increasing the magnetic field leads to an enlargement of charge puddles in bulk $\mathrm{TlBi_xSb_{1-x}Te_2}$. An increased puddle size enhances the localization length and thereby promotes hopping transport, providing a natural explanation for the observed increase of g_e, the reduction of the breakdown threshold U_{BD}, and the gradual evolution toward more metallic behavior in our data. At the same time, other experiments have reported the opposite trend, namely an improvement of quantization at high magnetic fields, particularly in samples that are not initially charge-neutral [79].
Taken together, these seemingly contrasting observation points to a common and more fundamental mechanism: a magnetic-field-induced shift of the chemical potential. In perfectly compensated samples, such a shift can move the chemical potential out of the exchange gap and increase bulk conduction, whereas in lightly uncompensated samples, it may instead shift the chemical potential into the gap, thereby improving quantization. This scenario naturally harmonizes the seemingly contrasting experimental trends and provides the most consistent explanation for the magnetic-field dependence observed in our measurements.
In our material platform, we consistently observe the best quantization and lowest dissipation at zero magnetic field. This is encouraging for applications that operate in the zero-field limit, such as topological superconductivity or nonreciprocal microwave devices. In contrast, the reduction of the breakdown bias to values of only a few mV limits the applicability of QAH insulators as dissipationless devices. Therefore, we next investigate how the plasmon transport depends on the microwave excitation voltage U_{rf}.

3.5.3 Dissipation in strong electric fields

The plasmon transport is also strongly influenced by the amplitude of the excitation voltage U_{rf}. Figures 3.20a and 3.20b show the amplitude and phase of $S_{21}(f)$ for a propagation length of $L = 20\,\mu\mathrm{m}$ at different excitation voltages, together with fits using our circuit model.
At low frequencies, the transmitted amplitude increases with increasing U_{rf}, indicating more efficient capacitive coupling between the rf gate and the edge channel. At the same time, the amplitude above 1 GHz is strongly suppressed and the overall frequency dependence becomes significantly flatter. This flattening is a hallmark of a more metallic, less dispersive response. The same trend

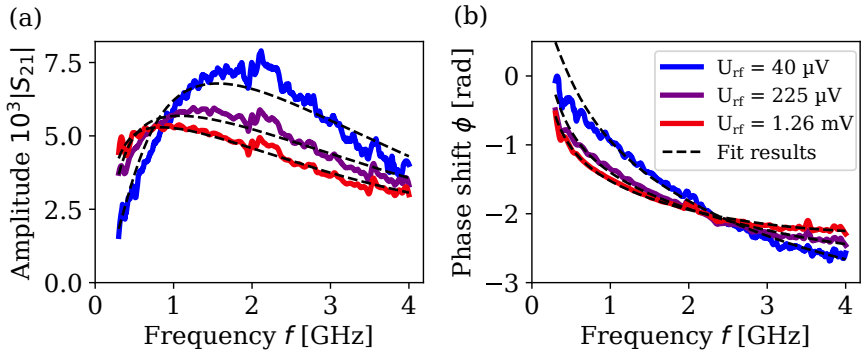

Figure 3.20: Amplitude-dependence of amplitude and phase. (a) Measurements (solid colored lines) and fits (dashed lines) of the amplitude $|S_{21}|$ in device C for $L = 20\,\mu\text{m}$, $T = 20\,\text{mK}$, and $\mu_0 H = 2\,\text{T}$ for varying excitation voltages U_{rf}. (b) same as (a) for the Phase $\phi = \arg(S_{21})$. All data measured on MBE_VBST_20221204a.

is observed in the phase, where the characteristic dispersion becomes less pronounced, and the phase slope decreases, consistent with faster propagation and enhanced coupling at higher excitation amplitudes.

Remarkably, the circuit model continues to fit the data over the full voltage range, despite the substantial evolution of the spectra. In the following, we discuss how the extracted circuit parameters vary with excitation voltage and what this reveals about dissipation mechanisms in the QAH regime.

As anticipated from the raw spectra, the excitation voltage has a strong influence on the extracted fit parameters—most notably on the coupling capacitance C_g. Figure 3.21a shows that C_g increases by nearly an order of magnitude, rising from approximately 4 fF at 10 µV to about 35 fF at 2 mV. Such a pronounced increase indicates that higher excitation voltages progressively activate bulk charge carriers, making the bulk more metallic and reducing the impedance mismatch between the edge channel and the gates.

This interpretation is supported by the fitted DC-like conductance g_e, shown in Fig. 3.21b[3]. The strong rise of g_e with excitation voltage mirrors the increase of the longitudinal conductance g_{xx} in dc transport, again pointing toward activated bulk transport [20, 22, 56, 70, 79]. In contrast, the internal edge capacitance c_p decreases substantially from roughly 220 pF/m to 100 pF/m as U_{rf} increases. Together, the strong increase in C_g and reduction in c_p indicate a crossover from a well-isolated chiral edge channel to a regime where the bulk contributes significantly to screening and dissipation. Because the plasmon velocity scales as

[3]Negative values of g_e are an artifact of our model since g_e accounts for all frequency-independent losses, including discrepancies in calibration. The real bulk conductance g_{xx} cannot be negative.

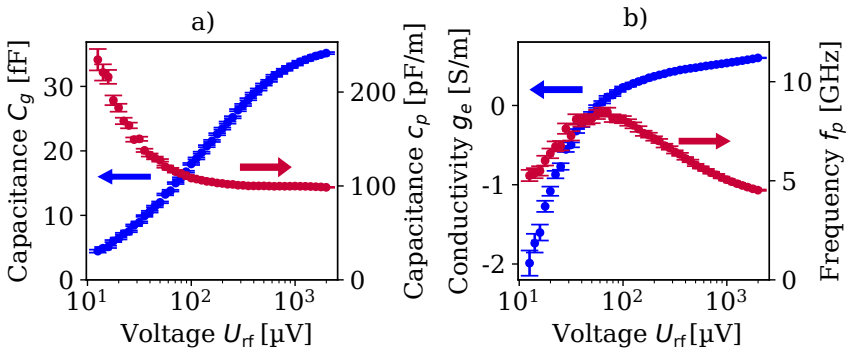

Figure 3.21: Amplitude-dependence of Fit parameter. Results of the fit model for the frequency-dependent transmission at different voltages U_{rf}. (a) The coupling capacitance C_g and puddle capacitance c_p vs. the excitation voltage (b) The conductivity g_e and the frequency f_p vs. excitation voltage U_{rf}. All curves show a transition at an excitation voltage of $U_{\mathrm{rf}} \simeq 60\,\mu\mathrm{V}$. All data measured on MBE_VBST_20221204a.

$v \propto 1/c_p$, the decrease of c_p results in a notable increase of the velocity from about 1.6×10^5 m/s at low bias to nearly 3.8×10^5 m/s at the highest applied voltages. The low-voltage velocity agrees well with the prediction of quantum Hall edge state in a dielectric environment [111]:

$$v = \frac{1}{2\sqrt{2}\, R_K\, \epsilon}, \tag{3.16}$$

which yields $v \simeq 1.6\text{–}2.2 \times 10^5\,\mathrm{m/s}$ for an effective dielectric constant of $\epsilon \simeq 7\epsilon_0$–$10\epsilon_0$. We note, however, that additional screening by bulk puddles and possible velocity enhancement from inter-edge Coulomb interactions—neglected here—might also contribute.

A particularly striking feature is the behavior of the characteristic puddle frequency f_p. As shown in Fig. 3.21b, f_p exhibits a pronounced maximum of approximately 8.5 GHz at an excitation voltage of $U_{\mathrm{rf}} \simeq 60\,\mu\mathrm{V}$. This voltage marks the crossover between a low-voltage regime, where dissipation is dominated by capacitive coupling to localized puddles, and a high-voltage regime, where activated bulk conduction dominates.

The corresponding energy scale $eU \approx 60\,\mu\mathrm{eV}$ coincides with activation energies extracted from dc studies of QAH breakdown [20, 22, 56, 70, 79]. This agreement strongly supports the picture that increasing the excitation voltage activates the same dissipative bulk channels that are responsible for QAH breakdown in dc transport.

An alternative viewpoint is that increasing voltage enhances the bulk–edge coupling, effectively broadening the edge channel. A wider conducting channel

couples more strongly to the rf gates, consistent with the observed increase in C_g. In addition, wider edge channels are known to support higher plasmon velocities [18, 46], in agreement with our data.

3.6 Summary and outlook

The work presented in this chapter explores the dynamics of edge plasmons in the QAH state of V-doped BST thin films, with a focus on their microwave transport, dissipation mechanisms, and robustness under varying environmental conditions. Chiral edge states are central to the QAH effect, providing dissipationless transport in the ideal limit. In our broadband study of edge state transmission, we have systematically characterized the edge plasmon transport under changes in temperature, excitation amplitude, and magnetic field, allowing us to map out the regimes in which they remain well-defined and identify the mechanisms that limit their coherence.

In the low-temperature and low-excitation regime where the QAH state is most robust, we observe a plasmon velocity $v \simeq 1.6\text{–}2.2 \times 10^5\,\mathrm{m/s}$, in close quantitative agreement with the universal, interaction-limited velocity predicted by recent theory for an ideal, disorder-free chiral edge channel [111]. This result indicates that, in the optimal regime, the chiral channel behaves largely as a clean one-dimensional edge mode minimally perturbed by bulk conduction. As temperature or excitation voltage increases, the QAH state becomes progressively less quantized, and correspondingly, the plasmon velocity increases. The observed velocities in this regime are comparable to those previously reported in Cr-doped BST thin films [16, 17], highlighting similarities in plasmonic behavior across different material platforms.

Furthermore, we identified two distinct dissipation mechanisms. A frequency-dependent loss due to the Coulomb interaction with charge puddles. These puddles absorb energy at finite frequency due to their finite charging times, and the resulting admittance introduces a frequency-dependent imaginary component. This loss mechanism is dominant in the well-quantized regime for small excitation voltages, temperatures, and magnetic fields.

Once the system leaves the well-quantized regime — either by increased excitation voltage, elevated temperature, or large magnetic fields — the dissipation mechanism crosses over to a frequency-independent regime dominated by activated bulk conduction. This transition is marked experimentally by a sudden rise in the fitted conductance g_e, which is proportional to the longitudinal dc

conductance g_{xx}. The close tracking between these two quantities demonstrates that microwave losses in this regime directly reflect dissipative bulk transport rather than edge–puddle coupling.

Taken together, our findings establish that QAH edge plasmons can propagate over long distances (up to 100 µm) and remain well defined up to at least 4 GHz. This confirms magnetically doped topological insulators as a promising platform for high-frequency chiral plasmonics. Using the experimentally extracted device parameters, we estimate that microwave circulators and resonators [112] based on these films could achieve quality factors of approximately $Q \simeq 100$ at frequencies of a few tens of megahertz, even without targeted materials optimization. However, the quality factor is expected to decrease with increasing frequency ($Q \propto f^{-1}$), limiting device performance in the GHz regime (see Appendix C for details). Such chiral devices may play an important role in low-power nonreciprocal microwave circuits [15, 16] and may form a building block for more exotic applications such as the generation of flying Majorana quasiparticles [60].

However, a key limitation in the practical use of QAH insulators is the breakdown of the zero-resistance state under relatively small dc biases or under moderate rf excitation amplitudes, as also observed in this work. To gain deeper insight into the microscopic mechanism responsible for this breakdown, the next chapter investigates the response of the QAH state to microwave fields in the range of 1–25 GHz. We characterize the breakdown by measuring the longitudinal resistance in rf Hall-bar devices and rf Corbino structures patterned from V-doped $(\mathrm{Bi},\mathrm{Sb})_2\mathrm{Te}_3$ films. In addition, we present equivalent measurements on a graphene Corbino device, allowing us to directly compare the breakdown mechanisms in the QAH and QH regimes.

Chapter 4

Breakdown of edge state transport under microwave drives

A key limitation for using QAH insulators in technologically relevant devices is the breakdown of the zero-resistance state at low temperatures or at modest bias voltages [20, 21, 58]. This phenomenon has been investigated mainly under dc bias, and several mechanisms have been proposed, including variable-range hopping (VRH) [70], bootstrap electron heating [22], and electric field–driven percolation through charge puddles [20]. Despite extensive experimental and theoretical work, the microscopic origin of the breakdown remains under debate. Fijalkowski et al. [58] showed that the breakdown current in a Corbino device can be shifted to larger voltages by sourcing currents of opposite polarity through the inner and outer contacts. A Corbino device consists of a ring-shaped mesa with concentric inner and outer contacts, such that current flows radially through the two-dimensional bulk rather than along the sample edges. In this geometry, edge transport is eliminated, and the measured conductance directly probes bulk properties. This result indicates that a transverse electric field across the bulk of the QAH insulator plays a central role.

This interpretation relates to an ongoing debate about the microscopic current distribution in QAH devices. While chiral edge states are expected from the non-trivial topology and have been shown to contribute to transport up to elevated temperatures [21, 58], this does not necessarily imply that they carry the dominant fraction of the current under all experimental conditions. Complementary studies have argued that a substantial part of the current can flow through the bulk, even in regimes where the Hall resistance remains quantized [23, 113]. Thus, the existence of measurable edge transport is not incompatible with bulk-dominated current flow. Rather, quantization constrains the global Hall response, whereas the local current distribution can depend sensitively on disorder, charge

puddles, temperature, and bias. In this picture, breakdown is governed primarily by bulk processes such as electron heating or field-driven hopping between disorder-induced charge puddles. Recent magnetic-imaging experiments support this interpretation and report that dissipation is dominated by electron heating due to strongly suppressed thermalization at low temperatures [114].

In contrast to the extensive work under dc bias, the breakdown of quantization under rf excitation remains largely unexplored. As discussed in Chapter 3, edge transport at microwave frequencies is not dissipationless: charge puddles, which are effectively isolated in the dc limit, couple capacitively to the edge channel at high frequencies, resulting in dissipation that increases approximately as f^2. This raises the central question addressed in this chapter: whether the breakdown mechanism under rf drive differs qualitatively from the dc case.

Two scenarios appear plausible. First, microwave photons may promote hopping transitions between localized states, enabling photon-assisted VRH [85, 86]. In this case, the breakdown threshold would explicitly depend on frequency. Second, the rf field may couple capacitively to charge puddles and induce Joule heating, thereby raising the electronic temperature and indirectly increasing the dc bulk conductance, even if the microscopic hopping dynamics themselves remain frequency independent.

In this chapter, we investigate the breakdown of the QAH state in the presence of microwave excitation and assess the relative roles of hopping and heating. To compare different frequencies on equal footing, we use the dc longitudinal conductance σ_{xx} as a frequency-independent probe while applying microwave fields between 1 and 25 GHz.

After establishing a consistent picture for QAH devices, we extend our study to the breakdown of the QH effect in high-mobility graphene Corbino devices. Graphene offers a unique opportunity to systematically tune the localization strength of bulk states by varying the filling factor, which directly controls the hopping energy scale $k_{\mathrm{B}}T_0$. Together with the presence of both large cyclotron gaps and smaller spin- and valley-splitting gaps [115], this enables the study of breakdown across a wide range of energy scales within a single device. Using the same methodology as for the QAH devices, we identify a crossover from a non-Ohmic, electric field-driven regime to an Ohmic regime dominated by Joule heating, providing a direct benchmark for interpreting the breakdown behavior observed in QAH systems.

The chapter is structured as follows. Section 4.1 describes the experimental setup and the rf power calibration. Section 4.2 presents the core experimental results

and the frequency dependence of the breakdown in QAH samples. It furthermore analyzes the origin of breakdown and shows that electron heating provides a consistent explanation of the data, motivating a simple Joule-heating model. Finally, Section 4.3 discusses the rf breakdown of the QH effect in high-mobility graphene and compares it to the behavior observed in QAH devices. The results in this chapter are partially published in Ref. [116] and Ref. [117]

4.1 Experimental setup and power calibration

For the study of the QAH breakdown, we use the same devices as in Sec. 3.1. Therefore, we omit the device fabrication details here and focus on the experimental setup relevant for the breakdown measurements. We investigate the breakdown behavior in three devices: two rf Hall bars and one rf Corbino device. In a Hall bar geometry, transport can occur both via dissipationless edge states and through the bulk, making it difficult to disentangle the origin of the breakdown. In contrast to Hall bar devices, the Corbino geometry removes chiral edge channels from the direct transport path between contacts. As a result, any current flowing between the inner and outer contacts must traverse the bulk, providing direct access to bulk conduction. The majority of measurements are therefore performed on the rf Hall bars, while the rf Corbino device serves as a control to verify whether the onset of dissipation arises from bulk conduction rather than edge transport. All devices feature Ohmic contacts for dc characterization of the longitudinal and Hall resistances, as well as narrow capacitive contacts. While these capacitive contacts are used for plasmon propagation experiments in Chapter 3, in the present chapter, they serve solely to irradiate the sample with microwave signals to trigger the breakdown, without measuring the transmitted rf response.

A microscope image of a representative rf Hall bar is shown in Fig. 4.1a. The rf Corbino device, shown in Fig. 4.1b, follows the conventional ring-shaped geometry and provides a direct probe of bulk transport by eliminating edge contributions. All experiments are performed in a dilution refrigerator with a base temperature below 20 mK. Each device exhibits a quantized Hall resistance ($R_{yx} = h/e^2$) with an accuracy of approximately 2 % and longitudinal sheet resistances between 90 Ω and 120 Ω in the low-voltage regime. This shows that bulk transport is suppressed and electronic transport is confined to the edge states in this regime. The measurement scheme is sketched in Fig. 4.1c. To isolate the frequency dependence of the breakdown mechanism, we measure the longitudinal

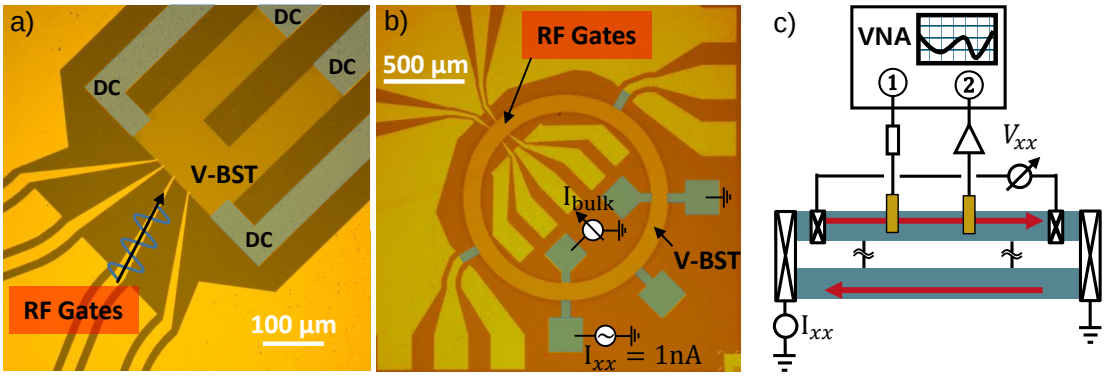

Figure 4.1: Experimental setup and dc characterization. a) Microscope image of Sample MBE_VBST_Feb6A in an rf Hall bar geometry. The mesa is false-colored in dark yellow, the Ohmic contacts in blue, and the rf finger gates are shown in the bottom left. All remaining contacts are Ohmic contacts. b) Microscope image of Sample MBE_VBST_Jul5A in an rf Corbino geometry. The Ohmic contacts are false-colored in blue, and the rf finger gates are placed at the top left. The Corbino device has a width of 100 µm. c) Schematic of the microwave measurement setup. A vector network analyzer (VNA) is used as a signal generator and connected via broadband coaxial cables and a coplanar waveguide. Longitudinal resistance R_{xx} is measured using a four-terminal lock-in configuration.

resistance R_{xx} in dc, thereby realizing a frequency-independent probe. A small probe current of 1 nA, well below the breakdown current, is sourced through the device. The longitudinal voltage drop is measured between two additional Ohmic contacts located between the source and the drain. From the measured resistances, we compute the longitudinal bulk conductance

$$\sigma = \sigma_{xx} = \frac{R_{xx}}{R_{xx}^2 + R_{yx}^2}. \tag{4.1}$$

Since the device geometries differ from an ideal Hall bar, geometrical corrections are required. For example, the longitudinal resistance measured in the Corbino device in Fig. 4.1b corresponds to a current path of 300 µm length and 100 µm width, such that the measured resistance is divided by a factor of three. The Hall resistance remains exact in the quantized regime but acquires a small systematic deviation for large bulk conductance. In our measurements, the bulk contribution remains sufficiently small such that this deviation stays below 5% and does not affect the conclusions. Importantly, since this factor is constant, it does not affect the voltage or frequency scaling discussed below. The Corbino device further allows us to directly measure the bulk current I_{bulk}, providing an independent confirmation that the observed increase in resistance originates from bulk transport.

Microwave signals are applied using a VNA with a maximum frequency of 26 GHz and guided to the capacitive contacts via broadband coaxial cables (dc to 40 GHz). The rf voltage U_{rf} at the sample is obtained from calibrated power measurements. Two independent calibration procedures are employed. First, we measure the transmission through a reference sample containing a 50 Ω-matched coplanar waveguide using identical cryostat lines, allowing us to extract and correct for the scattering matrix of the setup. Second, the calibration is cross-checked using a tunnel diode detector (*Herotek DT1-40*) placed at the sample stage. The tunnel diode measures the power P delivered to the sample stage. All voltages U_{rf} and powers P quoted in the following refer to these corrected values.

4.2 Quantum anomalous Hall breakdown under rf drives

Figure 4.2a shows the bulk conductance σ as a function of the rf voltage U_{rf} for frequencies between 1 GHz (blue symbols) and 25 GHz (red symbols), plotted on logarithmic axes. All curves exhibit an identical shape but are shifted towards lower voltages with increasing frequency. To quantify this shift, we define a breakdown voltage U_{bd} at which the conductance reaches $\sigma = 1\,\mu\mathrm{S}$. As shown in Fig. 4.2b, the breakdown voltage decreases approximately as $U_{\mathrm{bd}} \propto 1/\sqrt{f}$.

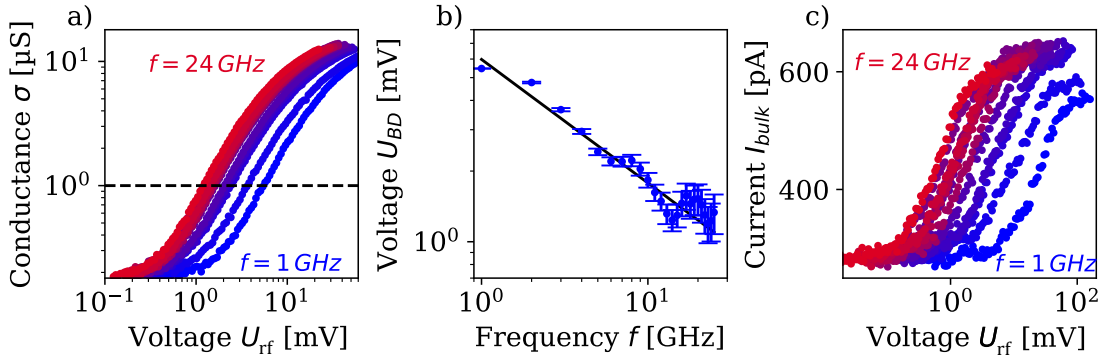

Figure 4.2: Breakdown driven by rf excitation. a) Conductance σ as a function of the rf voltage U_{rf} for frequencies f between 1 and 25 GHz. b) The breakdown rf voltage U_{bd} (defined at $\sigma = \sigma_{\mathrm{bd}} = 1\,\mu\mathrm{S}$) as a function of the microwave frequency f. The black line corresponds to a fit of $U_{\mathrm{bd}} \propto 1/\sqrt{\omega}$. The measurement was performed at $B = 1\,\mathrm{T}$, $T \simeq 20\,\mathrm{mK}$ on Sample MBE_VBST_Feb6A. c) Direct Measurement of the bulk current I_{bulk} in the Corbino geometry, as a function of the microwave voltage U_{rf} for frequencies from 1 GHz to 24 GHz. 1 nA is sourced on the outer edge (see Fig. 4.1b). The remaining current does not traverse the bulk and is drained on the outer edge. Measurements taken on sample MBE_VBST_Jul5A at $B = 1\,\mathrm{T}$, $T \simeq 20\,\mathrm{mK}$.

Notably, while the threshold shifts with frequency, the overall shape of $\sigma(U_{\mathrm{rf}})$ remains frequency independent and resembles the temperature dependence (see Fig. 3.17) and hence suggests a VRH origin of the breakdown. At the same time, it rules out photon-assisted hopping, which is predicted to scale with the number of photons, which scales as $\propto U_{\mathrm{rf}}^2$ [86, 118].
To verify that the observed increase in longitudinal resistance is indeed caused by bulk transport, we perform direct bulk-current measurements in the Corbino device, shown in Fig. 4.2c. A current of 1 nA is sourced, and the fraction flowing through the bulk to the inner contact is recorded. Although Corbino measurements are typically voltage-biased, the presence of a finite residual bulk conductance in our samples favors a current-biased configuration. Analogous to the Hall bar data, the bulk current increases with rf voltage, and the curves shift systematically to lower voltages at higher frequencies. The frequency dependence mirrors that observed in $\sigma(U_{\mathrm{rf}})$, confirming that the breakdown is governed by the onset of bulk conduction rather than edge effects.

4.2.1 Joule heating model

We now examine whether the observed frequency dependence of the breakdown can be explained by electron heating alone. To this end, we develop a minimal model based on Joule heating combined with VRH transport in the bulk. Before introducing the model in detail, we note that this approach relies on two key assumptions. First, that the dominant effect of dc or rf excitation is to raise an effective electronic temperature, and second, that the resulting conductance can be described by the same VRH law that governs equilibrium transport. Alternative mechanisms are discussed in Sec. 4.2.4.
The Joule heating model is illustrated schematically in Fig. 4.3a. The rf or dc excitation leads to dissipation of power P_{diss} in the electronic system, raising the electronic temperature T_e. The electrons relax by emitting phonons with power P_{out} to a phonon bath at temperature T_p. In a steady state, the electronic temperature is determined by the balance between heating and cooling. For microwave excitation, P_{diss} is generally smaller than the injected power P_{in}, as a large fraction of the rf power is reflected due to a strong impedance mismatch between the coaxial line of the microwave setup ($Z_0 = 50\,\Omega$) and the sample ($Z = R_K$). To relate the bulk conductance to the electronic temperature, we first establish the temperature dependence of the conductance σ in the absence of rf excitation. In this equilibrium configuration, the electronic system is assumed to be thermally

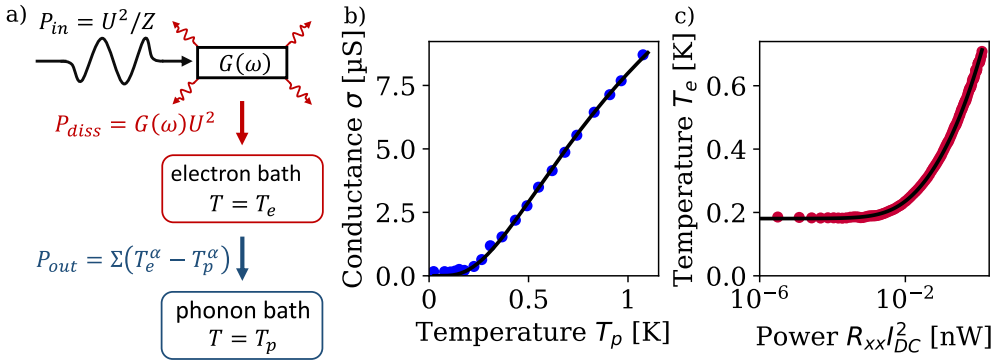

Figure 4.3: Joule heating and electronic thermometry. a) Joule heating model: The applied power P_{in} is partially absorbed and dissipated with power P_{diss}, raising the electronic temperature T_e. The electrons cool via phonon emission with power P_{out}. b) Bulk conductance σ as a function of the refrigerator temperature T_p (blue symbols). The curve is fitted with the VRH model in Eq. 4.2 and serves as an electronic thermometer, yielding $T_0 = (17.0 \pm 0.3)\,\mathrm{K}$ and $\sigma_0 = (490 \pm 20)\,\mu\mathrm{S\,K}$. c) Electronic temperature T_e extracted from σ as a function of dissipated dc power $P_{\mathrm{diss}} = R_{xx} I_{\mathrm{dc}}^2$. The black line shows a fit to Eq. 4.4 with $\alpha = 4$, yielding $\Sigma = (4.94 \pm 0.02)\,\mathrm{nW/K^4}$ and $T_p = (0.18 \pm 0.01)\,\mathrm{K}$. All data measured on MBE_VBST_20230206a.

coupled to the phonon bath, such that the electronic temperature equals the refrigerator temperature, $T_e = T_p$. Under these conditions, the bulk conductance is governed by phonon-assisted VRH and follows a well-established temperature dependence,

$$\sigma(T_e) = \frac{\sigma_0}{T_e} \exp\left(-\sqrt{T_0/T_e}\right), \tag{4.2}$$

The measured temperature dependence of σ, together with a fit to Eq. 4.2, is shown in Fig. 4.3b and yields an activation temperature $T_0 = (17.0 \pm 0.3)\,\mathrm{K}$. This calibration allows us to define an effective electronic temperature T_{eff} by mapping a measured conductance value σ onto the corresponding temperature via $\sigma(U_{\mathrm{rf}}) = \sigma(T = T_{\mathrm{eff}})$. Since $\sigma(T)$ is strictly monotonic over the relevant temperature range, this mapping is unique. This procedure has been employed in previous studies of QH breakdown [3, 24].

To describe the breakdown curves $\sigma(U_{\mathrm{rf}})$, we must next connect the electronic temperature T_e to the applied voltage U_{rf}. Cooling of the electronic system occurs predominantly via electron–phonon scattering[1], which is commonly described

[1] In addition to electron-phonon cooling, bulk thermal transport might also contribute to heat removal. Melcer et al. reported finite bulk thermal transport in the QH state of GaAs–AlGaAs heterostructures, even in the absence of electronic conduction [119]. However, this effect is only visible below 100 mK and therefore likely negligible for our experiments.

by a power-law dependence

$$P_{\mathrm{out}} = \Sigma \left(T_e^{\alpha} - T_p^{\alpha}\right), \tag{4.3}$$

where Σ is a coupling constant. The exponent α reflects the microscopic mechanism of electron–phonon coupling and depends on the dimensionality, disorder, and screening properties of the electronic system, with values $\alpha = 5$ for a clean 3D system [120] and $\alpha = 4$ in the diffusive regime [121]. Experiments on thin-films show that the exponent α typically lies between 3 and 5 [114, 122–125]. In steady state, the cooling power P_{out} balances the dissipated power P_{diss}, yielding

$$T_e = \left(T_p^{\alpha} + \frac{P_{\mathrm{diss}}}{\Sigma}\right)^{1/\alpha}. \tag{4.4}$$

Combining Eqs. 4.2 and 4.4 establishes a direct relation between the dissipated power P_{diss} and the bulk conductance σ, with three fitting parameters: Σ, α, and T_p.

We first test this model using dc bias data, shown in Fig. 4.3c. In this case, the dissipated power is given by $P_{\mathrm{diss}} = R_{xx} I_{\mathrm{dc}}^2$. The extracted electronic temperature T_e follows Eq. 4.4 remarkably well for $\alpha = 4$, yielding $\Sigma = (4.94 \pm 0.02)\,\mathrm{nW/K^4}$ and $T_p = (0.18 \pm 0.01)\,\mathrm{K}$. To the best of our knowledge, no previous reports exist for the electron–phonon coupling constant Σ in this specific material platform. However, the obtained value is consistent with measurements in related systems [114, 124, 125].

We note that both Σ and α vary between samples, likely reflecting differences in disorder, geometry, and thermal coupling to the substrate. The extracted fits remain robust against moderate changes in α and T_p. Importantly, the fitted value of T_p does not correspond to the actual lattice temperature, which lies below 100 mK. Instead, T_p reflects a residual conductance channel not captured by the VRH model and therefore sets an effective lower bound for conductance-based thermometry. As a consequence, the mapping $\sigma \to T_e$ becomes insensitive below this scale. This limitation does not affect our analysis, as we focus on the breakdown regime where σ exceeds the residual background by more than an order of magnitude.

4.2.2 Heating from rf drives

We now apply the same framework to the rf-induced breakdown curves $\sigma(U_{\mathrm{rf}})$ shown in Fig. 4.2a. The corresponding electronic temperatures $T_e(P_{\mathrm{in}})$ extracted

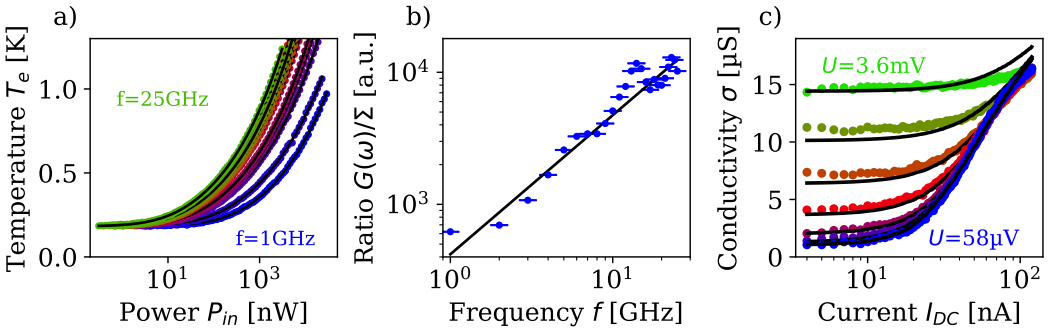

Figure 4.4: rf-induced heating. a) Calculated electronic temperature T_e as a function of the applied microwave power P_{in} for frequencies between 1 and 25 GHz (same data as in Fig. 4.2a). The black lines show the fitted curve of the Joule heating model, yielding $\alpha = 3.5 \pm 0.1$ and the ratio $G(\omega)/\Sigma$ shown in b). Measurements taken from Sample MBE_VBST_20230206a. b) Frequency dependence and fit of the parameter $G(\omega)/\Sigma = A\omega^s$, yielding $A = (420 \pm 50)\,\mathrm{K}^{\alpha}\mathrm{S/GHz}^s/\mathrm{W}$ and $s = 1.05 \pm 0.05$. c) Onset of conductivity σ as a function of the dc current I_{dc} while applying a microwave drive at 8 GHz and varying voltage (U_{rf} = 0.1, 0.2, 0.5, 0.9, 1.8, 3.6 mV). The measurements where taken on Sample MBE_VBST_20230705a at $T \approx 20\,\mathrm{mK}$ and $B = 2\,\mathrm{T}$. The black lines correspond to a fit with the Joule heating model, using the fit parameters obtained in dc ($\Sigma = (37 \pm 2)\,\mathrm{nW/K}^{\alpha}$, $\alpha = 4.5 \pm 0.1$) as fixed parameter and fitting the impedance Z as a free fit parameter, yielding $Z = (3280 \pm 60)\,\Omega$.

from the conductance are plotted in Fig. 4.4a. For rf excitation, the injected power $P_{\mathrm{in}} = U_{\mathrm{rf}}^2/Z_0$ differs from the dissipated power P_{diss} because of reflections caused by the large impedance mismatch between the microwave line and the sample. The dissipated power is instead given by

$$P_{\mathrm{diss}} = G(\omega)U_{\mathrm{rf}}^2. \tag{4.5}$$

The exponent α shows no systematic frequency dependence and varies between 3.2 and 3.5, slightly smaller than the dc value $\alpha = 4$. Since this variation is not reproducible across all samples, we attribute it to experimental uncertainty rather than a fundamental difference in the underlying mechanism. In contrast, the ratio $G(\omega)/\Sigma$ exhibits a clear frequency dependence, increasing approximately as $G(\omega)/\Sigma \propto \omega^s$ with $s = 1.05 \pm 0.05$, as shown in Fig. 4.4b. This frequency dependence can be understood intuitively by considering the inhomogeneous bulk of the QAH insulator as a network of finite-size charge puddles embedded in an otherwise insulating background (see schematic in Fig. 2.6). In the dc limit, these puddles are effectively isolated and contribute only weakly to transport via thermally assisted hopping. At radio and microwave frequencies, however, time-dependent electric fields can charge the puddles and induce oscillating currents within their finite extent. As a result, the charge puddles act as lossy elements

that absorb rf power locally and convert it into heat, thereby raising the electronic temperature and indirectly enhancing the dc bulk conductance measured in our experiments.

For frequencies below the inverse Thouless time, $f \lesssim 1/\tau_{\mathrm{Th}}$, the ac conductance of an individual puddle is expected to scale linearly with frequency, consistent with our observations. The Thouless time $\tau_{\mathrm{Th}} = L_p^2/D$ is set by the puddle size L_p and the diffusion constant D [72]. Physically, it corresponds to the characteristic diffusion time required for charge carriers to travel across the entire puddle. For excitation frequencies smaller than $1/\tau_{\mathrm{Th}}$, charge carriers can diffuse across the puddle within one oscillation period, allowing the system to establish a spatially equilibrated charge distribution. Similar frequency-dependent absorption has been reported in other strongly disordered systems [82, 126]. In some samples, a steeper frequency dependence is observed, which may reflect additional capacitive coupling between edge states and bulk puddles and can lead to a quadratic ω^2 scaling, as predicted from our charge puddle model in Chapter 3 and as reported in the literature [18, 38].

Notably, the plasmon measurements of Chapter 3 were performed in the lower frequency range of 0.3–4 GHz, whereas the breakdown measurements presented here probe frequencies between 1 and 25 GHz. Within a simple RC picture of edge-coupled puddles, the dissipative conductance is expected to evolve from a low-frequency $G \propto \omega^2$ dependence toward a weaker, approximately linear frequency dependence as the excitation frequency approaches or exceeds the characteristic puddle frequency $f_p \simeq 4 - 8\,\mathrm{GHz}$. Consequently, the distinct frequency dependences observed in the two chapters do not necessarily imply different microscopic origins but may reflect different dynamical regimes of the same puddle network. While our experiment does not allow a unique microscopic distinction between these absorption mechanisms, all samples consistently exhibit enhanced rf absorption at higher frequencies.

Having established that dc and rf breakdown can be described independently within the same framework, we next investigate their combined effect. Within the Joule heating model, one expects the dissipated powers to add. Figure 4.4c shows σ as a function of dc bias current I_{dc} for different rf voltages U_{rf}. At low I_{dc}, the conductance saturates at a value set by the rf excitation, consistent with Fig. 4.2a. At low rf voltages, increasing I_{dc} drives the system into the breakdown regime. At sufficiently large I_{dc}, all curves collapse, indicating that dc heating

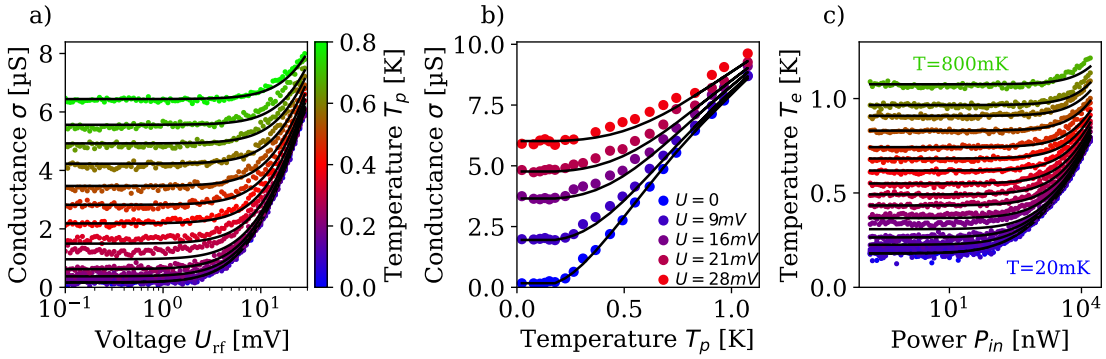

Figure 4.5: rf-induced heating at elevated temperatures. a) Conductance $\sigma(U_{\mathrm{rf}})$ for temperatures between 20 mK and 800 mK at $f = 8$ GHz. Black lines show fits of the Joule heating model. b) Conductance $\sigma(T_p)$ for different rf voltages, showing the VRH behavior in the absence of rf excitation. c) Electronic temperature T_e extracted from σ as a function of applied microwave power for different T_p. Black lines correspond to simulations using Eq. 4.4. Measurements taken from Sample MBE_VBST_20230206a.

dominates. To model this dataset, we define

$$P_{\mathrm{diss}} = R_{xx} I_{\mathrm{dc}}^2 + \frac{U_{\mathrm{rf}}^2}{Z}, \tag{4.6}$$

fix $\alpha = 4$, and treat Z as an effective impedance parameter. The resulting fits, shown as black lines in Fig. 4.4c, reproduce the overall trends, although with reduced quantitative accuracy compared to the dc- or rf-only cases. This is expected given the simplified treatment of rf absorption.

Finally, we investigate the breakdown behavior at elevated refrigerator temperatures T_p. Figure 4.5a shows $\sigma(U_{\mathrm{rf}})$ for temperatures up to 800 mK. As expected, the residual conductance at low voltages increases with temperature due to VRH. The breakdown persists but shifts to higher voltages and becomes less pronounced. Plotting the same data as $\sigma(T_p)$ for different rf voltages (Fig. 4.5b) reveals that rf excitation and temperature act additively.

We apply the Joule heating model without introducing additional fit parameters and simply by setting T_p in Eq. 4.4 to the fridge temperature. We find excellent agreement with the data as shown in Fig. 4.5c. All observed temperature- and electric field-driven breakdown phenomena can thus be consistently explained by a unified model combining Joule heating and VRH transport. This strongly supports electron heating as the dominant breakdown mechanism in the QAH regime under rf excitation. The resulting frequency dependence of the breakdown voltage, $U_{\mathrm{bd}} \propto 1/\sqrt{f}$, places stringent constraints on the operation of lossless high-frequency QAH-based devices [15, 16]. While the Joule-heating

model provides a consistent description of all observed breakdown phenomena, it relies on several simplifying assumptions. In the following, we discuss the main approximations underlying the model and outline the regime of validity of our analysis.

4.2.3 Model approximations and assumptions

The Joule-heating model introduced above relies on several simplifying assumptions that are important to state explicitly to clarify the regime of validity of our analysis. First, the temperature parameter T_e entering the VRH expression (Eq. 4.2) formally describes both the electronic temperature and the phonon bath assisting the hopping process. Using this relation as an effective electronic thermometer, therefore implicitly assumes that the relevant phonons within the 8 nm-thin V-BST layer are thermalized with the electronic system at temperature T_e. In contrast, phonons in the much thicker InP substrate (350 µm) are assumed to remain in thermal equilibrium with the refrigerator at temperature T_p and act as an efficient heat sink.
Second, we assume that both the electronic temperature T_e and the phonon temperature T_p are spatially homogeneous across the device. This approximation neglects local temperature variations, in particular near contacts and device corners where enhanced dissipation is expected [114]. Possible temperature differences between the top and bottom surfaces of the topological insulator film are also neglected, as their separation (8 nm) is much smaller than the relevant phonon wavelengths in the temperature range of the experiment.
Furthermore, the model does not explicitly account for the detailed geometry of the microwave field, which is expected to be strongest near the excitation finger gates and to vary with excitation frequency. Instead, rf absorption is described phenomenologically by a single effective, frequency-dependent dissipation parameter $G(\omega)$. Finally, energy relaxation is treated using a phenomenological power-law cooling model characterized by the parameters α and Σ. This approach does not distinguish between different microscopic phonon modes or scattering mechanisms and assumes a single dominant energy-loss channel across the relevant temperature and power ranges. Despite these simplifications, the model captures all observed trends quantitatively and provides a self-consistent framework for interpreting the breakdown behavior under both dc and rf excitation.

4.2.4 Discussion of alternative mechanisms

Given the observed frequency dependence, photon-assisted hopping was initially considered as a possible breakdown mechanism. In this picture, microwave photons assist transitions between localized states, playing a role analogous to phonons in VRH [86, 118]. However, photon-assisted hopping predicts an exponential dependence on frequency and a quadratic dependence on excitation voltage, neither of which is observed experimentally.
An alternative scenario is electric field-driven hopping, as described by Polyakov and Shklovskii [90]. In this case, the conduction is non-Ohmic as we will discuss in the following section 4.3. In this model, transport is governed by an effective electronic temperature set by the Hall electric field, leading to

$$\sigma = \frac{\sigma_{0,U}}{U} \exp\left(-\sqrt{U_0/U}\right). \tag{4.7}$$

This model differs from Joule heating only in the scaling exponent. The model by Polyakov and Shklovskii yields a scaling of $T \propto U$, while the Joule heating model yields $T \propto U^{2/\alpha}$. Hence, they yield the same result for $\alpha = 2$. However, since we consistently extract values of $\alpha \gtrsim 3.4$ that are incompatible with the Polyakov-Shklovskii prediction for purely electric field-driven hopping. We emphasize, however, that field-induced hopping and Joule heating are not mutually exclusive mechanisms. Both processes are generically present under strong electric fields and compete in assisting hopping events. In the present QAH devices, transport is dominated by heating, indicating that the electronic temperature rises sufficiently rapidly to be the controlling factor. Electric field-driven hopping may nevertheless become relevant in regimes of stronger localization (lower residual bulk conductance) or at smaller electric fields than those accessible here. This competition between electric field-driven and heating-dominated transport will be discussed explicitly in the context of graphene in Sec. 4.3, where the localization strength can be tuned systematically, and both regimes can be observed within a single device.

4.3 Non-Ohmic to Ohmic crossover of quantum Hall breakdown in graphene devices

To disentangle universal aspects of QH breakdown from material-specific effects observed in QAH insulators, we now turn to graphene. Owing to its high mobility and well-understood Landau level spectrum, graphene provides a

clean platform for studying QH breakdown mechanisms in the absence of magnetic doping. We therefore investigate the breakdown of quantized transport in graphene as a function of the filling factor and applied electric field. This approach allows us to distinguish between non-Ohmic, electric field-driven, and heating-dominated transport. And it allows us to establish a benchmark for comparison with QAH systems.

In contrast to QAH insulators, where the localization strength of bulk states is largely fixed by material disorder and film thickness, graphene offers continuous tunability of bulk localization within a single device by varying the filling factor. This tunability can be conveniently parameterized by the hopping energy scale $k_{\mathrm{B}}T_0$, which quantifies the degree of localization of bulk states and can be extracted directly from temperature-dependent transport measurements (by fitting $\sigma(T)$ with the VRH law in Eq. 4.2). In the following, the parameter T_0 serves as a quantitative measure of bulk localization and provides a unifying axis for comparing breakdown behavior across different filling factors. Graphene provides access to a broad range of localization regimes, spanning from strongly localized states deep within Landau level gaps to weakly localized states near plateau transitions [115, 127–129]. By studying breakdown behavior across this wide range of $k_B T_0$, we directly probe the crossover from non-Ohmic hopping transport to an Ohmic regime dominated by Joule heating, thereby establishing a quantitative framework for interpreting the breakdown behavior observed in QAH systems. In the QH regime, disorder broadens the Landau levels and gives rise to localized states away from the Landau level centers. At low temperatures, bulk transport proceeds via VRH between these localized states, as described by Polyakov and Shklovskii [90]. A key difference between graphene and QAH systems lies in the microscopic nature of these bulk states. In graphene, spatial fluctuations of the electrostatic potential lead to local crossings between Landau levels and the chemical potential, forming quasi-one-dimensional closed trajectories encircling electron and hole puddles, as illustrated in Fig. 4.6a. In contrast, in V-BST, the QAH insulator studied in the previous chapter, bulk states are two-dimensional and filled, resulting in a qualitatively different landscape of localization and screening, as illustrated in Fig. 4.6b. While the hopping between the localised states can be well described by VRH in either case, the intra-puddle conductance and the magnetic field dependence will be altered.

Another important distinction arises from the Landau level spectrum of graphene. Due to the linear dispersion of Dirac fermions, the Landau levels are

located at energies [130, 131]

$$E_N = \pm v_F \sqrt{2e\hbar B|N|}, \tag{4.8}$$

where N is the Landau level index and v_F the Fermi velocity of the Dirac dispersion. As a result, the cyclotron gaps scale as $\sqrt{B}$ and are substantially larger than in conventional two-dimensional electron gases. In addition, in high out-of-plane magnetic fields, the fourfold spin and valley degeneracy of the Landau levels is lifted by exchange interactions, giving rise to smaller symmetry-broken gaps associated with spin or valley polarization [115]. Graphene, therefore, exhibits a hierarchy of energy gaps, ranging from a few kelvin for symmetry-broken states to several hundred kelvin for cyclotron gaps at magnetic fields of the order of 10 T. The electronic properties of graphene in magnetic fields are discussed in detail in Chapter 5.

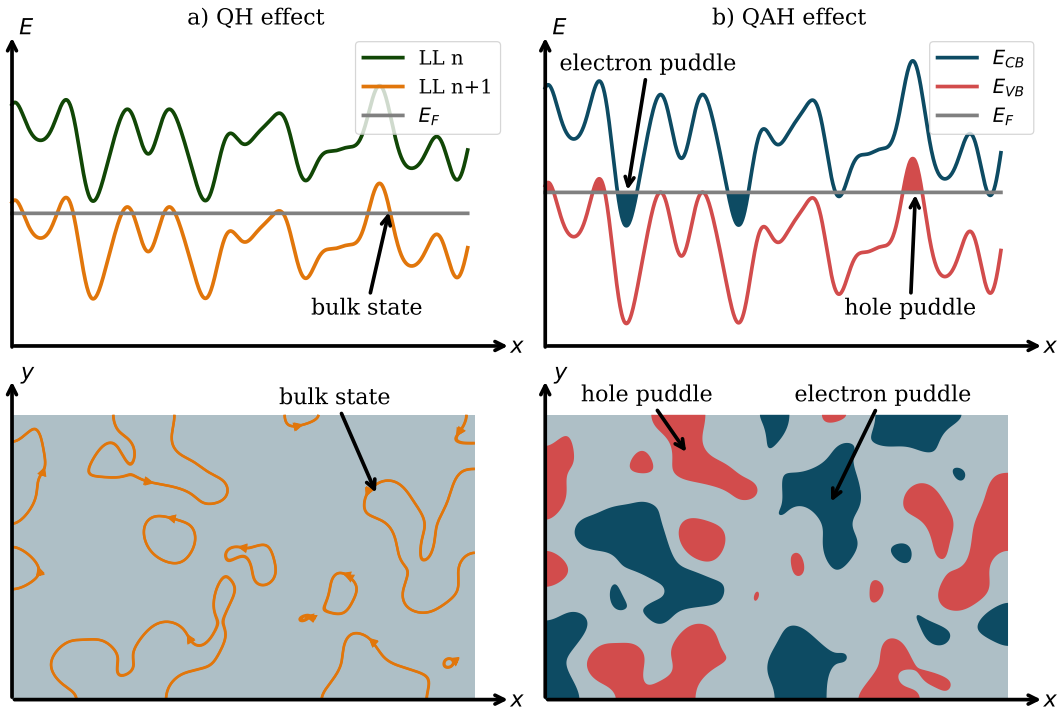

Figure 4.6: Bulk states in the QH and QAH regimes. a) Quantum Hall (QH) effect. Top: Spatial fluctuations of the Landau levels LL_n and LL_{n+1} in a disordered potential landscape. Whenever a Landau level crosses the Fermi energy E_F, bulk states appear. Bottom: In real space, these crossings correspond to closed, one-dimensional drift trajectories that percolate at the center of each Landau level. b) Quantum anomalous Hall (QAH) effect. Top: Spatial variations of the conduction band edge E_{CB} and valence band edge E_{VB} relative to the Fermi level give rise to electron- and hole-like regions. Bottom: These fluctuations result in two-dimensional electron and hole puddles in the bulk, which are separated by locally gapped regions. In contrast to the QH case, the bulk states in the QAH regime are not associated with Landau quantization.

The breakdown of the QH effect under strong electric fields has been extensively studied in conventional two-dimensional electron systems [3, 26] and later extended to graphene [4, 24, 25]. A widely used description is provided by the Polyakov–Shklovskii model [90], which interprets non-Ohmic transport in terms of an effective electronic temperature T_{eff} proportional to the local Hall electric field E, $k_{\mathrm{B}}T_{\mathrm{eff}} = e\xi E/2$, where ξ is the localization length (see Sec. 2.3). The key idea is that the electrostatic potential gain $e\xi E/2$ replaces the thermal energy $k_B T$. Within this framework, nonlinear current–voltage characteristics at breakdown reflect field-assisted hopping rather than Joule heating.

Graphene provides an experimentally accessible platform for probing different hopping regimes in the QH effect. In addition to localization physics, energy relaxation plays a crucial role in the breakdown of the QH effect in graphene. Baker et al. showed that hot Dirac fermions in graphene exhibit energy loss rates [25] that are more than an order of magnitude larger than in GaAs-based two-dimensional electron systems [132]. This rapid energy relaxation leads to unusually high breakdown current densities and has important consequences for the crossover from non-Ohmic transport to regimes where Joule heating dominates the response.

Despite significant progress, two important gaps remain in the literature. First, most studies focus on selected filling factors or fixed magnetic fields, either deep inside a gap or near plateau transitions, rather than providing a systematic mapping of breakdown across a broad range of localization energies. As a result, the crossover from non-Ohmic VRH to Ohmic, heating-dominated transport has not been explored within a unified framework. Second, previous investigations are almost exclusively restricted to dc or low-frequency measurements. This is a significant limitation, as many envisioned applications of graphene QH systems operate at radio and microwave frequencies, including single-electron quantum optics experiments [28, 133] and non-reciprocal microwave components [15, 134]. Addressing QH breakdown in this frequency range is therefore essential from both fundamental and applied perspectives.

We investigate the breakdown of QH states in graphene under dc and rf excitation up to 10 GHz. As in the QAH study, we use the dc conductance σ as a frequency-independent probe of bulk transport while applying electric fields over a wide range of voltages and frequencies. Throughout this section, we use the bulk conductance σ as an effective thermometer by mapping $\sigma(U_{\mathrm{dc,rf}})$ onto $\sigma(T = T_{\mathrm{eff}})$. T_{eff} is the temperature that would yield the same conductance in equilibrium as the voltage $U_{\mathrm{dc,rf}}$. We analyze the scaling $T_{\mathrm{eff}} \propto U_{\mathrm{dc,rf}}^{\beta}$ as a function

of filling factor and magnetic field, and show that the crossover from non-Ohmic transport to heating-dominated Ohmic behavior is controlled solely by the localization strength encoded in $k_{\mathrm{B}}T_0$. We first introduce the device geometry and dc characterization before presenting the breakdown measurements in detail.

4.3.1 Device layout and dc characterization

The samples were fabricated by Aifei Zhang under the supervision of François D. Parmentier and Olivier Maillet at the University of Paris-Saclay. Therefore, we do not detail the fabrication process here and instead focus on the sample geometry. To disentangle bulk transport from edge-state contributions, the graphene sheet is patterned into a Corbino geometry, which is convenient for studying breakdown mechanisms governed by VRH and electronic heating.

A microscope image of the device is shown in Fig. 4.7a. The heterostructure consists, from bottom to top, of graphite–hBN–graphene–hBN–hBN. The bottom graphite layer serves as a local back gate, capacitively coupled to the graphene through the bottom hBN layer, allowing continuous tuning of the filling factor ν. Encapsulation in hBN suppresses charge inhomogeneity and yields high carrier mobility, which is essential for stabilizing symmetry-broken QH states. The graphene layer is etched into a disk with lateral dimensions of $7.5 \times 10\,\mu\mathrm{m}^2$. Four Ohmic contacts are fabricated: one at the center and three at the perimeter. The central contact defines the inner radius of the Corbino device, with a diameter of approximately 2 µm, and is electrically isolated by an additional hBN flake (blue contrast in Fig. 4.7a). The separation between bulk and edge transport in the Corbino geometry is illustrated in Fig. 4.7b. In the QH regime, edge states form along both the inner and outer perimeters, but they are not directly connected. Consequently, when a voltage bias is applied between the inner and outer contacts, the resulting current must flow through the bulk. The two-terminal configuration employed here therefore provides a direct measure of the bulk conductance σ.

To probe the bulk conductance, a small ac voltage of 100 µV at 7 Hz, well below the breakdown threshold, is applied to the central contact, while the outer contacts are grounded (Fig. 4.7a). The voltage drop across the device and across a 20 kΩ series resistor is measured using lock-in detection, allowing the current and hence the bulk conductance σ to be determined. Independent measurements in the metallic regime confirm that contact resistances are negligible ($R \approx 3\,\mathrm{k}\Omega$). This low-frequency lock-in technique is used throughout as a sensitive probe of the bulk conductance under temperature variation as well as under dc and rf

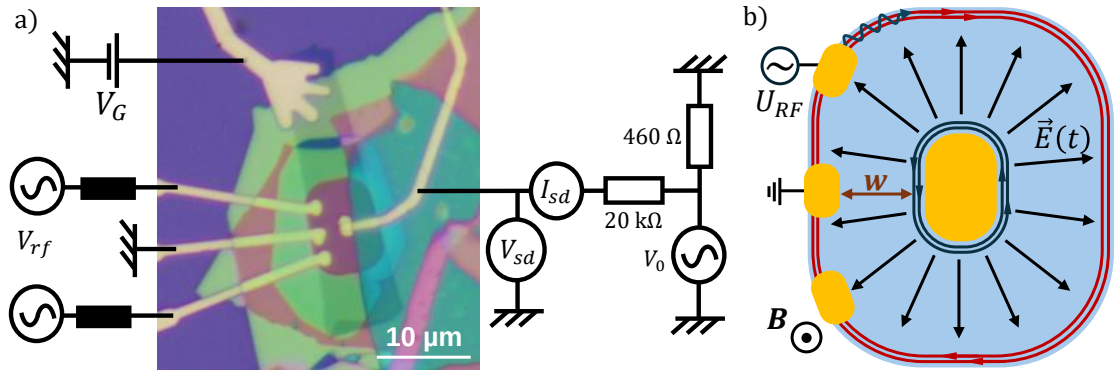

Figure 4.7: Sample layout and experimental setup. a) Microscope image of the device. The top contact is connected to a graphite back gate (grey contrast). The graphene Corbino device is sandwiched between hBN flakes (shown in green). The blue flake is an additional hBN flake, avoiding shorts between the graphene and the central Ohmic contact(right). The left Ohmic contacts are grounded, and two are connected to rf sources via bias-tees. The conductance is obtained by voltage-biasing the central contact. b) Sketch of the corbino device for $\nu = 2$ (for simplicity). The outer edge states (red lines) and the inner edge states (blue lines) are only connected via bulk states. Hence, the conductance σ measured between the inner and outer has no edge state contribution. A dc bias voltage U_{dc} creates a static radial electric field of approx $E = U_{\mathrm{dc}}/w$. An rf voltage U launches an edge plasmon that propagates around the outer edge, creating a time- and space-dependent electric field across the bulk.

drives.

For dc breakdown measurements, a dc offset U_{dc} is added to the low-frequency excitation, generating a static radial electric field across the bulk. To first approximation, the average electric field strength can be estimated as $E \approx U_{\mathrm{dc}}/w$, where w denotes the distance between the inner and outer contacts. A filling-factor-dependent correction arises from the impedance mismatch between the $50\,\Omega$ measurement circuit and the edge-state impedance $Z = R_K/\nu$, which affects the effective voltage drop across the device.

In the case of rf breakdown, our setup does not allow us to apply the excitation to the inner contact. Instead, an rf voltage with root-mean-square amplitude U_{rf} is applied to one of the outer contacts, as sketched in Fig. 4.7b. This excitation launches collective charge oscillations (edge plasmons) along the outer edge, which generate a time- and position-dependent radial electric field across the bulk. While the detailed spatial profile depends on geometry and frequency, the characteristic field amplitude scales with the applied rf drive, $E \propto U_{\mathrm{rf}}$. Conceptually, both dc and rf excitation generate an effective radial electric field across the bulk, allowing breakdown to be compared on equal footing. Importantly, the measured quantity remains the dc bulk conductance between the inner and outer contacts. The rf excitation modifies the bulk response only through the

induced time-dependent electric field. Above 1 GHz, the absolute rf voltage amplitude carries a systematic calibration uncertainty due to reflections and standing waves in the setup. This affects the absolute field scale but not the relative trends discussed below. At low temperatures and in the absence of strong electric fields, the bulk conductance exhibits well-developed QH plateaus as a function of the filling factor ν at $B = 9\,\mathrm{T}$, as shown in Fig. 4.8. Wide plateaus appear at $\nu = 2, 6, 10$, corresponding to large cyclotron gaps. Narrower plateaus at $\nu = 4$ and 8 originate from spin splitting. The plateau at $\nu = 8$ is not fully developed at the maximum magnetic field accessible in our setup. Valley-split gaps at $\nu = 3, 5, 7, 9$ remain too small to yield insulating bulk behavior. While the discussion below focuses on electron doping and $B = 9\,\mathrm{T}$, additional measurements at negative filling factors and smaller magnetic fields are shown in Appendix E. In the following, we concentrate on the cyclotron gaps at $\nu = 6, 10$ and the spin gaps at $\nu = 4, 8$, which provide access to a broad range of localization strengths.

4.3.2 Observation of the electric field-driven breakdown

Having established the low-bias measurement scheme, we now turn to the response of the bulk under a strong static electric field (U_{dc}). Figure 4.9a shows the bulk conductance σ (measured by the 100 µV, 7 Hz bias voltage) as a function of filling factor ν for increasing dc bias voltages U_{dc}. The blue curve corresponds to zero bias and reproduces the well-developed QH plateaus shown in Fig. 4.8. With increasing U_{dc}, the plateaus progressively shrink. The spin gaps at $\nu = 4, 8$ collapse already at bias voltages of the order of 1 mV, whereas the larger cyclotron gaps at $\nu = 6, 10$ remain insulating up to the maximum applied voltage

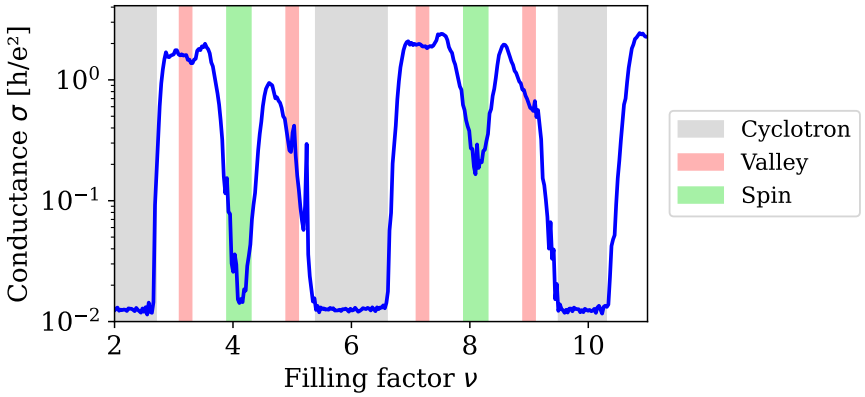

Figure 4.8: Low-bias, low-temperature conductance. Conductance σ as a function of the filling factor ν at $B = 9\,\mathrm{T}$ and $T \simeq 20\,\mathrm{mK}$. The different gaps are highlighted by color coding: grey → cyclotron gap, red → spin gap, green → valley gap.

of $U_{\mathrm{dc}} = 50\,\mathrm{mV}$ when the Fermi level is tuned to the center of the gap. Nevertheless, even for the cyclotron gaps, a continuous reduction of the plateau width with increasing bias voltage is observed.

The corresponding voltage dependence of the conductance for selected filling factors is shown in Fig. 4.9d. For all filling factors, the curves exhibit a characteristic VRH–like behavior, with an exponential onset of conductance at small voltages followed by a gradual increase at larger bias voltages. This functional form already suggests that hopping between localized bulk states governs the onset of dissipation.

The same analysis is performed under rf excitation at a frequency of 6 GHz, as shown in Fig. 4.9b. The evolution of $\sigma(\nu)$ closely mirrors the dc case: the spin gaps at $\nu = 4, 8$ disappear first, followed by a gradual narrowing of the cyclotron gaps at $\nu = 6, 10$. The primary difference lies in the overall voltage scale, which is shifted by approximately a factor of 10. We attribute this shift to uncalibrated attenuation in the microwave lines between the vector network analyzer and the sample. Importantly, once this overall scaling is taken into account, the voltage

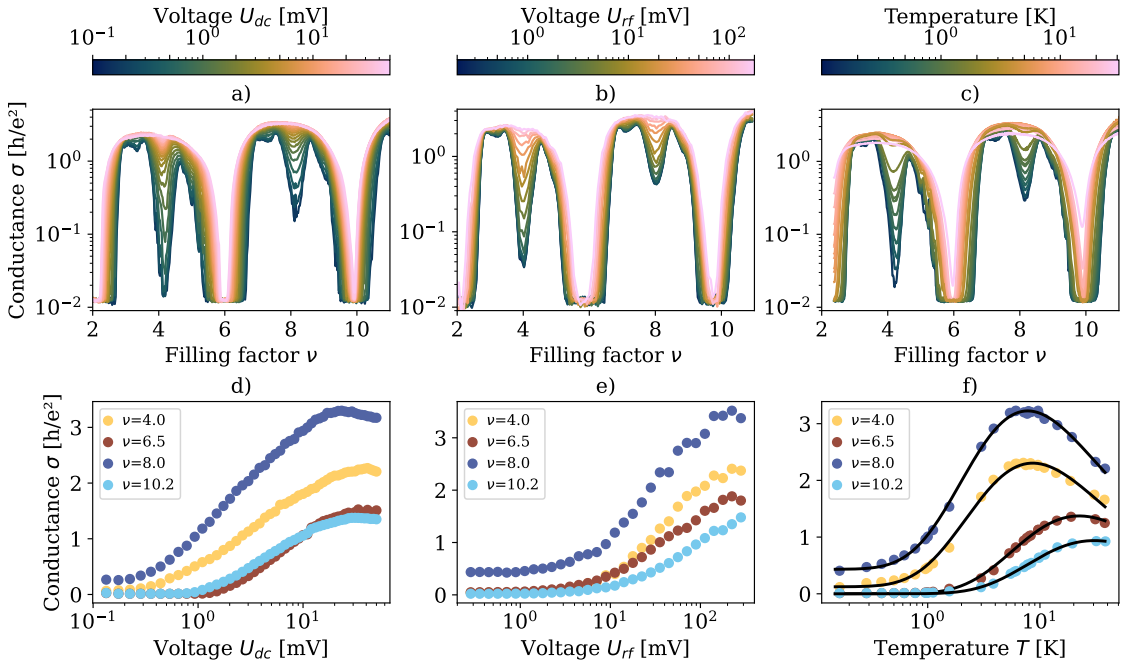

Figure 4.9: Breakdown under dc/rf excitation and temperature. (a–c) dc bulk conductance σ vs. filling factor ν for increasing dc bias voltages U_{dc} (a), increasing microwave power at 6 GHz (b), and increasing temperature (c). (d–f) Corresponding line cuts, showing dc bulk conductance σ vs. dc bias voltage U_{dc} (d), microwave voltage U_{rf} (e), and temperature T (f) at selected filling factors. The black lines in f) correspond to a fit with Eq. 4.2 with T_0 and σ_0 as fitting parameters (with an offset for not fully developed gaps). All measurements are taken at $B = 9\,\mathrm{T}$.

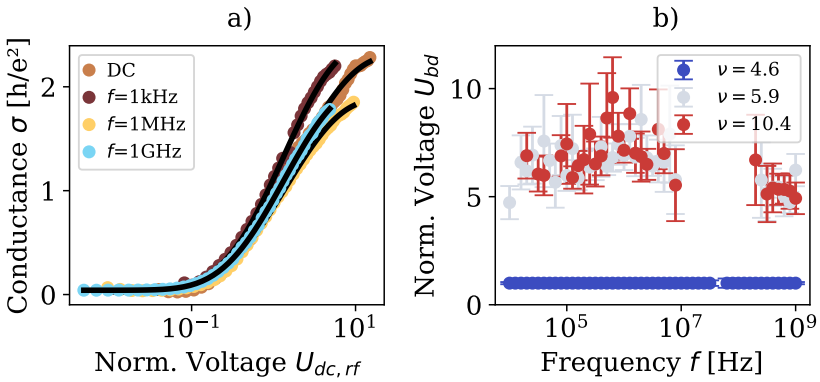

Figure 4.10: Frequency dependence of breakdown. (a) Conductance σ vs. dc bias voltage U_{dc} for selected excitation frequencies at $\nu = 4$. The voltage is normalized by U_{bd}, defined where the conductance reaches half of its maximum ($\sigma(U = U_{\mathrm{bd}}) = \sigma_{\mathrm{max}}/2$. (b) The breakdown voltage U_{BD} normalized by its value at $\nu = 4$ for the filling factor $\nu = 4.0, 5.9$ and 10.4, showing weak intrinsic frequency dependence within the error margin. All measurements are taken at $B = 9\,\mathrm{T}$.

dependence of the conductance, shown in Fig. 4.9e, is indistinguishable from the dc case. This indicates that the underlying breakdown mechanism is the same for dc and rf excitation.

To test explicitly whether the breakdown mechanism depends on frequency, we repeat the measurement for excitation frequencies ranging from dc up to 10 GHz. Figure 4.10a shows the conductance as a function of bias voltage for representative frequencies (dc, 1 kHz, 1 MHz, and 1 GHz). To correct for frequency-dependent losses in the measurement setup, the voltage axis is normalized by a breakdown voltage U_{bd}, defined as the voltage at which the conductance reaches half of its maximum $\sigma(U_{\mathrm{bd}}) = \sigma_{\mathrm{max}}/2$. After this normalization, all curves overlap, demonstrating that the voltage dependence of the breakdown is independent of frequency over the investigated range. This conclusion is further supported by Fig. 4.10b, which shows the normalized breakdown voltage U_{bd} as a function of frequency for several filling factors ($\nu = 4.6, 5.9, 10.4$). The normalization is performed with respect to the value at $\nu = 4.6$ to eliminate setup-related effects that are independent of the filling factor. The absolute values of U_{bd} differ between gaps, reflecting the larger stability of cyclotron gaps compared to spin gaps, but no systematic frequency dependence is observed within the experimental uncertainty. This demonstrates that, in contrast to QAH devices, the breakdown mechanism in graphene is frequency independent up to at least 10 GHz.

Finally, the similarity between the voltage-driven and temperature-driven suppression of the QH plateaus suggests that VRH plays a central role in the onset of dissipation. We therefore turn next to the temperature dependence of the conductance, which is known to follow a VRH law [4, 24, 90]. This analysis allows us to extract the relevant energy scales and to assess whether electric field–driven and temperature-driven breakdown share a common microscopic origin.

4.3.3 Breakdown at elevated temperatures

The temperature-dependent conductance σ as a function of filling factor ν is shown in Fig. 4.9c. Similar to the electric field–driven breakdown, we observe a continuous closing of the QH gaps with increasing temperature. The spin gaps at $\nu = 4, 8$ close at temperatures of approximately 1 K, whereas the larger cyclotron gaps only close at temperatures above approximately 20 K. Compared with electric field–driven breakdown, temperature-driven measurements allow us to access slightly larger energy scales, leading to the onset of conductance even in the center of large cyclotron gaps.
The temperature dependence of the conductance for four representative filling factors, corresponding to different gaps, is shown in Fig. 4.9f. The curves exhibit the same characteristic shape as the voltage-dependent conductance shown in Fig. 4.9d–e. All curves are well described by the Efros–Shklovskii VRH law given in Eq. 4.2. The corresponding fits, shown as black lines in Fig. 4.9f, are in excellent agreement with the experimental data.

From these fits, we extract the hopping energy scale $k_{\mathrm{B}}T_0$, which we use in the following as a quantitative measure of the localization strength of the bulk carriers. Using Eq. 2.12, we can further estimate the localization length ξ and the average hopping distance

$$r_{\mathrm{hop}} = \xi\sqrt{\frac{T_0}{T}}, \tag{4.9}$$

which will later be used to estimate the electrostatic energy eEr_{hop} associated with a hopping event in the presence of a strong electric field E.
We perform this fitting procedure for various filling factors across all four gaps, thereby extracting $T_0(\nu)$, as shown in Fig. 4.11. The extracted hopping energy $k_{\mathrm{B}}T_0$ is systematically larger for the cyclotron gaps ($\nu = 6, 10$) than for the spin gaps ($\nu = 4, 8$) and generally decreases as the filling factor is tuned from the center of a gap toward the transition to the neighboring Landau level. This dependence on filling factor is theoretically predicted to scale as $T_0 \propto |\nu - \nu_c|^{2.3}$ [135–138], where ν_c corresponds to the center of a Landau level. This scaling law has

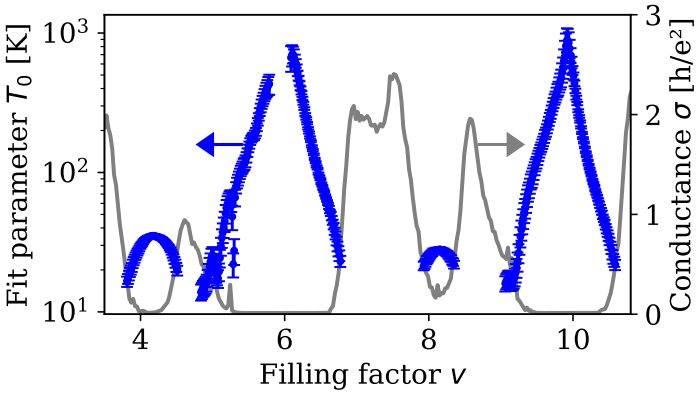

Figure 4.11: Temperature T_0 vs. filling factor ν. Fit parameter T_0 and its error are shown as a function of the filling factor ν. T_0 is extracted from fits of the temperature-dependent conductance $\sigma(T)$ with the VRH law in Eq. 4.2. The secondary axis shows the low-bias, low-temperature conductance $\sigma(\nu)$. Both measurements are taken at $B = 9\,\mathrm{T}$.

been investigated in numerous experimental studies [3, 24, 127–129, 139]. Since the scaling behavior itself is not the focus of this work, we do not analyze it further and instead use $k_\mathrm{B}T_0$ solely as a parameter characterizing the localization strength.

In the following, we use the VRH fits as a thermometer by mapping the measured $\sigma(U_\mathrm{dc})$ onto the calibration curve according to $\sigma(U_\mathrm{dc}) = \sigma(T = T_\mathrm{eff})$ (as in Sec. 4.2.1). This yields an effective temperature T_eff that would produce the same conductance in equilibrium as the voltage U_dc. In the following, we analyze its dependence on the applied voltage U_dc to differentiate between non-Ohmic and Ohmic conduction.

4.3.4 Non-Ohmic and Ohmic regime

As discussed in Sec. 4.2.3, the scaling between the effective temperature T_eff and the applied voltage U_dc provides a direct way to distinguish between two transport regimes: (1) non-Ohmic conduction, when hopping is driven by the electric field between hopping sites and (2) Ohmic conduction, when hopping is driven by temperature (phonons) due to Joule heating. In the non-Ohmic case, the electric field E plays a role analogous to temperature and leads to a linear scaling $T_\mathrm{eff} \propto U_\mathrm{dc}$. In the Ohmic case, the transport is dominated by Joule heating, and we find $T_\mathrm{eff} \propto U_\mathrm{dc}^{2/\alpha}$, where α is the exponent governing the electron–phonon cooling power. This results in a power-law dependence $T_\mathrm{eff} \propto U_\mathrm{dc}^{\beta}$ with $\beta \simeq 0.4$–0.67 for $\alpha = 3$–5 [114, 122, 123, 126]. By plotting T_eff as a function of U_dc on double-logarithmic axes, the dominant transport mechanism can therefore be identified

from the slope.

Figure 4.12a shows T_{eff} as a function of dc bias voltage for four representative filling factors. For the cyclotron gaps ($\nu = 6.4, 10.2$), T_{eff} remains approximately constant up to bias voltages of about 1 mV, followed by a linear increase with U_{dc}. The apparent plateaus at low voltages are an artifact of the thermometry: when the conductance falls below the experimental resolution, T_{eff} is mapped to the temperature at which an onset of conductance becomes detectable. Above this threshold, a clear linear scaling $T_{\text{eff}} \propto U$ is observed.

In contrast, for the smaller spin gaps ($\nu = 4.0, 8.1$), T_{eff} approximately follows a $U^{1/2}$ dependence over a wide voltage range, although a slightly steeper slope is visible at low bias. At first glance, this suggests that breakdown in the large cyclotron gaps is in the non-Ohmic regime ($\beta \approx 1$), whereas breakdown in the smaller spin gaps is governed by Ohmic transport ($\beta \approx 1/2$).

This observation immediately raises the question of whether the same cyclotron gap can exhibit Ohmic conduction behavior when the Fermi level is tuned closer to the plateau edges, where the hopping energy $k_{\text{B}}T_0$ is reduced. To address this, we repeat the analysis of Fig. 4.12a for a wide range of filling factors and fit the data with a power-law form $T_{\text{eff}}(U) = A\,U^{\beta}$. The extracted exponent β, together with its uncertainty, is plotted as a function of the hopping energy $k_{\text{B}}T_0$ in Fig. 4.12b. We observe a continuous increase of the exponent from $\beta \simeq 0.4$ at small T_0 to $\beta \simeq 1$ at large T_0. This demonstrates a smooth crossover from Ohmic transport ($\beta \simeq 0.40$–0.66) to non-Ohmic transport ($\beta \simeq 1.0$) as the localization strength increases. Importantly, this shows that field-driven hopping and heating are not mutually exclusive mechanisms. Instead, they are both contributing, and only their relative importance changes with the degree of localization encoded in $k_{\text{B}}T_0$.

The crossover can also be probed as a function of bias voltage. For filling factors with intermediate hopping energies, we observe effective exponents β between 0.7 and 0.9, which lie between the two limiting regimes. Figure 4.12c shows $T_{\text{eff}}(U_{\text{dc}})$ for four filling factors spanning the transition between $\nu = 6.34$ and $\nu = 6.64$, corresponding to $T_0 \simeq 180\,\text{K}$ and $T_0 \simeq 40\,\text{K}$ respectively. For all curves, the slope evolves from approximately unity at low voltages to approximately $1/2$ at higher voltages. The characteristic crossover voltage U_{c}, at which this change in slope occurs, shifts to higher values as the filling factor is tuned deeper into the gap.

To quantify this behavior, we perform a sliding-bias analysis in which six consecutive data points are fitted with a power law $T_{\text{eff}} \propto U_{\text{dc}}^{\beta}$. The resulting exponent

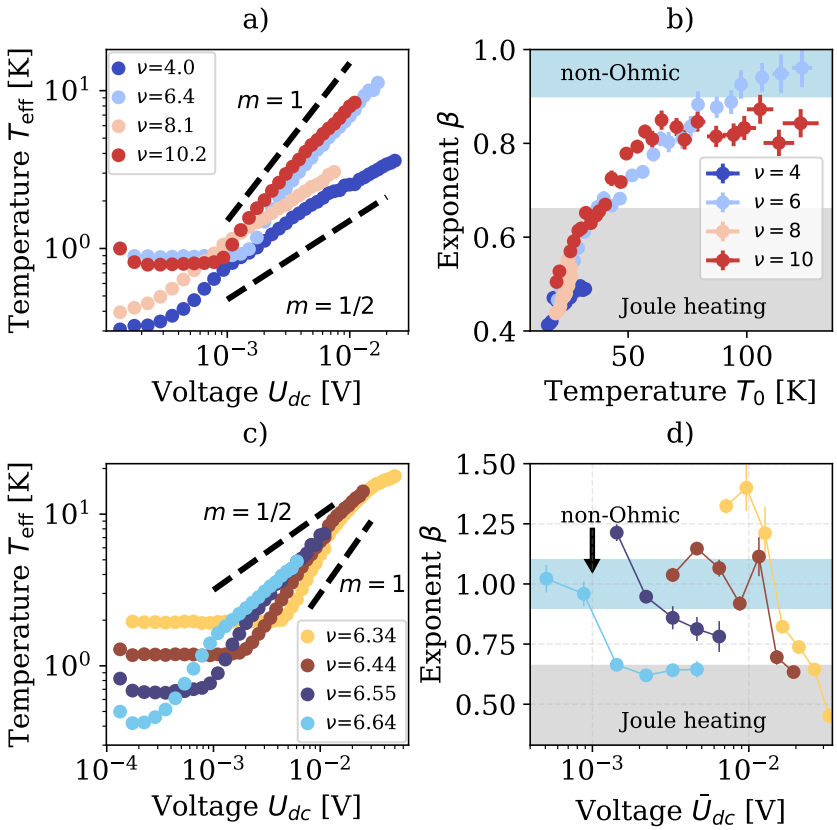

Figure 4.12: Heating analysis (a) Effective electronic temperature T_{eff}, extracted by mapping the measured conductance $\sigma(U)$ onto the temperature-dependent VRH calibration $\sigma(T)$ (see Fig. 4.9f), vs. the dc bias voltage U_{dc} for four representative gaps. One observes $T_{\mathrm{eff}} \propto U$ for $\nu = 6.4, 10.2$ and $T_{\mathrm{eff}} \propto U^{1/2}$ for $\nu = 4.0, 8.1$. The dashed lines indicate a scaling of $T_{\mathrm{eff}} \propto U_{\mathrm{dc}}$ and $T_{\mathrm{eff}} \propto U_{\mathrm{dc}}^{1/2}$. (b) Exponent β from a fit of the power law $T_{\mathrm{eff}} \propto U^{\beta}$, plotted vs. the hopping energy T_0 at the same ν. Grey and blue regions indicate the expected ranges for Joule-heating–dominated and non-Ohmic transport, respectively. (c) Same as a) for various filling factors within the $\nu = 6$ gap. (d) Bias-dependent power-law exponent β from sliding-window fits: each fit uses six adjacent data points of $T_{\mathrm{eff}}(\bar{U}_{\mathrm{dc}})$, with the exponent β plotted at the mean $\bar{U}_{\mathrm{dc}}$ if the MSE is $< 10\%$. The plots contain the same data as in Fig. 4.9.

β is assigned to the center of the corresponding bias window, provided the mean squared error of the fit is below 10%. The extracted bias dependence of β is shown in Fig. 4.12d as a function of the mean voltage $\bar{U}_{\mathrm{dc}}$ of the corresponding bias window. We observe a systematic decrease of β with increasing bias voltage, with the crossover shifting to higher voltages for larger hopping energies $k_{\mathrm{B}}T_0$. This confirms that the localization strength ($k_B T_0$) plays a central role in determining the transition from the non-Ohmic to the Ohmic regime.

4.3.5 Discussion of the crossover behavior

The physical origin of the observed crossover can be understood by comparing the electrostatic energy eEr_{hop} associated with a hopping event to the thermal energy $k_{\mathrm{B}}T_e$. Both contributions assist hopping and are therefore always present simultaneously. The dominant transport mechanism is determined by which energy scale is larger. For $eEr_{\mathrm{hop}} > k_{\mathrm{B}}T_e$, transport is non-Ohmic. This regime may be viewed as a "cold" regime, in which the electronic temperature remains close to equilibrium. When $k_{\mathrm{B}}T_e > eEr_{\mathrm{hop}}$, transport is governed by the thermal activation of hopping processes and follows the usual VRH law, with T_e determined by Joule heating (see Eq. 4.4).

Since the hopping distance depends on temperature as $r_{\mathrm{hop}} \propto T_e^{-1/2}$, the crossover between these regimes is not trivial. Moreover, the electronic temperature T_e is not directly experimentally accessible. Instead, we extract an effective temperature T_{eff}, which corresponds to the temperature T_e, which would yield the same conductivity σ for low bias voltages. In the non-Ohmic regime, T_{eff} exceeds the true electronic temperature because it is defined through the electrostatic energy scale $e\xi E/(2k_{\mathrm{B}})$. To estimate the actual electronic temperature, we use a Joule-heating model of the form $T_e = (\sigma(U)U^2/\Sigma)^{1/\alpha}$ (assuming $T_e \gg T_p$). For simplicity, we set $\alpha = 3$ and adjust Σ such that $T_e = T_{\mathrm{eff}}$ at high bias, where heating-dominated transport is confirmed by the exponent β.

The resulting comparison between T_e and T_{eff} is shown in Fig. 4.13a for $\nu = 6.6$. A consistent description is obtained for all filling factors using electron–phonon coupling constants Σ in the range 0.1–$0.4\,\mathrm{WK^4/m^2}$, consistent with values reported in the literature [124, 125]. Based on this comparison, we define an alternative crossover voltage U_{c} by the condition $T_e \approx 0.8\,T_{\mathrm{eff}}$. While the numerical value of the prefactor is arbitrary, the qualitative conclusions are insensitive to its precise choice.

Figure 4.13b compares this definition of U_{c} with the crossover voltage extracted from the bias dependence of β. Both measures show an increase of U_{c} with hopping energy $k_{\mathrm{B}}T_0$, although their shapes differ, which we attribute to uncertainties in estimating the true electronic temperature. Notably, the crossover voltage follows the same qualitative dependence on T_0 as the conductance onset U_{bd}, defined here as the bias at which σ reaches half of its maximum value ($\sigma(U_{\mathrm{bd}}) = \sigma_{max}/2$). This indicates that heating becomes dominant once the dissipated Joule power σU^2 is sufficiently large to raise the electronic temperature.

Bennaceur et al. [24] reported similar changes in the exponent β, which they attributed to the activation of carriers in higher Landau levels. However, their

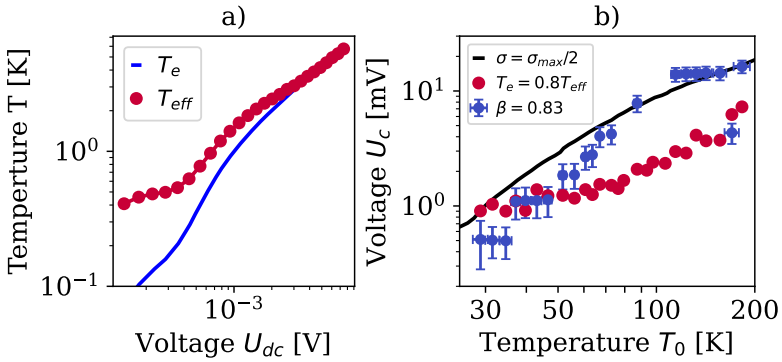

Figure 4.13: Transition from non-Ohmic to Ohmic. (a) Effective temperature T_{eff} and estimated electronic T_{e} vs. the dc bias voltage U_{dc}. T_{eff} is estimated by mapping $\sigma(U_{\mathrm{dc}})$ to $\sigma(T)$. T_{e} is estimated from the Joule heating model ($\alpha = 3$ and $\Sigma = 1.9 \times 10^{-11}\,\mathrm{W/K^4}$). The curves correspond to a filling factor of $\nu = 6.6$. (b) Crossover voltage U_{c} vs. hopping energy T_0 for filling factors $\nu = 6.16 - 6.69$. U_c is estimated using two different criteria: (1) the bias voltage U_{dc}, where β crosses 0.83 (blue, see example in Fig. 4.12d), or (2) the bias voltage U_{dc}, where $T_{\mathrm{e}} = 0.8\,T_{\mathrm{eff}}$ (red, see example in a). The black line corresponds to the breakdown voltage U_{bd}, defined where $\sigma = \sigma_{max}/2$. The plots use the same raw data as Fig. 4.9a,c.

analysis was restricted to cyclotron gaps at higher magnetic fields and did not access the regime in which heating dominates. By systematically mapping breakdown across a wide range of hopping energies $k_{\mathrm{B}}T_0$, we can distinguish the two regimes and demonstrate a continuous crossover from non-Ohmic VRH at large T_0 to Joule-heating–dominated transport at weaker localization.

4.4 Summary and conclusions

In this chapter, we investigated the breakdown of dissipationless edge-state transport in QAH insulators under microwave excitation and compared it to the breakdown of the conventional QH effect in high-mobility graphene. The central goal was to clarify whether rf excitation introduces qualitatively new breakdown mechanisms compared to dc bias, and to identify the microscopic parameters that control the transition from dissipationless to dissipative transport. Our measurements on QAH devices demonstrate that the breakdown of quantization under rf excitation is governed primarily by electron heating. Although the breakdown voltage decreases with increasing frequency, the underlying conductance curves collapse when expressed in terms of the electronic temperature extracted from a fit with a VRH law. A minimal Joule-heating model, combined with VRH transport in the bulk, consistently accounts for the observed rf- and dc-driven breakdown, the temperature dependence, and the combined action of dc

and rf excitation. These findings strongly support a picture in which microwave irradiation raises the electronic temperature via bulk absorption, thereby indirectly enhancing the dc bulk conductance.

To place the QAH results into a broader context, we performed a systematic comparison with a graphene Corbino device, which allows us to study the breakdown across a wide range of localization strengths. In graphene, we identified a clear crossover from a non-Ohmic regime to an Ohmic regime with increasing bias voltage. Crucially, this crossover is controlled solely by the hopping energy scale $k_{\mathrm{B}}T_0$, which quantifies the localization strength of the bulk states. In the studied range of bias voltages and for large hopping energies k_BT_0, transport is dominated by field-assisted hopping and exhibits non-Ohmic behavior. As k_BT_0 decreases, either by tuning the filling factor toward plateau transitions or by considering smaller gaps, Joule heating becomes increasingly dominant, and transport is dominated by an Ohmic regime. Importantly, this crossover occurs continuously and does not depend on the excitation frequency up to 10 GHz, in contrast to the finding in the QAH insulator, where bulk conduction is enhanced at higher frequencies.

This finding provides a unifying framework to interpret the QAH breakdown results. The characteristic hopping energies $T_0 \simeq 17\,\mathrm{K}$ extracted for QAH devices are comparable to the smallest values of $k_{\mathrm{B}}T_0$ studied in graphene. In this regime, graphene already exhibits heating-dominated transport, which explains why QAH devices do not show a pronounced non-Ohmic regime and why electron heating provides a consistent description of both dc and rf breakdown. Within this framework, the apparent absence of a non-Ohmic regime in QAH systems is not a qualitative difference, but rather a consequence of operating in a parameter range where heating dominates. At smaller voltages or less disordered samples, there might be a regime dominated by the field-induced hopping.

A key difference between QAH devices and graphene emerges in the frequency dependence of rf-induced breakdown. In QAH systems, we observe a clear frequency dependence of the absorbed power, which we attribute to finite-size charge puddles in the bulk. At radio frequencies, these puddles act as lossy elements that absorb rf energy through capacitive coupling, leading to enhanced heating at higher frequencies. In graphene, by contrast, bulk states form extended, quasi-one-dimensional edge states around charge puddles. As a result, no intrinsic frequency dependence of the breakdown mechanism is observed in

graphene up to 10 GHz. This comparison highlights that the frequency dependence in QAH systems is not an inherent property of hopping transport itself, but rather a geometric and electrostatic effect associated with finite-size bulk inhomogeneities.

The unified picture of heating developed in this chapter also enables direct predictions of dc transport. While non-Ohmic hopping may contribute at very small currents in strongly localized regimes, transport becomes unavoidably dominated by Joule heating once the longitudinal resistance reaches values of a few hundred ohms. Beyond this point, the electronic temperature rises rapidly with applied power, and the transport is dominated by heating at finite bias voltages, irrespective of whether the excitation is dc or rf. This explains why dc breakdown measurements at finite bulk conductance often appear consistent with heating-based models [23, 114], while they appear consistent with non-Ohmic VRH at vanishing bulk conductance [20, 58].

Finally, these results have important implications for applications of QAH systems. The onset of dissipation under rf excitation sets an upper bound on the usable signal amplitude in the dissipationless regime. This bound decreases with increasing temperature and frequency, as both enhance electronic heating. Consequently, while QAH insulators are promising platforms for low-dissipation electronics and microwave devices, their operation is fundamentally constrained by heating-induced breakdown. This work highlights the importance of bulk inhomogeneity and thermalization and identifies safe operating regimes for lossless high-frequency quantum devices [15, 16].

Chapter 5

Single-electron sources in quantum dots

In this chapter, we explore the realization of a gate-defined single-electron source (SES) in bilayer graphene (BLG) and its characterization under radio-frequency (rf) excitation. The ability to control and manipulate individual electrons in solid-state systems is a central goal in modern condensed matter physics, as it enables the study of charge coherence, electron–electron interactions, and interference. A key requirement for such investigations is the controlled emission of individual electrons. Devices capable of releasing electrons in a periodic and well-defined manner are referred to as SESs. SESs enable the generation of quantized charge currents, opening the door to probing coherent charge propagation in mesoscopic circuits [27, 140–143]. Beyond metrological applications, SESs have enabled fundamental experiments in electron quantum optics. In particular, SESs allow two-particle interference measurements in quantum Hall systems, providing direct access to the quantum statistics of electrons [28]. More recently, similar techniques have been extended to the fractional quantum Hall regime, where SESs enabled the observation of anyonic exchange statistics [29, 144, 145]. BLG provides a promising platform for realizing such SESs. In contrast to conventional GaAs- or Si-based nanostructures, BLG combines high carrier mobility and long phase coherence lengths with electrostatic tunability [30, 32]. Its ambipolar nature allows a continuous transition between electron and hole transport within the same device [146], while the dual-gated (top and bottom gate) geometry enables local and independent control over both carrier density and band gap. Moreover, BLG can be integrated with superconducting contacts, enabling the fabrication of BLG–superconductor hybrid devices [147, 148]. Such structures provide a versatile platform for studying the interplay between superconducting proximity effects and charge, spin, and valley degrees of freedom. In contrast, conventional quantum Hall architectures rely on strong magnetic

fields, which constrain device design and hinder integration with superconducting components. As a result, BLG provides a flexible platform for exploring coherent charge dynamics and single-particle interference beyond the limitations of traditional quantum Hall systems.

5.1 Introduction to single-electron sources

The reliable operation of a SES is based on the following criteria. First, the emission must be on-demand, meaning that exactly one electron is emitted per drive cycle. Second, the process must be coherent. In this context, coherence implies that the phase of the emitted electron wave packet remains well-defined with respect to the periodic drive that triggers the emission. This phase stability is crucial because it allows emitted electrons to interfere with one another after propagation or with electrons emitted from another synchronized source, enabling quantum interference experiments and the study of decoherence in mesoscopic circuits. Finally, the source should exhibit quantized operation, i.e., the emitted charge per cycle should remain robust against small variations in the drive parameters. Fulfilling these conditions requires a clean, tunable conductor with well-controlled tunnel barriers, a discrete level spectrum, and compatibility with high-frequency excitation.

To meet these requirements, several architectures for SESs have been developed. The most established ones are **single-electron pumps and turnstiles**, where quantized charge transfer is achieved through the cyclic modulation of tunnel barriers in semiconductor nanostructures [140–142, 149, 150]. These devices operate in the GHz regime and achieve high current quantization accuracy but do not allow precise control over the energy of the emitted electrons [151].

A second approach is based on the generation of **Levitons**, single-electron excitations created by Lorentzian voltage pulses applied to a coherent conductor with repetition rates in the GHz regime [143, 152]. These excitations propagate ballistically and coherently, making them suitable for electron-interference experiments. However, the absence of discrete confinement requires a precisely shaped Lorentzian pulse, which is experimentally challenging to generate due to signal distortions at GHz frequencies.

Another well-established realization is the **mesoscopic capacitor** [27, 153]. It consists of a quantum dot tunnel-coupled to a coherent conductor—typically a two-dimensional electron gas (2DEG) in the quantum Hall regime—and is driven by a high-frequency gate voltage. A quantum dot is a small, gate-defined

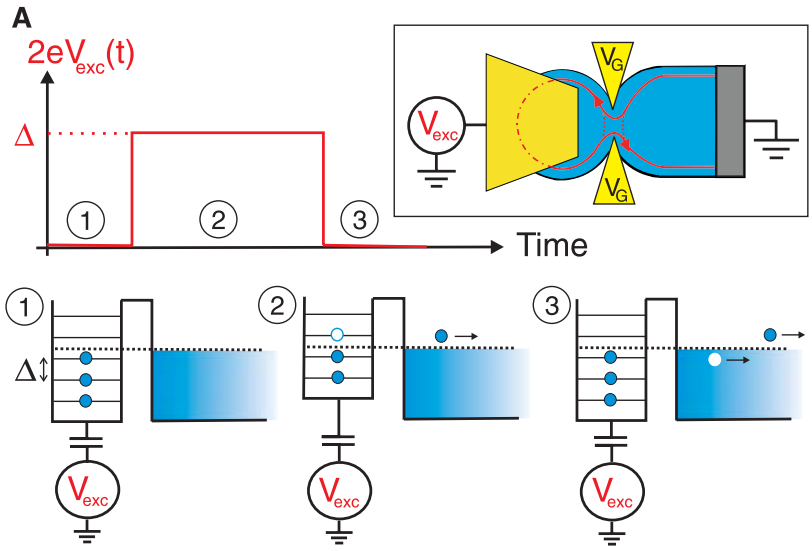

Figure 5.1: Single-electron emitter in a quantum Hall insulator. Top: time trace of the radio-frequency voltage U_{rf} (here V_{exc}) and sketch of the device geometry. The 2DEG is shown in blue, and the edge states are shown in red. The dot occupation is tuned by the excitation voltage U_{rf} and the barrier transparency by the plunger gate voltage U_{fg} (here V_{g}). Bottom: cycle of electron emission—1. initialization, 2. emission of an electron, 3. emission of a hole. Reproduced from Fève *et al.* [27] with permission from AAAS.

confinement region that traps electrons in discrete energy levels, allowing precise control over their charge occupation. During each excitation cycle, the dot alternately emits and reabsorbs a single electron, resulting in a quantized alternating current $I_{\mathrm{rf}} = 2ef$. While this architecture enables highly coherent emission along quantum Hall edge states, it requires large magnetic fields and offers limited independent control over the tunnel barriers and the dot potential (sweeping the tunnel barriers changes the dot potential and vice versa). These constraints motivate the search for alternative material platforms that allow full electrostatic tunability of the confinement potential and barrier transparency.

5.1.1 Mesoscopic capacitors

In this work, we use the concept of a driven mesoscopic capacitor to realize an SES in BLG. The idea of a mesoscopic capacitor was first proposed by Büttiker *et al.* [153] and later implemented by Fève *et al.* [27] to realize an on-demand SES. The working principle is shown in Fig. 5.1. The source consists of a quantum dot coupled to a quantum conductor via a tunnel barrier. The dot occupation is controlled by the excitation voltage U_{rf}, while the tunneling rate is determined by the potential of the plunger gate U_{fg}.

To realize the transmission of a single electron, the dot is first initialized by setting the Fermi level to a position between two discrete energy levels with an energy gap Δ. Subsequently, the Fermi level is raised by applying a voltage pulse of amplitude ΔU_{rf}, moving the upper energy level above the Fermi level. The electron occupying this level escapes the dot with a characteristic time $\tau \simeq h/(D\Delta)$, where D is the barrier transparency and Δ/h is the escape attempt frequency. Finally, the Fermi level is restored to its initial value, reoccupying the energy level and leaving a hole in the Fermi sea behind. Although single-electron detection is not possible directly, repeating this cycle at GHz rates yields an alternating current $I_{\mathrm{rf}} = 2ef$, corresponding to $I_{\mathrm{rf}} \approx f \cdot 320\,\mathrm{pA/GHz}$, which is within the measurement range. In the work of Fève *et al.*, the quantum dot was realized in a GaAs 2DEG in the quantum Hall regime, where the natural 1D confinement of edge states allows micron-sized dots to exhibit discrete energy levels.

The energy and coherence of the emitted charge carriers depend on the waveform of the excitation signal $U_{\mathrm{rf}}(t)$. A square-wave excitation allows tuning of the emission energy by varying the amplitude U_{rf}, whereas a sinusoidal drive emits low-energy carriers as long as the tunneling time is short compared to the drive period [154].

To demonstrate quantized single-electron emission, one typically maps the pumped current as a function of the plunger gate voltage and the excitation amplitude, as shown in Fig. 5.2a. Plateaus at integer multiples of $I_{\mathrm{rf}} = 2ef$ serve as the hallmark of quantized emission. The simulated quantization map in Fig. 5.2a reproduces the expected behavior of a SES driven by a sinusoidal modulation. The color scale represents the normalized ac current $I_{\mathrm{rf}}/(2ef)$ as a function of the plunger gate voltage U_{fg} and the excitation amplitude U_{rf} (corresponding to V_{exc} in Fig. 5.1).

When the Fermi level is aligned with a dot level (e.g., $U_{\mathrm{dc}} = 0$ in Fig. 5.2a and the excitation amplitude is small, the dot level oscillates only weakly around the Fermi energy, and no quantized emission occurs. As U_{rf} increases, the dot level is driven above and below the Fermi energy during each cycle. This results in the sequential emission of one electron and one hole per period, yielding a quantized current of $2ef$. The corresponding plateau forms a horizontal band of constant I_{rf}, and its width in plunger gate voltage grows with increasing drive amplitude, producing the characteristic diamond-shaped structure. At even larger excitation amplitudes, the modulation becomes strong enough for two discrete dot levels to cross the Fermi energy in each cycle. In this regime, two

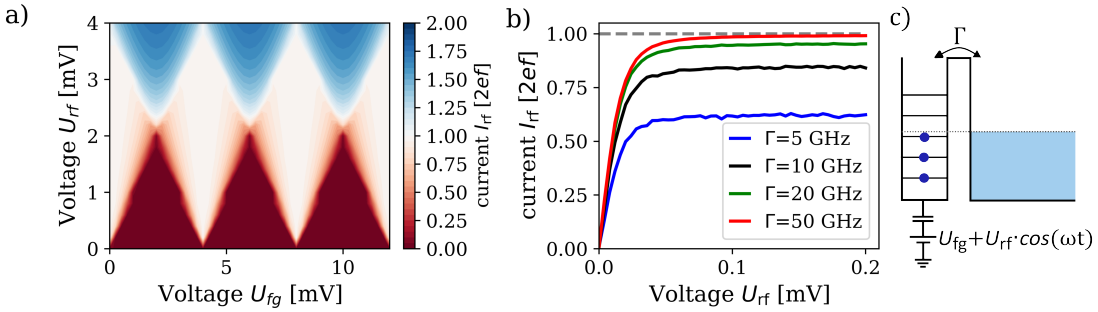

Figure 5.2: Simulated quantization map and dependence on tunneling rate. (a) Normalized ac current $I_{\mathrm{rf}}/(2ef)$ as a function of plunger gate voltage U_{fg} and excitation amplitude $U_{\mathrm{rf}}\cos(\omega t)$. The simulation reproduces the expected quantization plateaus at integer multiples of $I_{\mathrm{rf}} = 2ef$, corresponding to the emission of one electron and one hole per cycle. (b) Dependence of the normalized current on U_{rf} for different tunneling rates Γ at $T = 100\,\mathrm{mK}$ and $\omega/(2\pi) = 1\,\mathrm{GHz}$. Quantization is achieved for $\Gamma \gtrsim 50\,\mathrm{GHz}$, when the tunneling time becomes short compared to the drive period. The Monte Carlo simulation is described in detail in Appendix D. (c) Schematic illustration of the dot configuration: The chemical potential of the dot is set by $U_{\mathrm{FG}} + U_{\mathrm{RF}} \cdot \cos(\omega t)$.

electrons and two holes are emitted per period, and the current map exhibits the next plateau at $I_{\mathrm{rf}} = 4ef$.

In Fig. 5.2b, the current is shown as a function of U_{rf} for several tunneling rates Γ. The onset and quality of the quantization plateaus depend strongly on Γ. As Γ increases, the barrier becomes sufficiently transparent to allow the charge to escape within one half-period, and the current saturates at the quantized value $I_{\mathrm{rf}} = 2ef$. The parameter choice of $\omega/(2\pi) = 1\,\mathrm{GHz}$, $\Gamma = 5$–$50\,\mathrm{GHz}$, and $T = 100\,\mathrm{mK}$ corresponds closely to the expected regime in our BLG devices, where both the achievable tunnel rates and the experimental temperature are of comparable magnitude. Therefore, the simulation provides a realistic reference for our measurements and defines the operational window in which quantized single-electron emission can be expected. The following section examines whether such features can be achieved in our BLG device.

5.2 Gate-defined quantum dots in bilayer graphene

Graphene is a two-dimensional material consisting of a single layer of carbon atoms arranged in a honeycomb lattice (Fig. 5.3a). Since its first isolation in 2004 [155], it has attracted considerable attention due to its exceptional electrical and mechanical properties. Charge carriers in graphene behave as massless Dirac fermions, resulting in high mobilities and ballistic transport over micron length scales [30, 32]. These characteristics make it a promising platform for

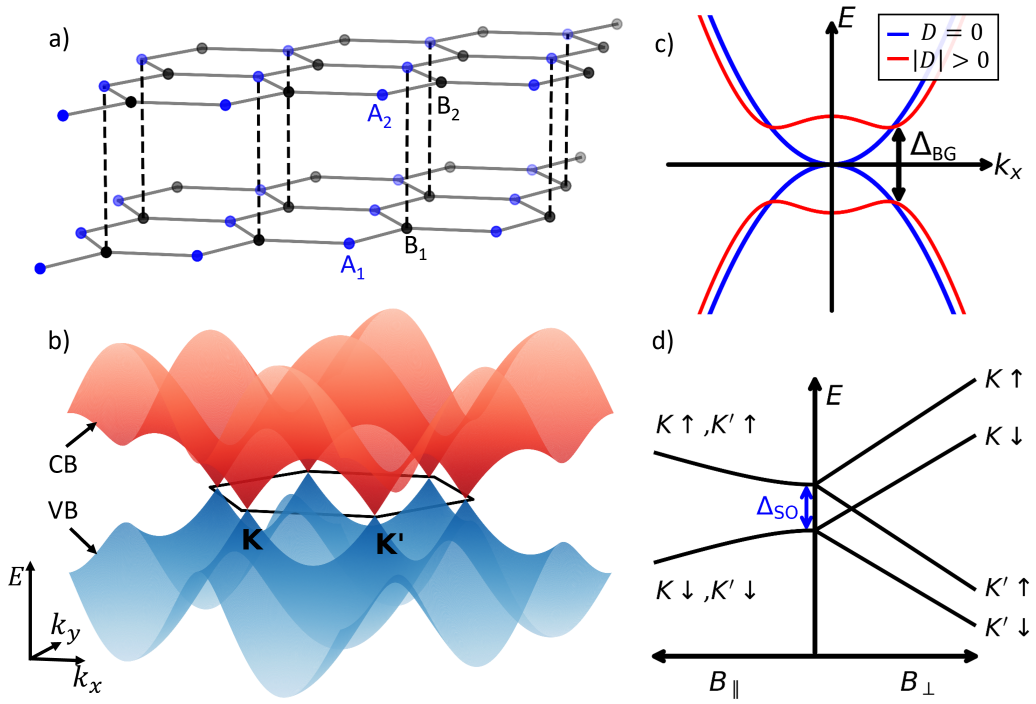

Figure 5.3: Electronic properties of Bilayer graphene a) The lattice structure of bilayer graphene consists of two monolayers with a honeycomb lattice. It shows an AB stacking, meaning that the A sublattice of the first layer aligns with the B sublattice of the second layer. b) Sketch of the first Brillouin zone for the valence (VB) and conduction band (CB). The band gap closes at the K and K' valleys, which are the symmetry points of the band structure. c) Zoom of the dispersion at the K/K' valley. Without an applied displacement field, the bands are gapless, as shown in blue. The red curve illustrates the opening of a band gap Δ_{BG} when a displacement field D is applied. d) Magnetic field dependence of a single particle energy spectrum. At zero field, the fourfold degeneracy is lifted due to a finite spin-orbit coupling Δ_{SO}. A parallel magnetic field only couples to the spin and does not lift the valley degeneracy. In contrast, a perpendicular magnetic field couples to both valley and spin, leading to four different slopes for the four states.

mesoscopic devices that rely on phase coherence and low disorder.

However, the linear band dispersion of monolayer graphene results in the absence of a band gap, which limits its suitability for electrostatic confinement and quantum-dot applications. BLG overcomes this limitation. It consists of two monolayers stacked in the AB configuration, where half of the atoms in the upper layer sit directly above those in the lower layer, as shown in Fig. 5.3a. At low energies, BLG exhibits parabolic band dispersion, and when a perpendicular displacement field is applied, inversion symmetry is broken, and a tunable band gap Δ_{BG} opens at the charge-neutrality point (shown in Fig. 5.3c) [156, 157]. The ability to induce and control this band gap electrostatically—while preserving high carrier mobility—enables the realization of gate-defined quantum dots without

relying on physical etching or magnetic confinement. This contrasts with QH mesoscopic capacitors, which require magnetic fields of several Tesla, exceeding the critical field of most superconductors. Additionally, graphene offers greater versatility, enabling control over the spin and valley of emitted electrons. This makes BLG an ideal platform to study, for example, Andreev reflections at the level of a single charge carrier.
Quantum dots in BLG are a well-established technology, mainly attracting attention due to the possibility to realize novel types of qubits, utilizing the spin or valley degree of freedom. [158–160]. However, they are so far operated in the dc to MHz-regime, which is not sufficient for engineering an SES, which typically requires GHz-control of the quantum dot.
In the following, we will introduce the concepts required to realize a SES in BLG. We begin with the low-energy electronic properties of BLG, focusing on the spin and valley degrees of freedom that determine the quantum dot spectrum, before describing the experimental implementation and transport characteristics of gate-defined quantum dots.

5.2.1 Electronic properties of bilayer graphene

At low energies, charge carriers in BLG reside near the two inequivalent valleys K and K' at the corners of the Brillouin zone. Each valley hosts states with spin $\uparrow, \downarrow$, resulting in a fourfold degeneracy that forms the basis of the low-energy spectrum [156, 161]. In the absence of external fields, the conduction and valence bands are approximately parabolic and symmetric around the charge-neutrality point. A perpendicular displacement field breaks the inversion symmetry between the two graphene layers by shifting their on-site energies. This layer asymmetry opens a band gap because the low-energy conduction and valence states are pushed to opposite layers and no longer remain degenerate. The gap grows with increasing electric field. This simultaneously induces a layer polarization of the low-energy states, leading to a finite Berry curvature of opposite sign at K and K' and magnetic moments perpendicular to the layer [156, 157]. As a consequence, electrons in the two valleys acquire opposite orbital magnetic moments, giving rise to the so-called valley Zeeman effect.
Because of this coupling, an external magnetic field interacts not only with the spin degree of freedom but also with the valley pseudospin. The valley Zeeman effect couples exclusively to the out-of-plane component of the magnetic field, while the spin Zeeman effect couples to both in-plane and out-of-plane fields. The resulting single-particle energy spectrum is illustrated in Fig. 5.3d. For an

in-plane magnetic field, only the spin degeneracy is lifted, leading to an energy splitting

$$\Delta E_{\uparrow,\downarrow} = \sqrt{\Delta_{\mathrm{SO}}^2 + (g_s \mu_B B_{\parallel})^2}, \tag{5.1}$$

where g_s is the spin g-factor, μ_B the Bohr magneton, and $\Delta_{\mathrm{SO}} \approx 40\text{–}80\,\mu\mathrm{eV}$ the intrinsic spin–orbit coupling energy [161–163]. In contrast, for a perpendicular magnetic field, both spin and valley degeneracies are lifted, resulting in four subbands ($K' \downarrow$, $K \downarrow$, $K' \uparrow$, $K \uparrow$) with approximate energy splitting

$$\Delta E_{K,K',\uparrow,\downarrow} \approx \pm g_s \mu_B B_{\perp} \pm g_v \mu_B B_{\perp}, \tag{5.2}$$

where g_v is the valley g-factor. Its magnitude depends on the confinement potential and can reach values as large as $g_v \approx 75$, more than an order of magnitude larger than the spin g-factor $g_s \approx 2$ [33, 34, 163]. Each subband therefore exhibits a different slope $\pm g_s \pm g_v$. The interplay of these spin and valley degrees of freedom governs the excitation spectrum and shell filling of gate-defined quantum dots in BLG [157, 162]. Having established the low-energy electronic structure and tunability of BLG, we now describe how electrostatic gating is used to define quantum dots within this system.

5.2.2 Quantum dot formation

As described above, a displacement field can be used to open a band gap in BLG. Experimentally, this is achieved by electrostatic gating, which allows tuning of both the Fermi level and the band gap simultaneously. In the following, we outline step by step how charge carriers are confined in a quantum dot. To apply a displacement field, the BLG is embedded in a capacitor formed by two electrodes separated from the BLG by an insulating layer (see Fig. 5.4). The field is generated by applying voltages of opposite signs to the top and bottom electrodes, resulting in a displacement field

$$D = \epsilon_{\mathrm{R}} \frac{U_{\mathrm{sg}} - U_{\mathrm{bg}}}{w}, \tag{5.3}$$

where ϵ_{R} is the dielectric constant of the insulator, w is its combined thickness, and $U_{\mathrm{sg}}/U_{\mathrm{bg}}$ are the applied voltages on the top and bottom gate. By splitting the top gate into two so-called split gates, separated by a narrow trench of approximately 100 nm, we can define a one-dimensional channel by tuning the Fermi level into the band gap beneath the split gates. The graphene region between the split gates will then be either in the conduction or valence band, depending on

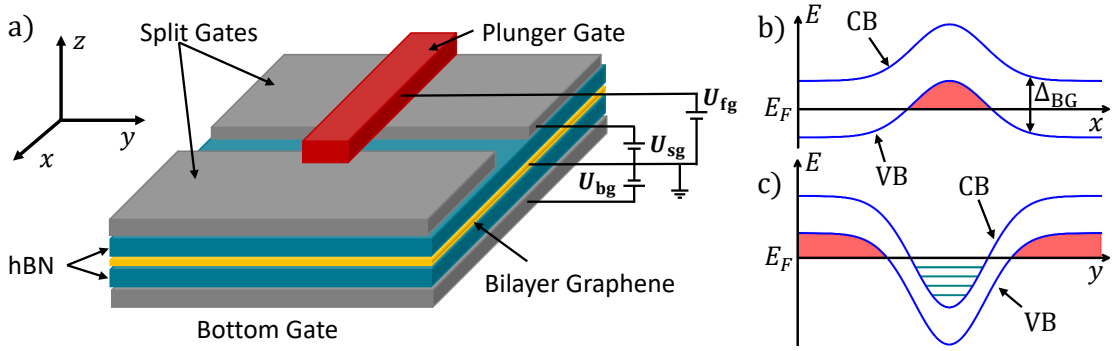

Figure 5.4: Quantum dot formation using electrostatic gating. a) Sketch of the device layout. The BLG (yellow) is sandwiched between gate insulators (hBN, blue). The bottom gate and the split gates (grey) confine the charge carrier into a one-dimensional channel. The corresponding band structure is shown in b): the Fermi level E_F lies within the band gap beneath the gates and in the valence band (VB) for negative back gate potentials. A plunger gate (red) locally pushes the Fermi level into the conduction band (CB). The corresponding band structure is shown in c). If the conducting region is sufficiently small, quantized energy levels (blue) form in the dot.

the polarity of the gate voltages (see Fig. 5.4b). This channel serves as the lead region of the quantum dot. To create a quantum dot along this channel, we locally modulate the Fermi level using narrow plunger gates (red in Fig. 5.4a), which are separated from the split gates by an additional thin insulating layer. For clarity, only one plunger gate is represented in Fig. 5.4a, but the real devices have several side by side. A key advantage of BLG is that it allows the formation of quantum dots with either the same or the opposite polarity as the leads. In the latter case, the Fermi level is locally tuned into the conduction band while the leads remain in the valence band, thereby forming tunnel barriers (sketched in Fig. 5.4c). If the confinement is sufficiently strong, discrete energy levels form in the dot, which can be charged on demand using the same plunger gate employed to define the dot. Alternatively, a dot can be defined using three neighboring plunger gates: the two outer gates create tunnel barriers by tuning the Fermi level into the band gap, while the central gate controls the dot potential and charges it with carriers of the same polarity as the leads.

Because all gates are capacitively coupled through the thin dielectric layers, tuning one gate voltage slightly affects the electrostatic potential of neighboring regions. This cross-talk necessitates careful compensation when forming a quantum dot.

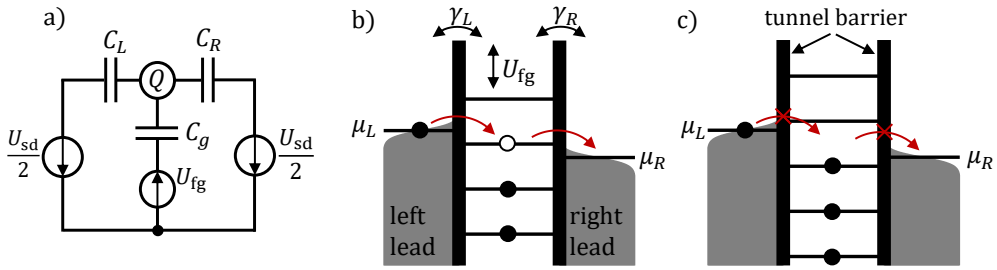

Figure 5.5: Transport in a quantum dot. a) Equivalent circuit: the quantum dot acts as an island of charge $Q = Ne$, capacitively coupled to source and drain electrodes ($C_{L,R}$) under a source–drain bias U_{sd}, and to a plunger gate (C_{g}) controlling its potential U_{fg}. b) Energy-level diagram: the dot states at chemical potential μ_{N} are tunnel-coupled to the leads ($\mu_{\mathrm{L,R}}$) with rates $\Gamma_{\mathrm{L,R}}$. c) Same as b) in the Coulomb blockade regime, where no energy level lies within the bias window.

5.2.3 Quantum dot transport: tunneling, resonances, and rate equations

Having described the electrostatic definition of a quantum dot, we now turn to the fundamental energy scales and transport mechanisms that govern charge transfer through it. We first introduce the relevant energy scales for charging and confinement before discussing Coulomb blockade, resonant tunneling, and their implications for high-frequency operation as an SES.

Quantum-dot energy scales

The quantum dot can be modeled as a charge island of charge $Q = Ne$, where N is the number of confined electrons. As shown in Fig. 5.5a, the quantum dot is capacitive coupled to a plunger gate (C_{g}) and to the source and drain via capacitance C_L and C_R, respectively. The total capacitance is $C_\Sigma = C_{\mathrm{L}} + C_{\mathrm{R}} + C_{\mathrm{g}}$. Adding an extra electron to the dot requires overcoming the Coulomb repulsion of the existing electrons. The corresponding **charging energy** is given by [1, 84]

$$E_C = \frac{e^2}{C_\Sigma}. \tag{5.4}$$

In addition, the finite confinement of the dot gives rise to discrete single-particle levels. In a circular quantum dot with a parabolic confinement potential, the energy of the N-th level is approximately [1]

$$E_{\mathrm{conf}}(N) = \frac{\hbar^2 \pi^2 N^2}{2m^* r^2}, \tag{5.5}$$

where m^* is the effective mass and r the dot radius. In BLG, the dispersion relation deviates from a simple parabolic form, and the precise single-particle spectrum $E_{\text{sp}}(N)$ must be determined numerically [164]. The chemical potential to occupy the N-th electron is therefore

$$\mu_{\text{N}} = NE_C + E_{\text{sp}}(N), \tag{5.6}$$

and the corresponding **addition energy** — the energy required to add one more electron — is

$$\Delta E_{\text{add}}(N) = \mu_{\text{N+1}} - \mu_{\text{N}} = E_{\text{C}} + \Delta E_{\text{sp}}, \tag{5.7}$$

with $\Delta E_{\text{sp}} = E_{\text{sp}}(N+1) - E_{\text{sp}}(N)$. For relatively large dots ($r \approx 100$ nm) or high occupancies, the charging energy typically exceeds the single-particle level spacing by an order of magnitude [1, 157]. Consequently, transport is dominated by Coulomb interactions, while the discrete spectrum plays a secondary role. The dot potential can be tuned via the plunger gate voltage U_{fg}, which shifts the chemical potential by $e\alpha_{\text{fg}}U_{\text{fg}}$, where $\alpha_{\text{fg}} = C_{\text{g}}/C_{\Sigma}$ is the lever arm.

Coulomb blockade

We now consider electron transport through the dot between source and drain. When a discrete energy level μ_{N} lies within the bias window, i.e., $\mu_{\text{L}} > \mu_{\text{N}} > \mu_{\text{R}}$ (Fig. 5.5b), electrons can tunnel sequentially from source to drain. This is called a **Coulomb resonance**. The resulting current depends on the tunnel couplings $\Gamma_{\text{L,R}}$, which determine the barrier transparency. If, however, no energy level lies within the bias window (Fig. 5.5c), the dot has a well-defined charge state and current flow is blocked. This regime is known as **Coulomb blockade**. At finite temperature, electrons in the leads occupy states according to the Fermi–Dirac distribution

$$f_{\text{L,R}} = \frac{1}{\exp\left(\frac{E-\mu_{\text{L,R}}}{k_B T}\right) + 1}. \tag{5.8}$$

Consequently, thermally excited carriers can occasionally overcome the blockade. To clearly resolve the Coulomb blockade, the thermal energy must satisfy $k_B T \ll E_C$. In our devices, with charging energies of $E_C = 2$–$10\,\text{meV}$, this corresponds to temperatures below 25–125 K, well above the experimental electron temperature of $T_e \approx 100\,\text{mK}$.

Transport equations

We now estimate the current through a quantum dot using a simple rate-equation approach. We consider a single spin- and valley-degenerate level at energy E (fourfold degeneracy) coupled to the source and drain electrodes via tunneling rates γ_{L} and γ_{R}. The level can be either empty ($N = 0$) or singly occupied ($N = 1$). If the level is occupied, an electron can tunnel out to one of the leads with a rate [165]

$$\Gamma_{1\to\mathrm{L,R}} = \gamma_{\mathrm{L,R}}(1 - f_{\mathrm{L,R}})\,, \tag{5.9}$$

where $f_{\mathrm{L,R}} = [\exp((E - \mu_{\mathrm{L,R}})/k_BT) + 1]^{-1}$ is the Fermi–Dirac distribution of the respective lead. Conversely, if the level is empty, it can be filled by an electron from the leads at a rate

$$\Gamma_{\mathrm{L,R}\to 0} = 4\,\gamma_{\mathrm{L,R}} f_{\mathrm{L,R}}, \tag{5.10}$$

where the prefactor 4 accounts for the fourfold spin and valley degeneracy of BLG. An electron (or hole) tunneling in can fill any of the four spin–valley states, while an electron tunneling out comes from a single state with defined spin and valley. The stationary occupation probability P_1 of the dot follows from balancing the tunneling rates into and out of the level, assuming a steady-state current ($\dot{P}_1 = 0$)

$$P_1 = \frac{\Gamma_{\mathrm{L}\to 0} + \Gamma_{\mathrm{R}\to 0}}{\Gamma_{\mathrm{L}\to 0} + \Gamma_{\mathrm{R}\to 0} + \Gamma_{1\to\mathrm{L}} + \Gamma_{1\to\mathrm{R}}} = \frac{4(\gamma_{\mathrm{L}} f_{\mathrm{L}} + \gamma_{\mathrm{R}} f_{\mathrm{R}})}{\gamma_{\mathrm{L}}(1 + 3f_{\mathrm{L}}) + \gamma_{\mathrm{R}}(1 + 3f_{\mathrm{R}})}. \tag{5.11}$$

The total current through the left barrier is then given by

$$I = |e|[\Gamma_{\mathrm{L}\to 0}(1 - P_1) - \Gamma_{1\to\mathrm{L}} P_1] = 4|e|\,\gamma_{\mathrm{L}}\left[f_{\mathrm{L}}(1 - P_1) - \tfrac{1}{4}(1 - f_{\mathrm{L}})P_1\right], \tag{5.12}$$

where the sign convention corresponds to current flowing from left to right. In the following, we calculate the current I through the dot in the case of a large bias U_{sd}, which is satisfied for $eU_{\mathrm{sd}} \gg k_BT$. In this limit, the Fermi functions can be approximated as step functions, meaning $f_{\mathrm{L}} = 1, f_{\mathrm{R}} = 0$ ($f_{\mathrm{L}} = 0, f_{\mathrm{R}} = 1$) for positive (negative) bias. The resulting currents I_+ and I_- are given by [165]

$$I_+ = 4|e|\,\frac{\gamma_{\mathrm{L}}\gamma_{\mathrm{R}}}{4\gamma_{\mathrm{R}} + \gamma_{\mathrm{L}}}, \qquad I_- = -4|e|\,\frac{\gamma_{\mathrm{L}}\gamma_{\mathrm{R}}}{\gamma_{\mathrm{R}} + 4\gamma_{\mathrm{L}}}. \tag{5.13}$$

The current is asymmetric under bias reversal, which originates from the combination of broken left–right symmetry ($\gamma_{\mathrm{L}} \neq \gamma_{\mathrm{R}}$) and the fourfold spin–valley degeneracy. Consequently, this allows us to determine the individual tunnel couplings from the height of the Coulomb resonances at positive and negative bias.

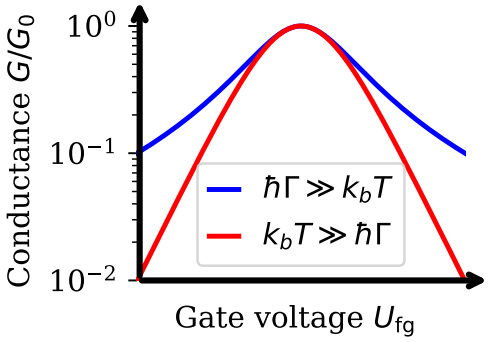

Figure 5.6: Broadening of Coulomb resonances. Differential conductance G/G_0 as a function of the plunger gate voltage U_{fg} for thermal broadening (red) and lifetime broadening (blue).

In this sequential-tunneling regime, the current is independent of the applied bias once $eU_{\mathrm{sd}} > k_BT,\ \hbar\Gamma$.
So far, we have only discussed the ideal case of a large bias and zero temperature. If we want to examine the source–drain current as a function of the plunger gate voltage U_{fg}, we need to take into account two processes: thermal broadening and tunnel (lifetime) broadening. The first originates from the thermal smearing of the Fermi distribution, while the second arises from the finite dwell time of electrons in the dot, which relaxes the resonance condition in the strongly coupled regime ($\hbar\Gamma > k_BT$). Depending on which process dominates, the shape of the Coulomb resonance differs, as illustrated in Fig. 5.6. In this work, we do not derive the full expressions and only give the resulting functional forms (see Ref. [1] for detailed derivations). The Coulomb resonance is dominated by tunnel broadening when $\hbar\Gamma \gg k_BT$, where $\Gamma = \Gamma_{\mathrm{L}}\Gamma_{\mathrm{R}}/(\Gamma_{\mathrm{L}} + \Gamma_{\mathrm{R}})$ is the combined tunneling rate (neglecting the degeneracy of the energy level). This leads to a Lorentzian-shaped resonance [166]

$$G(U_{\mathrm{fg}}) \propto \frac{(\hbar\Gamma)^2}{(\hbar\Gamma)^2 + [e\alpha(U_{\mathrm{fg}} - U^0_{\mathrm{fg}})]^2}, \tag{5.14}$$

where U^0_{fg} is the center of the resonance and α the gate lever arm. In contrast, for thermal broadening ($k_BT \gg \hbar\Gamma$), the conductance follows a $\cosh^{-2}$ dependence:

$$G(U_{\mathrm{fg}}) \propto \cosh^{-2}\left[\frac{e\alpha(U_{\mathrm{fg}} - U^0_{\mathrm{fg}})}{2k_BT}\right]. \tag{5.15}$$

When plotting both scenarios on a semi-logarithmic scale (see Fig. 5.6), the distinct line shapes allow one to determine the dominant broadening mechanism and to estimate either the combined tunneling rate Γ or the electronic temperature T.

5.3 Experimental realization of a quantum dot

We collaborate with the group of Prof. Dr. Christoph Stampfer at the RWTH Aachen, who is very experienced in the fabrication and characterization of BLG quantum dots. The devices measured in this work were fabricated by Hubert Dulisch and Katrin Hecker. Therefore, we will only briefly outline the final device layout and refer to the dissertations of Luca Banzerus and Samuel Möller for a more detailed description [166, 167].

5.3.1 Device layout and experimental setup

The samples are fabricated from a stack with the following order from bottom to top: Graphite-hBN-BLG-hBN. The hBN layer acts as a gate insulator and the graphite as a bottom electrode, as sketched in Fig. 5.4. The stack is on top of a Si-SiO_2 wafer. A microscope image of the stack before fabrication is shown in Fig. 5.7a. The same device after fabrication is shown in Fig. 5.7b and c. The fabrication includes the following steps:

1. Definition of four Ohmic contacts (red dots in Fig. 5.7b) by etching the top hBN and depositing a thin Cr/Au layer directly on top of the BLG. These contacts allow for a dc characterization of the source-drain conductance. The broad contacts are used for the detection of the rf current.

2. Deposition of split gates (highlighted gray in Fig. 5.7b) using a lift-off process (Cr/Au evaporation). They define the quasi-1D channel.

3. After the deposition of a global Al_2O_3 layer, the finger gates (green dots in Fig. 5.7b) are defined using Cr/Au evaporation. These will be used as a plunger gate to form a quantum dot.

4. Repetition of the third step defines the piano gates, which are placed between the previously defined finger gates and can be used to tune the barrier. Piano gates act analogously to the finger gates, but defining them in a separate step allows for a smaller distance to the neighboring gate

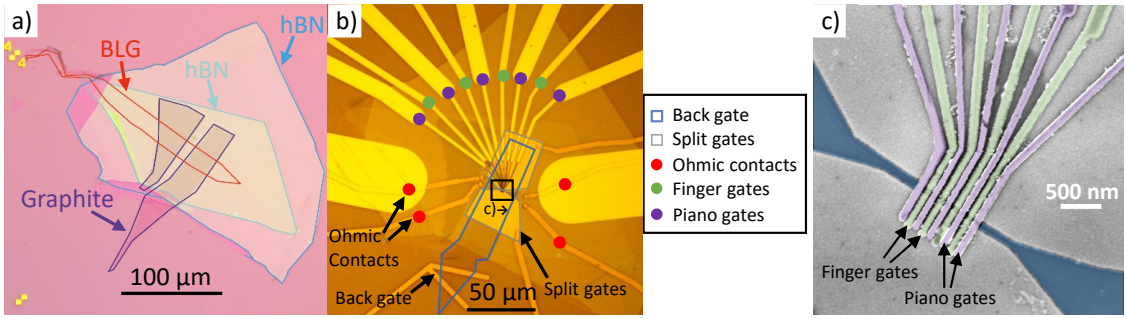

Figure 5.7: Layout of Sample. a) Microscope image of a stack before fabrication. Bottom-Top: Graphite-hBN-BLG-hBN. b) Microscope image of the same stack as in a) after fabrication. The contacts are labeled in the legend. Each side of the BLG has two Ohmic contacts, a narrow one for dc characterization and a broad one for the detection of the rf current. c) An SEM image (corresponding to the black rectangle shown in b) of the sample. The conducting area is highlighted in blue, the finger gates in green, and the piano gates in violet.

($< 10\,\mathrm{nm}$) compared to writing them in a single lithographic step ($> 50\,\mathrm{nm}$), which leads to better control of the barriers, with the drawback of having a smaller lever arm (due to the additional Al_2O_3 layer).

Fig. 5.7c shows a SEM image of the finger and piano gates on top of the channel. The channel has a width of approximately $110\,\mathrm{nm}$ and a length of approximately $2\,\mu\mathrm{m}$. Both the finger gates (highlighted in green in Fig. 5.7c) and the piano gates (highlighted in violet in Fig. 5.7c) have a width of approximately $90\,\mathrm{nm}$ and there is a gap of approximately $15\,\mathrm{nm}$ between neighboring gates. However, the finger gates are closer to the BLG and therefore have a bigger lever arm α compared to the piano gates. Therefore, we aim at defining the quantum dot below the finger gates, while using the piano gates to tune the barrier transparency (and hence the tunneling rates γ_L and γ_R).

To conduct transport experiments, the sample is loaded onto a cryostat and cooled down to $T \simeq 20\,\mathrm{mK}$. Therefore, we glue the silicon wafer (with the quantum dot device on it) into a printed circuit board (PCB) as shown in Fig. 5.8a. We are using a commercial PCB from the company QDevil, which has been modified to fit a $7 \times 7\,\mathrm{mm}^2$ sample. The modified PCB is equipped with 3 high-frequency channels for rf measurements and 36 dc and ground lines. The rf and dc channels are connected to the sample using wire bonds (see Fig. 5.8b). To ensure rf compatibility of the signal lines on the sample, we design them in a co-planar waveguide layout. The entire electrical circuit is sketched in Fig. 5.8c. We will first discuss the dc setup and then later discuss the rf setup (shown in orange in Fig. 5.8c). All dc voltages are supplied by a low-noise digital-to-analog converter and connected via filtered lines to the circuit board. The bias voltage

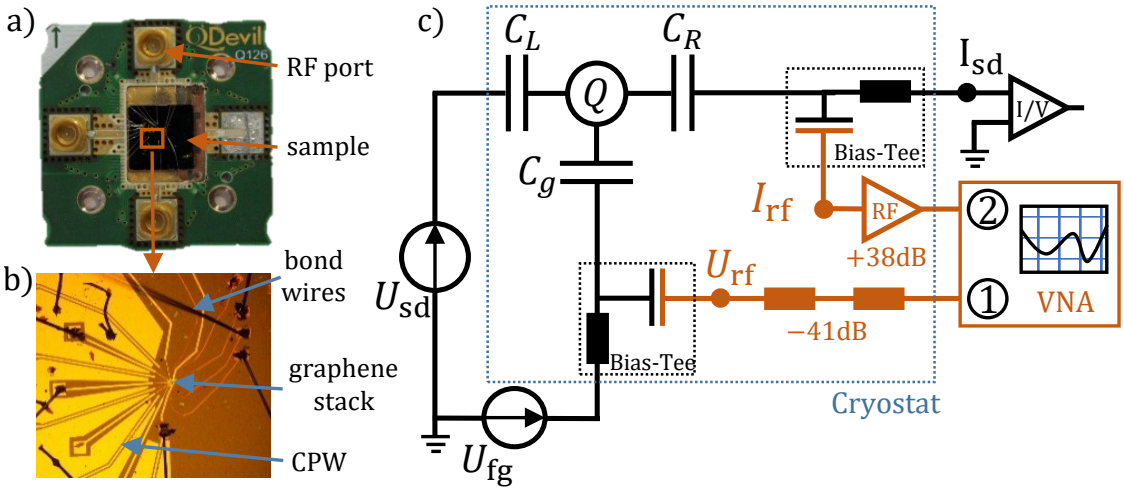

Figure 5.8: Experimental setup. a) Printed circuit board with a sample glued in the center, which is connected via bond wires. b) Zoom of the sample showing the circuitry of the sample itself. c) Electrical setup: The dc voltages $U_{\mathrm{sd}}, U_{\mathrm{fg}}$ are supplied by a Basel Instruments DAC SP1060 and cryogenic filtering. The source-drain current I_{sd} is measured using a trans-impedance amplifier (Basel Instruments SP983c). The rf setup (shown in orange) consists of a Keysight VNA P9375A, which measures the transmission coefficient S_{21}. The excitation signal is thermalised via an attenuator and coupled to the plunger gate via a bias-tee. The rf current in the right lead is isolated by a bias tee and amplified by a cryogenic low-noise amplifier (LNF-LNC0.3_14A).

U_{sd} is usually modulated with a 7 Hz and 100 µV sine signal for lock-in detection. The source-drain current is then amplified using a trans-impedance amplifier with a gain of usually 1×10^6 V/A and detected by a lock-in amplifier. Thanks to careful grounding and filtering, we can reduce the noise floor to below 10 pA, sufficient to resolve the single electron current of approx. 320 pA/GHz. It is also crucial to isolate the dc setup from the rf setup to avoid ground loops inducing noise into the circuit. Therefore, the device is capacitively coupled via a bias-tee to the VNA. Similarly, the ground is capacitively coupled by adding an inner-outer dc block.

The rf measurements are performed by a VNA. The output of the VNA provides a continuous wave signal of variable microwave power $P_{\mathrm{out}} = U_{\mathrm{out}}^2/Z_0$ ($Z_0 = 50\,\Omega$) and frequency f. This signal is guided via a broadband coaxial cable to the plunger gate, where it modulates the quantum dot's chemical potential. Since we aim to realize alternating emission of single electrons followed by single holes, we create a current with a zero dc component. Hence, we detect the current at the same frequency f as the plunger gate modulation. Therefore, we amplify the current in the lead using a cryogenic low-noise amplifier with a gain of +38 dB. The amplified signal is then guided via coaxial cable to the input of the VNA,

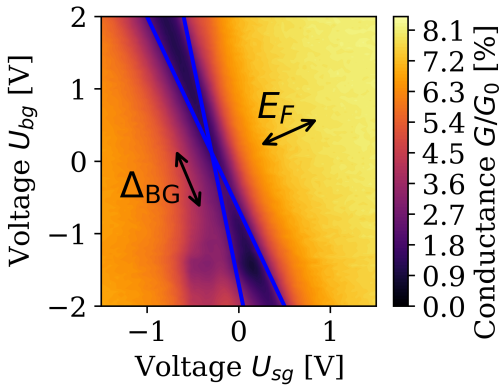

Figure 5.9: Opening a band gap. The normalized conductance G/G_0 is shown as a function of the applied back gate voltage U_{bg} and split gate voltage U_{sg}, for $U_{\mathrm{sd}} = 200\,\mu\mathrm{V}$ and $T \simeq 20\,\mathrm{mK}$. The dark region shows the quasi-1D conduction regime, along which the band gap Δ_{BG} varies. The Fermi level E_{F} is tuned orthogonal to it.

yielding the complex scattering parameter $S_{21} = U_2/U_1$. However, the scattering parameter captures the distortions and phase shifts of the entire setup and must be calibrated, as shown in Sec. 5.4.1.

5.3.2 Electrostatic formation of quantum dot

After cooling down the sample, we first test the functionality of the quantum dot device. Therefore, we first ensure that we are Ohmically connected to the source and drain contacts by measuring I_{sd} as a function of U_{sd}, which should show a linear dependence and a resistance of a few kΩ when all other gates are grounded. Afterwards, the functionality of each gate is tested. They should show no leakage current up to their breakdown voltage. After testing all contacts, we can first open a band gap and form a conduction channel between the leads. Therefore, we measure the dc source-drain conductance G while tuning the back gate voltage U_{bg} and the split gate voltage U_{sg} (both split gates are at the same potential). A 2D color map of this measurement is shown in Fig. 5.9. The blue lines highlight the quasi-1D conduction regime. The channel is n-doped for positive back gate voltages and negative split gate voltages, and consequently p-doped for the opposite polarities. The size of the band gap is increasing with increasing displacement field D, which can be seen by a widening of the dark region in Fig. 5.9. Furthermore, we observe that the lever arm of the split gates α_{sg} is stronger than that of the back gate α_{bg}. We can find the exact ratio from the slope of the channel $\alpha_{\mathrm{sg}}/\alpha_{\mathrm{bg}} \approx 4$. The split gates have a larger lever arm, because the top hBN ($d \approx 11\,\mathrm{nm}$) is thinner compared to the bottom hBN ($d \approx 42\,\mathrm{nm}$).

After realizing a one-dimensional (1D) channel, we can use one of the finger

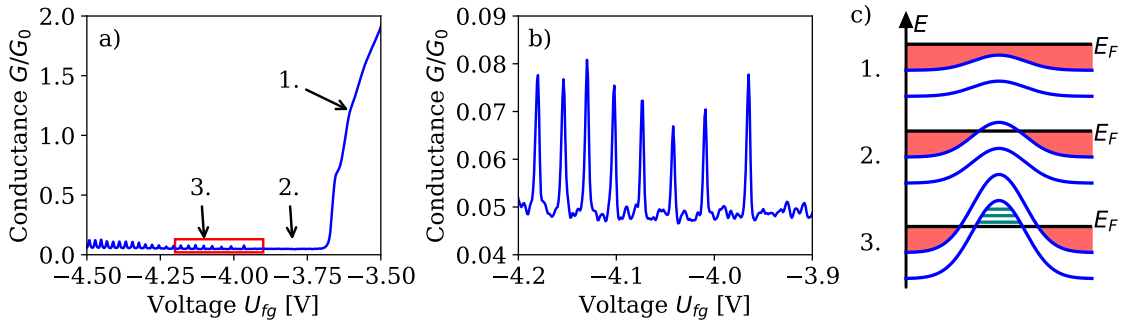

Figure 5.10: Coulomb resonances in a graphene quantum dot. a) Normalized differential conductance G/G_0 as a function of gate voltage U_{fg}. The three main transport regimes are marked by arrows: (1) Open dot regime, (2) Pinch-off regime, and (3) Few-electron (Coulomb blockade) regime, each illustrated schematically in c). b) Zoom-in of the Coulomb resonances (highlighted by the red rectangle in a), revealing discrete conductance peaks due to quantized charging. c) Schematic band diagrams corresponding to the three regimes in a): In regime (1), the Fermi level lies above the confinement barrier, allowing free transmission. In regime (2), the Fermi level aligns with the barrier, suppressing conductance. In regime (3), the discrete energy levels in the dot lead to Coulomb blockade and resonant tunneling. The measurements were performed at the following voltages of $U_{\mathrm{sd}} = 200\,\mu\mathrm{V}$, $U_{\mathrm{bg}} = 5.75\,\mathrm{V}$ and $U_{\mathrm{sg}} = -1.70\,\mathrm{V}$.

gates to locally define a quantum dot, as shown in Fig. 5.10 for an n-doped channel. By applying a negative voltage to a finger gate, we locally hole-dope the system, leading to a decrease in conductance (region 1 in Fig. 5.10a). In the following, we will refer to a plunger gate when describing the finger gate to align with the convention within the quantum dot community. At approximately $U_{\mathrm{fg}} = -3.75\,\mathrm{V}$, the conductance G nearly vanishes, indicating that the Fermi level beneath the plunger gate lies within the band gap, as sketched in Fig. 5.10c. In this device, the conductance did not fully drop to zero but saturated at a residual value of about 5% of G_0, likely caused by leakage currents below the split gates [168]. Increasing the displacement field D can suppress this residual current.

Further decreasing U_{fg} locally overcompensates the carrier density, forming a p-doped island within the n-doped channel, as illustrated in Fig. 5.10c. The emergence of this p-type quantum dot is marked by the appearance of discrete conductance peaks (Fig. 5.10b), corresponding to Coulomb resonances as discussed earlier. In this configuration, the tunnel barriers are p–n junctions, meaning that the barrier height—and hence the coupling to the leads—is governed primarily by the induced band gap. Consequently, there exists a "sweet spot" in the displacement field D that minimizes leakage currents while maintaining sufficient coupling to the leads. For our device, we find an optimal range of $U_{\mathrm{bg}} = 5.75\,\mathrm{V}$

to 6.75 V and $U_{\mathrm{sg}} = -1.7\,\mathrm{V}$ to $-2.2\,\mathrm{V}$.
Each conductance peak corresponds to the addition of one charge carrier to the quantum dot. This allows us to count the number of confined charges: starting from pinch-off at $U_{\mathrm{fg}} = -3.75\,\mathrm{V}$ (where $N = 0$), the dot is filled with N holes after observing N successive peaks at lower voltages. This charge quantization is crucial for realizing an SES, where the goal is to periodically modulate the Fermi level to emit one carrier per cycle. From the height of the Coulomb resonance $I_{\mathrm{sd}} \approx 200\,\mathrm{pA}$ (after subtracting the background), we can estimate the combined tunneling rate $\Gamma_L\Gamma_R/(\Gamma_L + \Gamma_R) \approx 1.2\,\mathrm{GHz}$. In comparison to our simulation in Fig. 5.2, the tunneling is still too low to reach single-electron emission ($\Gamma \gtrsim 20\,\mathrm{GHz}$). In principle, the neighboring piano gates allow tuning the barrier and further increase the tunneling rate. To gain deeper insight into the transport mechanism and extract the relevant energy scales of the quantum dot, we now present bias spectroscopy measurements.

5.3.3 Bias spectroscopy

To probe the energy scales of the quantum dot, we measure the differential conductance $G = dI_{\mathrm{sd}}/dU_{\mathrm{sd}}$ as a function of the dc bias voltage U_{sd} and the plunger gate voltage U_{fg}. A small ac modulation of $200\,\mu\mathrm{V}$ at a frequency of $7\,\mathrm{Hz}$ is added to the dc bias, and the resulting ac current is detected using lock-in techniques. Figure 5.11a shows the normalized differential conductance G/G_0 as a function of U_{sd} and U_{fg} for a back gate voltage of $U_{\mathrm{bg}} = 6.75\,\mathrm{V}$ and a split gate voltage $U_{\mathrm{sg}} = -2.2\,\mathrm{V}$). The background conductance, defined as $G(U_{\mathrm{sd}})$ at $U_{\mathrm{fg}} = -4.65\,\mathrm{V}$, has been subtracted for clarity.
At zero dc bias, we observe a series of Coulomb resonances, which split into two branches as $|U_{\mathrm{sd}}|$ increases. This behavior can be understood from the schematic in Fig. 5.11b: increasing U_{sd} shifts the electrochemical potentials of the source and drain, thereby enlarging the range of gate voltages U_{fg} for which resonant tunneling through the dot is energetically allowed. Since we measure the differential conductance, only the edges of this transport window are visible, forming the characteristic diamond-shaped regions of suppressed conductance [34, 168, 169].
When the bias voltage equals the addition energy E_{add}, the transport gap closes and current can always flow through the dot. The corresponding closure of the diamonds (marked by red arrows in Fig. 5.11a) defines E_{add}. In this device, we find addition energies ranging from approximately $10\,\mathrm{meV}$ for the first hole down to $3\,\mathrm{meV}$ for $N = 10$ holes. From the slope of the diamond edges, $dU_{\mathrm{sd}}/dU_{\mathrm{fg}}$,

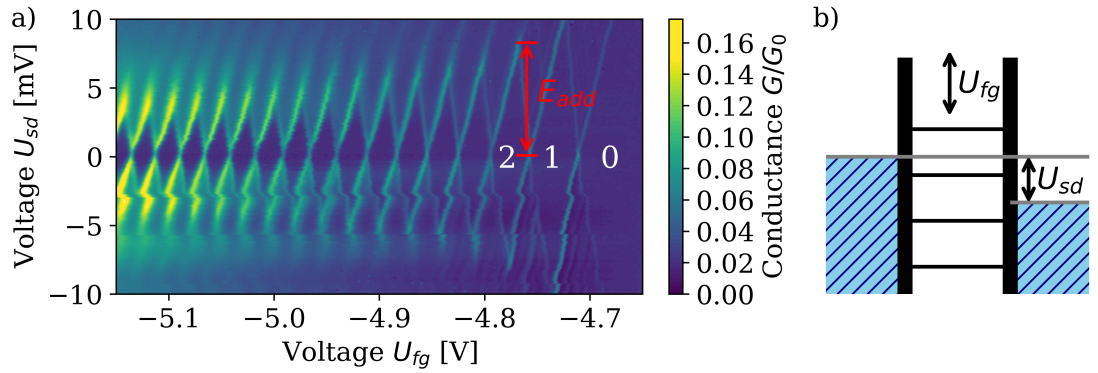

Figure 5.11: Bias spectroscopy of a quantum dot. a) Color plot of the norm. differential conductance G/G_0 as a function of gate voltage U_{fg} and bias voltage U_{sd}, for $U_{\mathrm{bg}} = 6.75\,\mathrm{V}$ and $U_{\mathrm{sg}} = -2.2\,\mathrm{V}$. The adding energy E_{add} is shown as a red arrow. We subtract the background, defined as $G(U_{\mathrm{sd}})$ at $U_{\mathrm{fg}} = -4.65\,\mathrm{V}$. b) Illustration of dot configuration: The bias voltage U_{sd} tunes the potential difference between the leads, while the gate voltage U_{fg} changes the occupation of the dot.

we extract the gate lever arm $\alpha_{\mathrm{fg}} \approx 400\,\mathrm{meV/V}$. The absolute magnitude and scaling of E_{add} indicate that the charging energy dominates over the confinement energy as discussed in Sec. 5.2.3. This is consistent with the observed smooth decrease of E_{add} with increasing occupation number, as expected when the confinement energy contributes only a small correction to the total addition energy. The Coulomb diamonds exhibit a slight asymmetry in their slopes with respect to positive and negative bias, reflecting different coupling strengths to the source and drain leads [31]. In the capacitor model (schematically shown in Fig. 5.8c), the diamond slopes are given by $dU_{\mathrm{sd}}/dU_{\mathrm{fg}} = \pm C_{\mathrm{fg}}/C_{S,D}$ [1]. Hence, an unequal capacitance ratio $C_S \neq C_D$ leads to different slopes and asymmetric diamonds. Such asymmetry typically arises from small geometrical or electrostatic variations of the tunnel barriers and is commonly observed in gate-defined quantum dots. From the slopes observed in Fig. 5.11, we estimate a capacitance ratio of $C_S/C_D \approx 2.7$, indicating that the left lead is more strongly coupled. This is consistent with the asymmetry in the height of the Coulomb resonances for positive and negative bias [31, 165].

For negative bias voltages, the Coulomb resonances show small horizontal shifts along U_{fg}, which we attribute to slow charge rearrangements in the local environment of the dot, likely due to charge traps in the dielectric or beneath the split gates. Bias spectroscopy provides direct access to the quantum dot's energy scales, which is crucial for tuning the dot into the regime suitable for dynamic operation as an SES.

5.4 RF-driven single-electron emission

The goal of this experiment is to realize an on-demand SES based on rf manipulation of a quantum dot, where the emission of an individual electron can be triggered with sub-nanosecond precision. Achieving this requires the ability to modulate the dot occupation at frequencies in the GHz regime.
To develop a detailed understanding of the dot dynamics under high-frequency driving, we begin with a simpler case: continuous-wave modulation at a single frequency. This approach offers two key advantages. First, it allows us to disentangle the response of the quantum dot from parasitic or stray signals in the rf circuitry. Second, by working with a well-defined periodic excitation, we can measure the phase-resolved current with respect to the modulation signal, enabling us to access the delay between the emitted current and the modulation signal. Before discussing the results of our rf experiments, we will discuss the calibration of the amplitude and phase.

5.4.1 Calibration of the radio frequency setup

The rf measurements are performed using a vector network analyzer that applies a microwave signal with adjustable output power P_{out} and frequency f and measures the transmitted signal. From the ratio of detected voltage U_2 and emitted voltage U_1, the complex scattering parameter $S_{21} = U_2/U_1$ is obtained. This quantity characterizes the microwave circuit but does not directly provide the transport parameters of interest. Instead, in analogy to dc measurements, we aim to determine the rf voltage at the plunger gate U_{rf} (c.f. U_{fg} in dc) and the rf current flowing into the leads I_{rf} (c.f. U_{sd} in dc).
The voltage at the plunger gate is obtained from the known attenuation of the input line. At $f = 1\,\mathrm{GHz}$ the total attenuation is approximately –21 dB. Converting the applied power from dBm to SI units requires subtracting 30 dB. The rf voltage at the gate is therefore estimated as

$$U_{\mathrm{rf}} \approx \sqrt{Z_0 \cdot 10^{\frac{P_{\mathrm{dBm}}-21-30}{10}}} \tag{5.16}$$

with $Z_0 = 50\,\Omega$. Estimating I_{rf} is more challenging due to the impedance mismatch between the graphene lead and the transmission line. The lead impedance can be approximated by $Z_{\mathrm{lead}} \approx R_{\mathrm{K}} \simeq 25.8\,\mathrm{k}\Omega$, which is much larger than Z_0. Consequently, most of the microwave power is reflected. In this high impedance limit, the current transmission coefficient $S_{21} = 2Z_{\mathrm{lead}}/(Z_{\mathrm{lead}} + Z_0)$ approaches 2,

so the current at the device is approximately doubled. Assuming the reflected signal is attenuated in the output line, the transmitted power can be written as $P \approx 4 \cdot Z_0 \cdot I_{\mathrm{rf}}^2$.
The total gain of the outgoing line is approximately 35 dB. Correcting for this amplification yields the estimate

$$I_{\mathrm{rf}} \approx \frac{1}{2}\sqrt{10^{-35/10} \cdot \frac{P_{\mathrm{out}}}{Z_0}} \cdot S_{21}. \tag{5.17}$$

This calibration allows us to convert the measured scattering parameter into the physical quantities U_{rf} and I_{rf} used in the following sections.

5.4.2 AC modulation of quantum-dot occupation

As a first step toward a driven SES, we verify that the dot occupation can be modulated by applying a sinusoidal voltage $\sqrt{2} \cdot U_{\mathrm{rf}} \cdot \cos(2\pi f t)$ to the plunger gate. We investigate frequencies between 500 MHz and 2 GHz. In principle, such modulation is sufficient to produce a quantized alternating current: when the dot chemical potential is tuned to a Coulomb resonance, an oscillating potential periodically brings the level into and out of the bias window, thereby triggering alternating emission of electrons and holes. Two conditions must be satisfied for reproducible emission. First, the tunnel barriers must be asymmetric so that electrons and holes preferentially exit into the intended lead. Second, the tunneling rate to the intended lead must be large enough for the dot to empty and refill within a single drive period, i.e., the relevant tunneling rate $\gamma \simeq 1 - 10\,\mathrm{GHz}$ should satisfy $\gamma \gtrsim f$. If $\gamma \ll f$, the dot cannot follow the drive, and the emission probability per cycle is reduced. Previous pulsed-gate experiments on BLG used square pulses at a few MHz to extract relaxation times [170, 171]. Our target frequencies are two orders of magnitude higher and therefore probe a different regime. Experimentally, we start with a dc readout of the source–drain conductance while applying the rf modulation. A small bias $U_{\mathrm{sd}} = 100\,\mu\mathrm{V}$ (with a 7 Hz lock-in modulation) is applied, and the resulting current I_{sd} is recorded as a function of the static plunger gate voltage U_{fg} and the rf amplitude U_{rf}. The resulting differential conductance $G = dI_{\mathrm{sd}}/dU_{\mathrm{sd}}$ is shown in Fig. 5.12a for an excitation frequency of 750 MHz.
Qualitatively, the rf modulation transforms each static Coulomb resonance into a broadened feature whose envelope reflects the time τ that the driven level spends within the bias window during one period T as sketched in Fig. 5.12b-e. The bias window is defined by the source-drain bias voltage U_{sd}. For small U_{rf},

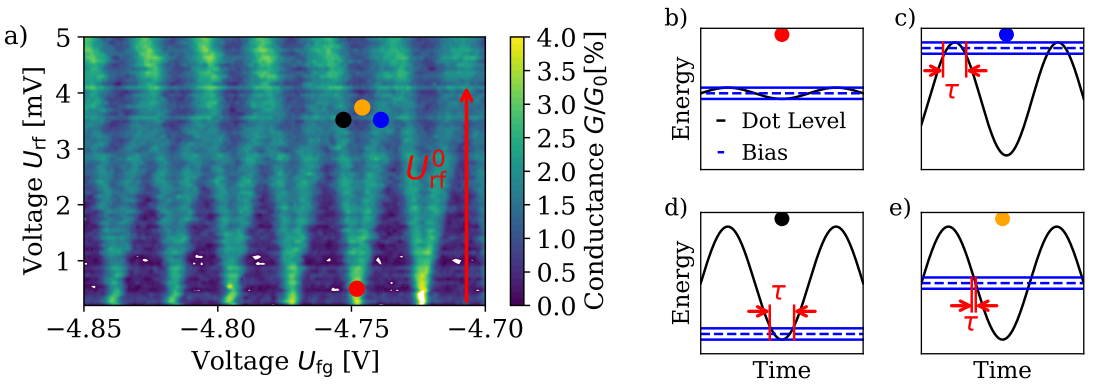

Figure 5.12: AC modulation of quantum dot occupation. (a) Normalized differential conductance G/G_0 as a function of plunger gate voltage U_{fg} and rf amplitude U_{rf}, measured at $U_{\mathrm{sd}} = 100\,\mu\mathrm{V}$, $U_{\mathrm{bg}} = 6.5\,\mathrm{V}$, $U_{\mathrm{sg}} = -2.4\,\mathrm{V}$, and $f = 750\,\mathrm{MHz}$. The background signal, measured in the Coulomb-blockade regime, has been subtracted. The colored dots mark four characteristic points corresponding to the schematics shown in (b-e). The red arrow indicates the rf amplitude U_{rf}^0 at which adjacent Coulomb resonances collide. (b-e) Schematic illustration of the time-dependent energy level under rf modulation in the presence of a finite bias. The four cases correspond to the positions marked in (a): (b) Small U_{rf}, energy level on resonance at equilibrium. (c) Large U_{rf}, resonance occurs during the positive voltage maximum. (d) Large U_{rf}, resonance occurs during the negative voltage minimum. (e) Large U_{rf}, equilibrium position on resonance.

the level remains inside the bias window for most of the cycle, and the conductance is maximal (see Fig. 5.12b). As U_{rf} increases, the fraction of the period during which the level lies in the window decreases, and the averaged conductance drops. When the rf amplitude exceeds the addition energy, the modulation can bring two different energy levels into the bias window during one cycle. In that regime, two transport channels contribute, and the conductance rises again. This explains the increase in conductance when two Coulomb resonances merge. The intuitive statement $G \propto \tau$ should be understood as follows. Let $T = 1/f$ be the drive period and τ the total time per period during which an energy level lies in the bias window (i.e., energetically aligned with the source–drain window). In the sequential-tunneling regime and for low temperature, the time-averaged conductance is approximately proportional to the duty cycle τ/T times the instantaneous (peak) conductance of the resonance,

$$G_{\mathrm{avg}} \simeq \frac{\tau}{T} G_{\mathrm{peak}}, \tag{5.18}$$

where G_{peak} is the conductance when the level resides in the bias window (itself set by the tunnel rates and temperature). This proportionality holds when (i)

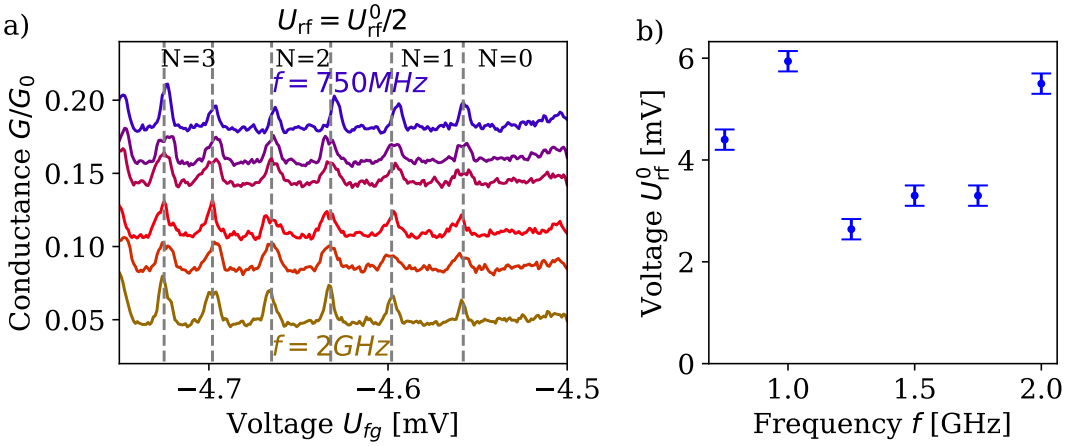

Figure 5.13: Frequency dependence of rf modulation. (a) Normalized conductance G/G_0 as a function of U_{fg} for $f = 0.75, 1.0, 1.25, 1.5, 1.75$ and 2 GHz, at $U_{\mathrm{rf}} = U^0_{\mathrm{rf}}/2$ (definition in Fig. 5.12a). The integer N indicates the equilibrium charge occupation of the dot at $U_{\mathrm{rf}} = 0$. (b) Extracted rf amplitude U^0_{rf} as a function of the drive frequency f for $U_{\mathrm{fg}} = -4.68$ V (where $N = 2$ and $N = 3$ are once per period in resonance). The frequency dependence reflects attenuation and impedance mismatch in the rf transmission line between the source and the device. Same $U_{\mathrm{bg}}, U_{sg}, U_{\mathrm{sd}}$ as in Fig. 5.12.

$\gamma \gg 1/T$ (so that tunneling is fast compared to the duration that the level spends in the window), and (ii) the level crossing is slow enough that the occupation reaches the quasi–steady-state value during the interval in the window. If $\gamma \lesssim f$, the dot cannot fully empty or fill during τ, and G_{avg} is reduced below this simple estimate. In the extreme limit $\gamma \ll f$, the response becomes strongly suppressed and frequency dependent.

Finally, note that the qualitative picture is largely independent of the exact drive frequency as long as the inequality $\gamma \gtrsim f$ holds. For the frequencies intended in this work ($\sim$ 500 MHz to 2 GHz), this condition determines whether the dot follows the drive adiabatically or not. In Fig. 5.13a, we show the frequency dependence of the ac modulation by presenting the conductance G as a function of the plunger gate voltage U_{fg} for frequencies between 750 MHz and 2 GHz. Furthermore, we tune the rf amplitude U_{rf} to half of U^0_{rf}, meaning that the dot chemical potential is modulated by half of the energy spacing to the adjacent energy level. We observe the same phenomenology across all excitation frequencies, indicating that the dot chemical potential can indeed follow the rf modulation adiabatically. The frequency dependence of U^0_{rf} is shown in Fig. 5.13b. The frequency dependence reflects the attenuation and impedance mismatch between the transmission lines and the device. It enables us to calibrate the rf amplitude, which is necessary to later tune the dot into a single-electron emission regime.

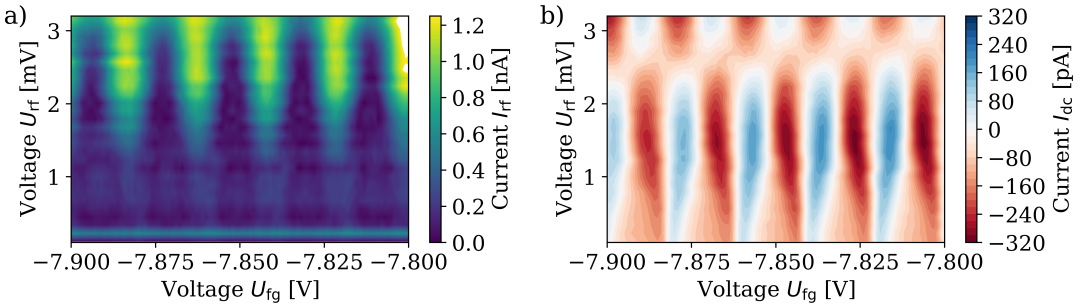

Figure 5.14: Emitted dc and ac current under ac modulation. a) Magnitude of the ac current I_{rf}, emitted in the right lead, as a function of the dc plunger gate voltage U_{fg} and the rf plunger gate voltage U_{rf} for $f = 1\,\mathrm{GHz}$. The background signal, defined at pinch-off, is subtracted. No dc bias is applied. b) The source-drain current I_{dc}, passing through the quantum dot while applying U_{rf} to the plunger gate, which is tuned to U_{fg} in equilibrium.

However, it also shows that any dc bias will generate an additional dc and rf current in this configuration of the quantum dot. In the following, we discuss the regime where no source–drain bias is applied to the quantum dot ($U_{\mathrm{sd}} = 0$) while an rf voltage U_{rf} is applied to the plunger gate. We simultaneously measure the dc source–drain current I_{dc} and the complex ac current I_{rf} at the right lead. Measuring on the right side is advantageous for two reasons. First, bias spectroscopy revealed that the dot couples more strongly to this lead, providing the asymmetry required for single-electron emission. Second, the capacitive cross-coupling between the plunger gate and the right lead is weaker due to their larger separation (see Fig. 5.7b). Figure 5.14a shows the magnitude of the emitted current I_{rf} in the right lead for a modulation frequency of $f = 1\,\mathrm{GHz}$. The background signal arising from direct capacitive coupling between the plunger gate and the lead has been subtracted. This background is estimated from the response measured in the Coulomb blockade regime ($N = 0$), where the dot remains empty. Ideally, we expect to observe half-diamond patterns of quantized current as shown in Fig. 5.2a. While faint diamond-like features are visible in Fig. 5.14a, the current within each diamond is not quantized. Instead, it increases gradually with U_{rf} and decreases with detuning from resonance $|\alpha U_{\mathrm{fg}} - \mu_{\mathrm{N}}|$. Furthermore, the measured current magnitude exceeds the expected quantized value of $2ef \approx 320\,\mathrm{pA}$. This deviation likely results from uncertainties in the amplitude calibration discussed in Sec. 5.4.1, and therefore, exact quantization cannot be expected. Nonetheless, the continuous variation of I_{rf} clearly indicates non-quantized transport. We attribute this behavior to an insufficient tunnel-barrier asymmetry. The left barrier Γ_{L} is still too large to suppress tunneling into the

left lead, and the right barrier Γ_{R} is too small to ensure that one electron and one hole are emitted by cycle into the right lead. We also tuned to the voltage of neighboring piano gates in this device, but found little to no lever arm on the tunnel transparency. Therefore, we cannot independently tune the asymmetry. Despite this limitation, we proceed to analyze the observed transport behavior in detail to understand better the underlying dynamics of the quantum dot.
We also record the dc source–drain current I_{dc}, shown in Fig. 5.14b. In the case of quantized charge emission, I_{dc} should vanish since equal numbers of electrons and holes are transferred per cycle. However, we observe finite dc currents up to $I_{\mathrm{dc}} \approx 320\,\mathrm{pA}$, which change sign as the gate voltage is swept across a Coulomb resonance. Each resonance splits into two regions of opposite current polarity: a positive current when the Nth level is above the Fermi level in equilibrium, and a negative current when it is below. At resonance ($U_{\mathrm{rf}} = 0$), I_{dc} vanishes, and the signal is also suppressed when U_{rf} approaches the addition energy E_{add}. For even larger amplitudes, the effect reverses sign again. These trends suggest that the dc current is sensitive to whether the energy level lies below or above the Fermi energy in equilibrium. When two levels contribute simultaneously ($\alpha U_{\mathrm{rf}} \approx E_{\mathrm{add}}$), their opposite contributions cancel, leading to $I_{\mathrm{dc}} \approx 0$. At larger U_{rf}, the transport is dominated by the level closer to the modulation extrema, which alternates in sign for adjacent levels.
However, the appearance of any dc current at all is surprising, since U_{sd} is nominally zero. Even a small offset bias could not explain the observed sign reversal. Interestingly, the observed current is close to the quantized current of $2ef \approx 320\,\mathrm{pA}$, which yet indicates that in average 2 charge carriers pass through the quantum dot per cycle. In the following section, we analyze this effect and show that it can be understood as a charge-pumping process arising from capacitive cross-talk.

5.4.3 Charge pumping from source to drain

The finite source–drain current I_{sd} observed in the absence of a bias voltage U_{sd} is reminiscent of single-electron pumps realized in semiconductor nanostructures [140–142]. These devices generate a quantized current by transferring single electrons from one lead to the other through the cyclic modulation of two tunnel barriers. A crucial requirement for nonzero charge pumping is the simultaneous modulation of at least two parameters with a finite phase offset. Otherwise, the system's dynamics remain time-reversible, and no net current is generated. We therefore suspect that in our case, the dot potential μ_{N} is not the

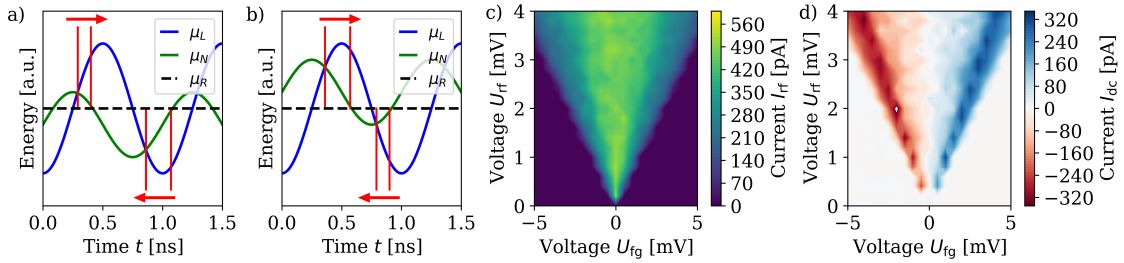

Figure 5.15: Simulation of charge pumping. a)+b) Time evolution of the leads potentials $\mu_\mathrm{L}, \mu_\mathrm{R}$ and the dot potential μ_N, which lies below (a) and above (b) the Fermi level in equilibrium. The time intervals in resonance, $\mu_\mathrm{L} > \mu_\mathrm{N} > \mu_\mathrm{R}$ for tunneling from left to right or $\mu_\mathrm{R} > \mu_\mathrm{N} > \mu_\mathrm{L}$ for tunneling from right to left, are highlighted in red. c)+d) Result of Monte Carlo simulation of charge pumping for stray coupling between the plunger gate U_fg and the left lead μ_L for $f = 1\,\mathrm{GHz}$, $\gamma_\mathrm{L} = \gamma_\mathrm{R} = 8\,\mathrm{GHz}$ and $T = 100\,\mathrm{mK}$. The magnitude of the ac current I_rf emitted in the right lead is shown in c), and the dc source-drain current I_sd in d).

only parameter modulated by the applied rf drive. As discussed earlier, a significant capacitive stray coupling exists between the plunger gate and the left lead (and to a lesser extent, the right lead—about 10 dB weaker). The stray coupling comes from spatial proximity. The waveguides for the left lead and the plunger gate are adjacent, while the right lead is separated by 3 other waveguides. Consequently, the chemical potential of the left lead μ_L is also modulated, but with a finite phase delay due to the RC time constant of the coupling circuit.

Figures 5.15a,b illustrate how such phase-shifted modulation leads to a net current. The plots show the time evolution of $\mu_\mathrm{L}(t)$, $\mu_\mathrm{R}(t)$, and $\mu_\mathrm{N}(t)$ for a phase lag of $-90°$, corresponding to a stray capacitance $C_\mathrm{stray} \lesssim 100\,\mathrm{fF}$. Current flows whenever $\mu_\mathrm{L} > \mu_\mathrm{N} > \mu_\mathrm{R}$ (electron transfer left→right) or $\mu_\mathrm{R} > \mu_\mathrm{N} > \mu_\mathrm{L}$ (transfer right→left). The fraction of time spent in either configuration depends on the static dot chemical potential set by U_fg. When the static dot chemical potential lies below the Fermi energy (Fig. 5.15a), the system spends longer in the left→right configuration, producing a net negative I_sd. Conversely, when the level lies above the Fermi energy (Fig. 5.15b), the current reverses direction.

To quantify this behavior, we simulated the stochastic tunneling dynamics using a time-resolved Monte Carlo approach based on the sequential-tunneling master equation (see Appendix D). The simulation tracks the instantaneous dot occupation under rf modulation, with $\mu_\mathrm{N}(t)$ varying sinusoidally at $f = 1\,\mathrm{GHz}$. The left-lead potential $\mu_\mathrm{L}(t)$ includes a 90° phase lag due to capacitive cross-talk, while μ_R is held fixed. At each time step Δt, tunneling events are sampled probabilistically according to the instantaneous Fermi functions and tunnel rates $\Gamma_{L,R}$. The resulting charge transfer per cycle yields both the dc current I_sd and the

first-harmonic ac response I_{rf}.
Figures 5.15c,d show the simulated results for $\Gamma_{\mathrm{L}} = \Gamma_{\mathrm{R}} = 8\,\mathrm{GHz}$ and $T = 100\,\mathrm{mK}$[1]. The model reproduces the experimentally observed sign reversal of I_{sd} as the static dot chemical potential crosses the Fermi energy (see Fig. 5.14b. This is consistent with a phase-shifted capacitive pumping mechanism rather than intentional two-parameter driving.

5.5 Summary and outlook

In this section, we investigated gate-defined quantum dots in BLG as a platform for coherent single-electron control. Using local electrostatic gates, we demonstrated charge confinement by opening a displacement-field-induced band gap. Bias spectroscopy revealed well-defined Coulomb blockade with addition energies of 3-10 meV and a lever arm for the plunger gate of $\alpha_{\mathrm{fg}} \approx 400\,\mathrm{meV/V}$. While we did not achieve an SES with quantized emission, the limiting factors are clear: (i) insufficient, independently tunable barrier asymmetry and (ii) significant capacitive cross-talk from the plunger to the leads, enabling unintended charge pumping. Reported BLG devices can tune Γ from $\sim 100\,\mathrm{Hz}$ to $\sim 60\,\mathrm{GHz}$ [172, 173], indicating that our target regime is realistic with improved gate leverage. To address the capacitive cross-talk observed in the present device generation, a revised sample layout and PCB architecture have been developed. The new design is shown in Fig. 5.16a)+b). It introduces several modifications to minimize stray coupling between the RF-driven gates and the reservoirs. First, the coplanar waveguides (CPWs) routing the finger gates and the Ohmic contacts are arranged orthogonally, reducing direct capacitive coupling. Second, neighboring gates are contacted from opposite sides of the device, increasing their spatial separation and suppressing gate-to-gate crosstalk. Third, the dimensions of the split gates (shown in blue in Fig. 5.16b) have been minimized to reduce the parasitic capacitance between the split gates and the finger and piano gates. Finally, a new PCB design provides dedicated CPW access from all four directions, enabling improved RF grounding and routing. Preliminary microwave measurements demonstrate a reduction of the stray transmission S_{21} by more than 20 dB across the investigated frequency range as shown in Fig. 5.16c). This is a substantial suppression of unwanted capacitive coupling. Finally, we also

[1]The tunneling rates of $\Gamma_{\mathrm{L}} = \Gamma_{\mathrm{R}} = 8\,\mathrm{GHz}$ are estimated to fit the observed DC current $I_{\mathrm{dc}} \approx 320\,\mathrm{pA}$. Furthermore, we simply assume $\Gamma_{\mathrm{L}} = \Gamma_{\mathrm{R}}$ for simplicity. However, we observe the same phenomenon for slightly asymmetric tunneling rates. Only a very asymmetric quantum dot, as shown in Fig. 5.2 realizes a SES with quantized I_{rf} and zero I_{dc}.

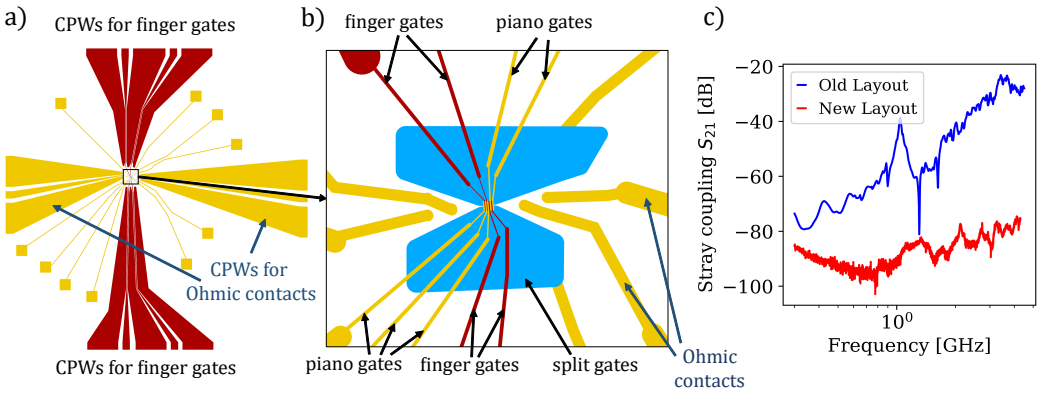

Figure 5.16: New Layout for optimised stray coupling: (a) Overview of the next-generation bilayer graphene quantum dot layout. The coplanar waveguides (CPWs) connected to the finger gates (red) and Ohmic contacts (yellow) are routed orthogonally to reduce direct capacitive coupling. (b) Magnified view of the gate architecture. Neighboring gates are contacted from opposite sides of the device, while the split-gate dimensions are minimized to reduce parasitic capacitance between split gates and finger/piano gates. (c) Preliminary microwave characterization comparing the stray transmission S_{21} of the previous and revised layouts. The new design exhibits a suppression of the parasitic transmission by more than $20\,\mathrm{dB}$ over a broad frequency range.

increased the width of the piano gates from 90 nm to 90 nm to improve the tunability of the tunnel barriers and realize an asymmetric configuration. These improvements are expected to enable independent tuning of the tunnel barriers and reduce parasitic charge pumping, bringing the device closer to the regime required for quantized single-electron emission.

Chapter 6

Conclusion

This thesis focused on the experimental investigation of charge transport in low-dimensional quantum systems using microwave techniques. Two complementary platforms were studied: chiral edge states in quantum anomalous Hall (QAH) insulators and electrostatically defined quantum dots in bilayer graphene (BLG). Although the underlying physical mechanisms in these systems differ fundamentally, both allow charge transport to be probed via time-dependent excitation and high-frequency readout.
By developing and applying a high-frequency experimental setup, this work demonstrates how dynamical transport properties of zero- and one-dimensional systems can be accessed beyond conventional dc measurements. In this way, the central objective of establishing experimental tools to probe charge-transport dynamics in mesoscopic systems has been achieved.
In the longer term, these approaches provide a basis for studying coherent single-particle transport across different material platforms. Such experiments open perspectives for investigating quantum transport phenomena at the level of individual charge carriers, including charge fractionalization and Andreev reflection.

6.1 Summary

6.1.1 Edge state transport in QAH edge states

First, we report on the propagation characteristics of edge plasmons in QAH edge states. For this purpose, devices were fabricated using cleanroom nanofabrication techniques to pattern and contact MBE-grown V-BST films, a magnetic topological insulator that exhibits the QAH effect. Using a broadband microwave setup, we perform phase-resolved measurements of the scattering parameters between narrow finger gates coupled to the edge state. From these

measurements, we extract the velocity and dissipation of edge plasmon transport as a function of frequency.

At small excitation voltages, we found a plasmon velocity of approximately 2×10^5 m/s. This velocity increases with excitation voltage or temperature and reaches values of approximately 4.5×10^5 m/s, comparable to those reported for the related compound Cr-doped BST [16, 17].

To analyze dissipation in edge-state transport, we model the transmission using an effective circuit based on a distributed transmission line. The bare edge state is described as a dissipationless transmission line, while dissipative circuit elements are introduced to capture the dominant loss mechanisms. Specifically, we identify two main sources of dissipation: a residual bulk conductance that leads to frequency-independent losses, and capacitive coupling to charge puddles, which results in dissipation that increases with frequency. We demonstrate that QAH edge states exhibit finite dissipation at microwave frequencies even at very low excitation voltages and temperatures below 100 mK. This behavior contrasts sharply with dc transport experiments, where the longitudinal resistance vanishes under the same conditions. Our analysis establishes charge puddles as the dominant source of dissipation in the investigated frequency range.

Beyond quasi-equilibrium transport, we investigate the breakdown of QAH edge state transport as a function of excitation voltage, temperature, and magnetic field. These measurements define clear operational boundaries for low-loss applications of QAH insulators. We observe the onset of dissipation for excitation voltages exceeding 100 µV, temperatures above 100 mK, and at finite magnetic fields. In addition to their technological relevance, these results provide insight into the mechanisms governing both equilibrium and non-equilibrium transport.

To further elucidate the breakdown mechanism, we combine rf excitation of the edge state with a dc probe of the bulk conductance, enabling us to study the frequency dependence of the breakdown using a frequency-independent probe. Using this technique, we identify Joule heating of charge puddles as the dominant dissipation mechanism at both microwave frequencies and dc bias voltages.

To place these findings in a broader context, we apply the same methodology to a graphene Corbino device, thereby studying breakdown physics in a complementary QH system. By varying the filling factor, we tune the localization strength of bulk carriers and explore breakdown mechanisms over a wide energy range. We found that dissipationless transport breaks down via

non-Ohmic, electric field-assisted hopping conduction for strongly localized carriers, such as those at the center of cyclotron gaps. In contrast, for weakly localized carriers, for example, near spin gaps or at the edges of cyclotron gaps, breakdown is dominated by Joule heating and exhibits Ohmic behavior. The crossover between these two regimes is continuous and frequency independent, depending solely on the hopping energy scale $k_B T_0$.

These results clarify why breakdown in the QAH insulator is dominated by Joule heating: the hopping energy of the QAH bulk, $T_0 \approx 17\,\mathrm{K}$, is comparable to the smallest gaps in the graphene QH system, which exhibits the same breakdown behavior. Altogether, this establishes heating as a key limitation for the application of QAH insulators and underscores the importance of efficient thermalization.

In summary, we systematically characterize edge plasmon propagation in QAH edge states and identify the dominant sources of dissipation. These results pave the way for future experiments operating at microwave frequencies, including studies of single-charge transport and charge fractionalization. Such experiments are discussed in Sec. 6.2.

6.1.2 Single-electron source in bilayer graphene

In this section of the thesis, we investigate microwave transport in electrostatically defined BLG quantum dots to achieve controlled single-electron emission in the absence of a magnetic field.

A band gap in the BLG is first induced by applying a displacement field. A narrow one-dimensional channel is defined using two split gates separated by approximately 100 nm. Local confinement is then achieved by applying voltages to narrow finger gates crossing the channel, thereby forming a quantum dot. Using low-frequency transport measurements, we demonstrate the formation of a well-defined quantum dot and characterize its basic properties, including the discrete energy spectrum, gate lever arms, and tunnel coupling to the source and drain leads.

Building on this dc characterization, we explore rf control of the quantum dot potential. By applying rf excitations to the gate electrodes, we induce time-dependent modulation of the dot levels and detect the resulting dc and rf currents. Although quantized single-electron emission has not yet been achieved in these devices, the observed current response demonstrates controlled charge transfer driven by rf excitation.

To interpret these observations, we develop a simple Monte Carlo simulation of

the dynamics of a driven quantum dot. The simulations indicate that the measured current originates from charge pumping between the leads rather than from quantized single-electron emission. This analysis identifies the main limitations of the current device design. In particular, cross-talk between gates and leads, as well as the lack of independent control over the tunnel barriers to the left and right leads, prevents robust single-electron operation.
Despite these limitations, the experiments establish an experimental framework for rf-controlled quantum dots in BLG. We expect that modest technical improvements, such as enhanced gate isolation and independent tuning of the tunnel barriers, will enable the realization of a reliable SES. More generally, this work lays the groundwork for future experiments on controlled single-electron emission and coherent single-particle phenomena, including entanglement generation and Andreev reflection, as discussed in Sec. 6.2.

6.2 Outlook

The results presented in this thesis open several directions for future experiments on coherent charge transport in low-dimensional systems. In the following, we outline possible experiments that build on the ability to generate, manipulate, and detect charge excitations using rf techniques.

6.2.1 Reducing edge plasmon dissipation

Chapters 3 and 4 exposed the fragility of the QAH effect in thin films of V-BST, which can be largely attributed to long-range Coulomb disorder. A key objective of future research is therefore to mitigate this limitation and thereby widen the otherwise restrictive operation window of QAH-based devices. Inevitably, charge disorder leads to localized bulk states in these films. Owing to the relatively small magnetic exchange gap, on the order of tens of meV [49, 50], a perfectly insulating bulk cannot be realized. Nevertheless, it remains possible to optimize the localization of charge disorder and thereby shift the breakdown of the QAH effect to higher bias voltages and excitation frequencies.
In the present material platform, charge defects are only weakly screened, such that the resulting localized states are spatially extended over tens of nanometers [73, 77, 78]. Improving the electrostatic screening of these charge defects is therefore expected to enhance their localization and reduce their spatial extent [77, 174, 175]. One established approach to achieve this is the

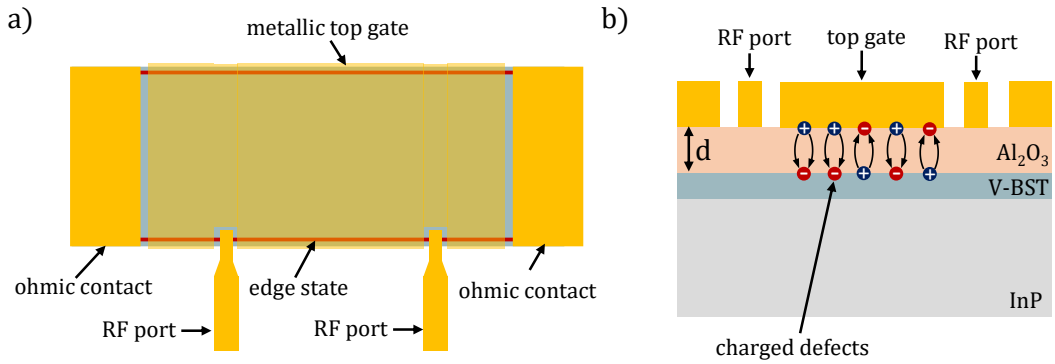

Figure 6.1: Schematic illustration of electrostatic screening by a metallic top gate. a) Device Layout of a QAH device with metallic top gate. The gate is interrupted for the rf ports used for the excitation and detection of edge plasmons. b) Cross-sectional view of the device in a). The top gate is covered by an insulator (here Al_2O_3) of thickness d and a metallic top gate. The top gate induces image charges at a distance d that suppress long-wavelength Coulomb fields, thereby reducing the spatial extent of charge puddles. Screening becomes effective when the gate–channel separation d is smaller than the intrinsic disorder correlation length.

use of a metallic gate placed in proximity to the electronic system. Electrostatic screening by a nearby metallic gate suppresses long-wavelength components of the Coulomb disorder potential, such that potential fluctuations on length scales larger than the gate distance d are strongly reduced. As a consequence, the characteristic size of charge puddles is limited to the order of the gate distance [176, 177]. This effect has been experimentally confirmed in related two-dimensional systems [178, 179].

Based on these considerations, we propose a modified device geometry, as sketched in Fig. 6.1a. A continuous gold gate is placed on top of the QAH insulator, with openings only in the vicinity of the rf ports required for excitation and detection of edge plasmons. A cross-sectional view of the structure is shown in Fig. 6.1b. The key design parameter of this geometry is the thickness of the gate dielectric, d. On the one hand, d must be sufficiently small to ensure efficient screening of long-range Coulomb fields. On the other hand, it must be large enough to prevent electrical leakage or shorting between the metallic gate and the QAH film. For the present material system, we estimate that a dielectric thickness of $d \simeq 10\,\mathrm{nm}$ represents a reasonable compromise.

In addition to screening charge disorder, the proximity gate will also screen the edge plasmon itself. This increases the geometric capacitance of the edge channel and consequently reduces the plasmon propagation velocity [38, 180]. While this effect may initially appear detrimental, reduced propagation velocities are

in fact advantageous for microwave applications, for example, by enabling further miniaturization of non-reciprocal devices such as circulators [16, 17]. We therefore consider proximity gating a promising strategy to improve both the robustness and practical applicability of QAH-based plasmonic devices.

6.2.2 Charge fractionalization in a QAH insulator

A natural next step is the realization of devices in which two edge states of neighboring QAH insulators are intentionally coupled. In the strong-coupling regime, interactions between adjacent edge states can give rise to fractionalized charge excitations [181–184]. At first glance, this may appear counterintuitive since the elementary excitation of an isolated QAH edge state carries an integer charge $q = e$. However, when two edge channels are strongly coupled, for example via capacitive interactions, the elementary excitations are no longer single electrons but collective charge modes. The coupled system can then be described as a Tomonaga–Luttinger liquid supporting interaction-induced charge fractionalization [93, 185–187].

Such interaction-induced charge fractionalization has been experimentally demonstrated in the integer QH regime. In particular, shot-noise measurements provided evidence for a fractional effective charge [188], while time-resolved transport experiments revealed the real-time splitting of charge wave packets into fractional components [93]. These experiments were performed at high magnetic fields, where the QH effect naturally provides multiple interacting edge channels. In contrast, the QAH effect offers the opportunity to investigate analogous charge fractionalization phenomena in the absence of an external magnetic field.

To this end, we propose a device geometry in which two counter-propagating QAH edge states are coupled via a floating metallic island, as sketched in Fig. 6.2a. The coupling between the edge channels and the metallic island is purely capacitive and characterized by a capacitance C_g, as illustrated in the cross-sectional view in Fig. 6.2b. The metallic island has two important effects. First, it significantly enhances the coupling strength, since the distance to the island is approximately 10 nm, whereas the direct separation between the edge states is 2–$3\,\mu\mathrm{m}$. Second, it mediates a long-range interaction between the edge states, as it couples to the total accumulated charge Q beneath each side of the island rather than to the local charge density.

The coupling strength is governed by the charging time of the island, $\tau = R_K C_g$, where $R_K = h/e^2$. Charge fractionalization is expected when this time scale

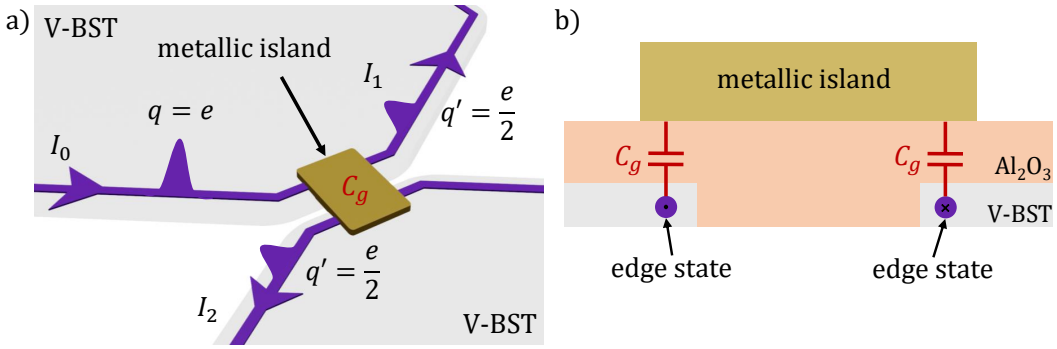

Figure 6.2: Schematic illustration of QAH charge fractionalizer. a) 3D model of a QAH device that couples two edge states via a metallic island. An incoming current I_0 containing a single charge carrier ($q = e$) is fractionalized by strongly coupling it to a neighboring edge state. It leads to half the current in each edge state with a fractional charge ($q = e/2$). b) Cross-sectional view of the metallic island in a). The strength of the coupling between the edge states depends on the capacitance C_g between the edge states and the metallic island.

exceeds the duration of the incident wave packet. In this regime, the island cannot instantaneously screen the injected charge, and the interaction dynamically redistributes the charge between the two edge channels. Microwave measurements of the outgoing edge currents provide a sensitive probe of this regime, for example, through modifications of the temporal profile or amplitude of the transmitted wave packets.

While microwave measurements can establish strong coupling and charge redistribution, they do not directly determine the effective charge of the excitations. Demonstrating charge fractionalization therefore requires shot-noise measurements, which provide direct access to the effective charge of the current-carrying modes [187, 189]. Combining time-resolved microwave techniques with noise measurements thus offers a powerful approach to investigate interaction-driven charge fractionalization in QAH edge states and to study the coherence and decoherence of the resulting collective excitations in the absence of a magnetic field.

6.2.3 Studying Andreev reflection using BLG quantum dots

Andreev reflection, first proposed by Andreev in 1964 [190], describes the conversion of an electron into a hole at a normal–superconductor interface, accompanied by the transfer of a Cooper pair into the superconductor. Its experimental

signatures were later quantitatively established within the Blonder–Tinkham–Klapwijk framework [191]. Although the Andreev reflection is now well established, its temporal dynamics remain largely unexplored. Recent theoretical works have addressed the expected time-dependent response of Andreev reflection in driven hybrid systems [192], as well as the dynamics of charge pulses in QH edge states with induced superconductivity [193]. On the experimental side, time-resolved studies have so far been largely limited to the dynamics of Andreev bound states in qubit-based architectures [194], whereas time-resolved measurements of individual Andreev reflection events remain absent.
We propose that the BLG quantum dots presented in Chapter 5 constitute an ideal platform for studying time-resolved Andreev reflection. Andreev bound states in graphene quantum dots have previously been investigated using low-frequency transport techniques [147, 148], demonstrating the compatibility of graphene-based quantum dots with superconducting proximity effects. A key advantage of BLG is that it enables both the implementation of a SES and the induction of superconductivity within the same material platform. In contrast, inducing superconductivity in the QH regime remains challenging due to the high magnetic fields required to achieve robust quantization.

The proposed experiment is schematically illustrated in Fig. 6.3a. The SES follows the same architecture as introduced in Chapter 5, with a quantum dot formed beneath the plunger gate (U_{PG}). By modulating the chemical potential of the quantum dot with an rf excitation, individual electrons are emitted. When the energy of an emitted electron lies below the induced superconducting gap Δ_{SC} of the proximitized BLG region, the electron undergoes Andreev reflection and is converted into a hole, while a Cooper pair is injected into the superconducting condensate (see Fig. 6.3b). For conventional (retro-)Andreev reflection, the hole is reflected along the same trajectory as the incident electron. Therefore, we apply an out-of-plane magnetic field to control the electron and hole trajectories, as sketched in Fig. 6.3a. However, when the Fermi energy is tuned close to the Dirac point in BLG, Andreev reflection can involve a transition between the conduction and valence bands. In this case, the hole is reflected under a specular angle rather than retracing the incoming path [195–197]. By tuning the magnetic field H, the electron and hole trajectories can be manipulated [198], allowing the distinction between retro- and specular-Andreev reflection.
The hole is drained into an Ohmic contact and subsequently detected using a cryogenic amplifier. This scheme requires ballistic transport in the BLG, such that the emitted electrons follow well-defined trajectories with an incident angle

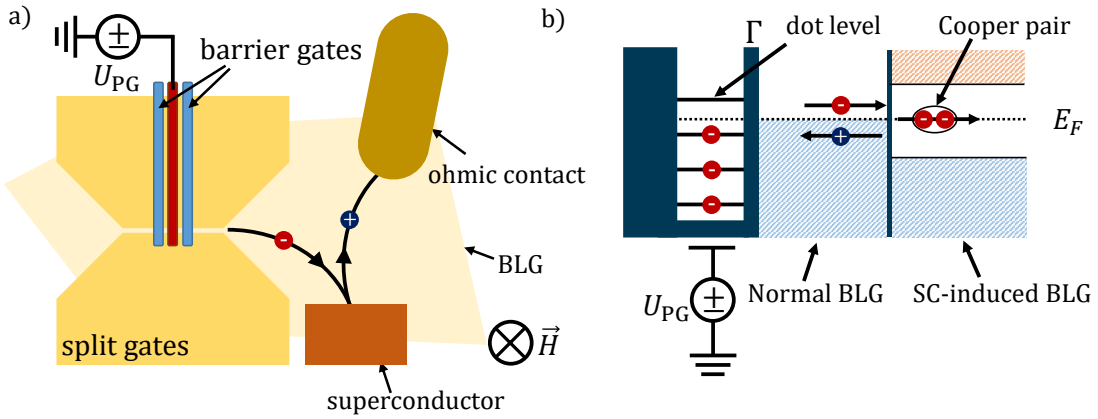

Figure 6.3: Andreev reflection measurement using SES. a) Device layout for detecting an Andreev reflection of a single charge carrier in BLG. The BLG quantum dot emits single electrons (holes). A superconducting island induces superconductivity (SC) into the BLG. The incident electron (hole) is reflected as a hole (electron) and detected by an Ohmic contact. An out-of-plane magnetic field controls the electron and hole trajectories, enabling the distinction between retro- and specular-Andreev reflection. b) Energy diagram of the device. A plunger gate controls the filling of the dot. By applying an rf pulse, an electron is emitted into the normal-conducting BLG lead and then reflected as a hole on the interface to the SC-induced BLG, if its energy is below the SC gap Δ_{SC}. This process is called Andreev reflections and leads to a Cooper pair emission inside the SC-induced BLG.

set by the one-dimensional channel formed between the split gates. In the presence of significant scattering, electrons would be deflected and partially drained directly into the Ohmic contact, thereby suppressing the Andreev reflection signal. In principle, this platform enables precise control over the incident electron's energy and time-resolved detection of the reflected charge pulse. More broadly, this approach extends concepts of single-electron quantum optics to superconducting hybrid systems, enabling the study of Andreev reflection at the level of individual, time-controlled charge excitations.

Appendix A

Synchronization of rf experiments

Synchronization becomes essential once more than one microwave instrument is used in an experimental setup. In such cases, a stable common time reference is required to avoid frequency offsets and uncontrolled phase drifts between different signal paths. To identify a suitable synchronization strategy, we systematically compare different experimental configurations and synchronization techniques.

The investigated setups consist of either a homodyne or a heterodyne detection scheme, each involving two signal generators that provide sinusoidal signals at microwave frequencies. In the heterodyne configuration (see Fig. A.1), the two signal generators operate at frequencies separated by 10 MHz to enable down-conversion. In contrast, for homodyne detection (see Fig. A.2), both signal generators operate at the same carrier frequency, and down-conversion is achieved by mixing the microwave signal with an external 10 MHz reference signal. This reference signal is provided either by a waveform generator (Rigol), a lock-in amplifier (Zurich Instruments MFLI), or a commercial quartz clock.

In addition, we compare different synchronization methods, including the use of a shared 10 MHz reference, a 1 GHz reference, and direct local-oscillator (LO) coupling between instruments. To assess the phase stability of the different platforms and synchronization schemes, a cable is used as a device under test (DUT), and the phase is monitored continuously over a period of 10 h. An example measurement for a configuration using two LO-coupled signal generators and the Rigol waveform generator is shown in Fig. A.3.

Ideally, the measured phase should remain constant over time. In practice, phase fluctuations can arise from imperfect synchronization, temperature drifts, or other instrumental instabilities. To quantitatively compare the different configurations, we analyze the standard deviation σ of the measured phase over time windows of 10 min and 10 h. The resulting values for all tested setups are summarized in Tab. A.1.

Two main conclusions can be drawn from these measurements. First, the homodyne detection scheme generally exhibits superior phase stability compared to the heterodyne configuration. Second, synchronization via direct LO coupling between signal generators yields better phase stability than synchronization using a shared 10 MHz reference. The best overall performance is obtained when using the Rigol waveform generator as the source of the 10 MHz reference signal, for which phase fluctuations remain well below 1° over 10 h. This level of stability is sufficient for all experiments presented in this thesis. Even the heterodyne configuration with LO-coupled signal generators provides adequate phase stability for the intended measurements.

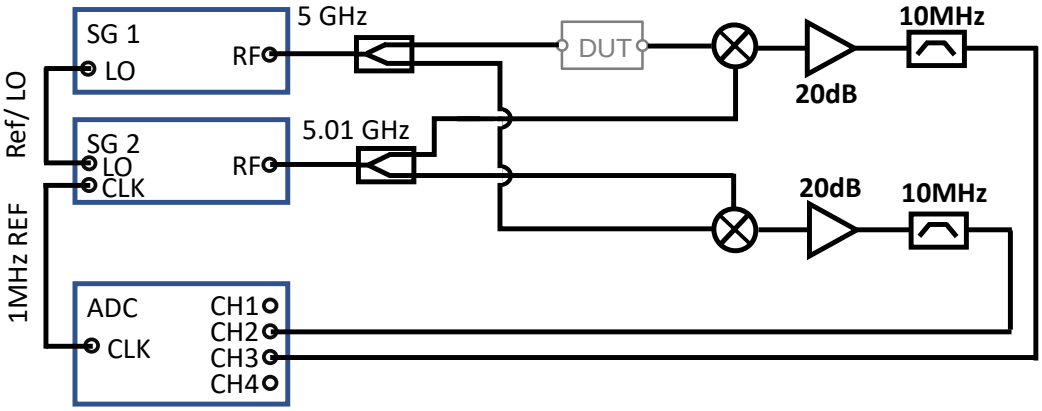

Figure A.1: Heterodyne detection: Schematic of the heterodyne measurement setup. Two signal generators (SG), synchronized either via a shared 10 MHz reference or by local-oscillator (LO) coupling, provide sinusoidal signals at 5 GHz and 5.01 GHz. Each signal is split using a power splitter. After passing the device under test (DUT, here a cable), the signals are mixed using a double-balanced mixer (Marki M1-0008). The down-converted signal is amplified by 20 dB using a broadband amplifier (Mini-Circuits ZX60-83LN-S+) and filtered by a 10 MHz band-pass filter. In a typical measurement, one signal bypasses the DUT and serves as a reference, while the other is transmitted through the DUT. The signal is digitized using an acquisition card (ADC) and demodulated at 10 MHz to extract amplitude and phase information.

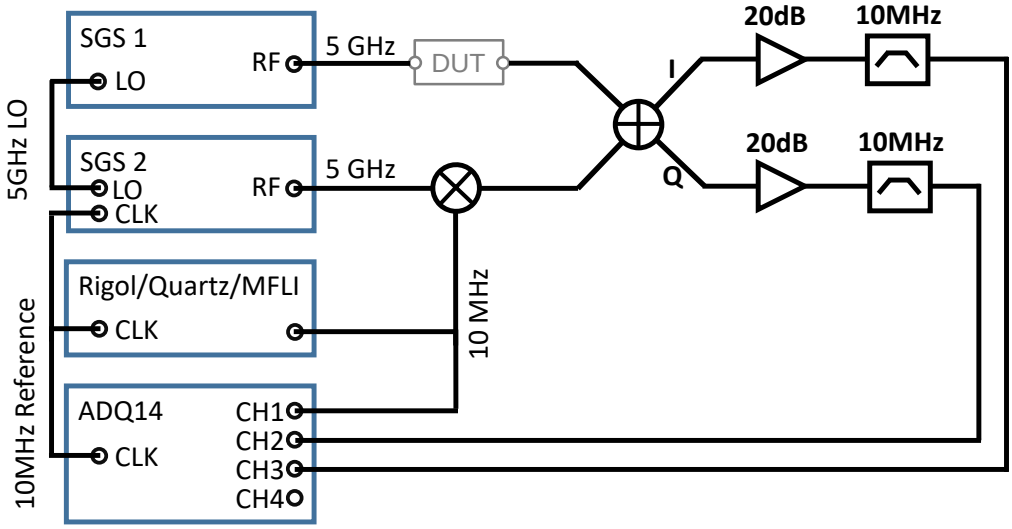

Figure A.2: Homodyne detection: Schematic of the homodyne measurement setup. Two signal generators (SG), synchronized via a shared 10 MHz reference or by local-oscillator (LO) coupling, provide sinusoidal signals at 5 GHz. One signal is sent to the device under test (DUT), while the second signal is mixed with a 10 MHz reference provided by a waveform generator (Rigol), a quartz clock, or a lock-in amplifier (Zurich Instruments MFLI). After passing the DUT (here, a cable), the signals are mixed using an IQ mixer (Marki MLIQ-0218). The down-converted in-phase (I) and quadrature (Q) components are amplified by 20 dB using a broadband amplifier (Mini-Circuits ZX60-83LN-S+) and filtered by a 10 MHz bandpass filter. The signals are digitized using an acquisition card (ADC) and demodulated at 10 MHz to determine the I and Q amplitudes.

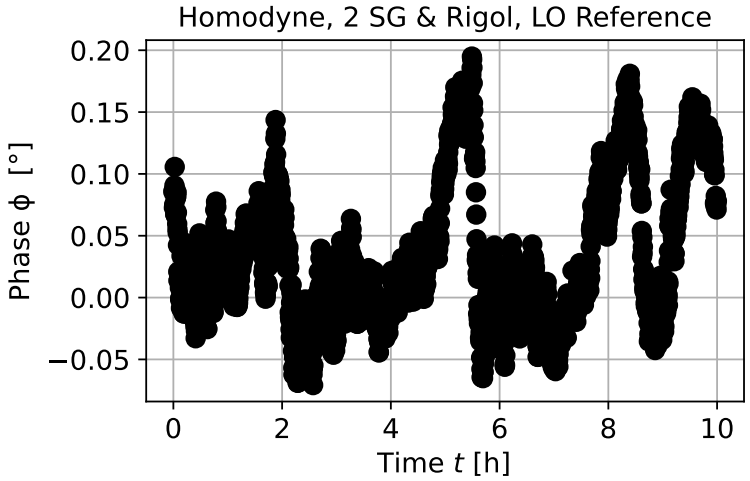

Figure A.3: Phase monitoring over time: Demodulated phase ϕ as a function of elapsed time t, measured for a homodyne configuration using two LO-coupled signal generators and a Rigol waveform generator. The standard deviations of the phase over 10 min and 10 h time intervals are summarized in Tab. A.1.

Table A.1: Phase stability comparison for different setups and synchronization schemes. The standard deviation of the phase σ is shown for a 10 min and a 10 h period. Colors indicate the evaluation of the phase stability (green=good, orange=acceptable, red=too large). The following abbreviations are used: SG: Rohde&Schwarz SGS100A signal generator, clock: Commercial quartz-clock providing a 10 MHz reference signal, LO: shared local oscillator between the two SG, Rigol: waveform generator.

Setup	**Instruments**	**Synchronization**	σ [°] **(10 min)**	σ [°] **(10 h)**
Homodyne	3 SG	1 GHz reference	0.086	0.222
Homodyne	2 SG & clock	10 MHz reference	1.086	1.271
Homodyne	2 SG & clock	10 MHz reference & shared L0	0.022	0.067
Homodyne	2 SG & Rigol	10 MHz reference & shared L0	0.018	0.059
Homodyne	2 SG & MFLI	10 MHz reference & shared L0	0.041	0.116
Heterodyne	3 SG	1 GHz reference	0.092	2.429
Heterodyne	2 SG	shared L0	0.249	0.958

Appendix B

Fabrication recipe for V-BST samples

Table B.1: Fabrication recipe for Quantum anomalous Hall devices

Step	Module	Process step	Target parameters (SI)	Notes / intent
1	V-BST growth	Molecular beam epitaxy	—	Growth of V-doped $(Bi,Sb)_2Te_3$ thin film on InP substrate.
2	Al_2O_3 encapsulation	Atomic layer deposition	47 cycles; thickness 4–5 nm	Passivation of V-BST film.
3	Markers + ohmic contacts	Spin coating	PMMA A6, 4000 rpm (≈300 nm); bake 10 min at 120 °C	Lithography stack for alignment markers and ohmic pads.
		Electron-beam lithography	Acceleration voltage 10 kV; aperture 60 µm; write field 100 µm; step size 100 nm; dose 70 µC/cm^2	Pattern definition for markers/contacts.
		Development	MIBK 30 s; IPA 90 s	Standard PMMA development.
		Al_2O_3 wet etch	Transene D at 50 °C for 10 s; DI rinse 2 min at 50 °C; DI rinse 2 min; N_2 dry	Open dielectric locally before metallization.
		Metal deposition (Pt/Au)	Sputter 5 nm Pt + 25 nm Au (Moorfield); no rotation	Pt as adhesion / diffusion barrier; Au for low-resistance pads.
		Lift-off	NMP at 50 °C for 30 min	Assist lift-off by gentle solvent pipette flow.

Continued on next page

Step	Module	Process step	Target parameters (SI)	Notes / intent
4	Mesa definition	Spin coating	AZ1505, 4000rpm, (≈300 nm); bake 1 min at 100 °C	Mask for mesa patterning.
		Laser writing	Laser power 10 mW; exposure 32 %	Define mesa geometry by optical lithography.
		Development	AZ326MIF 20 s; H_2O rinse 60 s	Develop and clean resist pattern.
		Al_2O_3 wet etch	Transene D at 50 °C for 10 s; DI rinse 2 min at 50 °C; DI rinse 2 min; N_2 dry	Remove Al_2O_3 in the mesa region prior to film etch.
		V-BST wet etch	H_2O_2 (35%) : H_2SO_4 (1 mol/L) = 3:1; etch 20 s at 21.5 °C	Etch time is typically verified visually to avoid over-etch.
		Solvent cleaning	Acetone, then IPA	Remove resist residues.
5	Al_2O_3 encapsulation	Atomic layer deposition	10 cycles; thickness 10 nm	Deposition of gate dielectric.
6	Open bond pads in Al_2O_3	Spin coating	AZ1505, 4000 rpm (≈300 nm); bake 1 min at 100 °C	Mask to open dielectric above bond pads.
		Laser writing (maskless)	Laser power 10 mW; exposure 32 %	optical pattern definition.
		Development	AZ326MIF 20 s; H_2O rinse 60 s	Standard development and rinse.

Continued on next page

Step	Module	Process step	Target parameters (SI)	Notes / intent
		Al_2O_3 wet etch	Transene D at 50 °C for 30 s; DI rinse 2 min at 50 °C; DI rinse 2 min; N_2 dry	Expose the underlying metal for wire bonding.
		Solvent cleaning	Acetone, then IPA	Remove resist residues.
7	Top gates + bond pads	Spin coating (bottom layer)	MMA EL9, 4000 rpm (≈300 nm); bake 10 min at 120 °C	Bilayer resist for reliable lift-off of gate metal.
		Spin coating (top layer)	PMMA A6, 4000 rpm (≈300 nm); bake 10 min at 120 °C	Defines high-resolution gate features.
		Electron-beam lithography	Acceleration voltage 10 kV; aperture 30 µm; write field 100 µm; step size 50 nm; dose 50 µC/cm^2	Gate and pad patterning with reduced step size.
		Development	MIBK 30 s; IPA 90 s	Development for MMA/PMMA bilayer.
		Metal deposition (Pt/Au)	Sputter 5 nm Pt + 50 nm Au (Moorfield); no rotation	Pt as adhesion / diffusion barrier; Au for low-resistance pads.
		Lift-off	NMP at 50 °C for 30 min	Assist lift-off by gentle solvent pipette flow.

Appendix C

Simulation of quantum anomalous Hall resonator

The circuit model developed in Chapter 3 can be used to predict the performance of a resonator formed from a disk of QAH insulator. Figure C.1(a) illustrates a disk-shaped geometry in which two microwave ports are capacitively coupled to the chiral edge channel. Since the edge state forms a closed propagation path around the disk perimeter, edge plasmons can circulate repeatedly and interfere constructively, giving rise to resonant modes. To estimate the resonator response, the same circuit model and parameter set introduced in Chapter 3 were employed. The transmission coefficient is given by

$$S_{21} = \frac{S_{ge} S_p S_{eg}}{1 - (S_p S_{pp})^2}, \tag{C.1}$$

where $S_p = \exp(-ik(\omega)\pi D/2)$ describes plasmon propagation between the two coupling ports (half perimeter) and S_{pp} accounts for plasmon reflection at the capacitively coupled ports. Resonances occur when the accumulated round-trip phase approaches an integer multiple of 2π, causing the denominator to become small and enhancing the transmission. Figure C.1(b) shows the simulated transmission spectra for different values of the edge dissipation parameter g_e. The case $g_e = 0$ corresponds to an ideal lossless QAH edge state and yields sharp, high-contrast resonances. The value $g_e = 0.3$ approximately corresponds to the experimentally extracted parameters of sample $\mathrm{MBE\_VBST\_20221204a}$ and still supports clearly visible resonances. In contrast, $g_e = 3$ represents a strongly dissipative device, for which the resonances become substantially broadened and reduced in amplitude. The resonance quality factor was extracted from the simulated linewidths using

$$Q = \frac{f_0}{\Delta f} \approx \frac{\pi^2 f_0 D}{2 v_p \ln |S_p S_{pp}|}, \tag{C.2}$$

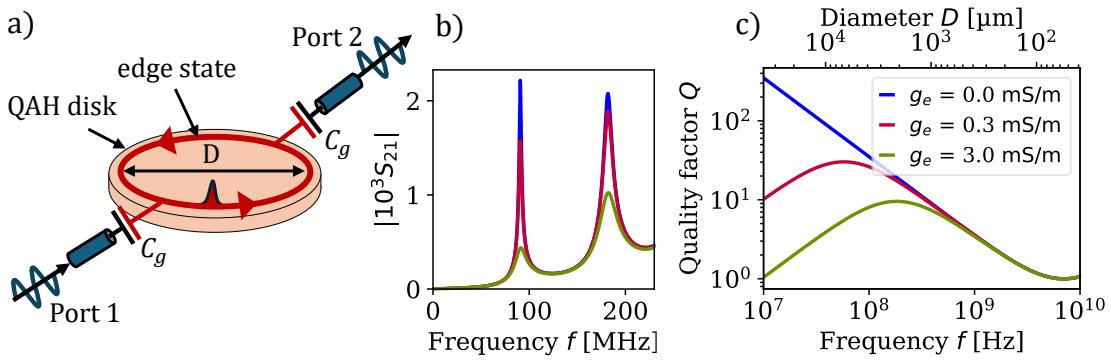

Figure C.1: Predicted response of a quantum anomalous Hall (QAH) edge-state resonator. (a) Schematic of a disk-shaped QAH device of diameter D with two microwave ports, which are coupled via the capacitance C_g. (b) Simulated transmission amplitude $|S_{21}|$ as a function of frequency for different conductivities g_e. Resonance peaks appear for $\phi/2\pi = n\pi Df/v$, with $n = 0, 1, ...$ Increasing dissipation (g_e) reduces the peak amplitude and broadens the resonances. (c) Corresponding quality factor Q obtained from the first resonances as a function of frequency f. The upper axis indicates the resonator diameter that is necessary to reach a matching resonance frequency. For low frequencies, the residual bulk conductance g_e limits the quality factor. At high frequencies, it is limited by the screening of charge puddles. The simulations are done for realistic model parameter: $C_g = 10\,\mathrm{fF}, c_p = 100\,\mathrm{pF/m}, f_p = 7\,\mathrm{GHz}$

where f_0 is the resonance frequency,Δf is the full width at half maximum of the resonance peak, and v_p is the plasmon velocity. As shown in Fig. C.1(c), the quality factor decreases with increasing frequency f and bulk conductance g_e. For ideal edge states, quality factors exceeding 10^2 are predicted at tens of MHz. However, even moderate bulk conductance g_e leads to a substantial reduction of Q. Calculations show that the quality factor scales as $Q \propto g_e^{-1}$. The quality factor for GHz frequencies is limited by the screening of charge puddles, leading to a decrease of the quality factor with increasing frequencies $Q \propto f^{-1}$. The upper axis in Fig. C.1(c) converts resonance frequency into the equivalent resonator diameter D, illustrating the device dimensions required to achieve resonances at a given frequency.

Appendix D

Monte Carlo simulation of rf-driven quantum dots

In this appendix, we describe a Monte Carlo simulation used to model electron transport through a single-level quantum dot driven by a radio-frequency (RF) excitation. The simulation provides a time-resolved, stochastic description of tunneling events between the quantum dot and its leads and allows the extraction of both DC and RF current components.

Physical Model

We consider a quantum dot coupled to two electronic reservoirs, referred to as the left (L) and right (R) leads, via tunnel barriers characterized by tunneling rates Γ_L and Γ_R. The dot is assumed to host at most a single excess electron at any given time, such that the system can be described by two charge states: empty or occupied.
The energy of the quantum dot level is modulated harmonically in time by an RF signal,

$$E_d(t) = E_0 + A\cos(\omega t), \tag{D.1}$$

where E_0 is a static energy offset controlled by a gate voltage, A is the RF amplitude, and $\omega = 2\pi f$ is the angular drive frequency. In addition, capacitive coupling to the right lead is included by allowing its electrochemical potential to oscillate in time,

$$\mu_R(t) = 2A\cos(\omega t - \phi), \tag{D.2}$$

while the left lead is kept at a fixed chemical potential $\mu_L = 0$. ϕ corresponds to the phase-shift of the stray signal.
Electron tunneling between the dot and the leads is treated as a stochastic process governed by the tunnel rates and the Fermi–Dirac occupation of the leads.

Monte Carlo Time Evolution

Time is discretized into steps of duration Δt, chosen to be small compared to the inverse tunneling rates,

$$\Delta t \ll \Gamma_{L,R}^{-1}. \tag{D.3}$$

The occupation of the quantum dot is updated probabilistically at each time step according to the instantaneous tunneling probabilities. For a given dot energy $E_d(t)$, the probability that an electron occupies an energy state in lead $\alpha \in \{L, R\}$ is given by the Fermi–Dirac distribution,

$$f_\alpha(E_d) = \frac{1}{1 + \exp\left(\frac{E_d - \mu_\alpha}{k_B T}\right)}, \tag{D.4}$$

where T is the electron temperature. The probability for a tunneling event to occur between the dot and lead α during a single time step is

$$p_\alpha = 1 - \exp(-\Gamma_\alpha \Delta t), \tag{D.5}$$

where Γ_α is the corresponding tunnel rate.

Update Rules

At each time step, the following update rules are applied:

- If the dot is occupied, the electron may tunnel out to the left lead with probability $p_L(1 - f_L)$ or to the right lead with probability $p_R(1 - f_R)$.
- If the dot is empty, an electron may tunnel in from the left lead with probability $p_L f_L$ or from the right lead with probability $p_R f_R$.

Random numbers drawn from a uniform distribution are used to determine whether a tunneling event occurs. At most one tunneling event is allowed per time step. Each tunneling event is recorded as a discrete current pulse of magnitude $\pm e$, with the sign determined by the direction of charge flow.

Time-Resolved Current

The instantaneous current in each lead is represented as a discrete time series of tunneling events. To extract the RF response at the drive frequency, the simulated

current is demodulated using a digital lock-in technique. For each lead α, the in-phase (X_α) and quadrature (Y_α) components are computed as

$$X_\alpha = 2\sum_n I_\alpha(t_n)\cos(\omega t_n), \tag{D.6}$$

$$Y_\alpha = 2\sum_n I_\alpha(t_n)\sin(\omega t_n), \tag{D.7}$$

where $I_\alpha(t_n)$ denotes the instantaneous current contribution at time step t_n. The complex RF current amplitude is then given by

$$I_\alpha^{(\mathrm{RF})} = \frac{e}{T}\left(X_\alpha + iY_\alpha\right), \tag{D.8}$$

where normalization by the total simulation time T converts the discrete sums into currents. The simulation is repeated for a range of static gate offsets E_0 and RF amplitudes A. For each parameter pair, we record the complex RF current into the left and right lead, and the net DC current averaged over the simulation time. An example implementation of the Monte Carlo simulation is shown in Listing D.1.

Limitations

The model intentionally neglects higher-order processes such as cotunneling, energy-dependent tunnel rates, and electron–electron interactions. Despite these simplifications, the simulation captures the essential stochastic dynamics of RF-driven tunneling and provides an intuitive connection between microscopic tunneling events and experimentally measured RF currents.

```
import numpy as np
import matplotlib.pyplot as plt
# Simulation Parameters
dt = 5e-12  # Time step (5 ps)
T = 2e-7    # Total simulation time (100 ns)
num_steps = int(T / dt)  # Number of time steps
# Quantum dot parameters
f = 1e9  # AC frequency (1 GHz)
omega = 2 * np.pi * f
# Tunneling rates (symmetric barriers)
Gamma_L = 8e9  # Left lead (5 GHz)
Gamma_R = 8e9  # Right lead (10 GHz)
# Electron temperature and Fermi function
kT = 10e-6  # Thermal energy (~10 ueV)

def fermi_function(E, mu): #Fermi-Dirac distribution
    return 1 / (1 + np.exp((E - mu) / kT))

E0=0 #  DC gate voltage
A=0 # RF amplitude
current_L = 0  # Net electron flow to left lead
current_R = 0  # Net electron flow to right lead
dot_occupied = False  # Initialize empty dot
time_array = np.linspace(0, T, num_steps)
E_d_array = E0 + A * np.cos(omega * time_array)  # Dot energy
   oscillation
E_right_array = 2*A * np.cos(omega * time_array-np.pi/4)  # Dot
   energy oscillation
fermi_L_array = fermi_function(E_d_array, 0)  # Time-dependent
   Fermi level in left lead
fermi_R_array = fermi_function(E_d_array, E_right_array)  #
   Right lead remains fixed
rand_vals = np.random.rand(num_steps, 2)  # Generate fresh
   random numbers
instantaneous_current_L = np.zeros(num_steps)
instantaneous_current_R = np.zeros(num_steps)
omega = 2 * np.pi * f
reference_cos = np.cos(omega * time_array)
reference_sin = np.sin(omega * time_array)
# Monte Carlo loop
```

```
for step in range(num_steps):
    f_L = fermi_L_array[step]
    f_R = fermi_R_array[step]
    if dot_occupied:
        # Electron can tunnel out to L or R
        if rand_vals[step, 0] < (1 - np.exp(-Gamma_L * dt))*(1-
           f_L):
            dot_occupied = False
            current_L += 1
            instantaneous_current_L[step] = 1
        elif rand_vals[step, 1] < (1 - np.exp(-Gamma_R *
           dt))*(1- f_R):
            dot_occupied = False
            current_R += 1
            instantaneous_current_R[step] = 1
    else:
        # Electron can tunnel in from L or R
        if rand_vals[step, 0] < (1 - np.exp(-Gamma_L * dt)) *
           f_L:
            dot_occupied = True
            current_L -= 1
            instantaneous_current_L[step] = -1
        elif rand_vals[step, 1] < (1 - np.exp(-Gamma_R * dt)) *
           f_R:
            dot_occupied = True
            current_R -= 1
            instantaneous_current_R[step] = -1
```

Listing D.1: Monte Carlo simulation of RF-driven transport through a quantum dot.

Appendix E

Non-ohmic to ohmic crossover for varying magnetic field and carrier type

This appendix provides additional measurements that test the robustness of the breakdown mechanism discussed in Section 4.3, which focuses on measurements at $B = 9\,\mathrm{T}$ on electron-doped states to establish the physical picture of the non-ohmic to ohmic crossover. The data presented here demonstrate that the same behavior persists for lower magnetic fields and for hole-doped states. These results support the generality of the interpretation but are not required for understanding the main conclusions and are therefore presented in the appendix for completeness.

We first examine the dependence of the breakdown behavior on the magnetic field. Figure E.1a shows the relation between the breakdown voltage U_{BD} and the activation temperature T_0 for the $\nu = 6$ quantum Hall gap measured at different magnetic fields. Within experimental uncertainty, the scaling of U_{BD} with T_0 is unchanged when the magnetic field is varied. This observation indicates that the relevant energy scales governing breakdown are set by the degree of bulk localization, as quantified by T_0, rather than by the absolute magnetic field strength.

Using the same analysis as in Section 4.3.4, we extract an effective electronic temperature T_{eff} by mapping the breakdown curves $\sigma(U_{\mathrm{dc}})$ onto the temperature calibration curve $\sigma(T = T_{\mathrm{eff}})$. By fitting the voltage dependence $T_{\mathrm{eff}}(U_{\mathrm{dc}})$ with a power-law relation, we extract the exponent β. The evolution of β as a function of the activation temperature T_0 is shown in Fig. E.1b. Consistent with the results presented in Section 4.3, β increases from values close to 0.5 to values approaching 1 with increasing T_0, reflecting a crossover from non-ohmic, field-driven hopping transport to an ohmic regime dominated by Joule heating.

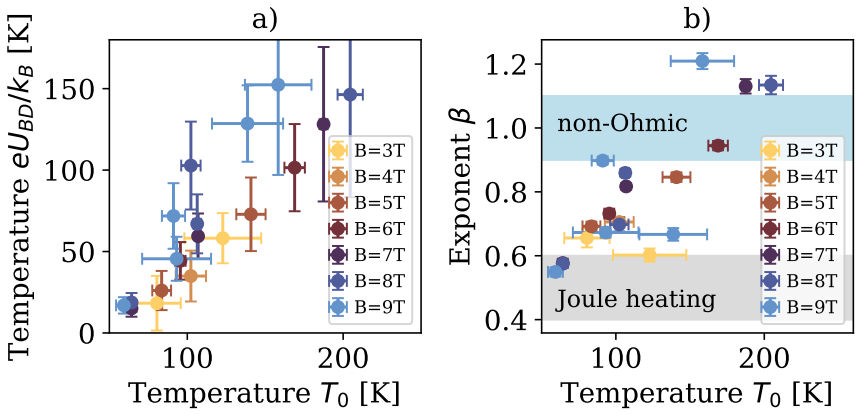

Figure E.1: Breakdown behavior at different magnetic fields. (a) Breakdown energy $eU_{\mathrm{BD}}/k_{\mathrm{B}}$ (defined as $\sigma(U_{\mathrm{BD}}) = \sigma_{\max}/2$) as a function of the activation temperature T_0, extracted from temperature-dependent bulk conductance measurements for the $\nu = 6$ gap at different magnetic fields. The data collapse onto a common trend, indicating field-independent scaling with T_0. (b) Exponent β obtained from power-law fits of the form $T_{\mathrm{eff}} \propto U^{\beta}$ as a function of T_0. The systematic increase of β from approximately 0.5 to 1 with increasing T_0 is observed for all magnetic fields.

Importantly, this evolution of β is independent of the applied magnetic field.
In addition, we investigate the breakdown behavior for hole-doped states at filling factors $\nu = -6$ and $\nu = -10$, shown in Fig. E.2. The dependence of the breakdown voltage on T_0, as well as the evolution of the exponent β extracted from the relation $T_{\mathrm{eff}} \propto U^{\beta}$, closely mirrors the behavior observed for electron-doped states in Section 4.3. This symmetry between electron and hole transport demonstrates that the variable-range-hopping-based breakdown mechanism applies independently of carrier type.
Taken together, these supplementary measurements confirm that the observed crossover from non-ohmic hopping transport to an ohmic, Joule-heating-dominated regime is governed by bulk localization physics. The breakdown behavior is robust against variations in magnetic field and carrier polarity, further supporting the interpretation developed in the main text.

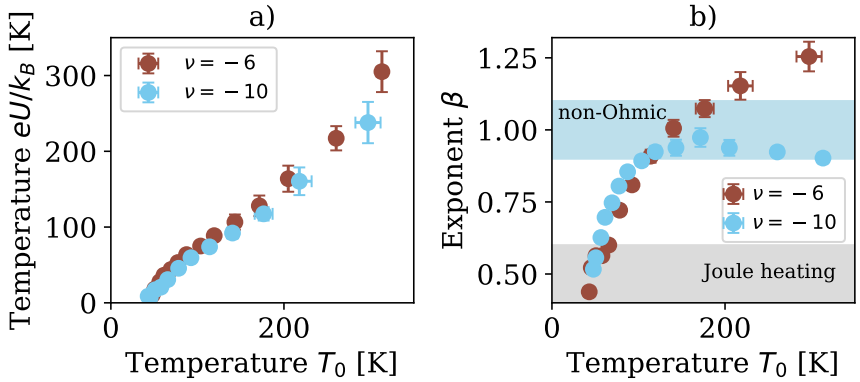

Figure E.2: Breakdown behavior for hole-doped quantum Hall states. (a) Breakdown energy $eU_{\mathrm{BD}}/k_{\mathrm{B}}$ (defined as $\sigma(U_{\mathrm{BD}}) = \sigma_{\mathrm{max}}/2$) as a function of the activation temperature T_0 for hole-doped states at filling factors $\nu = -6$ and $\nu = -10$ measured at $B = 9\,\mathrm{T}$. The scaling behavior matches that observed for electron-doped states. (b) Dependence of the exponent β on T_0, demonstrating the same crossover from non-ohmic transport to an ohmic, Joule-heating-dominated regime as found on the electron side.

Bibliography

[1] T. Ihn, *Semiconductor nanostructures: quantum states and electronic transport* (Oxford University Press, Oxford New York, 2015).

[2] K. v. Klitzing, G. Dorda, and M. Pepper, "New method for high-accuracy determination of the fine-structure constant based on quantized hall resistance", Phys. Rev. Lett. **45**, 494–497 (1980).

[3] M. Furlan, "Electronic transport and the localization length in the quantum hall effect", Phys. Rev. B **57**, 14818–14828 (1998).

[4] F. Hohls, U. Zeitler, and R. J. Haug, "Hopping conductivity in the quantum hall effect: revival of universal scaling", Phys. Rev. Lett. **88**, 036802 (2002).

[5] C.-Z. Chang, J. Zhang, X. Feng, J. Shen, Z. Zhang, M. Guo, K. Li, Y. Ou, P. Wei, L.-L. Wang, Z.-Q. Ji, Y. Feng, S. Ji, X. Chen, J. Jia, X. Dai, Z. Fang, S.-C. Zhang, K. He, Y. Wang, L. Lu, X.-C. Ma, and Q.-K. Xue, "Experimental Observation of the Quantum Anomalous Hall Effect in a Magnetic Topological Insulator", Science **340**, 167–170 (2013).

[6] Y. Deng, Y. Yu, M. Z. Shi, Z. Guo, Z. Xu, J. Wang, X. H. Chen, and Y. Zhang, "Quantum anomalous hall effect in intrinsic magnetic topological insulator $\mathrm{MnBi_2Te_4}$", Science **367**, 895–900 (2020).

[7] M. Serlin, C. L. Tschirhart, H. Polshyn, Y. Zhang, J. Zhu, K. Watanabe, T. Taniguchi, L. Balents, and A. F. Young, "Intrinsic quantized anomalous hall effect in a moiré heterostructure", Science **367**, 900–903 (2020).

[8] T. Han, Z. Lu, Y. Yao, J. Yang, J. Seo, C. Yoon, K. Watanabe, T. Taniguchi, L. Fu, F. Zhang, and L. Ju, "Large quantum anomalous hall effect in spin-orbit proximitized rhombohedral graphene", Science **384**, 647–651 (2024).

[9] T. Li, S. Jiang, B. Shen, Y. Zhang, L. Li, Z. Tao, T. Devakul, K. Watanabe, T. Taniguchi, L. Fu, J. Shan, and K. F. Mak, "Quantum anomalous hall effect from intertwined moiré bands", Nature **600**, 641–646 (2021).

[10] J. Cai, E. Anderson, C. Wang, X. Zhang, X. Liu, W. Holtzmann, Y. Zhang, F. Fan, T. Taniguchi, K. Watanabe, Y. Ran, T. Cao, L. Fu, D. Xiao, W. Yao, and X. Xu, "Signatures of fractional quantum anomalous hall states in twisted MoTe2", Nature **622**, 63–68 (2023).

[11] H. Park, J. Cai, E. Anderson, Y. Zhang, J. Zhu, X. Liu, C. Wang, W. Holtzmann, C. Hu, Z. Liu, T. Taniguchi, K. Watanabe, J.-H. Chu, T. Cao, L. Fu, W. Yao, C.-Z. Chang, D. Cobden, D. Xiao, and X. Xu, "Observation of fractionally quantized anomalous hall effect", Nature **622**, 74–79 (2023).

[12] Z. Lu, T. Han, Y. Yao, A. P. Reddy, J. Yang, J. Seo, K. Watanabe, T. Taniguchi, L. Fu, and L. Ju, "Fractional quantum anomalous hall effect in multilayer graphene", Nature **626**, 759–764 (2024).

[13] T. Cao, L. Fu, L. Ju, D. Xiao, and X. Xu, "Fractional quantum anomalous hall effect", Annu. Rev. Condens. Matter Phys. (2025).

[14] H. Park, W. Li, C. Hu, C. Beach, M. Gonçalves, J. F. Mendez-Valderrama, J. Herzog-Arbeitman, T. Taniguchi, K. Watanabe, D. Cobden, L. Fu, B. A. Bernevig, N. Regnault, J.-H. Chu, D. Xiao, and X. Xu, "Observation of dissipationless fractional chern insulator", Nat. Phys. (2026).

[15] G. Viola and D. P. DiVincenzo, "Hall Effect Gyrators and Circulators", Phys. Rev. X **4**, 021019 (2014).

[16] A. C. Mahoney, J. I. Colless, L. Peeters, S. J. Pauka, E. J. Fox, X. Kou, L. Pan, K. L. Wang, D. Goldhaber-Gordon, and D. J. Reilly, "Zero-field edge plasmons in a magnetic topological insulator", Nat. Commun. **8**, 1836 (2017).

[17] L. A. Martinez, G. Qiu, P. Deng, P. Zhang, K. G. Ray, L. Tai, M.-T. Wei, H. He, K. L. Wang, J. L. DuBois, and D.-X. Qu, "Edge magnetoplasmon dispersion and time-resolved plasmon transport in a quantum anomalous hall insulator", Phys. Rev. Res. **6**, 013081 (2024).

[18] N. Kumada, H. Kamata, and T. Fujisawa, "Edge magnetoplasmon transport in gated and ungated quantum hall systems", Phys. Rev. B **84**, 045314 (2011).

[19] M. Hashisaka, H. Kamata, N. Kumada, K. Washio, R. Murata, K. Muraki, and T. Fujisawa, "Distributed-element circuit model of edge magnetoplasmon transport", Phys. Rev. B **88**, 235409 (2013).

[20] G. Lippertz, A. Bliesener, A. Uday, L. M. C. Pereira, A. A. Taskin, and Y. Ando, "Current-induced breakdown of the quantum anomalous hall effect", Phys. Rev. B **106**, 045419 (2022).

[21] K. M. Fijalkowski, N. Liu, P. Mandal, S. Schreyeck, K. Brunner, C. Gould, and L. W. Molenkamp, "Quantum anomalous Hall edge channels survive up to the Curie temperature", Nat. Commun. **12**, 5599 (2021).

[22] E. J. Fox, I. T. Rosen, Y. Yang, G. R. Jones, R. E. Elmquist, X. Kou, L. Pan, K. L. Wang, and D. Goldhaber-Gordon, "Part-per-million quantization and current-induced breakdown of the quantum anomalous hall effect", Phys. Rev. B **98**, 075145 (2018).

[23] I. T. Rosen, M. P. Andersen, L. K. Rodenbach, L. Tai, P. Zhang, K. L. Wang, M. A. Kastner, and D. Goldhaber-Gordon, "Measured potential profile in a quantum anomalous hall system suggests bulk-dominated current flow", Phys. Rev. Lett. **129**, 246602 (2022).

[24] K. Bennaceur, P. Jacques, F. Portier, P. Roche, and D. C. Glattli, "Unveiling quantum hall transport by efros-shklovskii to mott variable-range hopping transition in graphene", Phys. Rev. B **86**, 085433 (2012).

[25] A. M. R. Baker, J. A. Alexander-Webber, T. Altebaeumer, and R. J. Nicholas, "Energy relaxation for hot dirac fermions in graphene and breakdown of the quantum hall effect", Phys. Rev. B **85**, 115403 (2012).

[26] F. Ladieu, D. L'Hôte, and R. Tourbot, "Non-ohmic hopping transport in $a-\mathrm{YSi}$: from isotropic to directed percolation", Phys. Rev. B **61**, 8108–8118 (2000).

[27] G. Fève, A. Mahé, J.-M. Berroir, T. Kontos, B. Plaçais, D. C. Glattli, A. Cavanna, B. Etienne, and Y. Jin, "An on-demand coherent single-electron source", Science **316**, 1169–1172 (2007).

[28] E. Bocquillon, V. Freulon, J.-M. Berroir, P. Degiovanni, B. Plaçais, A. Cavanna, Y. Jin, and G. Fève, "Coherence and indistinguishability of single electrons emitted by independent sources", Science **339**, 1054–1057 (2013).

[29] H. Bartolomei, M. Kumar, R. Bisognin, A. Marguerite, J.-M. Berroir, E. Bocquillon, B. Plaçais, A. Cavanna, Q. Dong, U. Gennser, Y. Jin, and G. Fève, "Fractional statistics in anyon collisions", Science **368**, 173–177 (2020).

[30] A. K. Geim, "Graphene: status and prospects", Science **324**, 1530–1534 (2009).

[31] C. Volk, C. Neumann, S. Kazarski, S. Fringes, S. Engels, F. Haupt, A. Müller, and C. Stampfer, "Probing relaxation times in graphene quantum dots", Nat. Commun. **4**, 1753 (2013).

[32] L. Banszerus, M. Schmitz, S. Engels, M. Goldsche, K. Watanabe, T. Taniguchi, B. Beschoten, and C. Stampfer, "Ballistic transport exceeding 28 μm in cvd grown graphene", Nano Letters **16**, 1387–1391 (2016).

[33] C. Tong, R. Garreis, A. Knothe, M. Eich, A. Sacchi, K. Watanabe, T. Taniguchi, V. Fal'ko, T. Ihn, K. Ensslin, and A. Kurzmann, "Tunable valley splitting and bipolar operation in graphene quantum dots", Nano Letters **21**, 1068–1073 (2021).

[34] A. Kurzmann, M. Eich, H. Overweg, M. Mangold, F. Herman, P. Rickhaus, R. Pisoni, Y. Lee, R. Garreis, C. Tong, K. Watanabe, T. Taniguchi, K. Ensslin, and T. Ihn, "Excited states in bilayer graphene quantum dots", Phys. Rev. Lett. **123**, 026803 (2019).

[35] A. Blais, R.-S. Huang, A. Wallraff, S. M. Girvin, and R. J. Schoelkopf, "Cavity quantum electrodynamics for superconducting electrical circuits: an architecture for quantum computation", Physical Review A **69**, 062320 (2004).

[36] A. Wallraff, D. I. Schuster, A. Blais, L. Frunzio, R.-S. Huang, J. Majer, S. Kumar, S. M. Girvin, and R. J. Schoelkopf, "Strong coupling of a single photon to a superconducting qubit using circuit quantum electrodynamics", Nature **431**, 162–167 (2004).

[37] P. Burke, "Luttinger liquid theory as a model of the gigahertz electrical properties of carbon nanotubes", IEEE Trans. Nanotechnol. **1**, 129–144 (2002).

[38] N. Kumada, P. Roulleau, B. Roche, M. Hashisaka, H. Hibino, I. Petkovi ć, and D. C. Glattli, "Resonant edge magnetoplasmons and their decay in graphene", Phys. Rev. Lett. **113**, 266601 (2014).

[39] R. C. Ashoori, H. L. Stormer, L. N. Pfeiffer, K. W. Baldwin, and K. West, "Edge magnetoplasmons in the time domain", Phys. Rev. B **45**, 3894–3897 (1992).

[40] D. M. Pozar, *Microwave engineering*, 4th ed (Wiley, Hoboken, NJ, 2012).

[41] R. E. Collin, *Foundations for microwave engineering, 2nd ed* (John Wiley & Sons, New York, NY, 2007).

[42] C. L. Kane, *Bosonization and luttinger liquids*, Lecture notes, Boulder Summer School for Condensed Matter and Materials Physics, 2017.

[43] M. Z. Hasan and C. L. Kane, "Colloquium: topological insulators", Rev. Mod. Phys. **82**, 3045–3067 (2010).

[44] C.-X. Liu, H. Zhang, B. Yan, X.-L. Qi, T. Frauenheim, X. Dai, Z. Fang, and S.-C. Zhang, "Oscillatory crossover from two-dimensional to three-dimensional topological insulators", Phys. Rev. B **81**, 041307 (2010).

[45] A. Gourmelon, "Radiofrequency studies of topological edge states in hgte quantum wells", Theses (Université Paris PSL, Sept. 2022).

[46] S. Takada, G. Georgiou, J. Wang, Y. Okazaki, S. Nakamura, D. Pomaranski, A. Ludwig, A. D. Wieck, M. Yamamoto, C. Bäuerle, and N.-H. Kaneko, "Eigenstate control of plasmon wavepackets with electron-channel blockade", Nat. Commun. **16**, 9942 (2025).

[47] S. Simbierowicz, V. Y. Monarkha, M. von Soosten, S. Andresen, and R. E. Lake, "Calibrated transmission and reflection from a multi-qubit microwave package", Rev. Sci. Instrum. **94**, 054713 (2023).

[48] S. Simbierowicz, V. Y. Monarkha, S. Singh, N. Messaoudi, P. Krantz, and R. E. Lake, "Microwave calibration of qubit drive line components at millikelvin temperatures", Appl. Phys. Lett. **120**, 054004 (2022).

[49] I. Lee, C. K. Kim, J. Lee, S. J. L. Billinge, R. Zhong, J. A. Schneeloch, T. Liu, T. Valla, J. M. Tranquada, G. Gu, and J. C. S. Davis, "Imaging dirac-mass disorder from magnetic dopant atoms in the ferromagnetic topological insulator $\mathrm{Cr_x(Bi_{0.1}Sb_{0.9})_{2-x}Te_3}$", PNAS **112**, 1316–1321 (2015).

[50] Y. X. Chong, X. Liu, R. Sharma, A. Kostin, G. Gu, K. Fujita, J. C. S. Davis, and P. O. Sprau, "Severe dirac mass gap suppression in sb2te3-based quantum anomalous hall materials", Nano Letters **20**, 8001–8007 (2020).

[51] R. Yu, W. Zhang, H.-J. Zhang, S.-C. Zhang, X. Dai, and Z. Fang, "Quantized anomalous hall effect in magnetic topological insulators", Science **329**, 61–64 (2010).

[52] G. Lippertz, "The quantum anomalous hall effect in magnetically doped topological insulators - a study of the current-induced breakdown", PhD thesis (Universität zu Köln, 2023).

[53] Y. Ando, "Topological insulator materials", J. Phys. Soc. Jpn. **82**, 102001 (2013).

[54] Y. Tokura, K. Yasuda, and A. Tsukazaki, "Magnetic topological insulators", Nat. Rev. Phys. **1**, 126–143 (2019).

[55] B. A. Bernevig, T. L. Hughes, and S.-C. Zhang, "Quantum spin hall effect and topological phase transition in hgte quantum wells", Science **314**, 1757–1761 (2006).

[56] A. J. Bestwick, E. J. Fox, X. Kou, L. Pan, K. L. Wang, and D. Goldhaber-Gordon, "Precise quantization of the anomalous hall effect near zero magnetic field", Phys. Rev. Lett. **114**, 187201 (2015).

[57] M. Götz, K. M. Fijalkowski, E. Pesel, M. Hartl, S. Schreyeck, M. Winnerlein, S. Grauer, H. Scherer, K. Brunner, C. Gould, F. J. Ahlers, and L. W. Molenkamp, "Precision measurement of the quantized anomalous Hall resistance at zero magnetic field", Appl. Phys. Lett. **112**, 072102 (2018).

[58] K. M. Fijalkowski, N. Liu, M. Klement, S. Schreyeck, K. Brunner, C. Gould, and L. W. Molenkamp, "A balanced quantum hall resistor", Nat. Electron. (2024).

[59] D. K. Patel, K. M. Fijalkowski, M. Kruskopf, N. Liu, M. Götz, E. Pesel, M. Jaime, M. Klement, S. Schreyeck, K. Brunner, C. Gould, L. W. Molenkamp, and H. Scherer, "A zero external magnetic field quantum standard of resistance at the 10^{-9} level", Nat. Electron. **7**, 1111–1116 (2024).

[60] C. W. Beenakker, P. Baireuther, Y. Herasymenko, I. Adagideli, L. Wang, and A. Akhmerov, "Deterministic Creation and Braiding of Chiral Edge Vortices", Phys. Rev. Lett. **122**, 146803 (2019).

[61] C. Beenakker, A. Grabsch, and Y. Herasymenko, "Electrical detection of the Majorana fusion rule for chiral edge vortices in a topological superconductor", SciPost Physics **6**, 022 (2019).

[62] A. Uday, G. Lippertz, K. Moors, H. F. Legg, R. Joris, A. Bliesener, L. M. C. Pereira, A. A. Taskin, and Y. Ando, "Induced superconducting correlations in a quantum anomalous hall insulator", Nat. Phys. **20**, 1589–1595 (2024).

[63] W. Yuan, L.-J. Zhou, K. Yang, Y.-F. Zhao, R. Zhang, Z. Yan, D. Zhuo, R. Mei, Y. Wang, H. Yi, M. H. W. Chan, M. Kayyalha, C.-X. Liu, and C.-Z. Chang, "Electrical switching of the edge current chirality in quantum anomalous hall insulators", Nat. Mater. **23**, 58–64 (2024).

[64] Y. Fan, P. Upadhyaya, X. Kou, M. Lang, S. Takei, Z. Wang, J. Tang, L. He, L.-T. Chang, M. Montazeri, G. Yu, W. Jiang, T. Nie, R. N. Schwartz, Y. Tserkovnyak, and K. L. Wang, "Magnetization switching through giant spin-orbit torque in a magnetically doped topological insulator heterostructure", Nat. Mater. **13**, 699–704 (2014).

[65] Y. Liu, A. Lee, K. Qian, P. Zhang, Z. Xiao, H. He, Z. Ren, S. K. Cheung, R. Liu, Y. Li, X. Zhang, Z. Ma, J. Zhao, W. Zhao, G. Yu, X. Wang, J. Liu, Z. Wang, K. L. Wang, and Q. Shao, "Cryogenic in-memory computing using magnetic topological insulators", Nat. Mater. **24**, 559–564 (2025).

[66] S. Bosco, F. Haupt, and D. P. DiVincenzo, "Self-impedance-matched hall-effect gyrators and circulators", Phys. Rev. Appl. **7**, 024030 (2017).

[67] L. A. Martinez, N. Du, N. Materise, S. O. Kelley, X. Wu, G. Qiu, K. L. Wang, P. Gianpaolo, T. Low, and D.-X. Qu, "Circulators based on coupled quantum anomalous hall insulators and resonators", arXiv 2505.07770 (2025).

[68] A. Tarascio, Y. Zhao, R. S. Eggli, T. Patlatiuk, C. Reichl, W. Wegscheider, S. Bosco, and D. M. Zumbühl, "Compact self-matched gyrators using edge magnetoplasmons", arXiv 2602.05439 (2026).

[69] K. Yasuda, M. Mogi, R. Yoshimi, A. Tsukazaki, K. S. Takahashi, M. Kawasaki, F. Kagawa, and Y. Tokura, "Quantized chiral edge conduction on domain walls of a magnetic topological insulator", Science **358**, 1311–1314 (2017).

[70] M. Kawamura, R. Yoshimi, A. Tsukazaki, K. S. Takahashi, M. Kawasaki, and Y. Tokura, "Current-driven instability of the quantum anomalous hall effect in ferromagnetic topological insulators", Phys. Rev. Lett. **119**, 016803 (2017).

[71] B. Skinner and B. I. Shklovskii, "Theory of the random potential and conductivity at the surface of a topological insulator", Phys. Rev. B **87**, 075454 (2013).

[72] M. Bagchi, L. Pitz-Paal, C. P. Grams, O. Breunig, N. Borgwardt, Z. Wang, Y. Ando, M. Grüninger, and J. Hemberger, "Large positive magnetoconductivity at microwave frequencies in the compensated topological insulator $BiSbTeSe_2$", Phys. Rev. B **99**, 161121 (2019).

[73] J. Brede, M. Bagchi, A. Greichgauer, A. Uday, A. Bliesener, G. Lippertz, R. Yazdanpanah, A. Taskin, and Y. Ando, "Characterizing the chemical potential disorder in the topological insulator $(\mathrm{Bi}_{1-x}\mathrm{Sb}_x)_2\mathrm{Te}_3$ thin films", Phys. Rev. Mater. **8**, 104202 (2024).

[74] N. Borgwardt, J. Lux, I. Vergara, Z. Wang, A. A. Taskin, K. Segawa, P. H. M. van Loosdrecht, Y. Ando, A. Rosch, and M. Grüninger, "Self-organized charge puddles in a three-dimensional topological material", Phys. Rev. B **93**, 245149 (2016).

[75] D. Kong, Y. Chen, J. J. Cha, Q. Zhang, J. G. Analytis, K. Lai, Z. Liu, S. S. Hong, K. J. Koski, S.-K. Mo, Z. Hussain, I. R. Fisher, Z.-X. Shen, and Y. Cui, "Ambipolar field effect in the ternary topological insulator (Bi(x)Sb(1-x))2Te3 by composition tuning", Nat. Nanotechnol. **6**, 705–709 (2011).

[76] J. Zhang, C.-Z. Chang, Z. Zhang, J. Wen, X. Feng, K. Li, M. Liu, K. He, L. Wang, X. Chen, Q.-K. Xue, X. Ma, and Y. Wang, "Band structure engineering in (Bi(1-x)Sb(x))(2)Te(3) ternary topological insulators", Nat. Commun. **2**, 574 (2011).

[77] T. Bömerich, J. Lux, Q. T. Feng, and A. Rosch, "Length scale of puddle formation in compensation-doped semiconductors and topological insulators", Phys. Rev. B **96**, 075204 (2017).

[78] P. Deng, P. Zhang, G. Qiu, T.-H. Yang, C. Niu, Y. Li, W. Cui, Y. Feng, P. D. Ye, K. He, K. Chang, and K. L. Wang, "Universal conductance fluctuations in quantum anomalous hall insulators", Advanced Materials, e18012 (2025).

[79] C.-Z. Chang, W. Zhao, D. Y. Kim, P. Wei, J. K. Jain, C. Liu, M. H. W. Chan, and J. S. Moodera, "Zero-field dissipationless chiral edge transport and the nature of dissipation in the quantum anomalous hall state", Phys. Rev. Lett. **115**, 057206 (2015).

[80] V. Ambegaokar, B. I. Halperin, and J. S. Langer, "Hopping conductivity in disordered systems", Phys. Rev. B **4**, 2612–2620 (1971).

[81] A. L. Efros and B. I. Shklovskii, "Coulomb gap and low temperature conductivity of disordered systems", J. Phys. C: Solid State Phys. **8**, L49 (1975).

[82] S. Baranovski, *Charge transport in disordered solids* (Wiley, Chichester, England, 2006).

[83] B. I. Shklovskii, "Half-century of efros–shklovskii coulomb gap: romance with coulomb interaction and disorder", Low Temp. Phys. **50**, 1101–1112 (2024).

[84] H. Bluhm, T. Brückel, M. Morgenstern, G. von Plessen, and C. Stampfer, *Electrons in solids, Mesoscopics, photonics, quantum computing, correlations, topology* (De Gruyter, Berlin, Boston, 2019).

[85] I. P. Zvyagin, "Hopping conduction in the presence of an electromagnetic wave", Physica Status Solidi (b) **88**, 149–154 (1978).

[86] R. Keiper and R. F. Schuchardt, "On the theory of photon-induced dc hopping conductivity in disordered semiconductors", Phys. Status Solidi B. **85**, 155–162 (1978).

[87] B. I. Shklovskii and A. L. Efros, *Electronic properties of doped semiconductors*, red. by M. Cardona, P. Fulde, and H.-J. Queisser, Vol. 45, Springer Series in Solid-State Sciences (Springer Berlin Heidelberg, Berlin, Heidelberg, 1984).

[88] G. Ebert, K. von Klitzing, C. Probst, E. Schuberth, K. Ploog, and G. Weimann, "Hopping conduction in the landau level tails in gaas-alxga1-xas heterostructures at low temperatures", Solid State Commun. **45**, 625–628 (1983).

[89] A. Briggs, Y. Guldner, J. P. Vieren, M. Voos, J. P. Hirtz, and M. Razeghi, "Low-temperature investigations of the quantum hall effect in $\mathrm{In}_x\mathrm{Ga}_{1-x}\mathrm{As}-\mathrm{InP}$ heterojunctions", Phys. Rev. B **27**, 6549–6552 (1983).

[90] D. G. Polyakov and B. I. Shklovskii, "Variable range hopping as the mechanism of the conductivity peak broadening in the quantum hall regime", Phys. Rev. Lett. **70**, 3796–3799 (1993).

[91] B. I. Shklovskii, "Hopping conduction in semiconductors subjected to a strong electric field.", Sov Phys Semicond **6**, 1964–1967 (1973).

[92] E. Bocquillon, V. Freulon, J.-. Berroir, P. Degiovanni, B. Plaçais, A. Cavanna, Y. Jin, and G. Fève, "Separation of neutral and charge modes in one-dimensional chiral edge channels", Nat. Commun. **4** (2013).

[93] H. Kamata, N. Kumada, M. Hashisaka, K. Muraki, and T. Fujisawa, "Fractionalized wave packets from an artificial Tomonaga-Luttinger liquid", Nat. Nanotechnol. **9**, 177–181 (2014).

[94] T. Röper, H. Thomas, D. Rosenbach, A. Uday, G. Lippertz, A. Denis, P. Morfin, A. A. Taskin, Y. Ando, and E. Bocquillon, "Propagation, dissipation, and breakdown in quantum anomalous hall edge states probed by microwave edge plasmons", Phys. Rev. B **110**, L161403 (2024).

[95] T. P. Ginley, Y. Wang, and S. Law, "Topological insulator film growth by molecular beam epitaxy: a review", Crystals **6** (2016).

[96] A. Bliesener, "Molecular beam epitaxy growth of topological materials", PhD thesis (Universität zu Köln, 2020).

[97] A. Gourmelon, H. Kamata, J.-M. Berroir, G. Fève, B. Pla çais, and E. Bocquillon, "Characterization of helical luttinger liquids in microwave stepped-impedance edge resonators", Phys. Rev. Res. **2**, 043383 (2020).

[98] C. Jozwiak, J. A. Sobota, K. Gotlieb, A. F. Kemper, C. R. Rotundu, R. J. Birgeneau, Z. Hussain, D.-H. Lee, Z.-X. Shen, and A. Lanzara, "Spin-polarized surface resonances accompanying topological surface state formation", Nat. Commun. **7**, 13143 (2016).

[99] Y. L. Chen, J.-H. Chu, J. G. Analytis, Z. K. Liu, K. Igarashi, H.-H. Kuo, X. L. Qi, S. K. Mo, R. G. Moore, D. H. Lu, M. Hashimoto, T. Sasagawa, S. C. Zhang, I. R. Fisher, Z. Hussain, and Z. X. Shen, "Massive dirac fermion on the surface of a magnetically doped topological insulator", Science **329**, 659–662 (2010).

[100] D. B. Chklovskii, B. I. Shklovskii, and L. I. Glazman, "Electrostatics of edge channels", Phys. Rev. B **46**, 4026–4034 (1992).

[101] C. d. C. Chamon and X. G. Wen, "Sharp and smooth boundaries of quantum hall liquids", Phys. Rev. B **49**, 8227–8241 (1994).

[102] H. Kamata, H. Irie, N. Kumada, and K. Muraki, "Time-resolved measurement of ambipolar edge magnetoplasmon transport in inas/ingasb composite quantum wells", Phys. Rev. Res. **4**, 033214 (2022).

[103] A. Gourmelon, E. Frigerio, H. Kamata, L. Lunczer, A. Denis, P. Morfin, M. Rosticher, J.-M. Berroir, G. Fève, B. Pla çais, H. Buhmann, L. W. Molenkamp, and E. Bocquillon, "Velocity and confinement of edge plasmons in hgte-based two-dimensional topological insulators", Phys. Rev. B **108**, 035405 (2023).

[104] T. Knispel, W. Jolie, N. Borgwardt, J. Lux, Z. Wang, Y. Ando, A. Rosch, T. Michely, and M. Grüninger, "Charge puddles in the bulk and on the surface of the topological insulator $BiSbTeSe_2$ studied by scanning tunneling microscopy and optical spectroscopy", Phys. Rev. B **96**, 195135 (2017).

[105] C. Lin, M. Hashisaka, T. Akiho, K. Muraki, and T. Fujisawa, "Time-resolved investigation of plasmon mode along interface channels in integer and fractional quantum hall regimes", Phys. Rev. B **104**, 125304 (2021).

[106] A. Gourmelon, H. Kamata, J.-M. Berroir, G. Fève, B. Pla çais, and E. Bocquillon, "Characterization of helical luttinger liquids in microwave stepped-impedance edge resonators", Phys. Rev. Res. **2**, 043383 (2020).

[107] M. Allen, Y. T. Cui, E. Y. Ma, M. Mogi, M. Kawamura, I. C. Fulga, D. Goldhaber-Gordon, Y. Tokura, and Z. X. Shen, "Visualization of an axion insulating state at the transition between 2 chiral quantum anomalous hall states", PNAS **116**, 14511–14515 (2019).

[108] J. Böttcher, C. Tutschku, L. W. Molenkamp, and E. M. Hankiewicz, "Survival of the quantum anomalous hall effect in orbital magnetic fields as a consequence of the parity anomaly", Phys. Rev. Lett. **123**, 226602 (2019).

[109] J. Böttcher, C. Tutschku, and E. M. Hankiewicz, "Fate of quantum anomalous hall effect in the presence of external magnetic fields and particle-hole asymmetry", Phys. Rev. B. **101** (2020).

[110] O. Breunig, Z. Wang, A. A. Taskin, J. Lux, A. Rosch, and Y. Ando, "Gigantic negative magnetoresistance in the bulk of a disordered topological insulator", Nat. Commun. **8**, 15545 (2017).

[111] F. Zhang, C. Ding, J. Zhou, and Y. Yao, "Chiral edge plasmons in quantum anomalous hall insulators", arXiv 2404.13930 (2024).

[112] E. Frigerio, G. Rebora, M. Ruelle, H. Souquet-Basiège, Y. Jin, U. Gennser, A. Cavanna, B. Plaçais, E. Baudin, J.-M. Berroir, I. Safi, P. Degiovanni, G. Fève, and G. C. Ménard, "Gate tunable edge magnetoplasmon resonators", Commun. Phys. **7** (2024).

[113] G. M. Ferguson, R. Xiao, A. R. Richardella, D. Low, N. Samarth, and K. C. Nowack, "Direct visualization of electronic transport in a quantum anomalous hall insulator", Nat. Mater. **22**, 1100–1105 (2023).

[114] G. M. Ferguson, R. Xiao, A. R. Richardella, A. Kaczmarek, N. Samarth, and K. C. Nowack, "Visualizing the breakdown of the quantum anomalous hall effect", arXiv 2503.02633 (2025).

[115] A. F. Young, C. R. Dean, L. Wang, H. Ren, P. Cadden-Zimansky, K. Watanabe, T. Taniguchi, J. Hone, K. L. Shepard, and P. Kim, "Spin and valley quantum hall ferromagnetism in graphene", Nat. Phys. **8**, 550–556 (2012).

[116] T. Röper, D. Rosenbach, A. Rosch, A. A. Taskin, Y. Ando, and E. Bocquillon, "Breakdown of the quantum anomalous hall effect under microwave drives", Phys. Rev. B **112**, L201301 (2025).

[117] T. Röper, A. Zhang, K. Watanabe, T. Taniguchi, O. Maillet, F. D. Parmentier, and E. Bocquillon, "Non-ohmic to ohmic crossover in the breakdown of the quantum hall states in graphene under broadband excitations", arXiv (2025).

[118] I. Zvyagin, "The theory of the photon-phonon-assisted hopping in disordered semiconductors", J. Non-Cryst. Solids **35-36**, 135–140 (1980).

[119] R. A. Melcer, A. Gil, A. K. Paul, P. Tiwari, V. Umansky, M. Heiblum, Y. Oreg, A. Stern, and E. Berg, "Heat conductance of the quantum hall bulk", Nature **625**, 489–493 (2024).

[120] N. W. Ashcroft and N. D. Mermin, *Solid state physics* (Holt, Rinehart & Winston, New York, 1976).

[121] E. Chow, H. P. Wei, S. M. Girvin, W. Jan, and J. E. Cunningham, "Effect of disorder on phonon emissions from a two-dimensional electron gas in $\mathrm{GaAs/Al}_x\mathrm{Ga}_{1-x}\mathrm{As}$ heterostructures", Phys. Rev. B **56**, R1676–R1679 (1997).

[122] S. Jezouin, F. D. Parmentier, A. Anthore, U. Gennser, A. Cavanna, Y. Jin, and F. Pierre, "Quantum limit of heat flow across a single electronic channel", Science **342**, 601–604 (2013).

[123] G. Le Breton, R. Delagrange, Y. Hong, M. Garg, K. Watanabe, T. Taniguchi, R. Ribeiro-Palau, P. Roulleau, P. Roche, and F. D. Parmentier, "Heat equilibration of integer and fractional quantum hall edge modes in graphene", Phys. Rev. Lett. **129**, 116803 (2022).

[124] K. C. Fong and K. C. Schwab, "Ultrasensitive and wide-bandwidth thermal measurements of graphene at low temperatures", Phys. Rev. X **2**, 031006 (2012).

[125] K. C. Fong, E. E. Wollman, H. Ravi, W. Chen, A. A. Clerk, M. D. Shaw, H. G. Leduc, and K. C. Schwab, "Measurement of the electronic thermal conductance channels and heat capacity of graphene at low temperature", Phys. Rev. X **3**, 041008 (2013).

[126] R. M. Hill and A. K. Jonscher, "Dc and ac conductivity in hopping electronic systems", J. Non-Cryst. Solids **32**, 53–69 (1979).

[127] S. Kaur, T. Chanda, K. R. Amin, D. Sahani, K. Watanabe, T. Taniguchi, U. Ghorai, Y. Gefen, G. J. Sreejith, and A. Bid, "Universality of quantum phase transitions in the integer and fractional quantum hall regimes", Nat. Commun. **15** (2024).

[128] C.-C. Yeh, P.-C. Liao, Y. Yang, W.-C. Lin, A. R. Panna, A. F. Rigosi, R. E. Elmquist, and C.-T. Liang, "Conformity experiment on inelastic scattering exponent of electrons in two dimensions", Phys. Rev. Lett. **133**, 096302 (2024).

[129] A. Zhang, T. Röper, M. Garg, K. Watanabe, T. Taniguchi, C. Altimiras, P. Roche, E. Bocquillon, O. Maillet, and F. D. Parmentier, "Non-universal localization transition in the quantum hall effect probed through broken-symmetry states of graphene", arXiv 2509.20163 (2025).

[130] Y. Zhang, Y.-W. Tan, H. L. Stormer, and P. Kim, "Experimental observation of the quantum hall effect and berry's phase in graphene", Nature **438**, 201–204 (2005).

[131] K. S. Novoselov, A. K. Geim, S. V. Morozov, D. Jiang, M. I. Katsnelson, I. V. Grigorieva, S. V. Dubonos, and A. A. Firsov, "Two-dimensional gas of massless dirac fermions in graphene", Nature **438**, 197–200 (2005).

[132] H. Akera, "Slow dynamics in the breakdown of the quantum hall effect", J. Phys. Soc. Jpn. **78**, 023708 (2009).

[133] E. Bocquillon, V. Freulon, F. D. Parmentier, J. M. Berroir, B. Placais, C. Wahl, J. Rech, T. Jonckheere, T. Martin, C. Grenier, D. Ferraro, P. Degiovanni, and G. Feve, "Electron quantum optics in ballistic chiral conductors", Annalen Der Physik **526**, 1–30 (2014).

[134] A. C. Mahoney, J. I. Colless, S. J. Pauka, J. M. Hornibrook, J. D. Watson, G. C. Gardner, M. J. Manfra, A. C. Doherty, and D. J. Reilly, "On-chip microwave quantum hall circulator", Phys. Rev. X **7**, 011007 (2017).

[135] M. M. Fogler, A. A. Koulakov, and B. I. Shklovskii, "Ground state of a two-dimensional electron liquid in a weak magnetic field", Phys. Rev. B **54**, 1853–1871 (1996).

[136] B. Huckestein and B. Kramer, "One-parameter scaling in the lowest landau band: precise determination of the critical behavior of the localization length", Phys. Rev. Lett. **64**, 1437–1440 (1990).

[137] A. M. M. Pruisken, "Universal singularities in the integral quantum hall effect", Phys. Rev. Lett. **61**, 1297–1300 (1988).

[138] B. Huckestein, "Scaling theory of the integer quantum hall effect", Rev. Mod. Phys. **67**, 357–396 (1995).

[139] H. P. Wei, D. C. Tsui, M. A. Paalanen, and A. M. M. Pruisken, "Experiments on delocalization and university in the integral quantum hall effect", Phys. Rev. Lett. **61**, 1294–1296 (1988).

[140] M. D. Blumenthal, B. Kaestner, L. Li, S. Giblin, T. J. B. M. Janssen, M. Pepper, D. Anderson, G. Jones, and D. A. Ritchie, "Gigahertz quantized charge pumping", Nat. Phys. **3**, 343–347 (2007).

[141] B. Kaestner, V. Kashcheyevs, S. Amakawa, M. D. Blumenthal, L. Li, T. J. B. M. Janssen, G. Hein, K. Pierz, T. Weimann, U. Siegner, and H. W. Schumacher, "Single-parameter nonadiabatic quantized charge pumping", Phys. Rev. B **77**, 153301 (2008).

[142] S. Giblin, M. Kataoka, J. Fletcher, P. See, T. Janssen, J. Griffiths, G. Jones, I. Farrer, and D. Ritchie, "Towards a quantum representation of the ampere using single electron pumps", Nat. Commun. **3**, 930 (2012).

[143] J. Dubois, T. Jullien, F. Portier, P. Roche, A. Cavanna, Y. Jin, W. Wegscheider, P. Roulleau, and D. C. Glattli, "Minimal-excitation states for electron quantum optics using levitons", Nature **502**, 659–663 (2013).

[144] J. Nakamura, S. Liang, G. C. Gardner, and M. J. Manfra, "Direct observation of anyonic braiding statistics", Nat. Phys. **16**, 931–936 (2020).

[145] M. Ruelle, E. Frigerio, E. Baudin, J.-M. Berroir, B. Plaçais, B. Grémaud, T. Jonckheere, T. Martin, J. Rech, A. Cavanna, U. Gennser, Y. Jin, G. Ménard, and G. Fève, "Time-domain braiding of anyons", Science **389**, eadm7695 (2025).

[146] L. Banszerus, A. Rothstein, T. Fabian, S. Möller, E. Icking, S. Trellenkamp, F. Lentz, D. Neumaier, K. Watanabe, T. Taniguchi, F. Libisch, C. Volk, and C. Stampfer, "Electron–hole crossover in gate-controlled bilayer graphene quantum dots", Nano Letters **20**, 7709–7715 (2020).

[147] T. Dirks, T. L. Hughes, S. Lal, B. Uchoa, Y.-F. Chen, C. Chialvo, P. M. Goldbart, and N. Mason, "Transport through Andreev bound states in a graphene quantum dot", Nat. Phys. **7**, 386–390 (2011).

[148] V. E. Calado, S. Goswami, G. Nanda, M. Diez, A. R. Akhmerov, K. Watanabe, T. Taniguchi, T. M. Klapwijk, and L. M. K. Vandersypen, "Ballistic josephson junctions in edge-contacted graphene", Nature Nanotech **10**, 761–764 (2015).

[149] F. Battista and P. Samuelsson, "Proposal for nonlocal electron-hole turnstile in the quantum hall regime", Phys. Rev. B **83** (2011).

[150] N. Maire, F. Hohls, B. Kaestner, K. Pierz, H. W. Schumacher, and R. J. Haug, "Noise measurement of a quantized charge pump", Appl. Phys. Lett. **92**, 082112 (2008).

[151] C. Bäuerle, D. Christian Glattli, T. Meunier, F. Portier, P. Roche, P. Roulleau, S. Takada, and X. Waintal, "Coherent control of single electrons: a review of current progress", Rep. Prog. Phys. **81**, 056503 (2018).

[152] L. S. Levitov, H. Lee, and G. B. Lesovik, "Electron counting statistics and coherent states of electric current", J. Math. Phys. **37**, 4845–4866 (1996).

[153] M. Büttiker, H. Thomas, and A. Prêtre, "Mesoscopic capacitors", Phys. Lett. A **180**, 364–369 (1993).

[154] E. Bocquillon, "Electron quantum optics in quantum Hall edge channels", PhD thesis (Université Pierre et Marie Curie - Paris VI, Nov. 2012).

[155] K. S. Novoselov, A. K. Geim, S. V. Morozov, D. Jiang, Y. Zhang, S. V. Dubonos, I. V. Grigorieva, and A. A. Firsov, "Electric field effect in atomically thin carbon films", Science **306**, 666–669 (2004).

[156] E. McCann, "Asymmetry gap in the electronic band structure of bilayer graphene", Phys. Rev. B **74**, 161403 (2006).

[157] R. Garreis, "Time-resolved charge detection of electrostatically defined quantum dots in bilayer graphene", PhD thesis (ETH Zurich, 2023).

[158] B. Trauzettel, D. V. Bulaev, D. Loss, and G. Burkard, "Spin qubits in graphene quantum dots", Nat. Phys. **3**, 192–196 (2007).

[159] R. Garreis, C. Tong, J. Terle, M. J. Ruckriegel, J. D. Gerber, L. M. Gächter, K. Watanabe, T. Taniguchi, T. Ihn, K. Ensslin, and W. W. Huang, "Long-lived valley states in bilayer graphene quantum dots", Nat. Phys. **20**, 428–434 (2024).

[160] L. Banszerus, S. Möller, K. Hecker, E. Icking, K. Watanabe, T. Taniguchi, F. Hassler, C. Volk, and C. Stampfer, "Particle-hole symmetry protects spin-valley blockade in graphene quantum dots", Nature **618**, 51–56 (2023).

[161] C. L. Kane and E. J. Mele, "Quantum spin hall effect in graphene", Phys. Rev. Lett. **95**, 226801 (2005).

[162] L. Banszerus, S. Möller, C. Steiner, E. Icking, S. Trellenkamp, F. Lentz, K. Watanabe, T. Taniguchi, C. Volk, and C. Stampfer, "Spin-valley coupling in single-electron bilayer graphene quantum dots", Nat. Commun. **12**, 5250 (2021).

[163] L. Banszerus, K. Hecker, L. Wang, S. Möller, K. Watanabe, T. Taniguchi, G. Burkard, C. Volk, and C. Stampfer, "Phonon-limited valley lifetimes in single-particle bilayer graphene quantum dots", Phys. Rev. B **112**, 035409 (2025).

[164] A. Knothe and V. Fal'ko, "Quartet states in two-electron quantum dots in bilayer graphene", Phy. Rev. B **101**, 235423 (2020).

[165] E. Bonet, M. M. Deshmukh, and D. C. Ralph, "Solving rate equations for electron tunneling via discrete quantum states", Phys. Rev. B **65**, 045317 (2002).

[166] L. Banszerus, "Gate-defined quantum dots in bilayer graphene", PhD thesis (RWTH Aachen University, 2022).

[167] S. W. H. Möller, "Multi-particle states in gate-defined bilayer graphene quantum dots", PhD thesis (RWTH Aachen University, 2024).

[168] L. Banszerus, B. Frohn, T. Fabian, S. Somanchi, A. Epping, M. Müller, D. Neumaier, K. Watanabe, T. Taniguchi, F. Libisch, B. Beschoten, F. Hassler, and C. Stampfer, "Observation of the spin-orbit gap in bilayer graphene by one-dimensional ballistic transport", Phys. Rev. Lett. **124**, 177701 (2020).

[169] M. Eich, F. š. Herman, R. Pisoni, H. Overweg, A. Kurzmann, Y. Lee, P. Rickhaus, K. Watanabe, T. Taniguchi, M. Sigrist, T. Ihn, and K. Ensslin, "Spin and valley states in gate-defined bilayer graphene quantum dots", Phys. Rev. X **8**, 031023 (2018).

[170] L. Banszerus, K. Hecker, E. Icking, S. Trellenkamp, F. Lentz, D. Neumaier, K. Watanabe, T. Taniguchi, C. Volk, and C. Stampfer, "Pulsed-gate spectroscopy of single-electron spin states in bilayer graphene quantum dots", Phys. Rev. B **103**, L081404 (2021).

[171] L. M. Gächter, R. Garreis, J. D. Gerber, M. J. Ruckriegel, C. Tong, B. Kratochwil, F. K. de Vries, A. Kurzmann, K. Watanabe, T. Taniguchi, T. Ihn, K. Ensslin, and W. W. Huang, "Single-shot spin readout in graphene quantum dots", PRX Quantum **3**, 020343 (2022).

[172] R. Garreis, J. D. Gerber, V. Stará, C. Tong, C. Gold, M. Röösli, K. Watanabe, T. Taniguchi, K. Ensslin, T. Ihn, and A. Kurzmann, "Counting statistics of single electron transport in bilayer graphene quantum dots", Phys. Rev. Res. **5**, 013042 (2023).

[173] L. Banszerus, S. Möller, E. Icking, K. Watanabe, T. Taniguchi, C. Volk, and C. Stampfer, "Single-electron double quantum dots in bilayer graphene", Nano Letters **20**, 2005–2011 (2020).

[174] B. Skinner and B. I. Shklovskii, "Anomalously large capacitance of a plane capacitor with a two-dimensional electron gas", Phys. Rev. B **82**, 155111 (2010).

[175] S. Adam, E. H. Hwang, and S. Das Sarma, "Two-dimensional transport and screening in topological insulator surface states", Phys. Rev. B **85**, 235413 (2012).

[176] S. Adam, E. H. Hwang, V. M. Galitski, and S. Das Sarma, "A self-consistent theory for graphene transport", PNAS **104**, 18392–18397 (2007).

[177] S. Das Sarma, S. Adam, E. H. Hwang, and E. Rossi, "Electronic transport in two-dimensional graphene", Rev. Mod. Phys. **83**, 407–470 (2011).

[178] C.-P. Lu, M. Rodriguez-Vega, G. Li, A. Luican-Mayer, K. Watanabe, T. Taniguchi, E. Rossi, and E. Y. Andrei, "Local, global, and nonlinear screening in twisted double-layer graphene", PNAS **113**, 6623–6628 (2016).

[179] D. Domaretskiy, Z. Wu, V. H. Nguyen, N. Hayward, I. Babich, X. Li, E. Nguyen, J. Barrier, K. Indykiewicz, W. Wang, R. V. Gorbachev, N. Xin, K. Watanabe, T. Taniguchi, L. Hague, V. I. Fal'ko, I. V. Grigorieva, L. A. Ponomarenko, A. I. Berdyugin, and A. K. Geim, "Proximity screening greatly enhances electronic quality of graphene", Nature **644**, 646–651 (2025).

[180] N. Kumada, N.-H. Tu, K.-i. Sasaki, T. Ota, M. Hashisaka, S. Sasaki, K. Onomitsu, and K. Muraki, "Suppression of gate screening on edge magnetoplasmons by highly resistive ZnO gate", Phys. Rev. B **101**, 205205 (2020).

[181] E. Berg, Y. Oreg, E.-A. Kim, and F. Von Oppen, "Fractional charges on an integer quantum hall edge", Phys. Rev. Lett. **102**, 236402 (2009).

[182] C. Wahl, J. Rech, T. Jonckheere, and T. Martin, "Interactions and charge fractionalization in an electronic hong-ou-mandel interferometer", Phys. Rev. Lett. **112**, 046802 (2014).

[183] T. Morel, J.-Y. M. Lee, H.-S. Sim, and C. Mora, "Fractionalization and anyonic statistics in the integer quantum hall collider", Phys. Rev. B **105**, 075433 (2022).

[184] J.-Y. M. Lee, C. Han, and H.-S. Sim, "Fractional mutual statistics on integer quantum hall edges", Phys. Rev. Lett. **125**, 196802 (2020).

[185] S.-i. Tomonaga, "Remarks on bloch's method of sound waves applied to many-fermion problems", Prog. Theor. Phys. **5**, 544–569 (1950).

[186] J. M. Luttinger, "An exactly soluble model of a many-fermion system", J. Math. Phys. **4**, 1154–1162 (1963).

[187] R. de-Picciotto, M. Reznikov, M. Heiblum, V. Umansky, G. Bunin, and D. Mahalu, "Direct observation of a fractional charge", Nature **389**, 162–164 (1997).

[188] H. Inoue, A. Grivnin, N. Ofek, I. Neder, M. Heiblum, V. Umansky, and D. Mahalu, "Charge fractionalization in the integer quantum hall effect", Phys. Rev. Lett. **112**, 166801 (2014).

[189] L. Saminadayar, D. C. Glattli, Y. Jin, and B. Etienne, "Observation of the $e/3$ fractionally charged laughlin quasiparticle", Phys. Rev. Lett. **79**, 2526–2529 (1997).

[190] A. F. Andreev, "The thermal conductivity of the intermediate state in superconductors", Soviet Physics-JETP **19**, 1228–1232 (1964).

[191] G. E. Blonder, M. Tinkham, and T. M. Klapwijk, "Transition from metallic to tunneling regimes in superconducting microconstrictions: excess current, charge imbalance, and supercurrent conversion", Phys. Rev. B **25**, 4515–4532 (1982).

[192] D. V. Averin, G. Wang, and A. S. Vasenko, "Time-dependent Andreev reflection", Phys. Rev. B **102**, 144516 (2020).

[193] B. Roussel, P. Burset, and C. Flindt, "Wigner representation of Andreev-reflected charge pulses", Phys. Rev. B **112**, 014506 (2025).

[194] M. Hays, G. De Lange, K. Serniak, D. J. Van Woerkom, D. Bouman, P. Krogstrup, J. Nygård, A. Geresdi, and M. H. Devoret, "Direct microwave measurement of Andreev-bound-state dynamics in a semiconductor-nanowire josephson junction", Phys. Rev. Lett. **121**, 047001 (2018).

[195] P. Ram, D. Beckmann, R. Danneau, and W. Belzig, "Andreev and normal reflections in gapped bilayer graphene–superconductor junctions", Phys. Rev. B **108**, 184510 (2023).

[196] W.-T. Lu and Q.-F. Sun, "Cone-dependent retro- and specular Andreev reflections in aa-stacked bilayer graphene", Phys. Rev. B **108**, 195425 (2023).

[197] A. Soori, M. R. Sahu, A. Das, and S. Mukerjee, "Enhanced specular Andreev reflection in bilayer graphene", Phys. Rev. B **98**, 075301 (2018).

[198] H. Hoppe, U. Zülicke, and G. Schön, "Andreev reflection in strong magnetic fields", Phys. Rev. Lett. **84**, 1804–1807 (2000).

List of publications

Publications as a first author

- **Torsten Röper**, Hugo Thomas, Daniel Rosenbach, Anjana Uday, Gertjan Lippertz, Anne Denis, Pascal Morfin, Alexey A. Taskin, Yoichi Ando, and Erwann Bocquillon, "Propagation, dissipation, and breakdown in quantum anomalous hall edge states probed by microwave edge plasmons", Phys. Rev. B 110, L161403 (2024).

- **Torsten Röper**, Daniel Rosenbach, Achim Rosch, Alexey A. Taskin, Yoichi Ando, and Erwann Bocquillon, "Breakdown of the quantum anomalous Hall effect under microwave drives",Phys. Rev. B 112, L201301 (2025).

- **Torsten Röper**, Aifei Zhang, Kenji Watanabe, Takashi Taniguchi, Olivier Maillet, François D. Parmentier, Erwann Bocquillon, "Non-Ohmic to Ohmic crossover in the breakdown of the quantum Hall states in graphene under broadband excitations", arXiv.2509.19978 (2025).

Publications as a contributing author

- Alina Rupp, Daniel Rosenbach, **Torsten Röper**, Dominik Hoborka, Alexey A. Taskin, Yoichi Ando, Erwann Bocquillon, "Dynamics of current-induced switching in the quantum anomalous Hall effect", Phys. Rev. Lett., accepted. (2026).

- Aifei Zhang, **Torsten Röper**, Manjari Garg, Kenji Watanabe, Takashi Taniguchi, Carles Altimiras, Patrice Roche, Erwann Bocquillon, Olivier Maillet, François D. Parmentier, 'Non-universal localization transition in the quantum Hall effect probed through broken-symmetry states of graphene', arXiv.2509.20163 (2025).

Acknowledgements

I feel very lucky and privileged to be submitting this thesis. I am grateful for having the opportunity to pursue my research and to travel the world to present it. This would not have been possible without the many people who supported me along the way, and I would like to express my sincere gratitude to all of them.

First and foremost, I would like to thank my supervisor, Erwann. This PhD would not have been possible without your support and guidance. Thank you for your continuous trust and support throughout these years and for teaching me so much about microwave engineering and transport experiments. I truly appreciated our discussions and always felt comfortable coming to you with questions or ideas.

I would also like to thank Daniel. You have supported me since my bachelor's studies (with some interruptions) and have always been there for me. I greatly enjoyed working with you and will miss having you around at the institute. And I will always be there if you want to cut a wafer!

Special thanks go to my former master's student and now fellow PhD student, Dominik. I enjoyed our endless discussions, whether about fractionalization or inventing a new standard time. You are not only an excellent physicist but also a good friend.

I would like to thank Alina for being such a supportive colleague and team player. Thank you for all your help. I am also grateful to all the other group members I had the pleasure of working with: Hugo, Ricardo, Michael, Doga, Mélanie, Calvin, Manya, Jagoda, and Femke. I truly enjoyed working with you and spending time together at group outings, football games, and retreats. You made Cologne feel like home. In particular, I would like to thank Mélanie and Femke for carefully proofreading parts of this thesis and for their thoughtful feedback.

I would like to thank Prof. Yoichi Ando and all the members of his group for welcoming us and for their continuous support. In particular, I thank the V-BST gang — Alexey, Gertjan, Anjana, and Bibek — for welcoming me, growing the layers, helping with fabrication, and discussing my results.

Special thanks also go to the microwave experts — Joachim, Chris, and Luc. Whether I needed access to a VNA or technical advice, you were always there to help.
My sincere thanks also go to Prof. Christoph Stampfer and his group in Aachen for fabricating the quantum dots. In particular, I thank Katrin and Hubert for the many hours spent on fabrication and for the numerous Zoom discussions about the measurements. I am also grateful to Annika and Cornelius for their advice and insightful discussions on quantum dot experiments.
I would like to thank the staff of the institute, including Carmen, Matteo, Harald, and Timur, as well as the electronic and mechanical workshops, for their essential support.
I am deeply grateful to my collaborators in Paris, François, Olivier, and Aifei. I could not have wished for a more fruitful collaboration. I truly enjoyed our scientific exchanges. I also thank Prof. Norio Kumada for the stimulating discussions and Prof. Masayuki Hashisaka for inviting me to Japan. I am also thankful to Prof. Achim Rosch for his theoretical support and valuable discussions.
I would like to thank Prof. Reinhold Egger, Prof. Simon Trebst, and Prof. Gwendal Fève for serving on my committee. I am especially grateful to Gwendal for the many fruitful discussions throughout my PhD and for traveling from Paris for my defense.
Finally, I would like to thank my family and friends. I am deeply grateful to my parents and my brother for their unconditional support throughout my life. You taught me discipline and humbleness, and without you, I would not be where I am today. I also thank the Bauwagen crew for being like a second family to me. I know you may not always know what I am working on, but you have always listened and supported me. Thanks also go to my close friend and former roommate, Daniel. You have been like a brother to me for the last 10 years! Robin and Benno, I am very glad that we ended up sharing this PhD journey. It is not always easy, but going through it together made it much lighter.
And last but not least, I want to thank the most important person in my life, Noka. Thank you for always believing in me and standing by my side. No matter how stressful or difficult things were, you always made me smile when I came home. I know I can always count on you!